NASA Technical Memorandum 110148

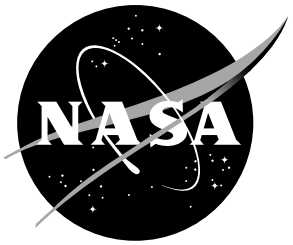

# Pressure Distributions From Subsonic Tests of a NACA 0012 Semispan Wing Model

Zachary T. Applin
*Langley Research Center, Hampton, Virginia*

September 1995

National Aeronautics and
Space Administration
Langley Research Center
Hampton, Virginia 23681-0001

# Summary

An unswept, semispan wing model incorporating a NACA 0012 airfoil section was tested in the Langley 14- by 22-Foot Subsonic Tunnel. This report contains pressure data which document effects of wing configuration and free-stream conditions on wing pressure distribution. The untwisted wing incorporated a full-span, leading-edge Krueger flap and a full-span, single-slotted trailing-edge flap. Three wing configurations were tested: cruise, trailing-edge flap only, and high-lift (Krueger flap and trailing-edge flap deployed). The trailing-edge flap was tested at a deflection angle of 40° and the Krueger flap at a deflection of 55°.

Tests were conducted at free-stream dynamic pressures of 15, 30 and 60 psf, with corresponding chord Reynolds numbers of $1.22 \times 10^6$ to $2.11 \times 10^6$, and Mach numbers of 0.12 to 0.20. Angles of attack presented range from 0° to 20°, depending on the wing configuration. The data are presented without analysis.


# Introduction

An unswept, semispan wing model incorporating a NACA 0012 airfoil section was tested in the Langley 14- by 22-Foot Subsonic Tunnel. This report contains pressure data which document effects of wing configuration and free-stream conditions on wing pressure distribution. The untwisted wing incorporated a full-span, leading-edge Krueger flap and a full-span, single-slotted trailing-edge flap. Detailed wing surface pressure distributions are presented for three wing configurations: cruise, trailing-edge flap only, and high-lift (Krueger flap and trailing-edge flap deployed). The trailing-edge flap was tested at a deflection angle of 40° and the Krueger flap at a deflection of 55°.

Tests were conducted at free-stream dynamic pressures of 15, 30 and 60 psf, with corresponding chord Reynolds numbers of $1.22 \times 10^6$ to $2.11 \times 10^6$, and Mach numbers of 0.12 to 0.20. Angles of attack presented range from 0° to 20°, depending on wing configuration. The data are presented without analysis. The report along with tabulated data are available electronically at the following URL address:

http://techreports.larc.nasa.gov/ltrs/ltrs.html

# Symbols

All measurements and calculations were made in U.S. Customary Units.

$b$ wing semispan, 116.01 in.

$C_p$ pressure coefficient

$c$ reference wing chord, 39.37 in.

$M$ free-stream Mach number

$q$ free-stream dynamic pressure, psf

$R$ Reynolds number based on reference wing chord

$x$ chordwise distance aft of leading edge, in.

$y$ spanwise distance from model centerline, in.

$z_l$ lower surface ordinate, in.

$z_u$ upper surface ordinate, in.

$\alpha$ angle of attack of model reference centerline, positive nose up, deg

$\delta_f$ trailing-edge flap deflection angle, deg

$\delta_K$ leading-edge Krueger deflection angle, deg

$\eta$ nondimensional semispan location

# Test Setup

The unswept semispan wing model was tested in the Langley 14- by 22-Foot Subsonic Tunnel which is a closed, single-return, atmospheric wind tunnel with a test section 14.50 ft high by 21.75 ft wide by 50.00 ft long. (See ref. 1) The test-section dynamic pressure is continuously variable from 0 to 144 psf. The tunnel is equipped with a floor boundary-layer removal system consisting of a floor-mounted suction grid located 8.2 ft upstream of the wing leading edge. The suction grid spans the floor of

the test section between the walls and reduces the boundary-layer thickness to approximately 1.6 in. at the wing location for the empty tunnel condition.

The model was mounted vertically, protruding through the floor, on a six-component stain-gauge balance which was located below a 15.8-ft-diameter turntable. The turntable could be rotated throughout the angle-of-attack range of the wing. Angle of attack of all configurations was referenced to the wing reference plane of the cruise configuration. The angle of the turntable was detected by a digital shaft encoder geared to the turntable mechanism and provided an angle-of-attack accuracy to within ±0.02°.

The 116.01 in. semispan, rectangular, untwisted wing model had a 39.37-in. chord incorporating a NACA 0012 airfoil section. The model was designed to be rigid at the conditions tested, so aeroelastic deflections are assumed to be minimal. The Krueger flap was 0.12$c$ and the trailing-edge flap was 0.30$c$. Both high-lift components were full span and had rounded tips. The gap and overlap of the Krueger, relative to the wing, was 0.012$c$ and 0.016$c$, respectively; the gap and overlap for the trailing-edge flap were 0.02$c$ and 0.00$c$, respectively. Gap and overlap are defined according to the procedure in reference 2. Pressure tap locations for the cruise wing, main wing of the high-lift configuration, and the trailing-edge flap are presented in tables 1-3. Surface coordinates for the leading-edge Krueger, which has no pressure taps, are presented in table 4. The chordwise distance, $x$, is relative to the leading edge of each component. Sketches of the wing model planform and cross-sections of wing configurations tested are shown in figures 1 and 2, respectively. Photographs of the model installed in the tunnel are presented in figure 3.

Boundary-layer transition strips 1/8 in. wide were applied using No. 60 grit. The transition roughness was sized according to the procedure outlined in reference 3. These transition strips were located on both the upper and lower surfaces at approximately 2 in. downstream of the wing leading edge for the cruise wing and main component of the high-lift configuration, and extended across the entire span. For the high-lift configuration, the same grit was used at approximately 1 in. downstream of the leading edge

on the Krueger and trailing-edge flaps. The grit location and size used on this model was exactly the same as the model reported in reference 4. The start of boundary-layer transition, forced by the grit application, was confirmed on that model with sublimating chemicals.

Pressure measurements were obtained with an electronically scanned pressure (ESP) system. This system consisted of modules which contained a 720-psf-range silicon pressure transducer for every port. Manufacturer's stated accuracy for the pressure system is ±0.72 psf (0.1% of full scale). The ESP system has the capability for online calibration of each pressure transducer to maintain a high degree of accuracy. The ESP system scans through all transducers at rates of up to 20 kHz, acquiring all pressure data at nearly the same instant. These data are passed to the tunnel data acquisition system at the rate of 1 sample per second. The data acquisition system averages 20 of these samples into each data point.

# Test Procedures

Tests were conducted in the closed, solid-wall test section at free-stream dynamic pressures of 15 to 60 psf, with corresponding Reynolds numbers of $2.36 \times 10^6$ to $4.71 \times 10^6$, based on reference wing chord. Mach numbers corresponding to the above dynamic pressures were 0.10 to 0.20. The angle-of-attack range varied with wing configuration, free-stream dynamic pressure, and was also limited by the load capacity and stability of the balance and supporting hardware.

Wing and wake blockage corrections, determined according to reference 5, were used to correct free-stream dynamic pressure. No corrections were made to the data for tunnel flow angularity.

# Presentation of Results

Surface pressure distributions for each wing component are presented in figures 4 through 12 as pressure coefficient ($C_p$) versus nondimensional chord location ($x/c$). Chord locations are nondimensionalized by the reference wing chord. The data are presented without analysis.

# References

1. Gentry, Garl L., Jr.; Quinto, P. Frank; Gatlin, Gregory M.; and Applin, Zachary T.: *The Langley 14- by 22-Foot Subsonic Tunnel: Description, Flow Characteristics, and Guide for Users*. NASA TP-3008, 1990.

2. Morgan, Harry L., Jr.; and Paulson, John W., Jr.: *Low-Speed Aerodynamic Performance of a High-Aspect-Ratio Supercritical-Wing Transport Model Equipped With Full-Span Slat and Part-Span Double-Slotted Flaps*. NASA TP-1580, 1979.

3. Braslow, Albert L.; and Knox, Eugene C.: *Simplified Method for Determination of Critical Height of Distributed Roughness Particles for Boundary-Layer Transition at Mach Numbers From 0 to 5*. NASA TN 4363, 1958.

4. Applin, Zachary T.; and Gentry, Garl L., Jr.: *Experimental and Theoretical Aerodynamic Characteristics of a High-Lift Semispan Wing Model*. NASA TP-2990, 1990.

5. Herriot, John G.: *Blockage Corrections for Three-Dimensional-Flow Closed-Throat Wind Tunnels, With Consideration of the Effect of Compressibility.* NACA Rep. 995, 1950. (Supersedes NACA RM A7B28.)

Table 1. Pressure tap locations for cruise wing.

| $\frac{x}{c}$ | $\frac{z_u}{c}$ | $\frac{z_l}{c}$ |
|---|---|---|
| 0.0000 | 0.0000 | 0.0000 |
| .0019 | .0078 | -.0078 |
| .0051 | .0124 | -.0124 |
| .0084 | .0158 | -.0158 |
| .0120 | .0186 | -.0186 |
| .0155 | .0211 | -.0211 |
| .0202 | .0237 | -.0237 |
| .0267 | .0269 | -.0269 |
| .0434 | .0335 | -.0335 |
| .0680 | .0404 | -.0404 |
| .0964 | .0462 | -.0462 |
| .1277 | .0509 | -.0509 |
| .1616 | .0546 | -.0546 |
| .1980 | .0573 | -.0573 |
| .2363 | .0590 | -.0590 |
| .2770 | .0599 | -.0599 |
| .3194 | .0599 | -.0599 |
| .3638 | .0592 | -.0592 |
| .4103 | .0576 | -.0576 |
| .4585 | .0554 | -.0554 |
| .5090 | .0524 | -.0524 |
| .5611 | .0487 | -.0487 |
| .6155 | .0443 | -.0443 |
| .6716 | .0394 | -.0394 |
| .7282 | .0338 | -.0338 |
| .7860 | .0278 | -.0278 |
| .8439 | .0212 | -.0212 |
| .9004 | .0144 | -.0144 |
| .9562 | .0072 | -.0072 |
| .9962 | .0018 | -.0018 |
| 1.0000 | 0.0000 | 0.0000 |

Table 2. Pressure tap locations for high-lift configuration main wing.

| $\frac{x}{c}$ | $\frac{z_u}{c}$ |
|---|---|
| 0.0000 | 0.0000 |
| .0019 | .0078 |
| .0051 | .0124 |
| .0084 | .0158 |
| .0120 | .0186 |
| .0155 | .0211 |
| .0202 | .0237 |
| .0267 | .0269 |
| .0434 | .0335 |
| .0680 | .0404 |
| .0964 | .0462 |
| .1277 | .0509 |
| .1616 | .0546 |
| .1980 | .0573 |
| .2363 | .0590 |
| .2770 | .0599 |
| .3194 | .0599 |
| .3638 | .0592 |
| .4103 | .0576 |
| .4585 | .0554 |
| .5090 | .0524 |
| .5611 | .0487 |
| .6155 | .0443 |
| .6716 | .0394 |
| .7282 | .0338 |
| .7860 | .0278 |
| .8439 | .0212 |
| .8700 | .0181 |

| $\frac{x}{c}$ | $\frac{z_l}{c}$ |
|---|---|
| 0.0000 | 0.0000 |
| .0019 | -.0078 |
| .0051 | -.0124 |
| .0084 | -.0158 |
| .0120 | -.0186 |
| .0155 | -.0211 |
| .0202 | -.0237 |
| .0267 | -.0269 |
| .0434 | -.0335 |
| .0680 | -.0404 |
| .0964 | -.0462 |
| .1277 | -.0509 |
| .1616 | -.0546 |
| .1980 | -.0573 |
| .2363 | -.0590 |
| .2770 | -.0599 |
| .3194 | -.0599 |
| .3638 | -.0592 |
| .4103 | -.0576 |
| .4585 | -.0554 |
| .5090 | -.0524 |
| .5611 | -.0487 |
| .6155 | -.0443 |
| .6433 | -.0396 |
| .6716 | -.0301 |
| .6996 | -.0163 |
| .7428 | .0068 |
| .7860 | .0156 |
| .8292 | .0184 |
| .8650 | .0174 |
| .8700 | .0181 |

Table 3. Pressure tap locations for trailing-edge flap.

| $\frac{x}{c}$ | $\frac{z_u}{c}$ |
|---|---|
| 0.0000 | 0.0000 |
| .0015 | .0046 |
| .0030 | .0105 |
| .0120 | .0154 |
| .0226 | .0210 |
| .0452 | .0281 |
| .0901 | .0333 |
| .1355 | .0323 |
| .1806 | .0267 |
| .2258 | .0179 |
| .2709 | .0080 |
| .2950 | .0027 |

| $\frac{x}{c}$ | $\frac{z_l}{c}$ |
|---|---|
| 0.0000 | 0.0000 |
| .0015 | -.0056 |
| .0060 | -.0090 |
| .0151 | -.0109 |
| .0452 | -.0108 |
| .1355 | -.0085 |
| .2258 | -.0051 |
| .2950 | -.0016 |

Table 4. Surface coordinates of leading-edge Krueger flap.

| $\frac{x}{c}$ | $\frac{z_u}{c}$ | $\frac{z_l}{c}$ |
|---|---|---|
| 0.0000 | 0.0000 | 0.0000 |
| .0011 | .0056 | -.0044 |
| .0022 | .0078 | -.0067 |
| .0033 | .0100 | -.0083 |
| .0044 | .0122 | -.0094 |
| .0056 | .0139 | -.0108 |
| .0067 | .0150 | -.0117 |
| .0078 | .0161 | -.0122 |
| .0089 | .0172 | -.0128 |
| .0100 | .0183 | -.0133 |
| .0111 | .0194 | -.0139 |
| .0133 | .0206 | -.0142 |
| .0156 | .0217 | -.0141 |
| .0178 | .0228 | -.0136 |
| .0200 | .0239 | -.0117 |
| .0222 | .0244 | .0000 |
| .0244 | .0256 | .0200 |
| .0267 | .0261 | .0233 |
| .0289 | .0267 | .0250 |
| .0311 | .0272 | .0261 |
| .0333 | .0276 | .0264 |
| .0389 | .0279 | .0268 |
| .0444 | .0280 | .0269 |
| .0500 | .0276 | .0264 |
| .0556 | .0267 | .0256 |
| .0611 | .0256 | .0244 |
| .0667 | .0242 | .0231 |
| .0722 | .0222 | .0211 |
| .0778 | .0206 | .0194 |
| .0833 | .0183 | .0172 |
| .0889 | .0156 | .0144 |
| .0944 | .0133 | .0122 |
| .1000 | .0109 | .0098 |
| .1056 | .0080 | .0069 |
| .1111 | .0053 | .0042 |
| .1167 | .0022 | .0011 |
| .1200 | .0006 | -.0006 |

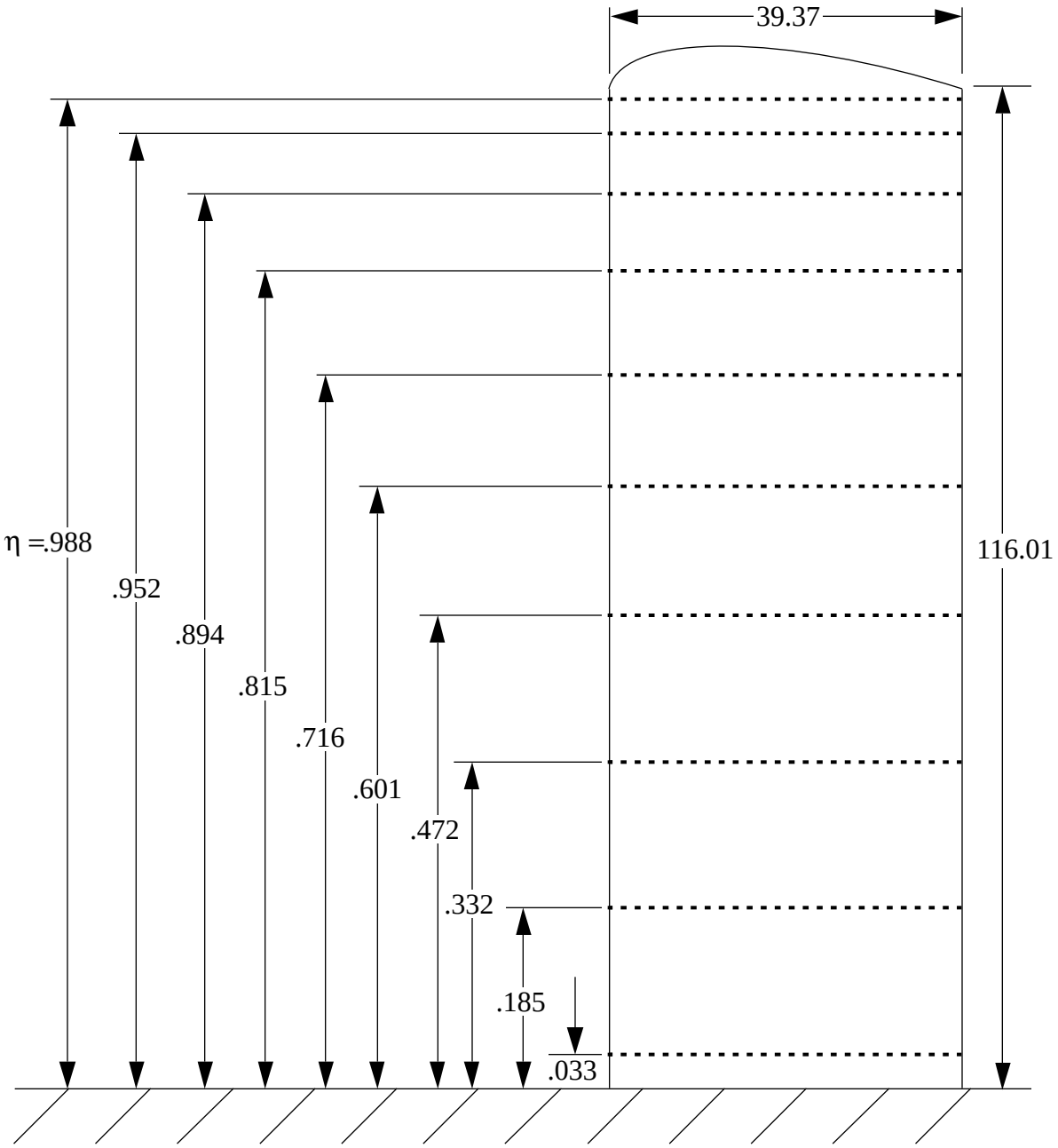


Figure 1. Plan view of semispan wing indicating pressure tap stations.
(All dimensions in inches.)

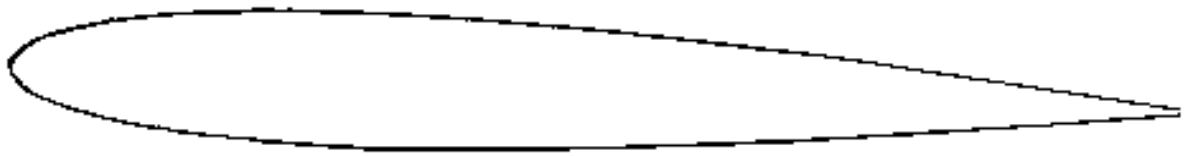

(a) Cruise.

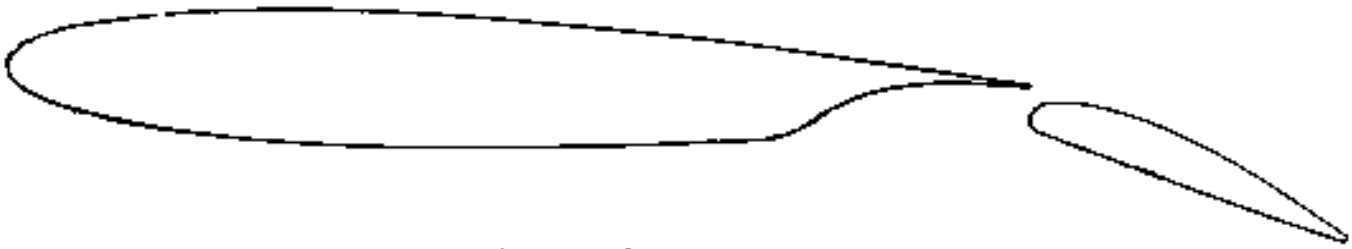

(b) Trailing-edge-flap-only.

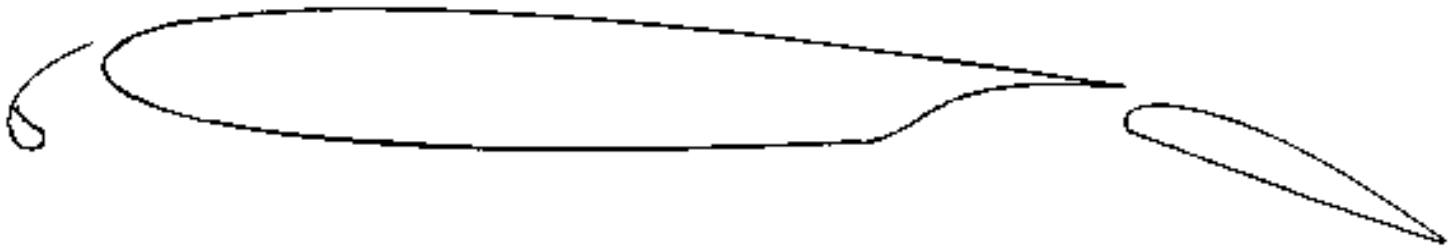

(c) High-lift.

Figure 2. Wing configurations tested.

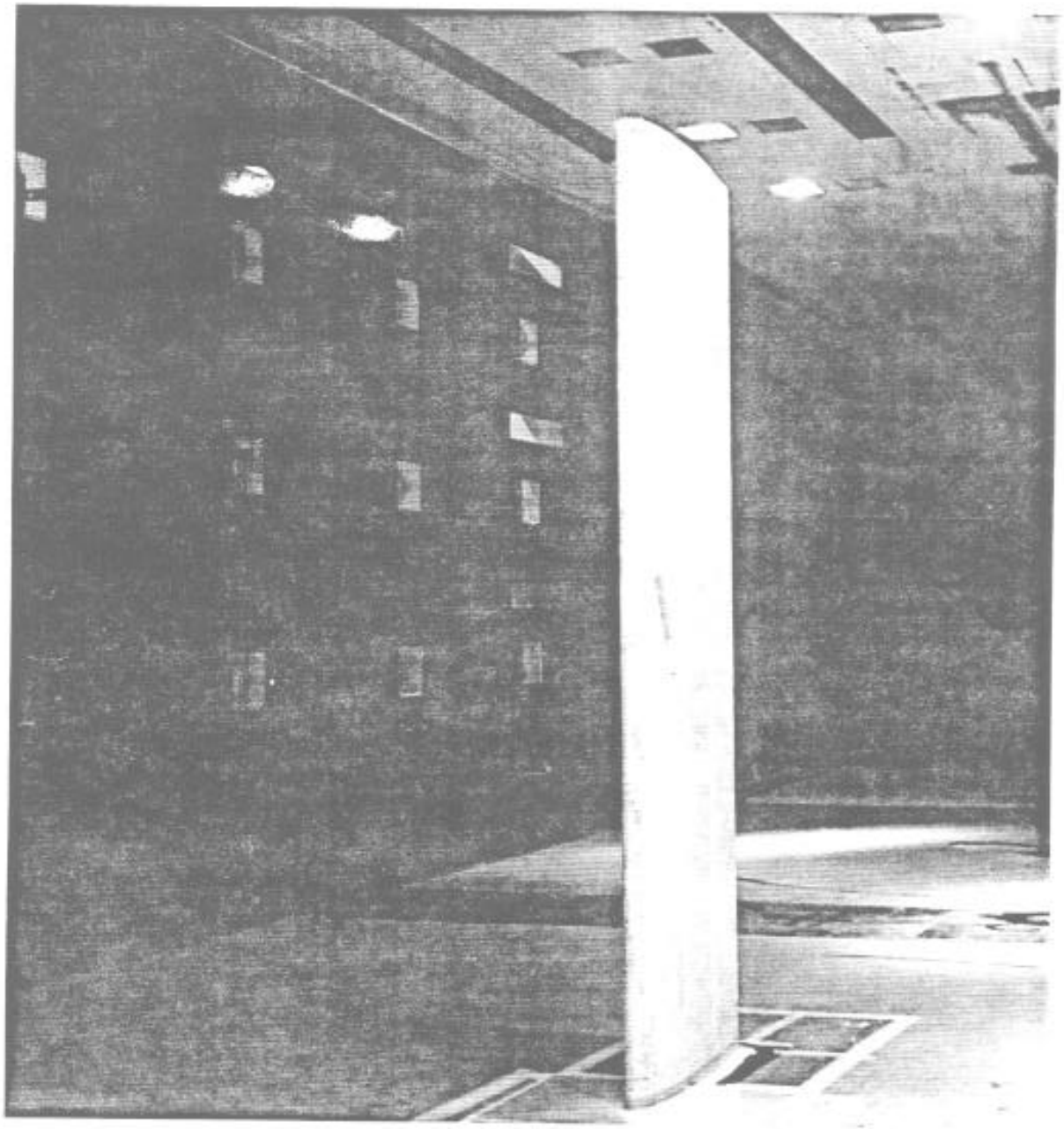

(a) Cruise configuration.

Figure 3. Semispan wing model installed in Langley 14- by 22-Foot Subsonic Tunnel.

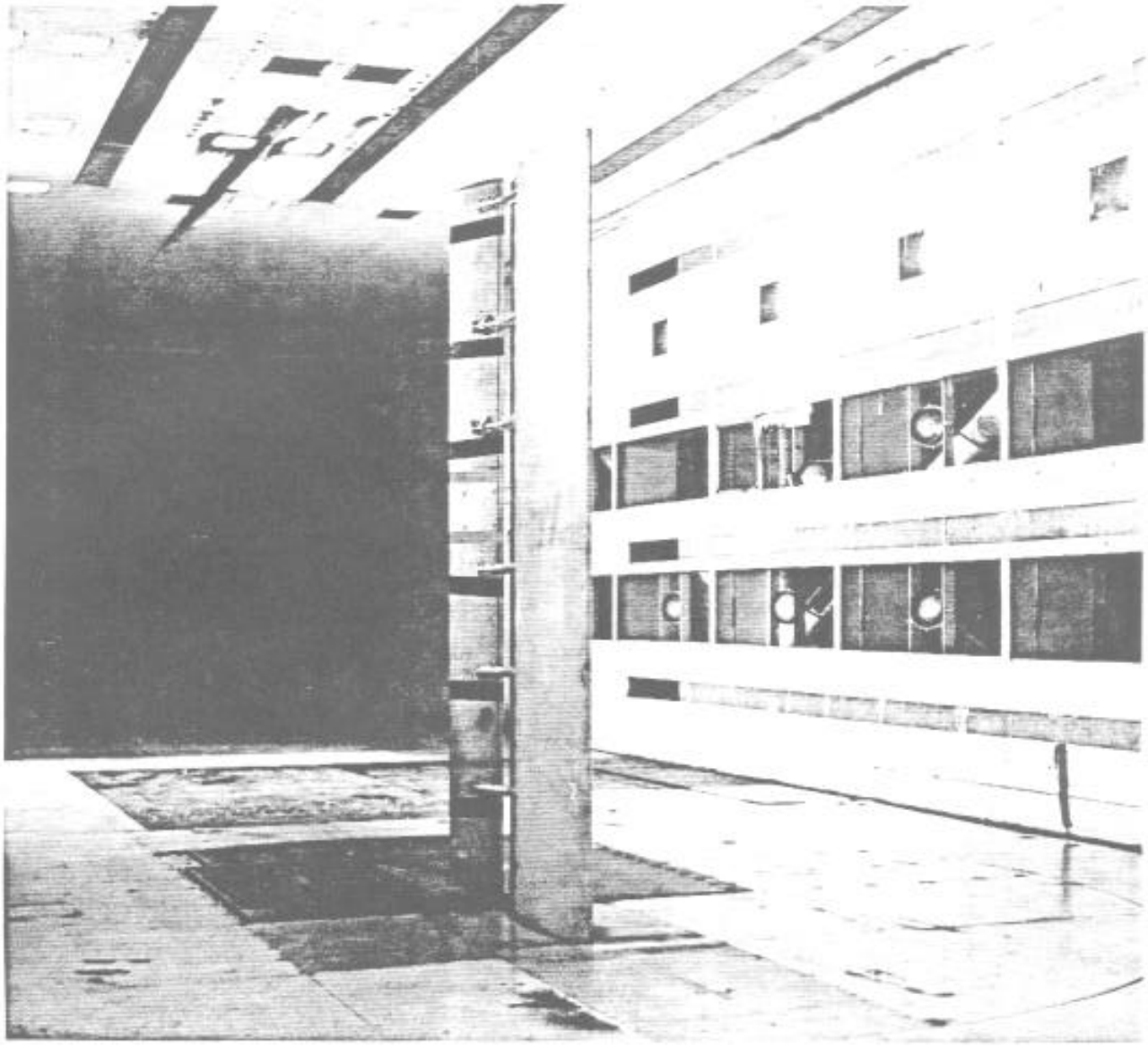

(b) Trailing-edge-flap-only configuration.

Figure 3. Concluded.

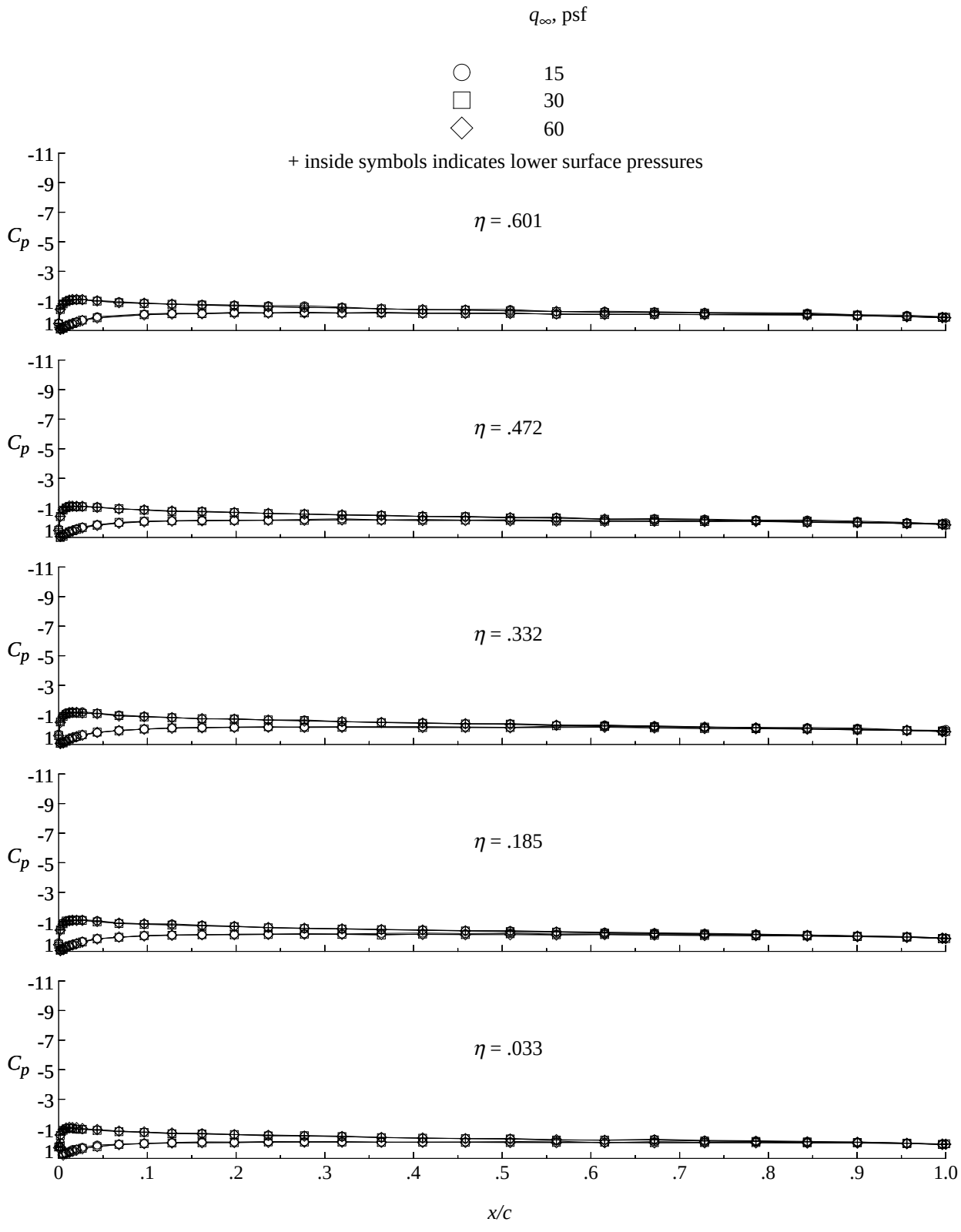


(a) $\alpha$ = - 4°.

Figure 4. Free-stream speed effect on cruise wing pressure distribution. Tunnel floor boundary layer suction off.

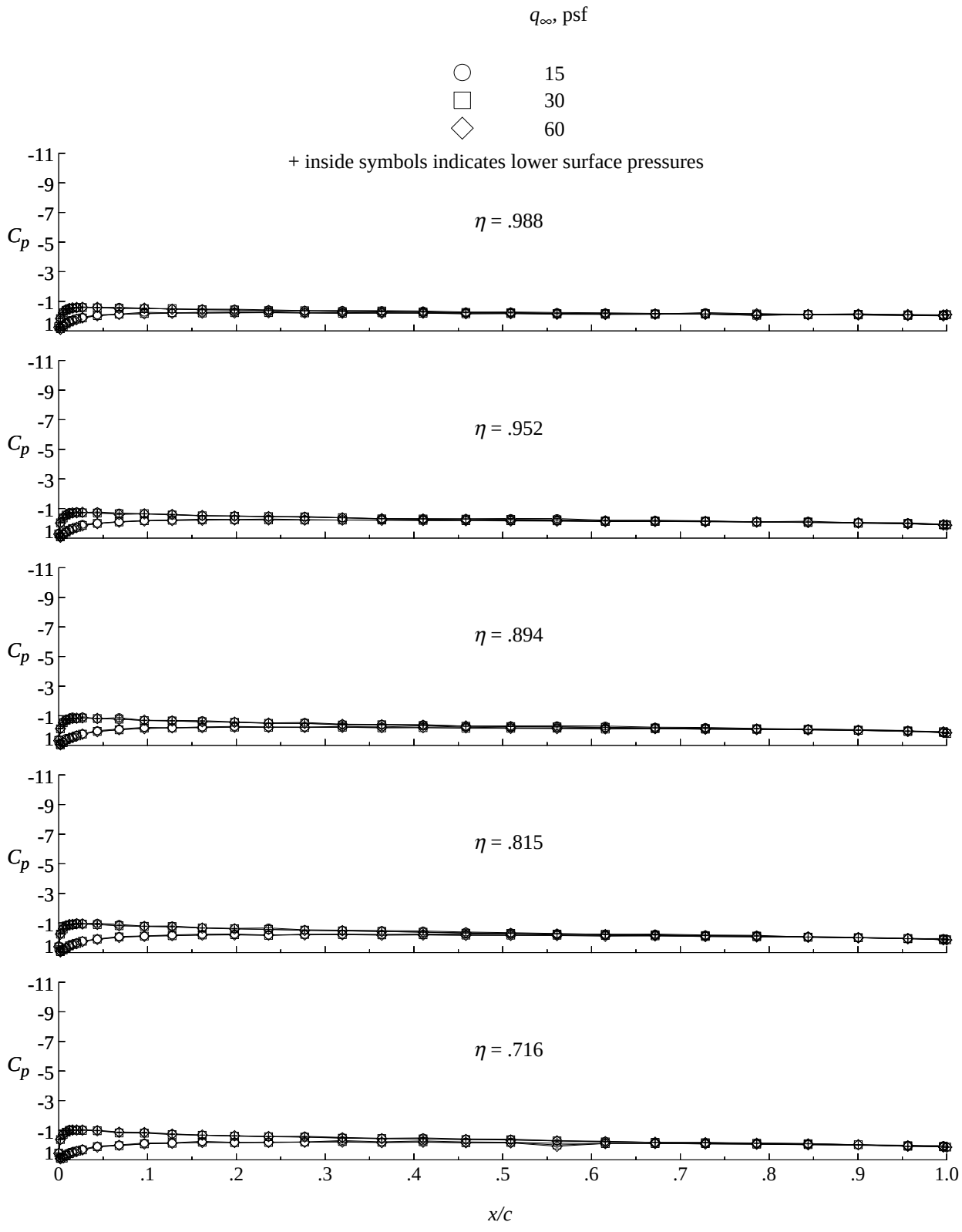


(a) Concluded.

Figure 4. Continued.

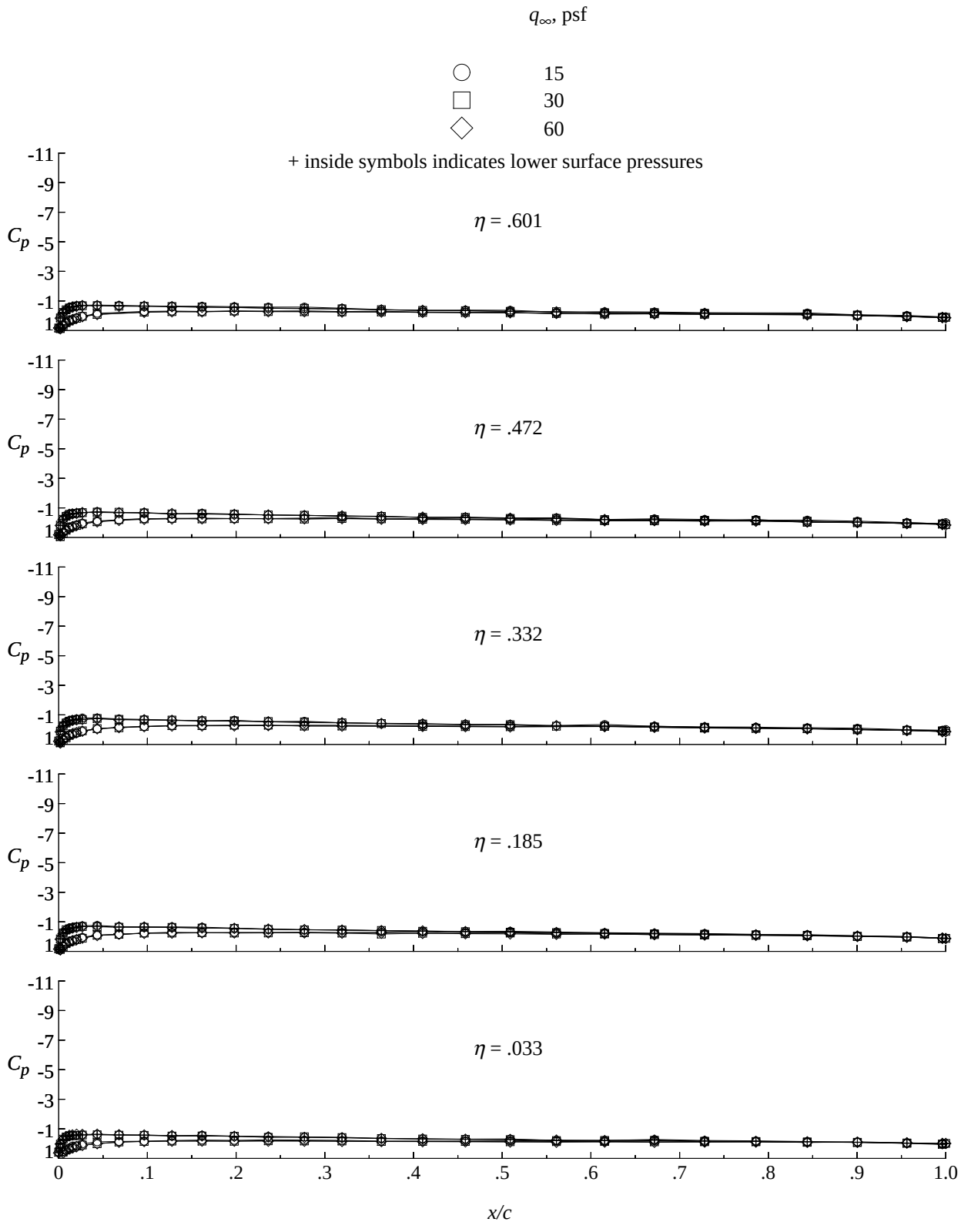


(b) $\alpha$ = - 2°.

Figure 4. Continued.

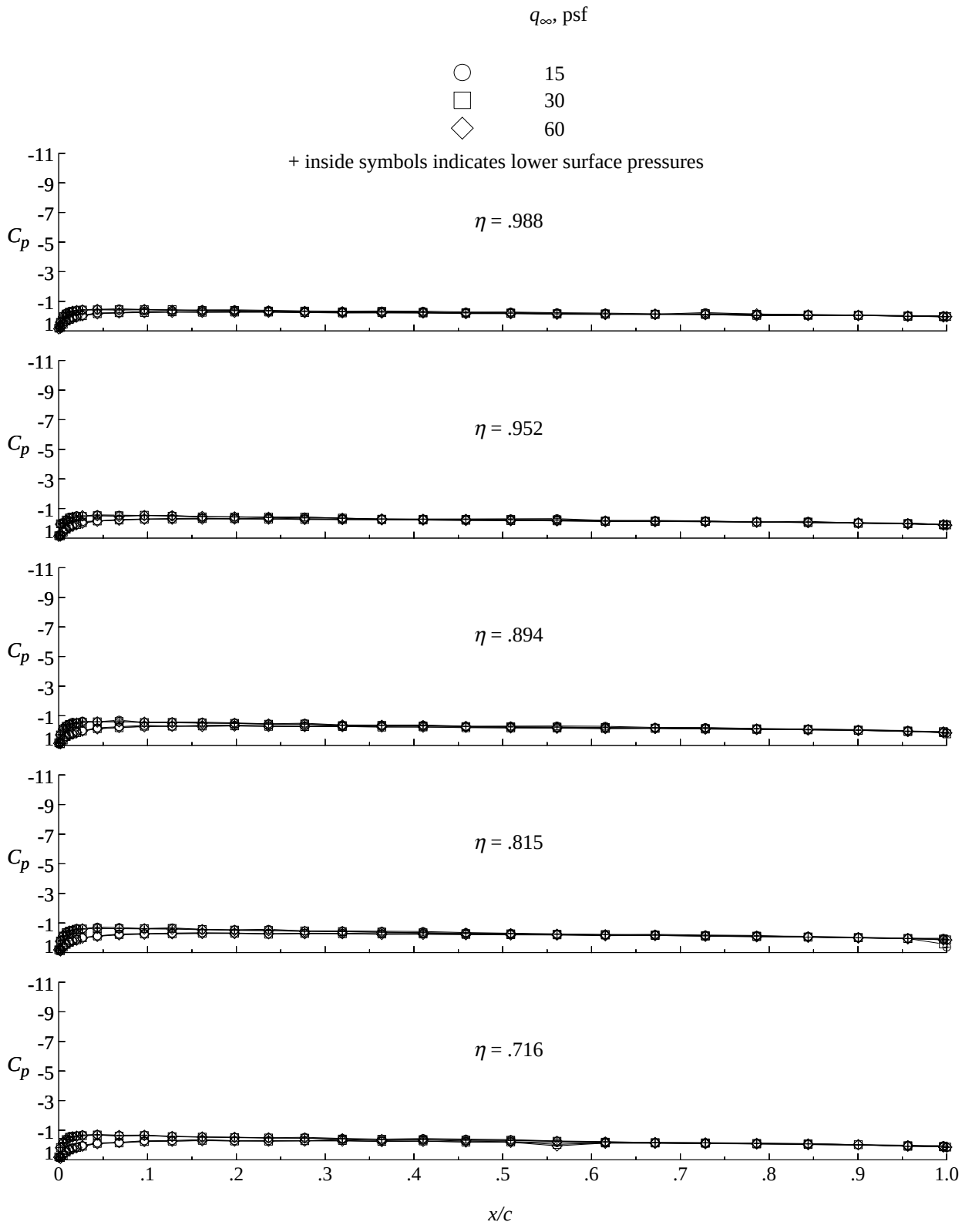


(b) Concluded.

Figure 4. Continued.

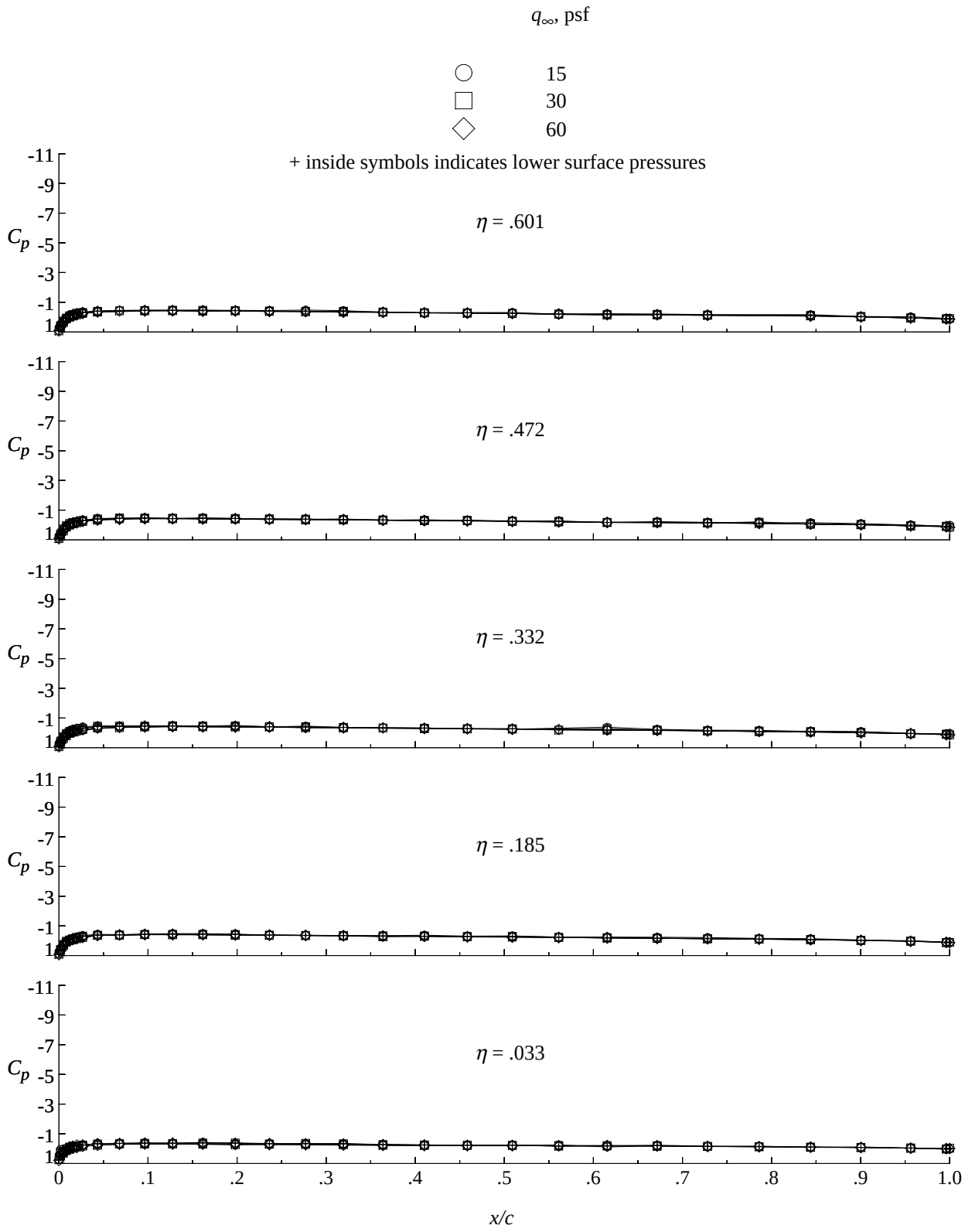


(c) $\alpha = 0°$.

Figure 4. Continued.

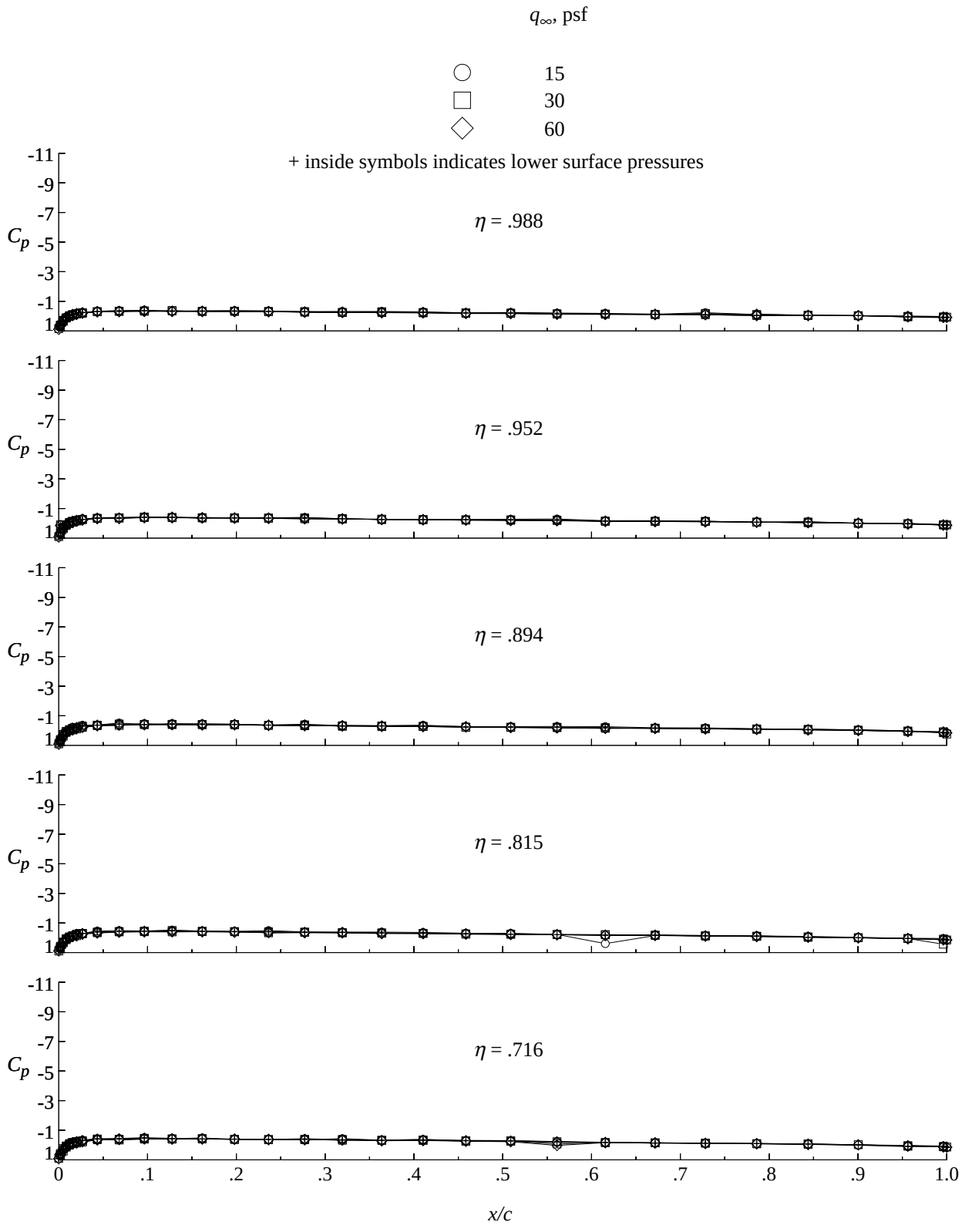


(c) Concluded.

Figure 4. Continued.

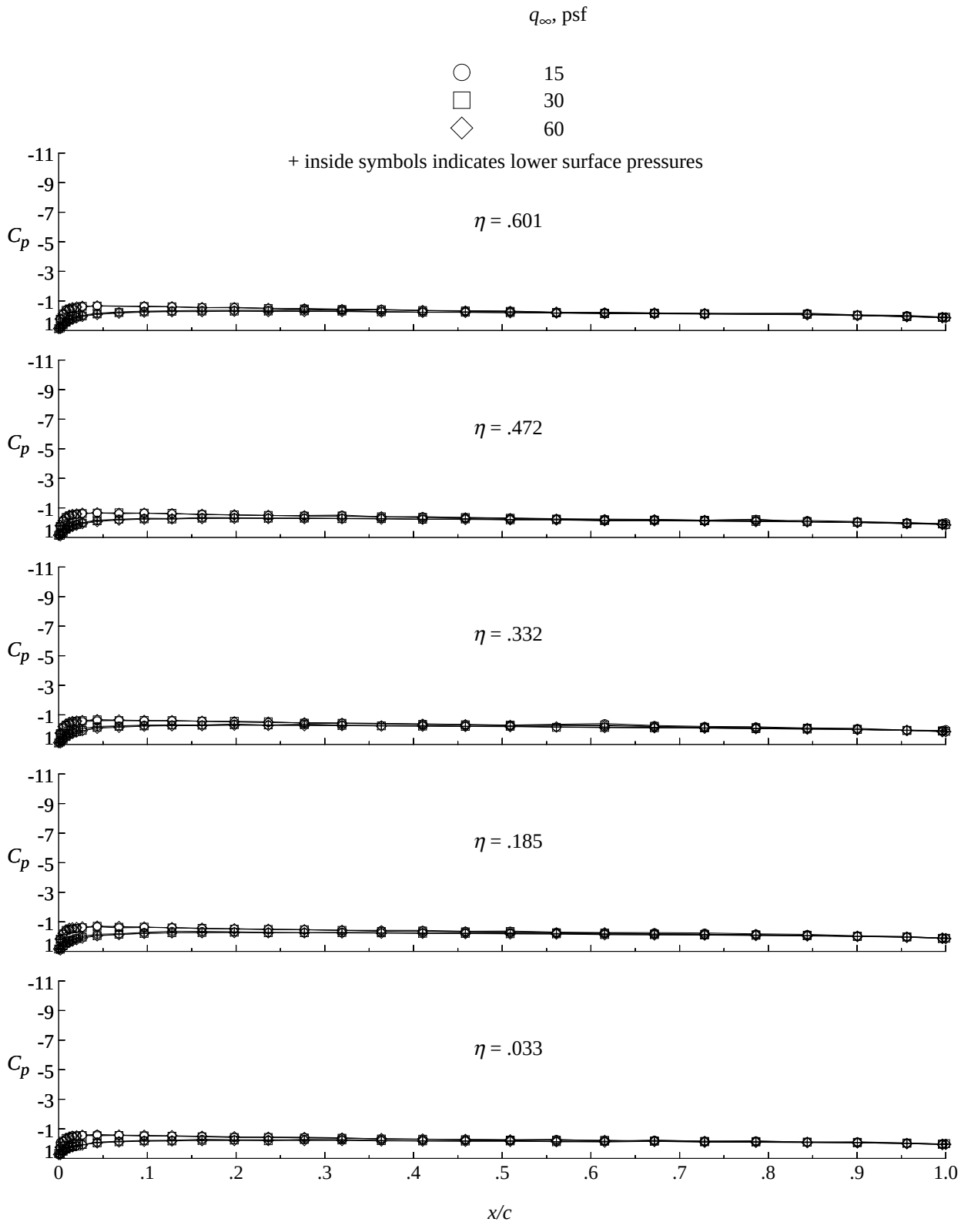


(d) $\alpha = 2°$.

Figure 4. Continued.

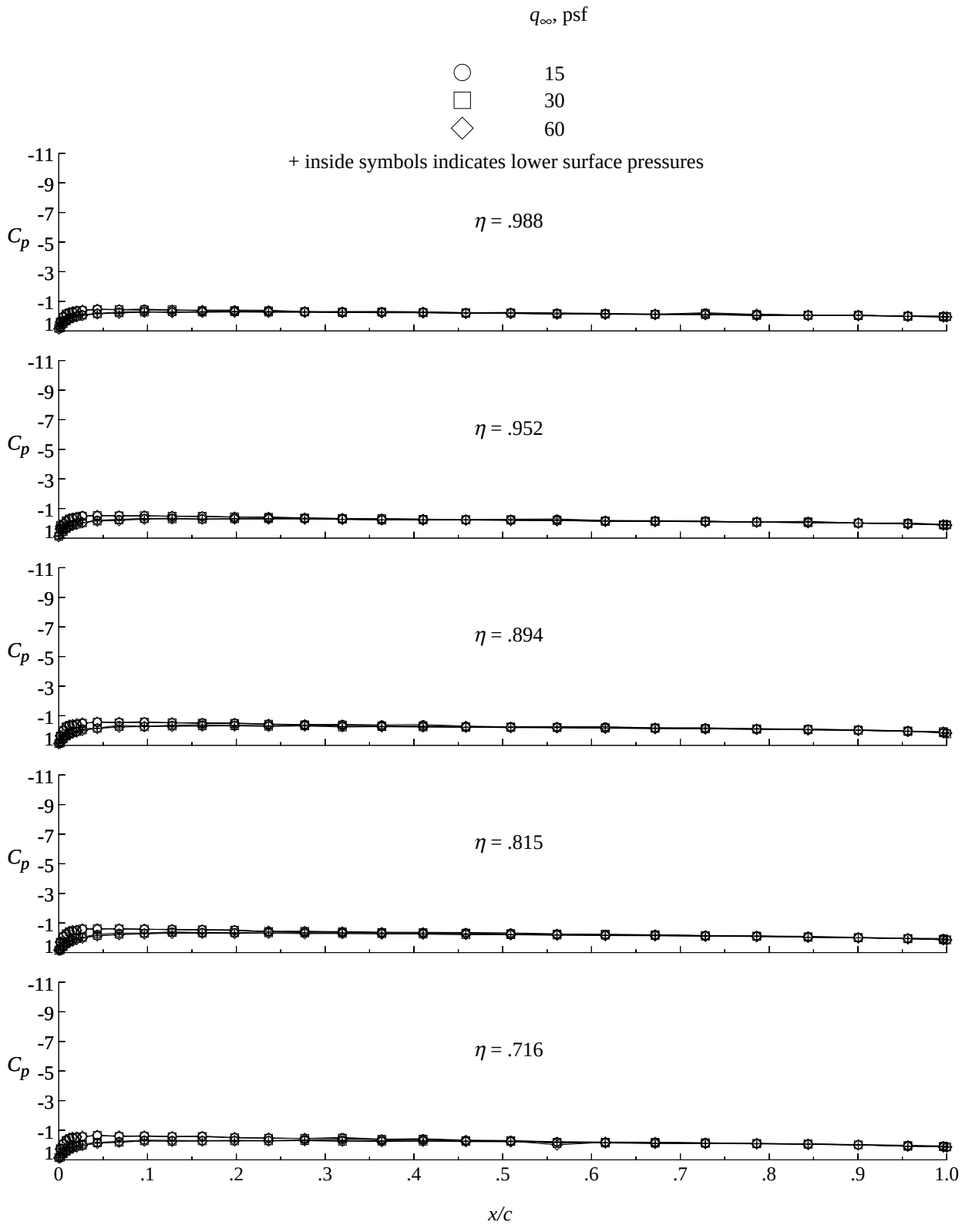


(d) Concluded.

Figure 4. Continued.

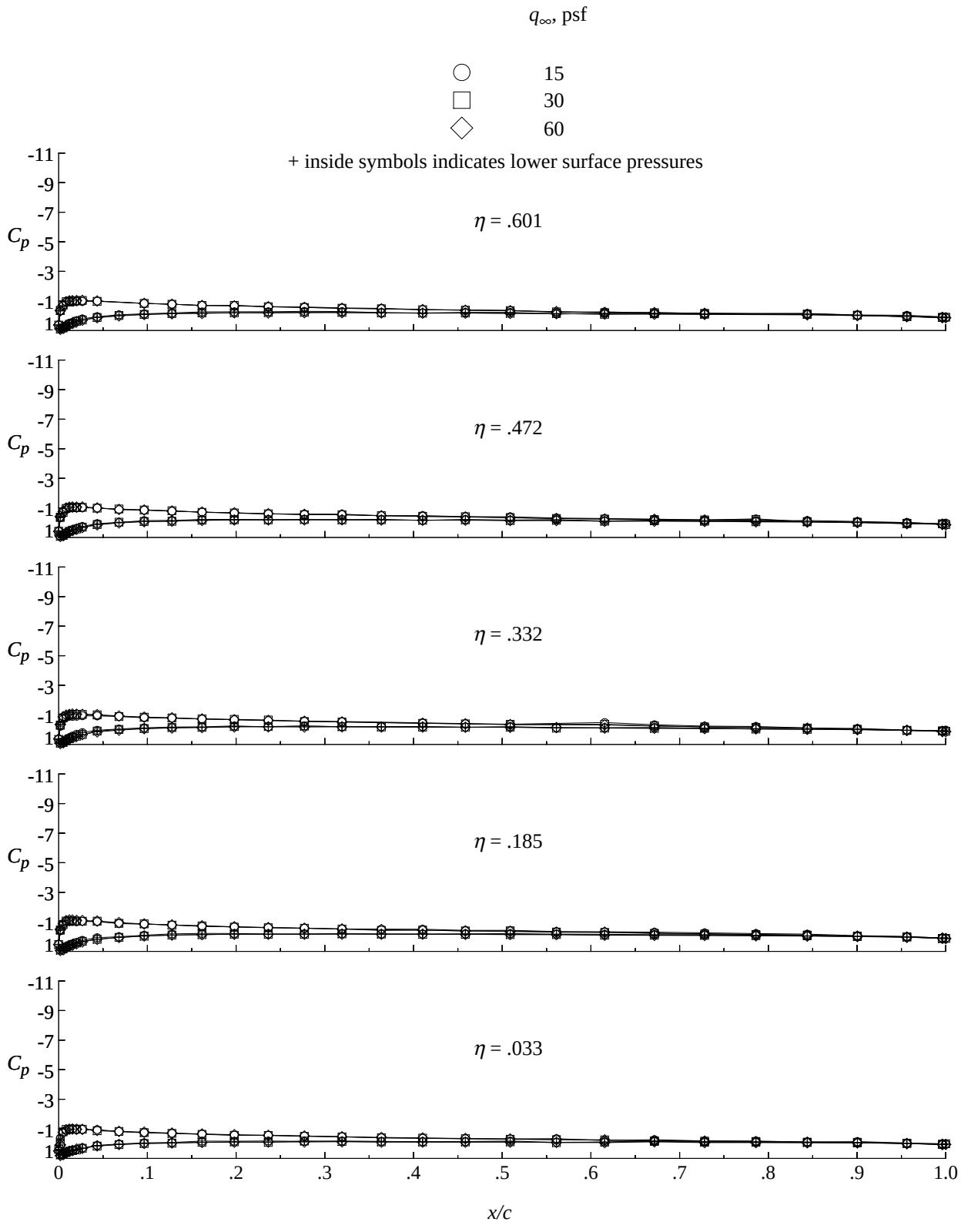


(e) $\alpha = 4°$.

Figure 4. Continued.

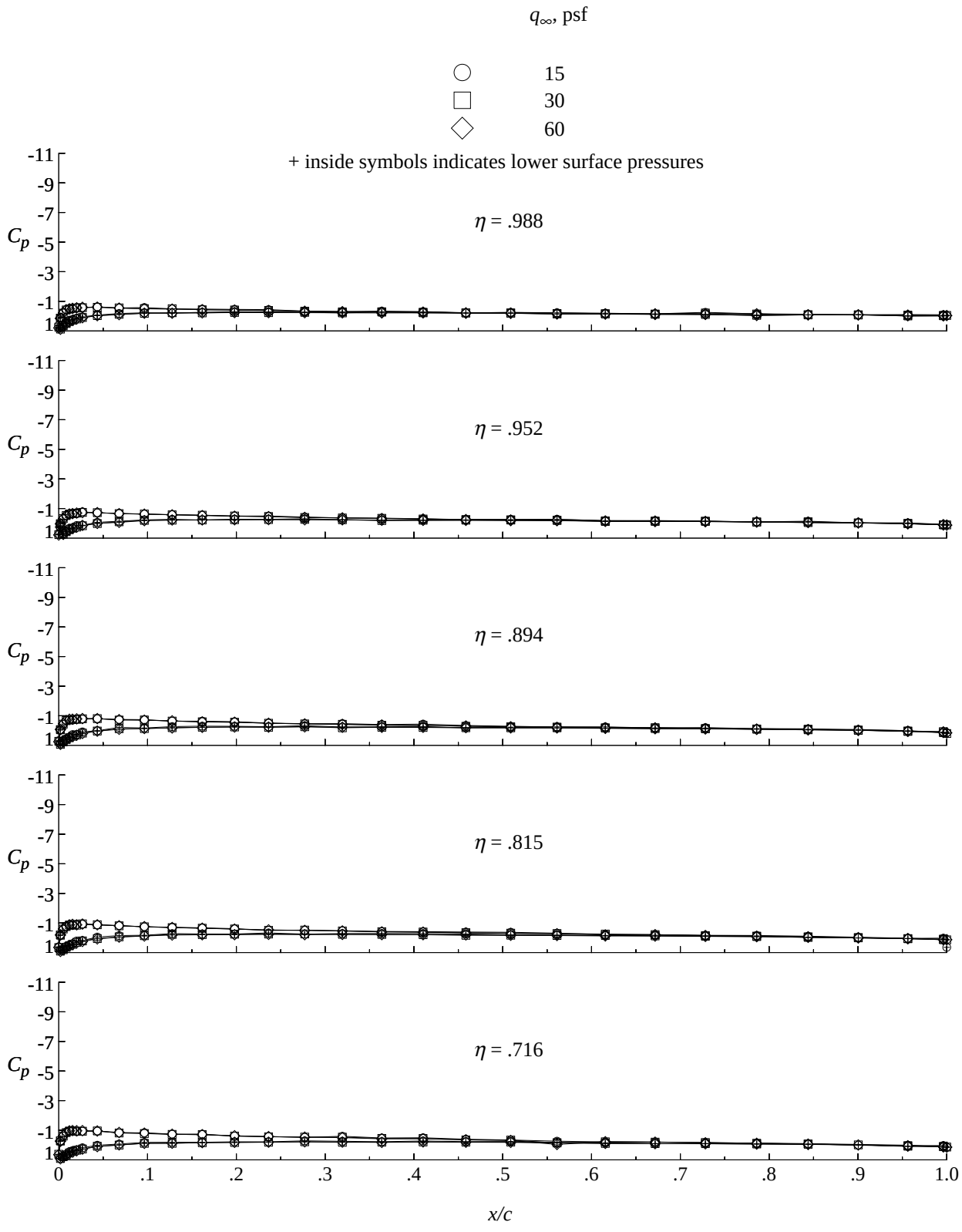


(e) Concluded.

Figure 4. Continued.

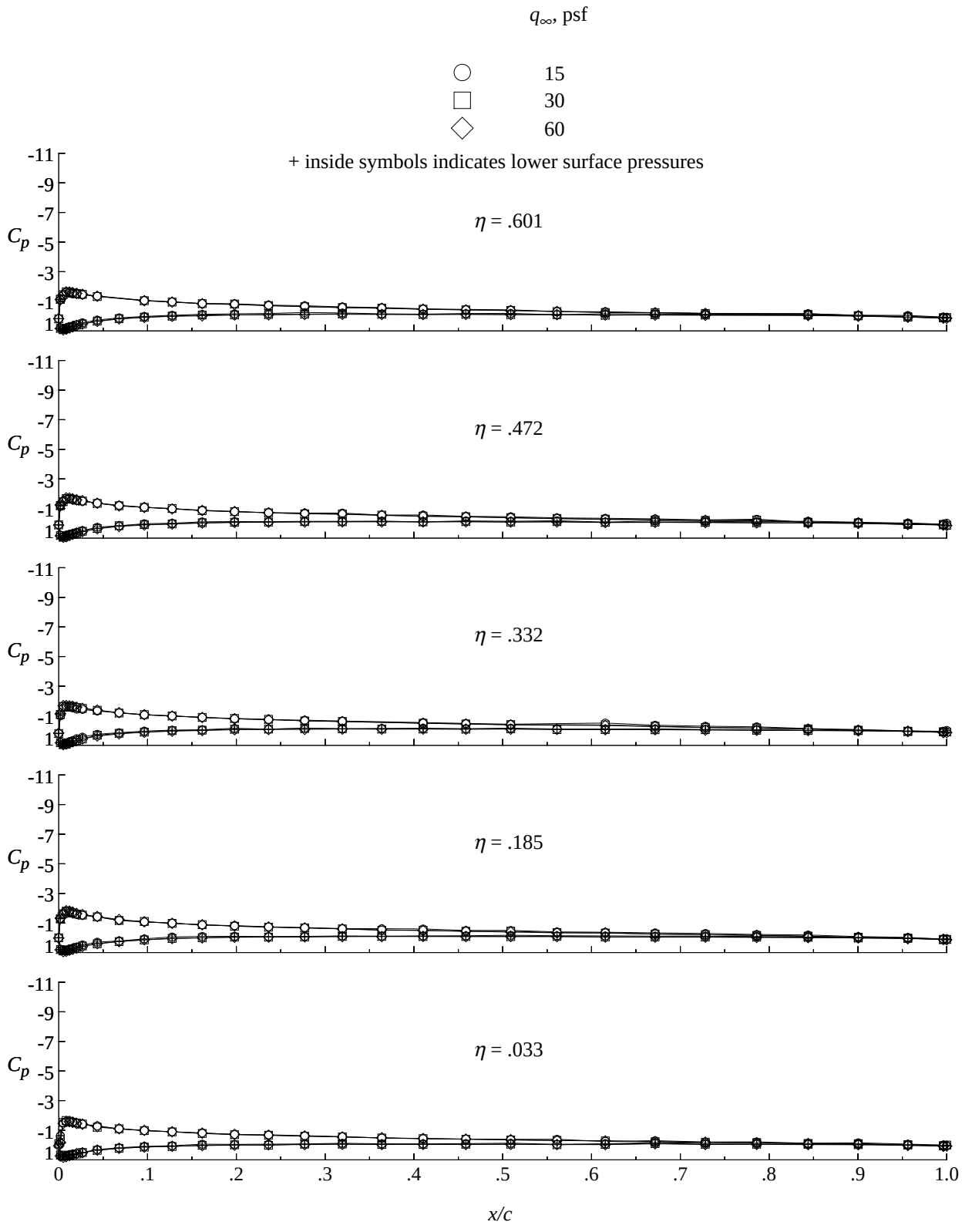


(f) $\alpha = 6°$.

Figure 4. Continued.

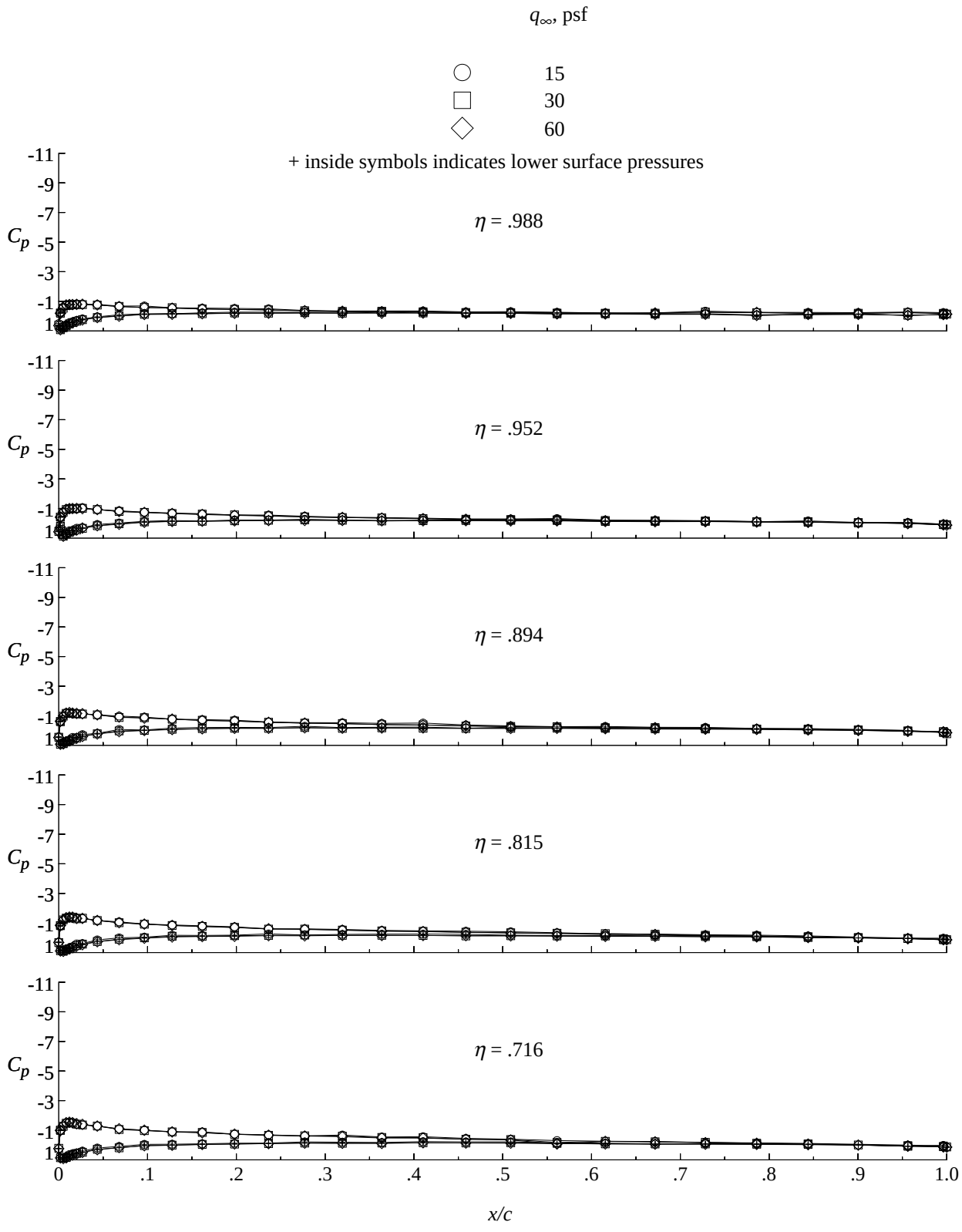


(f) Concluded.

Figure 4. Continued.

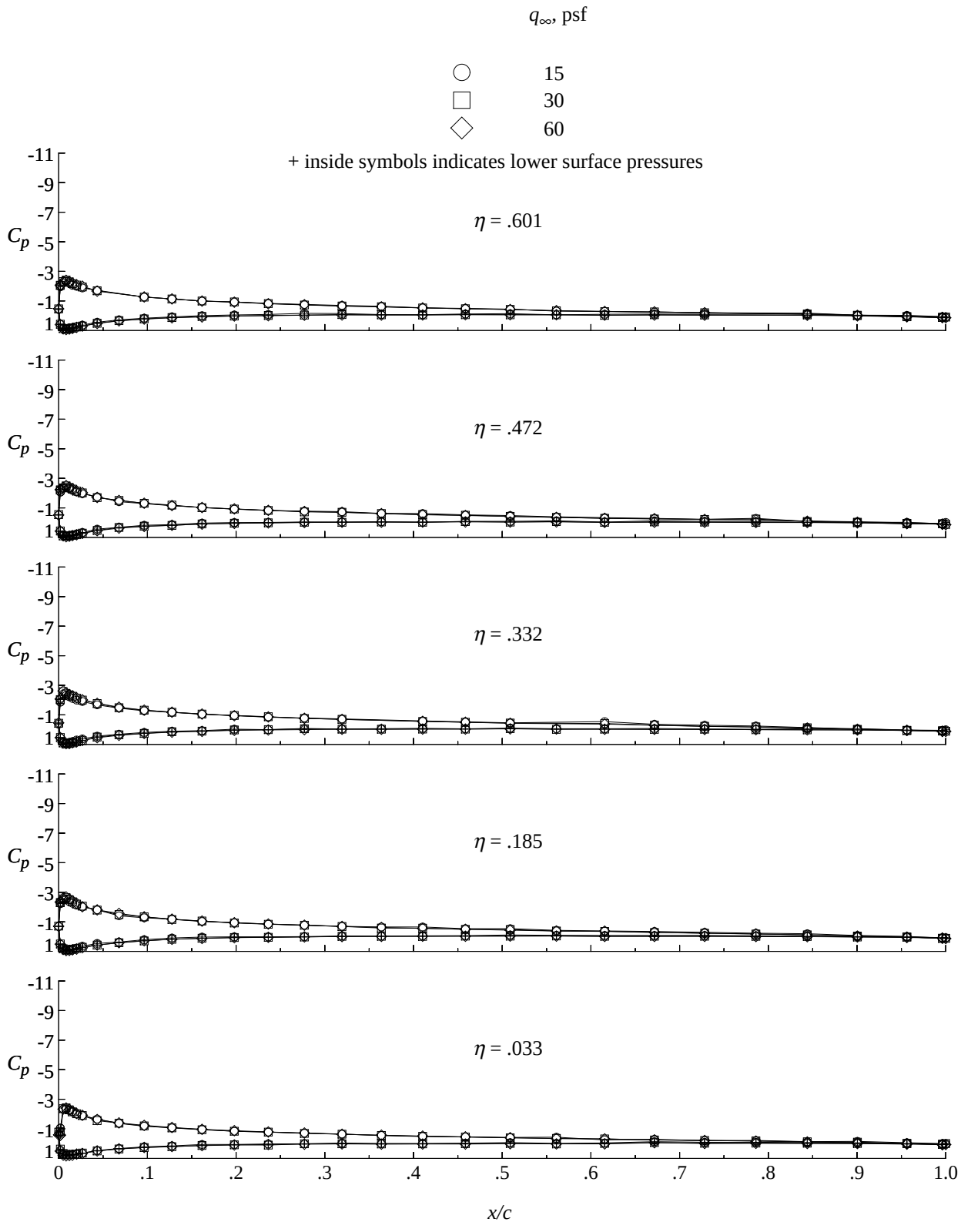


(g) $\alpha = 8°$.

Figure 4. Continued.

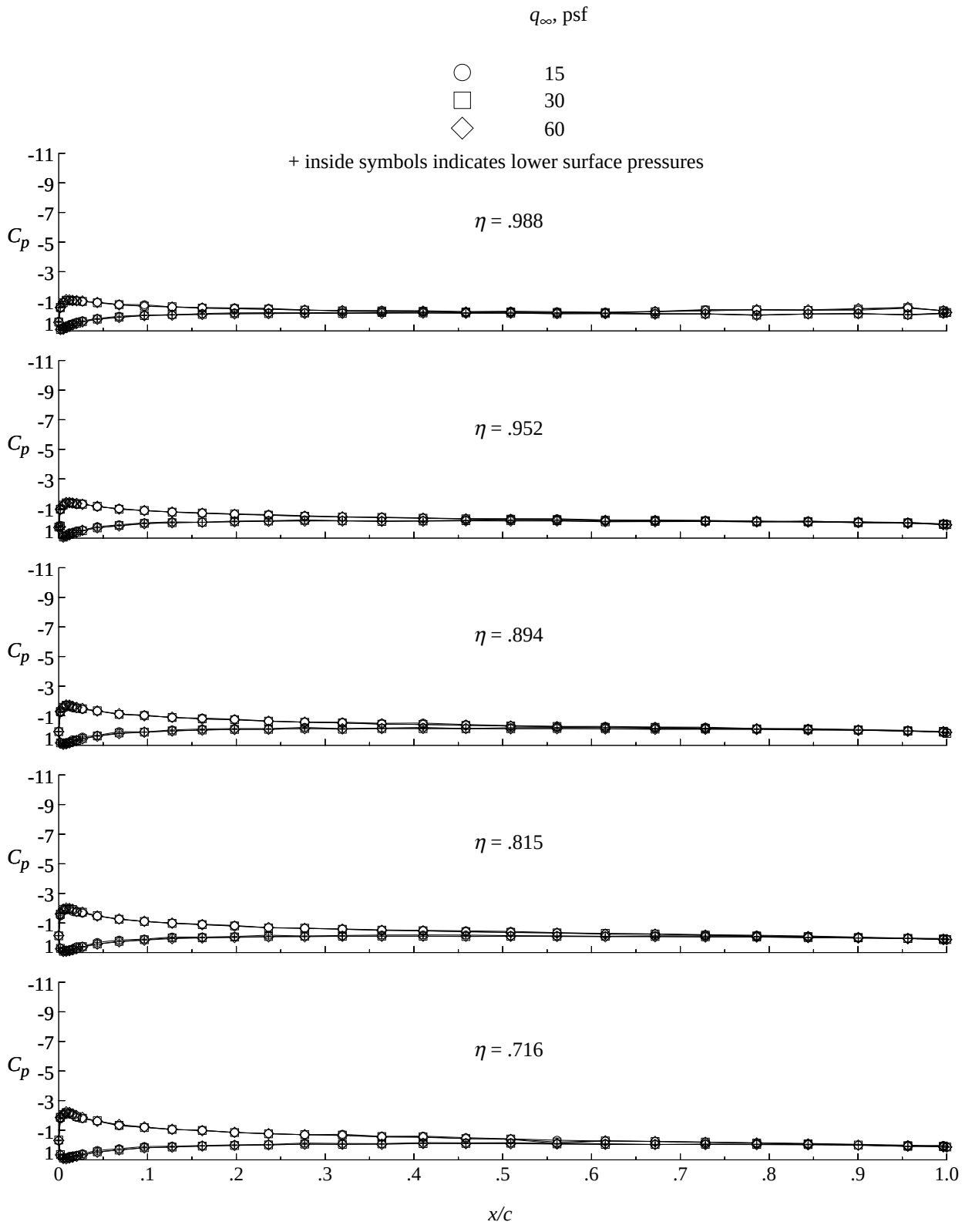


(g) Concluded.

Figure 4. Continued.

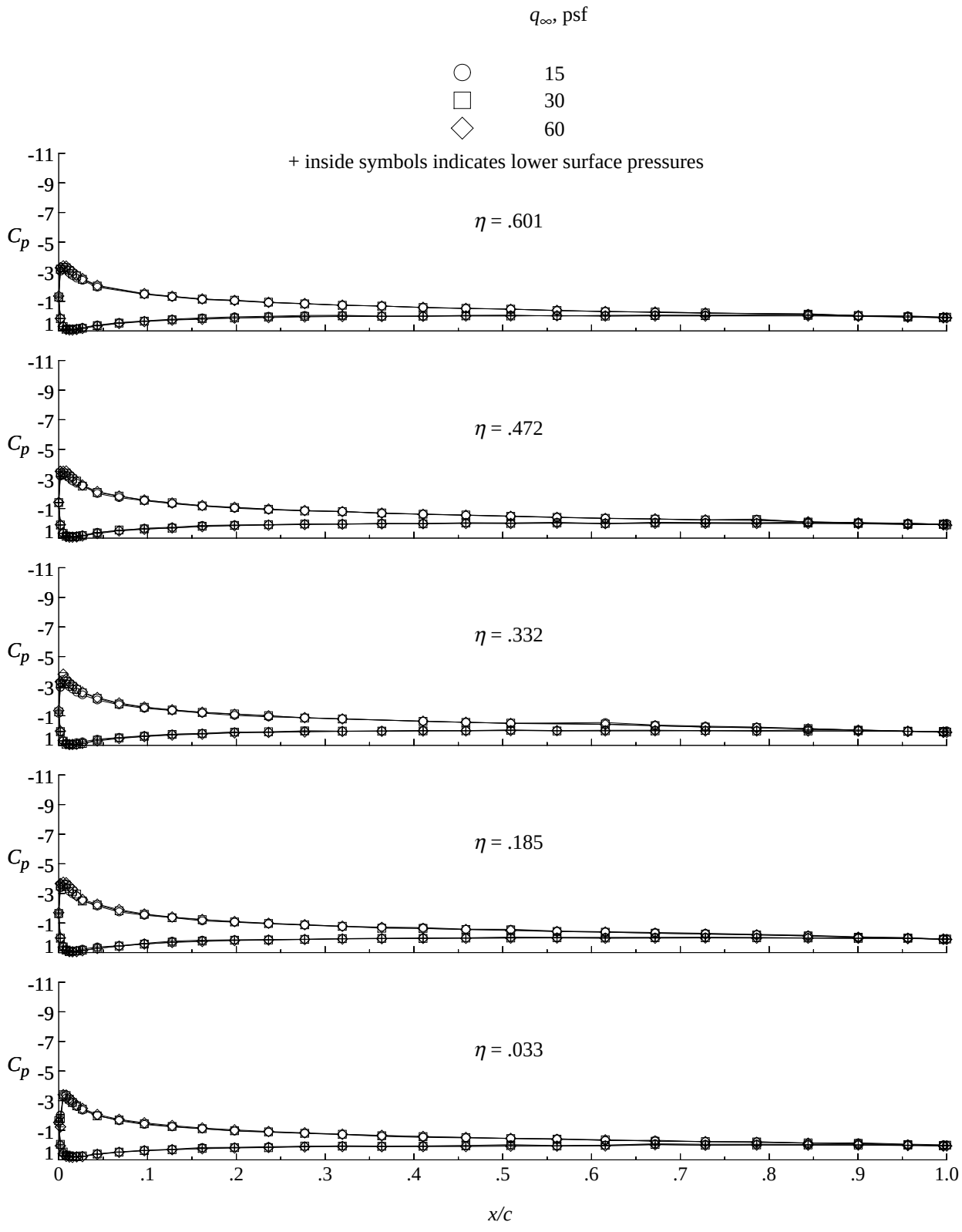


(h) $\alpha = 10°$.

Figure 4. Continued.

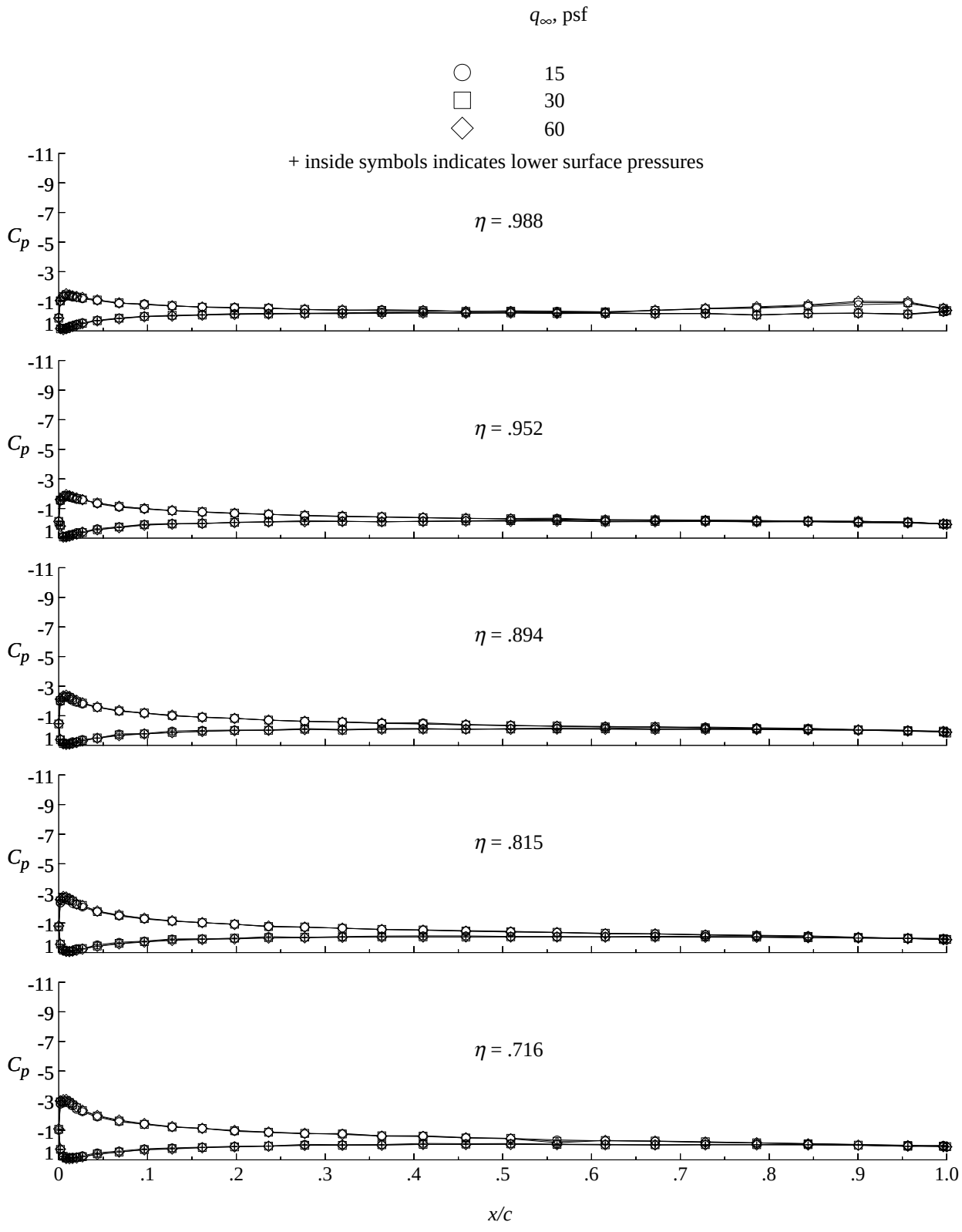


(h) Concluded.

Figure 4. Continued.

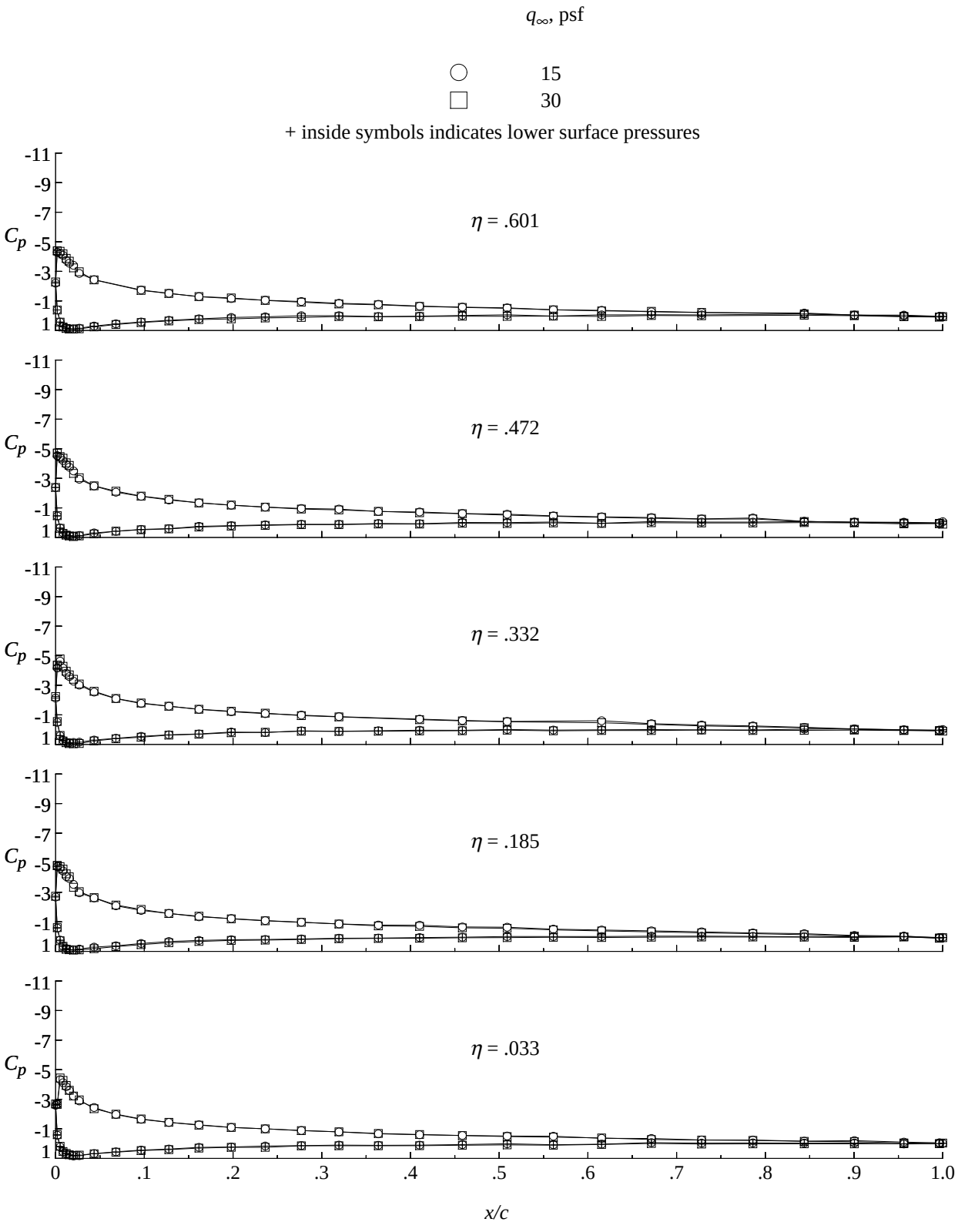


(i) $\alpha = 12°$.

Figure 4. Continued.

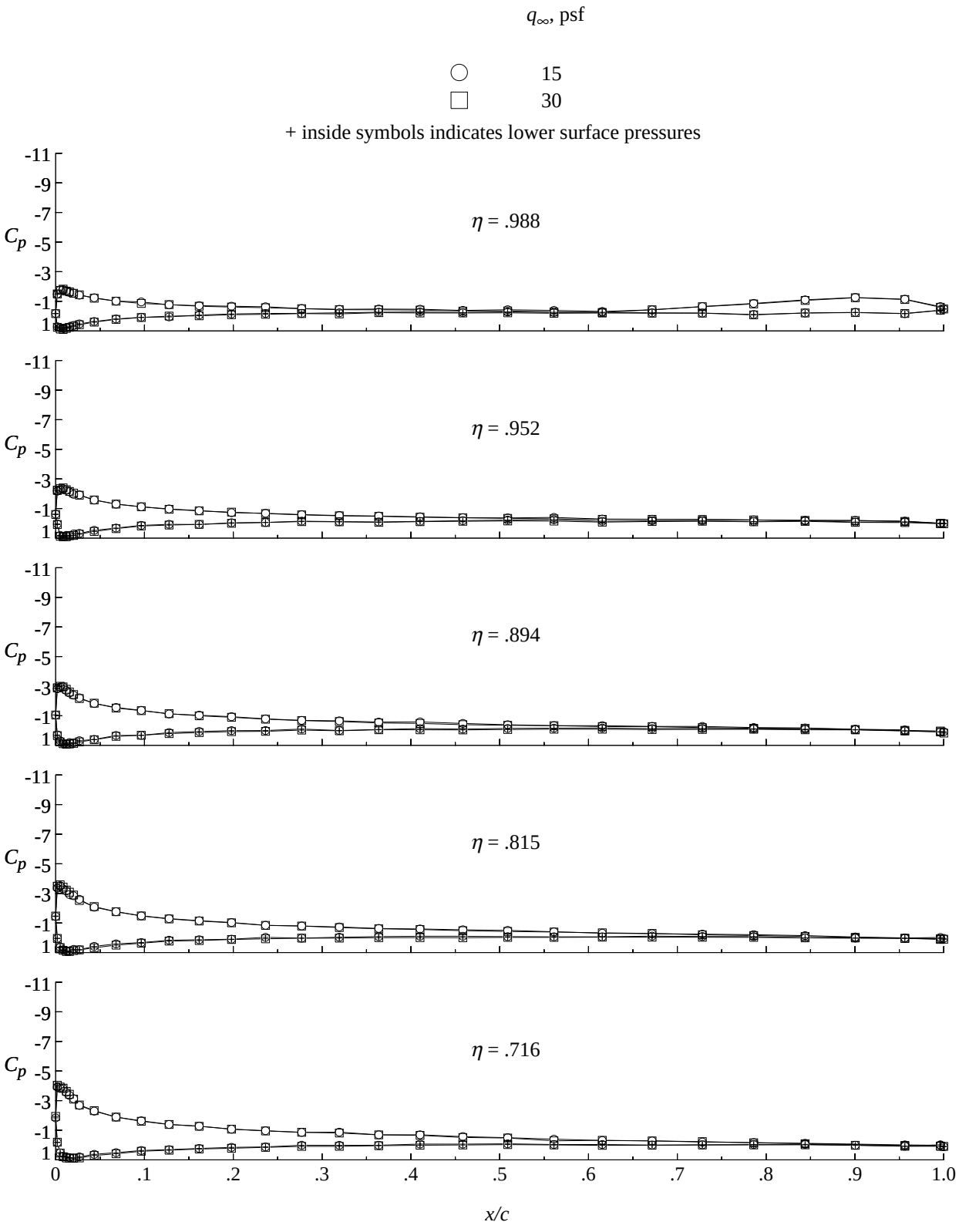


(i) Concluded.

Figure 4. Continued.

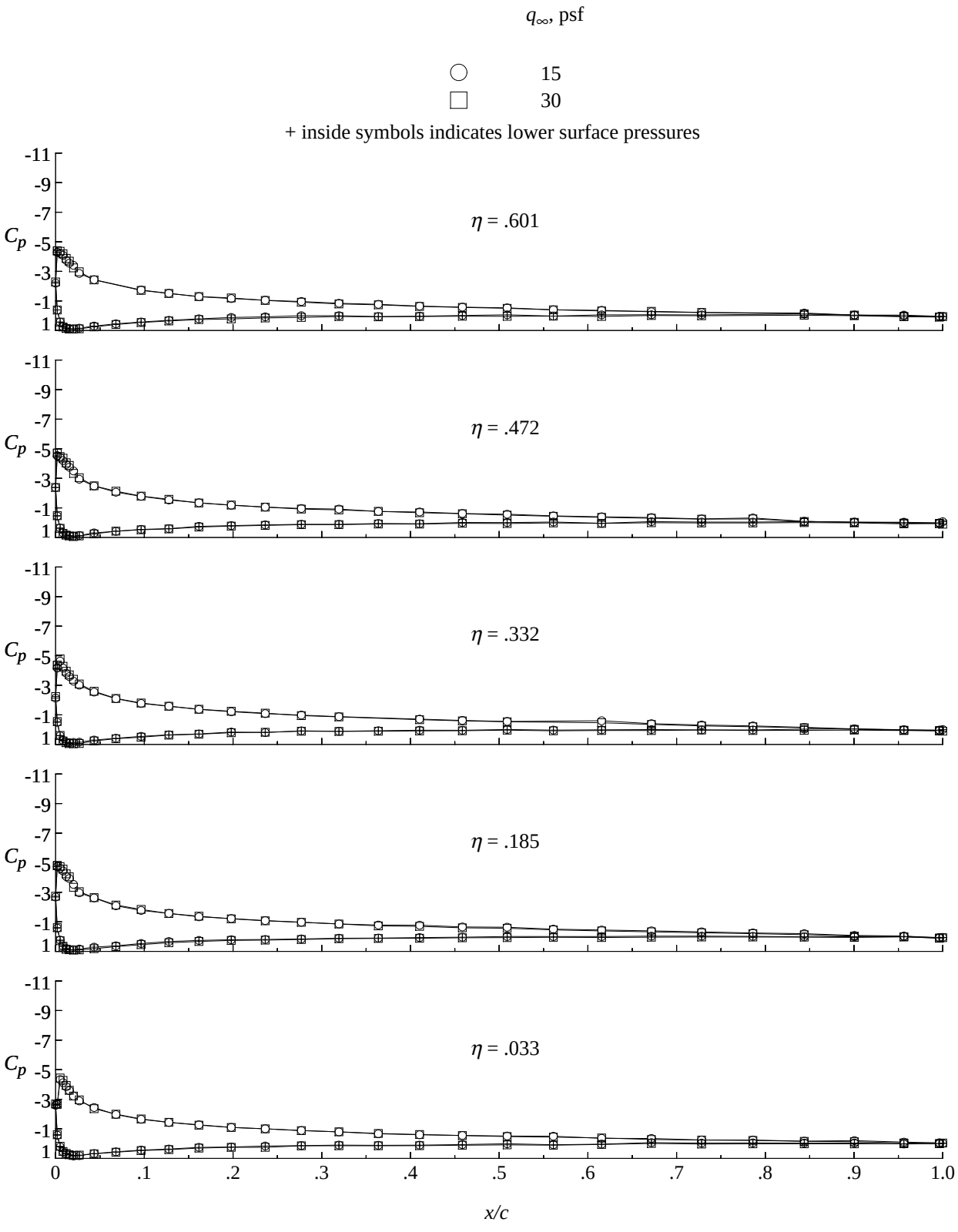


(j) $\alpha = 14°$.

Figure 4. Continued.

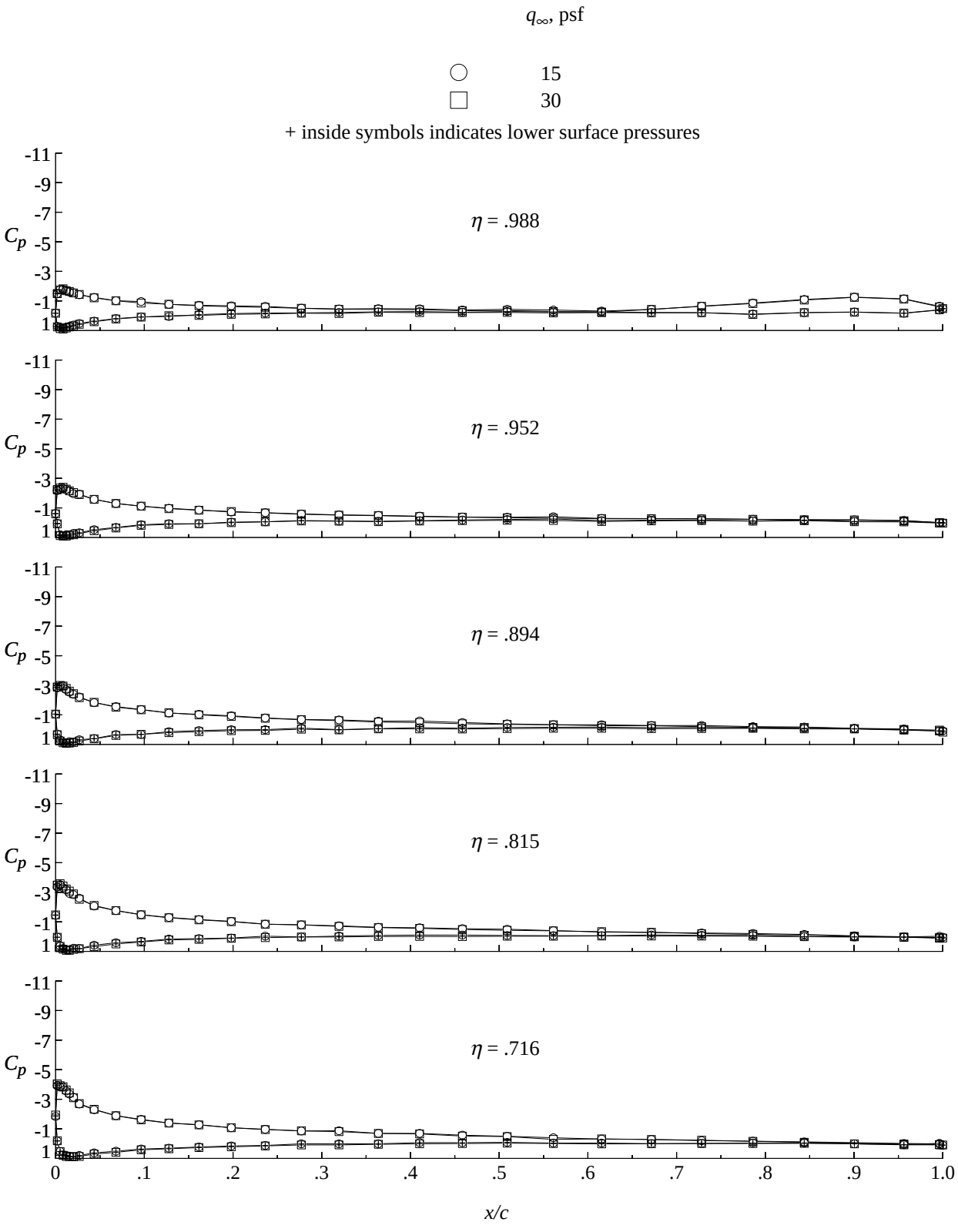


(j) Concluded.

Figure 4. Continued.

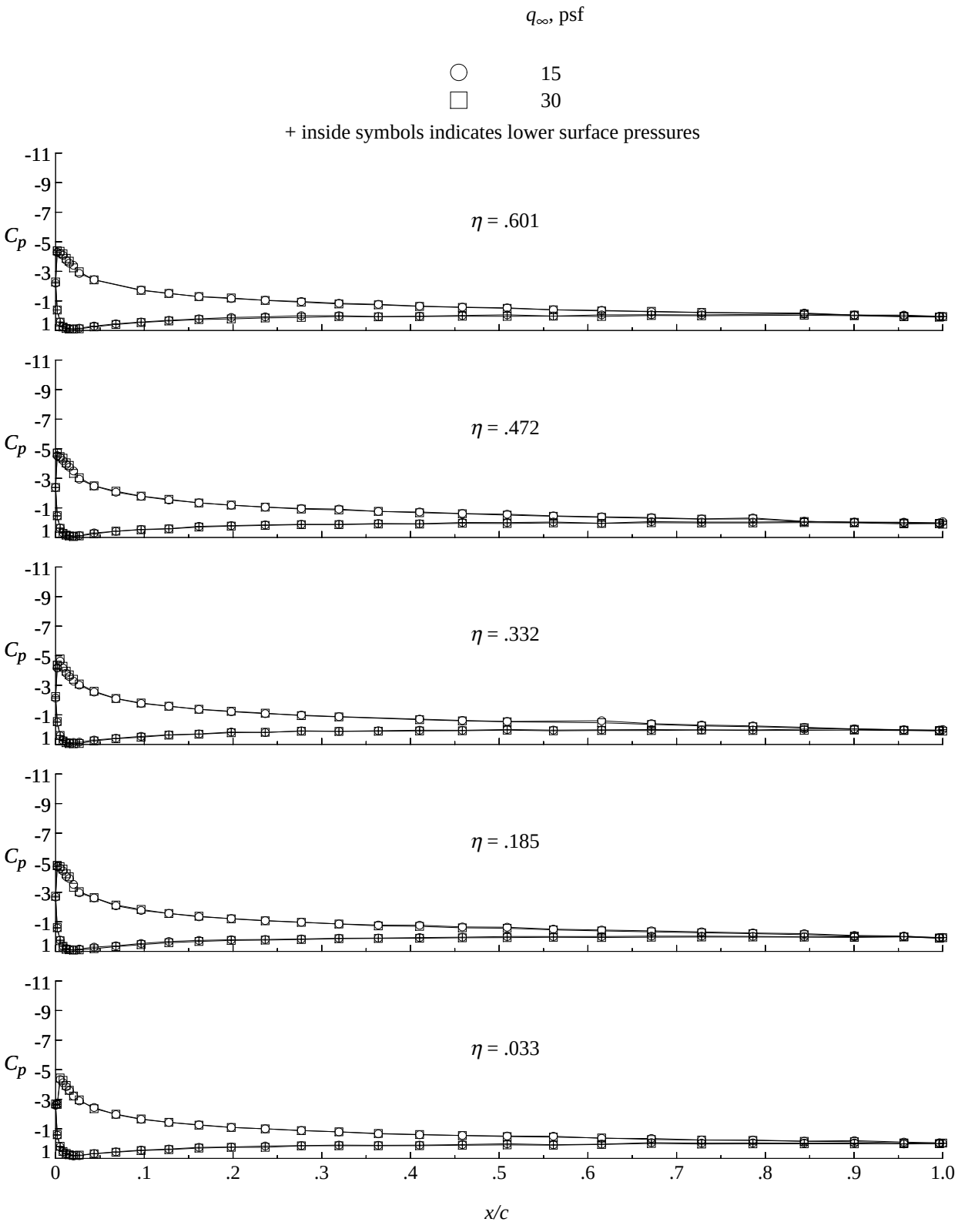


(k) $\alpha = 16°$.

Figure 4. Continued.

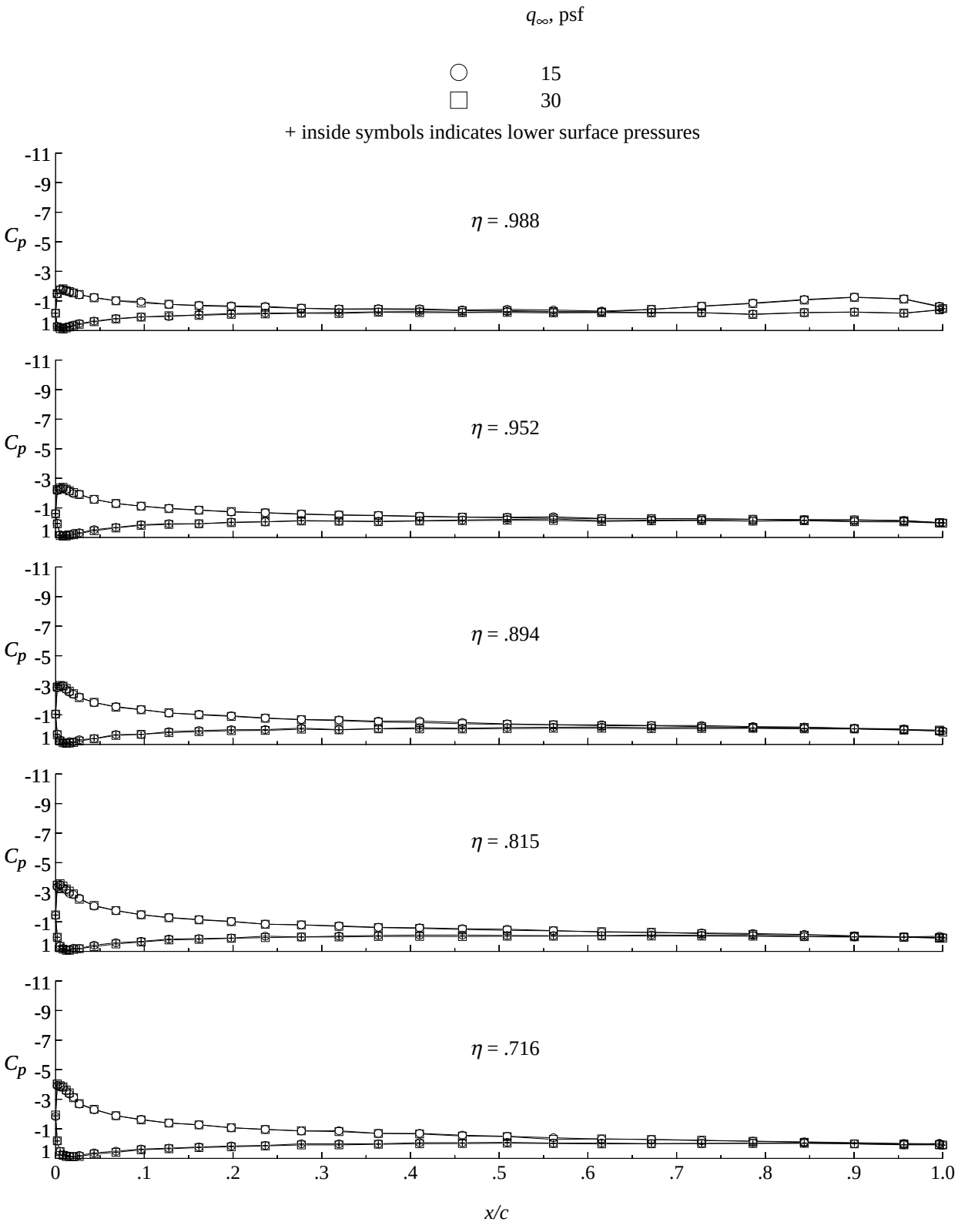


(k) Concluded.

Figure 4. Continued.

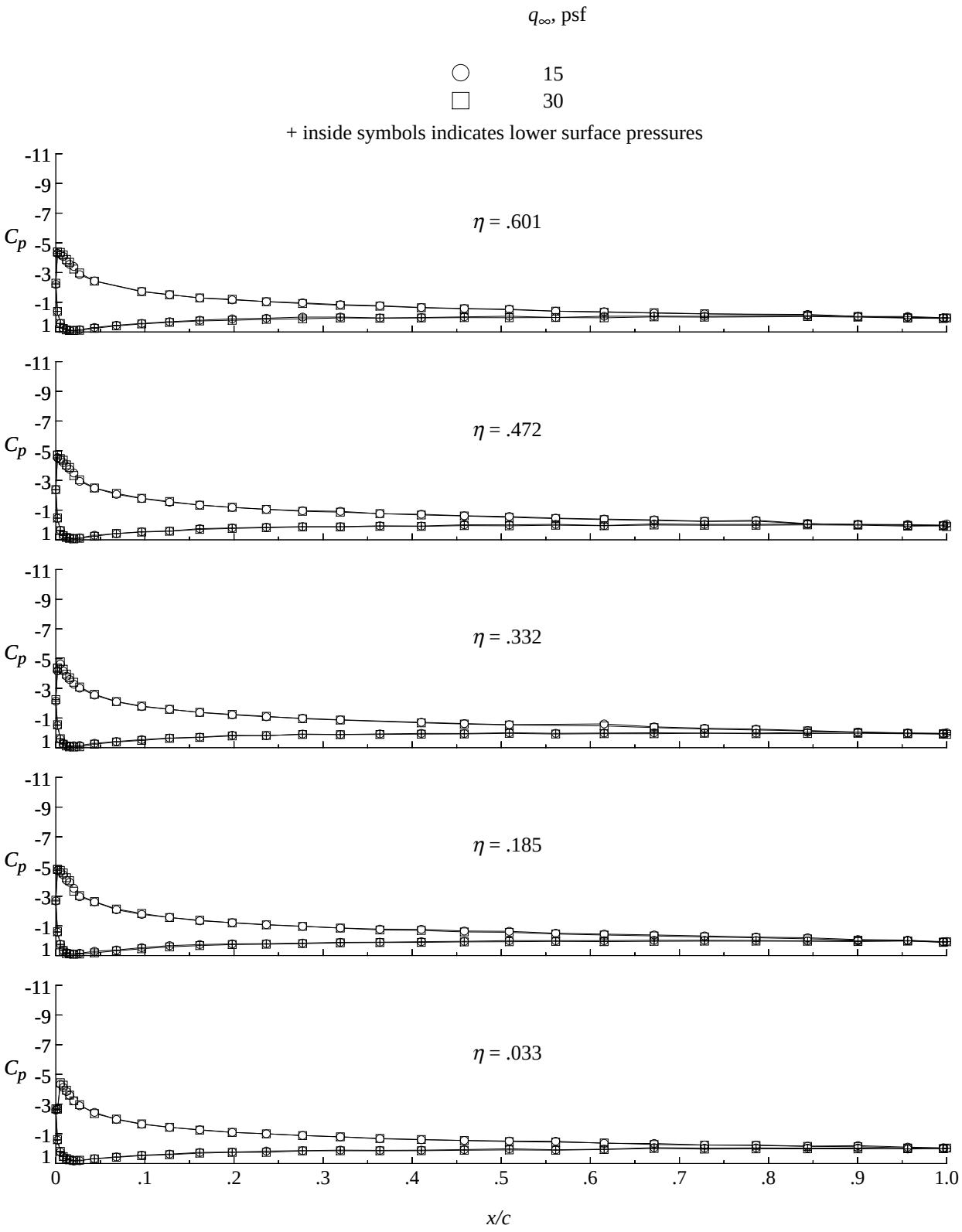


(l) $\alpha = 18°$.

Figure 4. Continued.

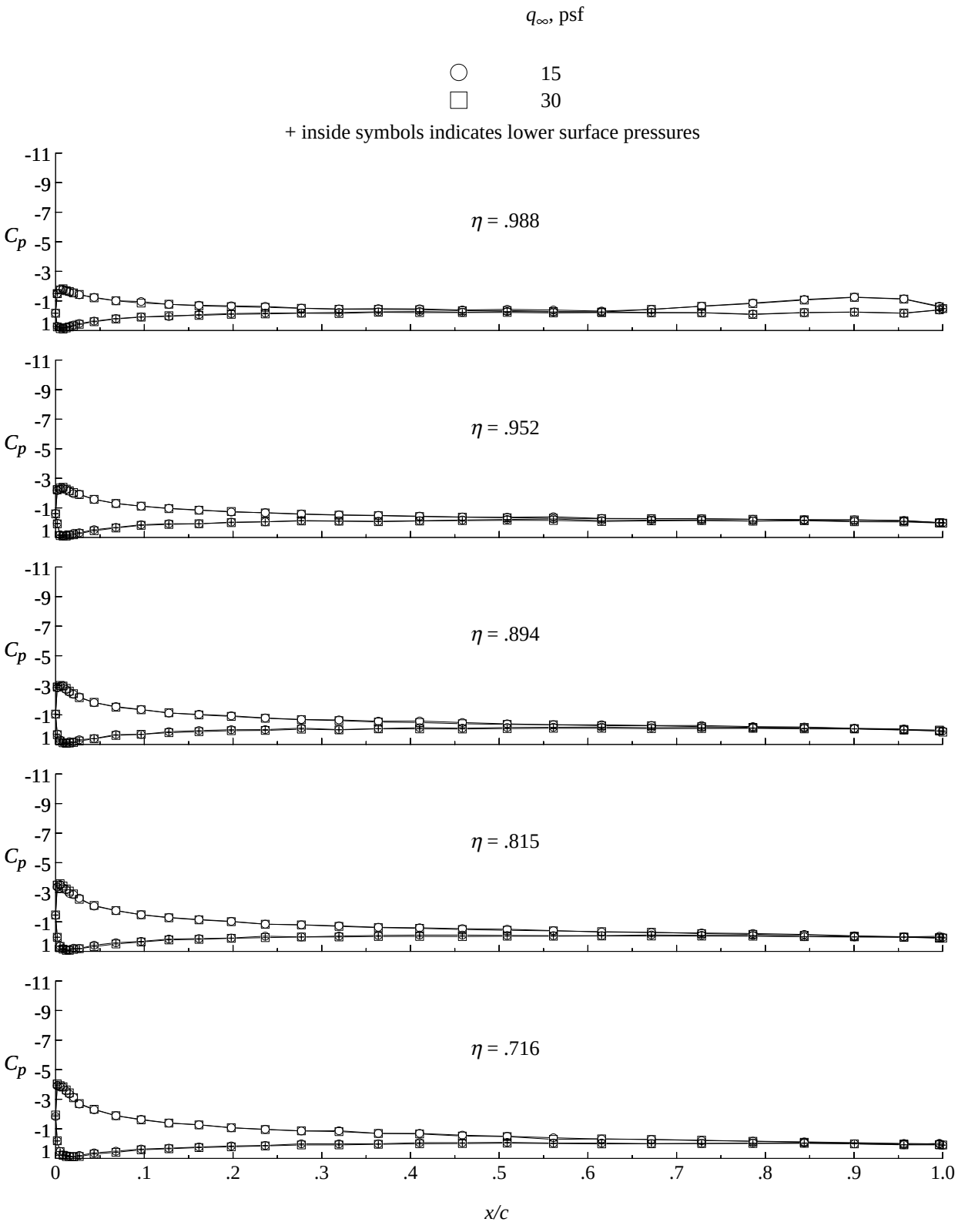


(l) Concluded.

Figure 4. Continued.

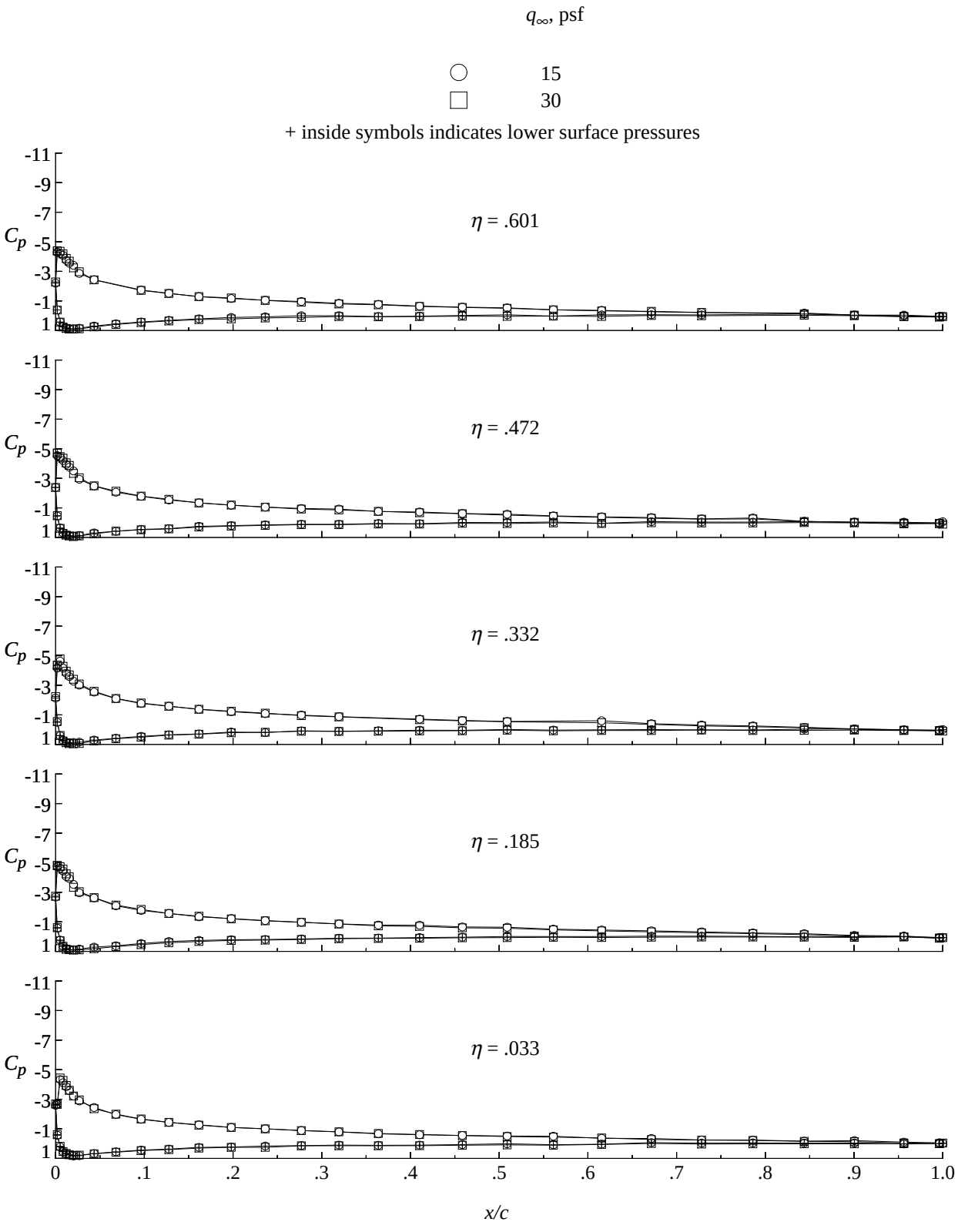


(m) $\alpha = 20°$.

Figure 4. Continued.

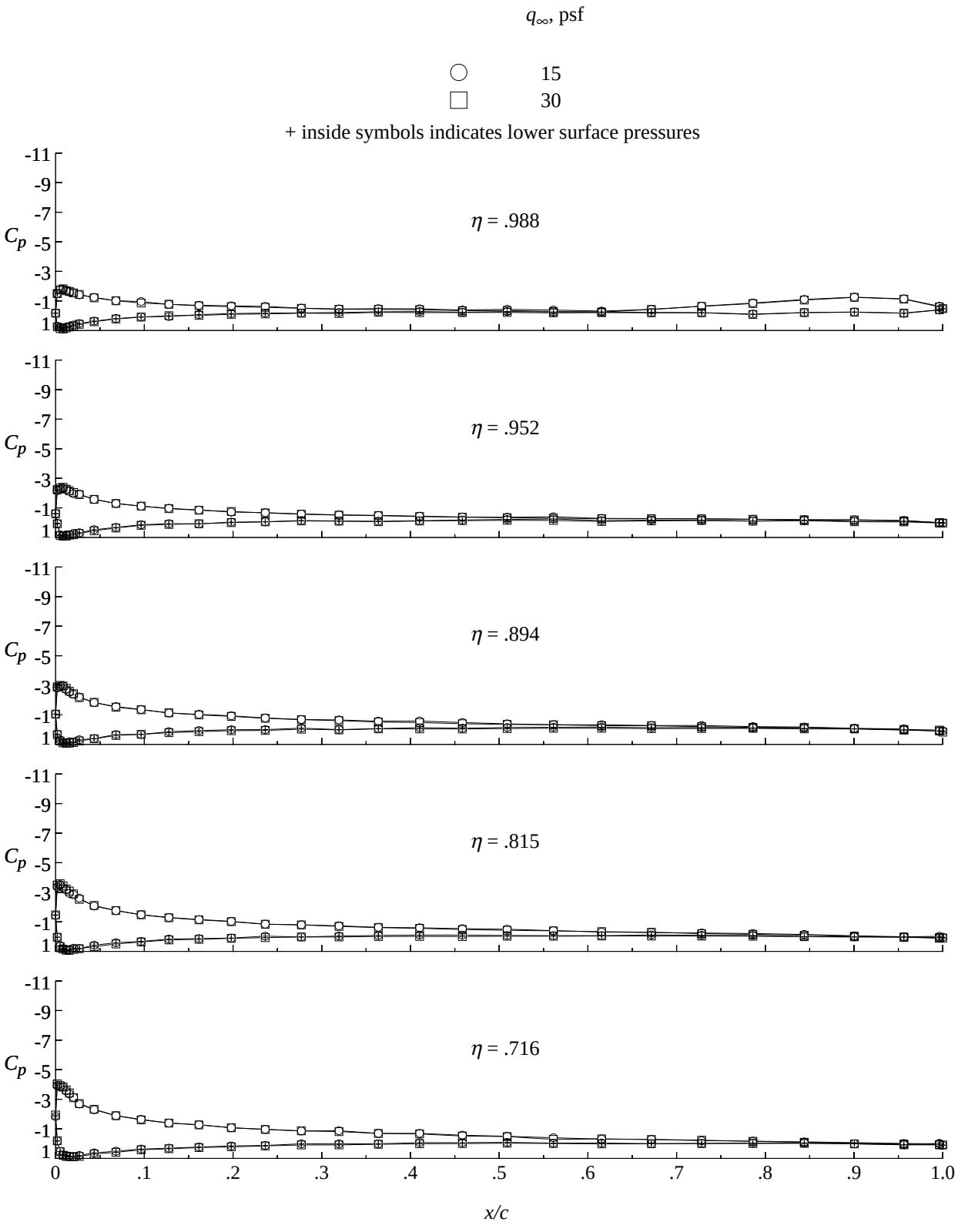


(m) Concluded.

Figure 4. Concluded.

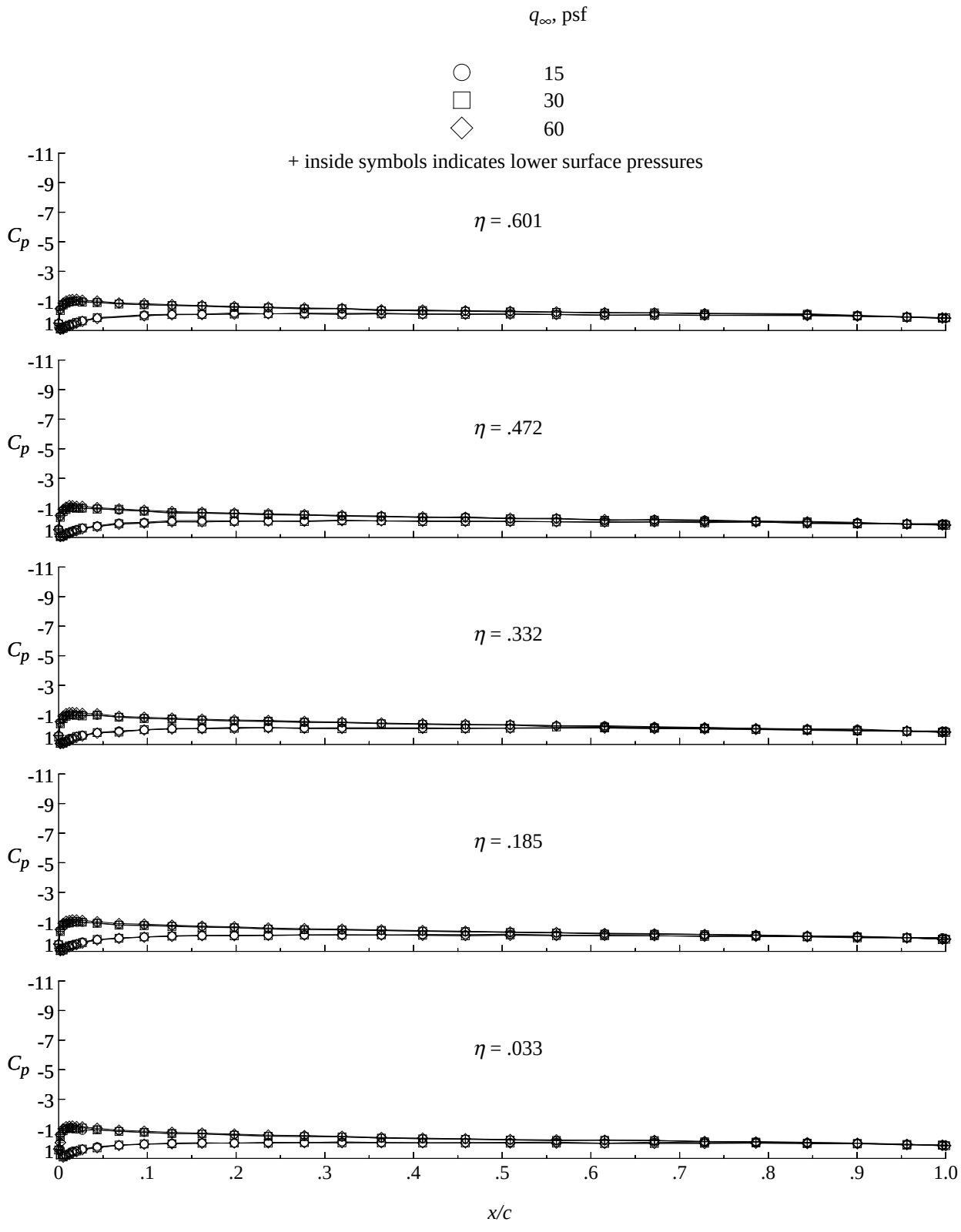


(a) $\alpha$ = - 4°.

Figure 5. Free-stream speed effect on cruise wing pressure distribution. Tunnel floor boundary layer suction on.

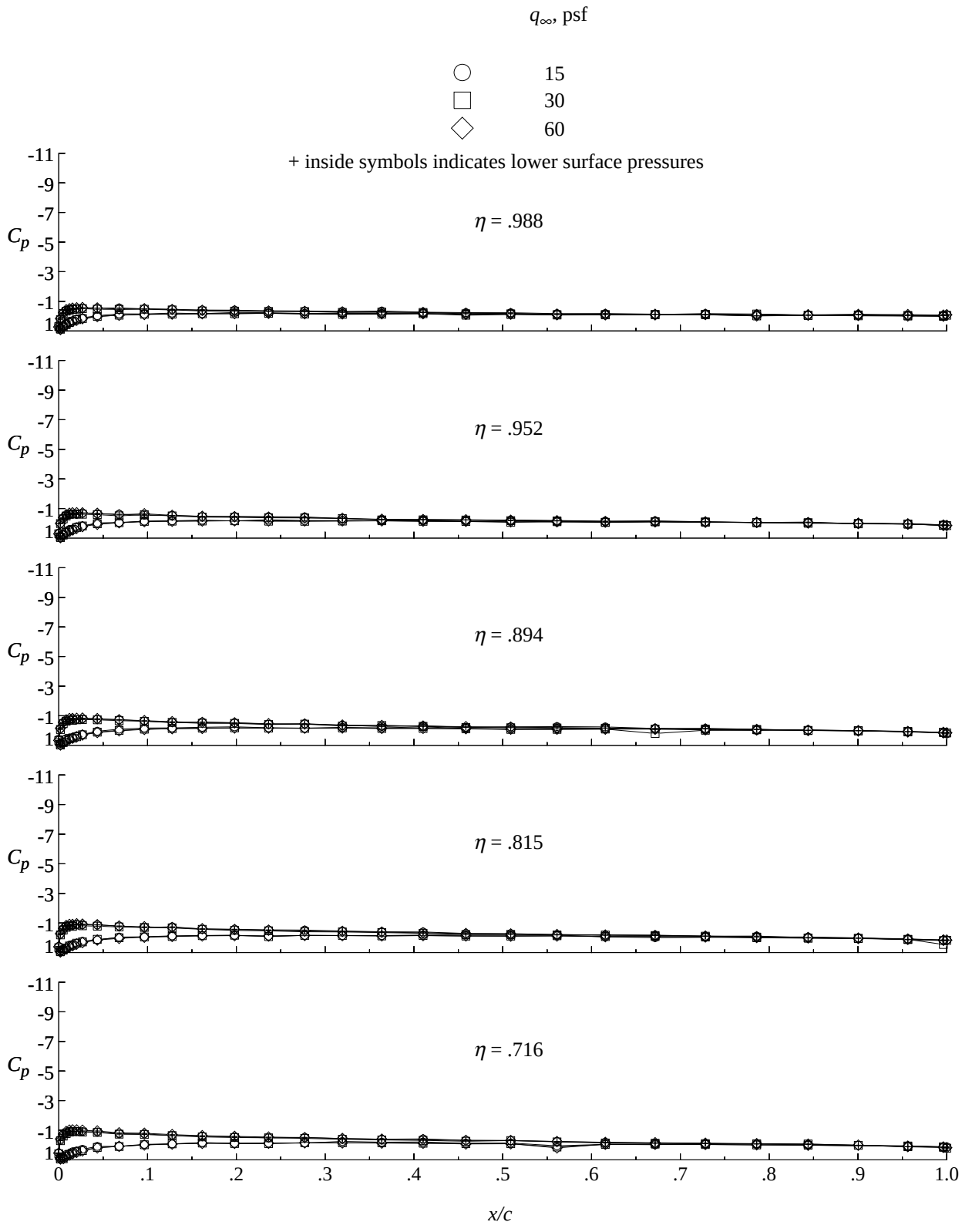


(a) Concluded.

Figure 5. Continued.

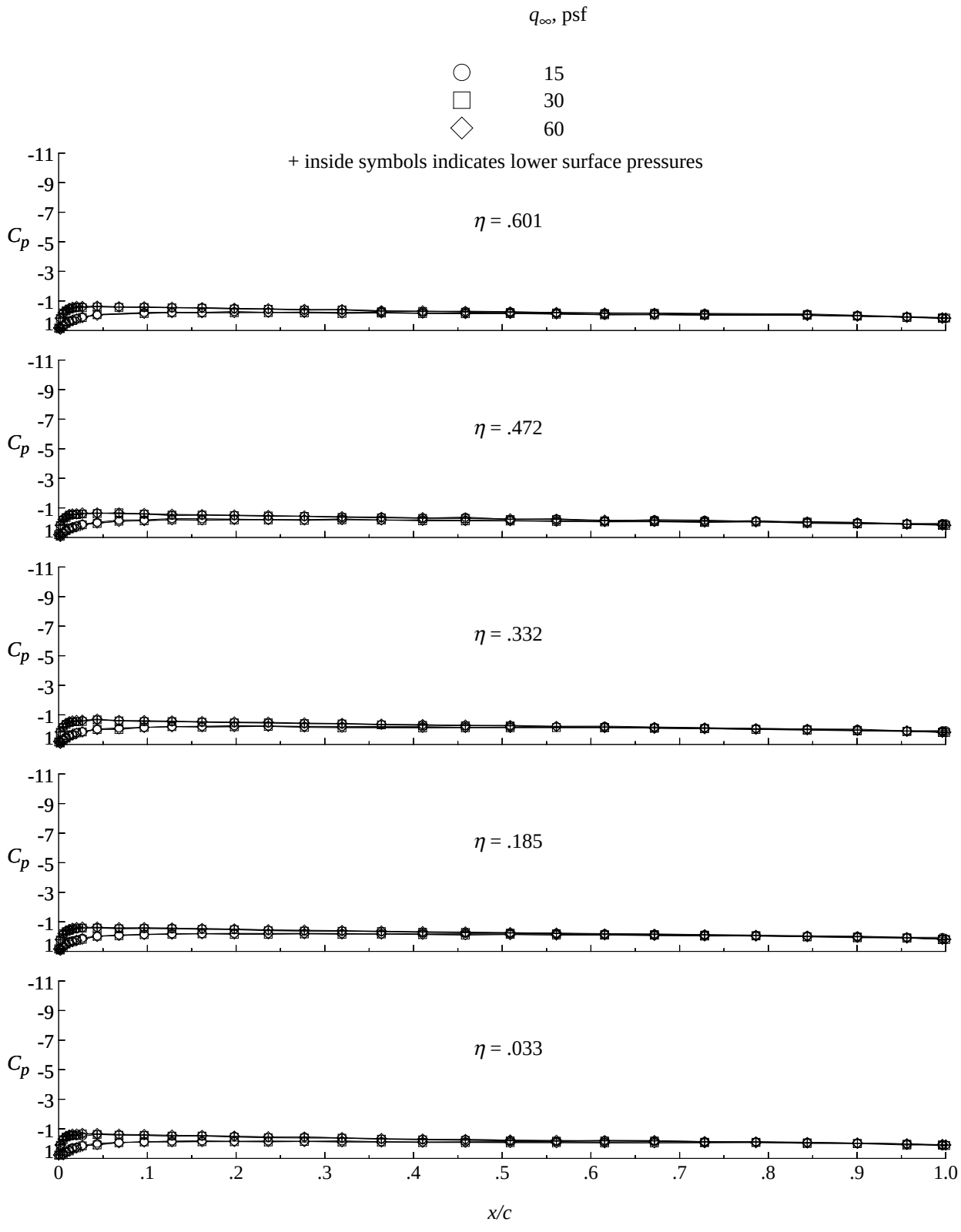


(b) $\alpha$ = - 2°.

Figure 5. Continued.

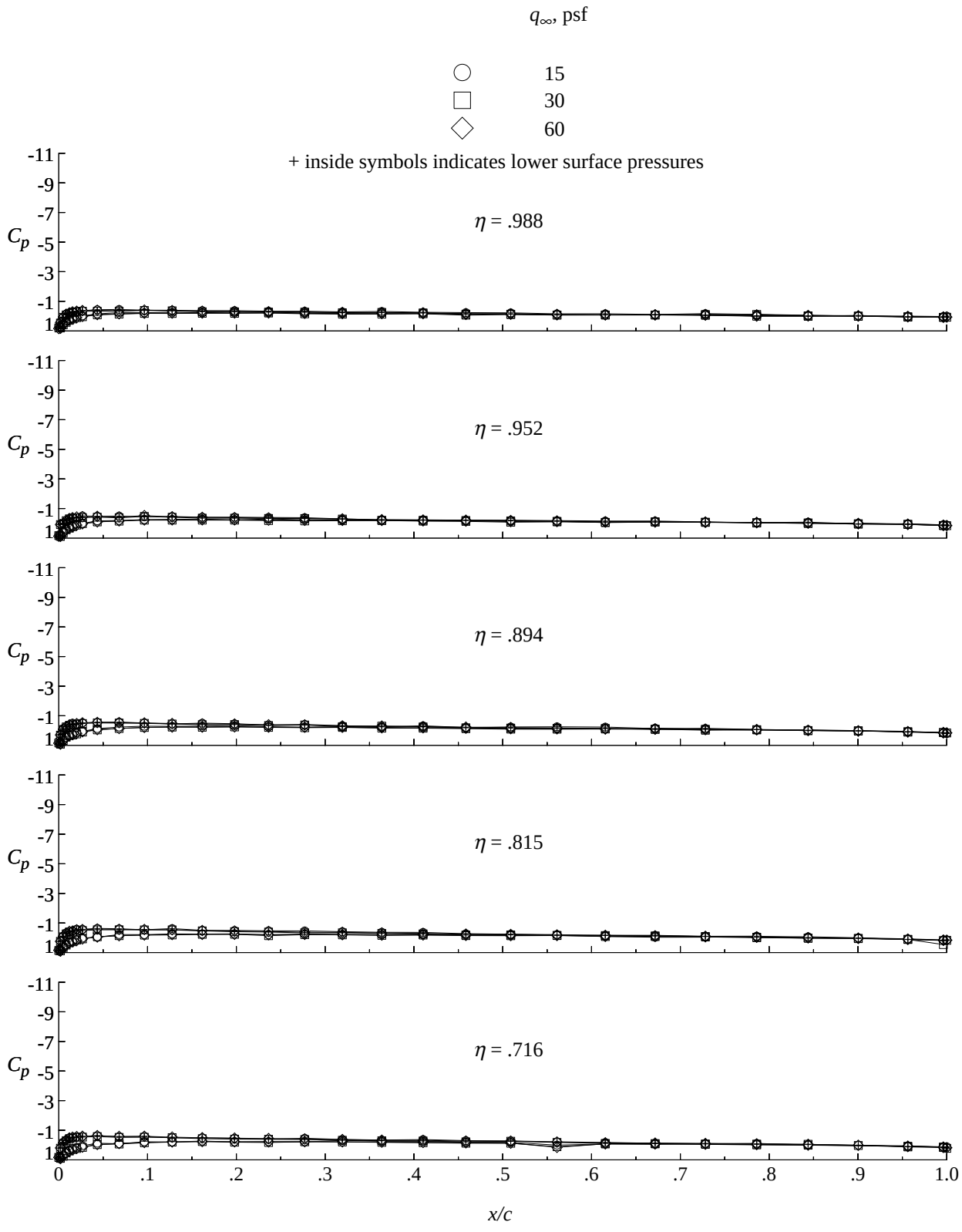


(b) Concluded.

Figure 5. Continued.

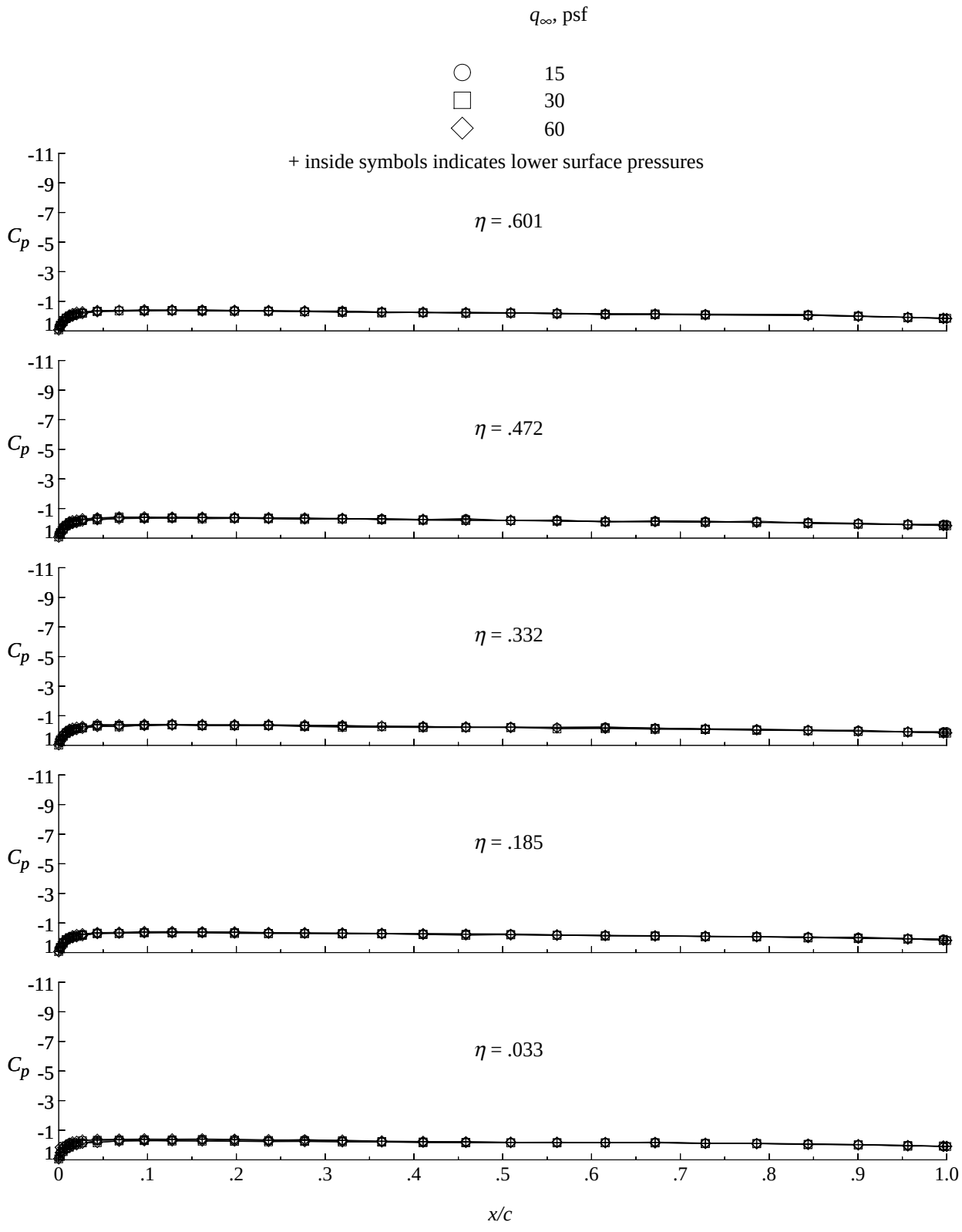


(c) $\alpha = 0°$.

Figure 5. Continued.

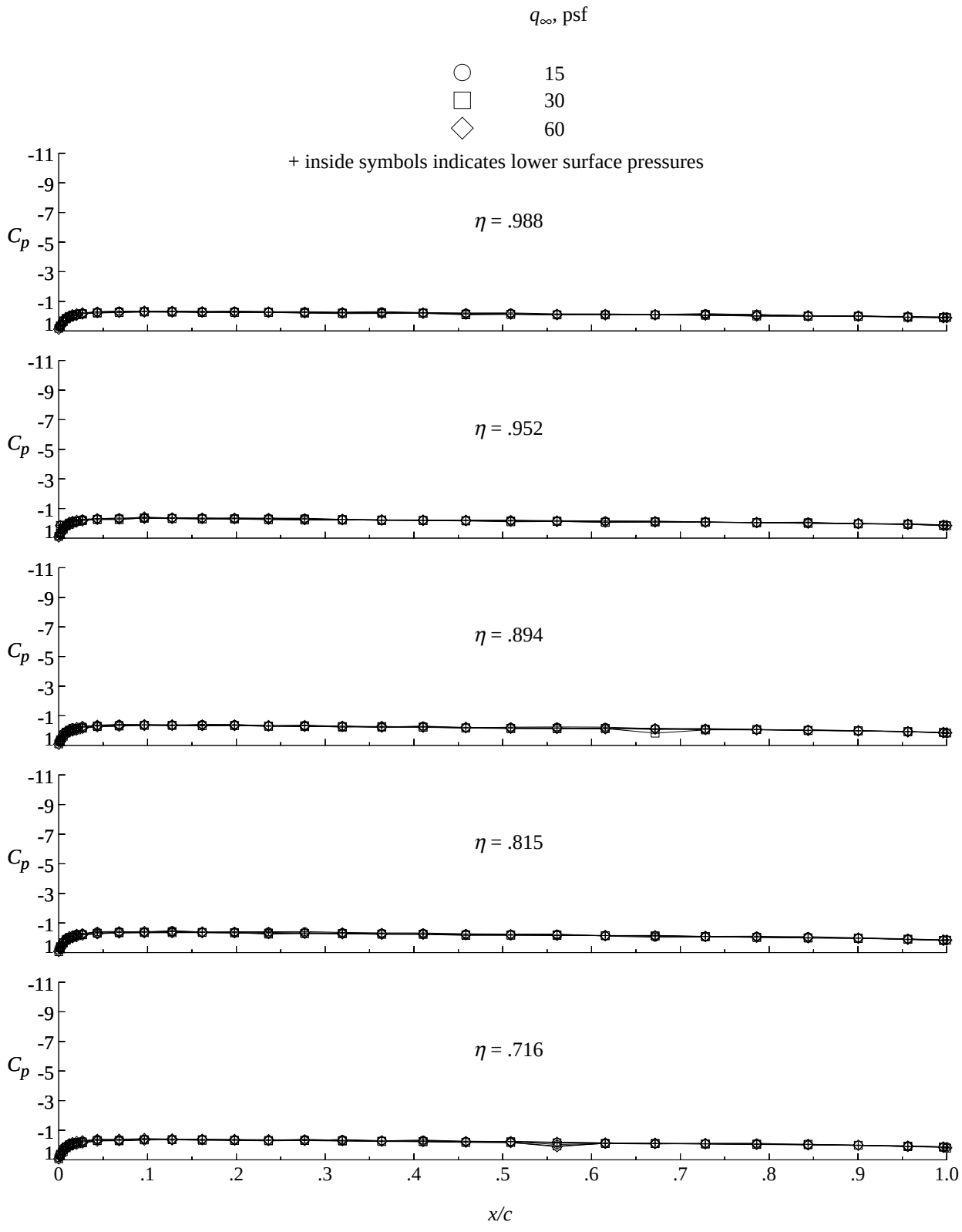


(c) Concluded.

Figure 5. Continued.

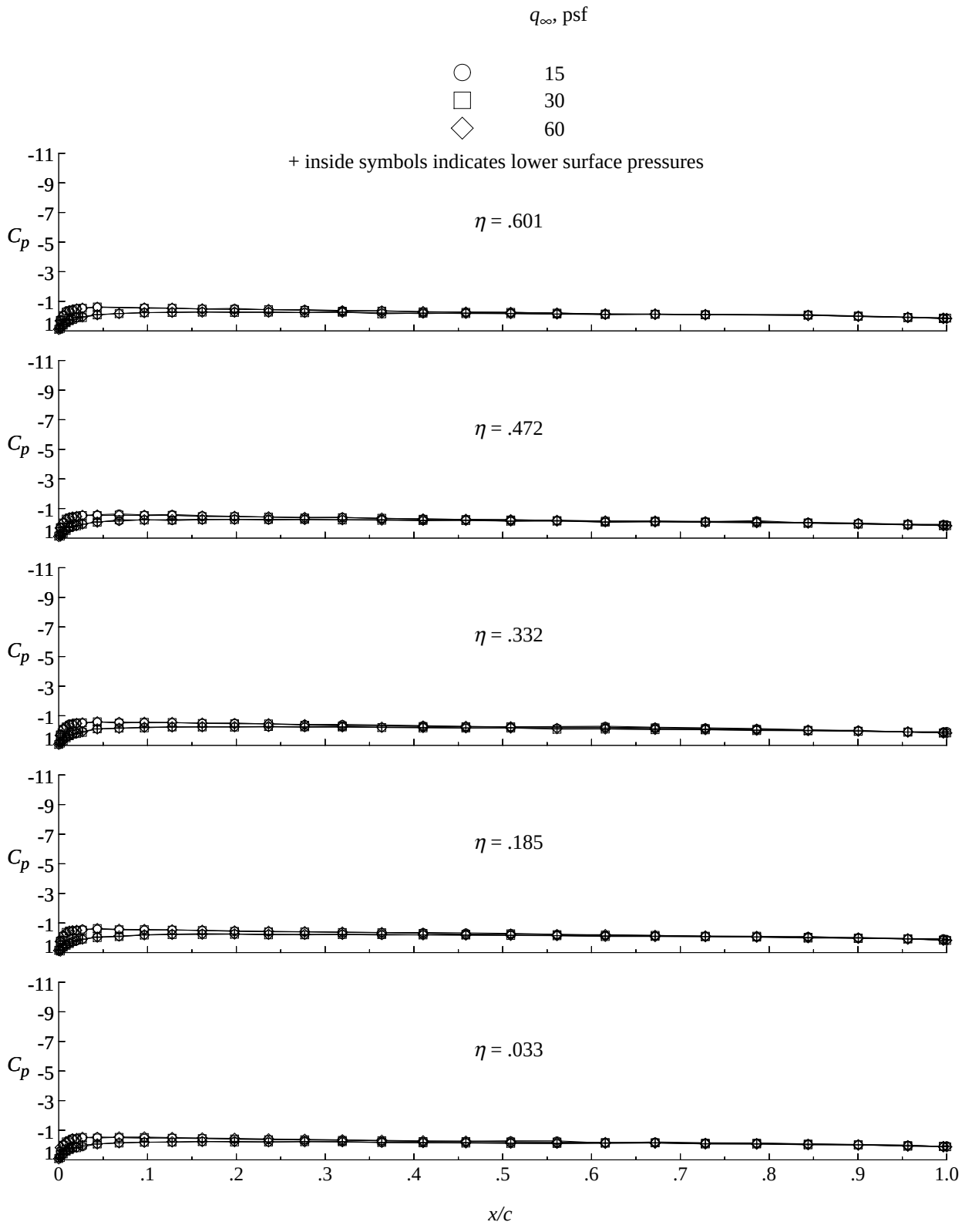


(d) $\alpha = 2°$.

Figure 5. Continued.

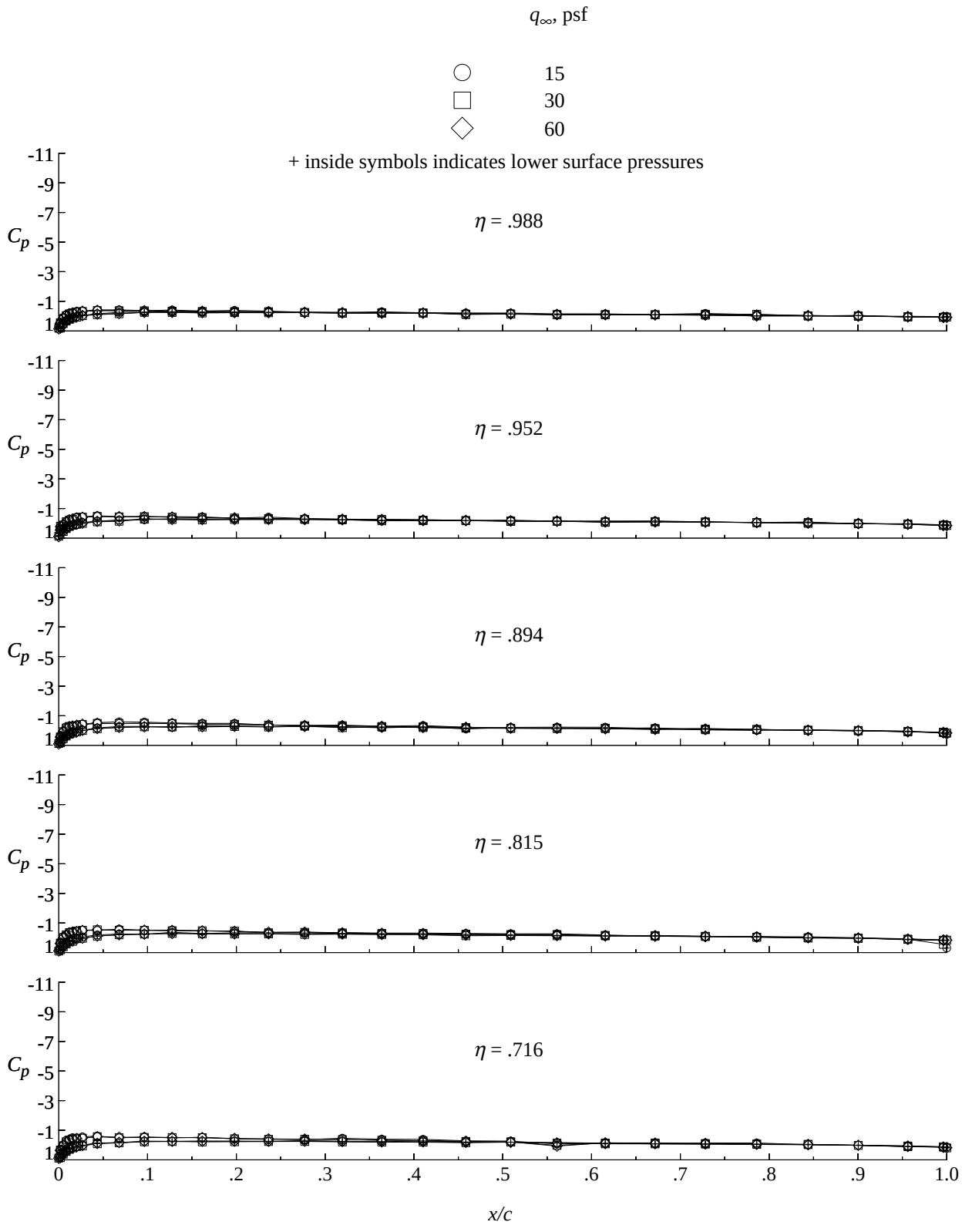


(d) Concluded.

Figure 5. Continued.

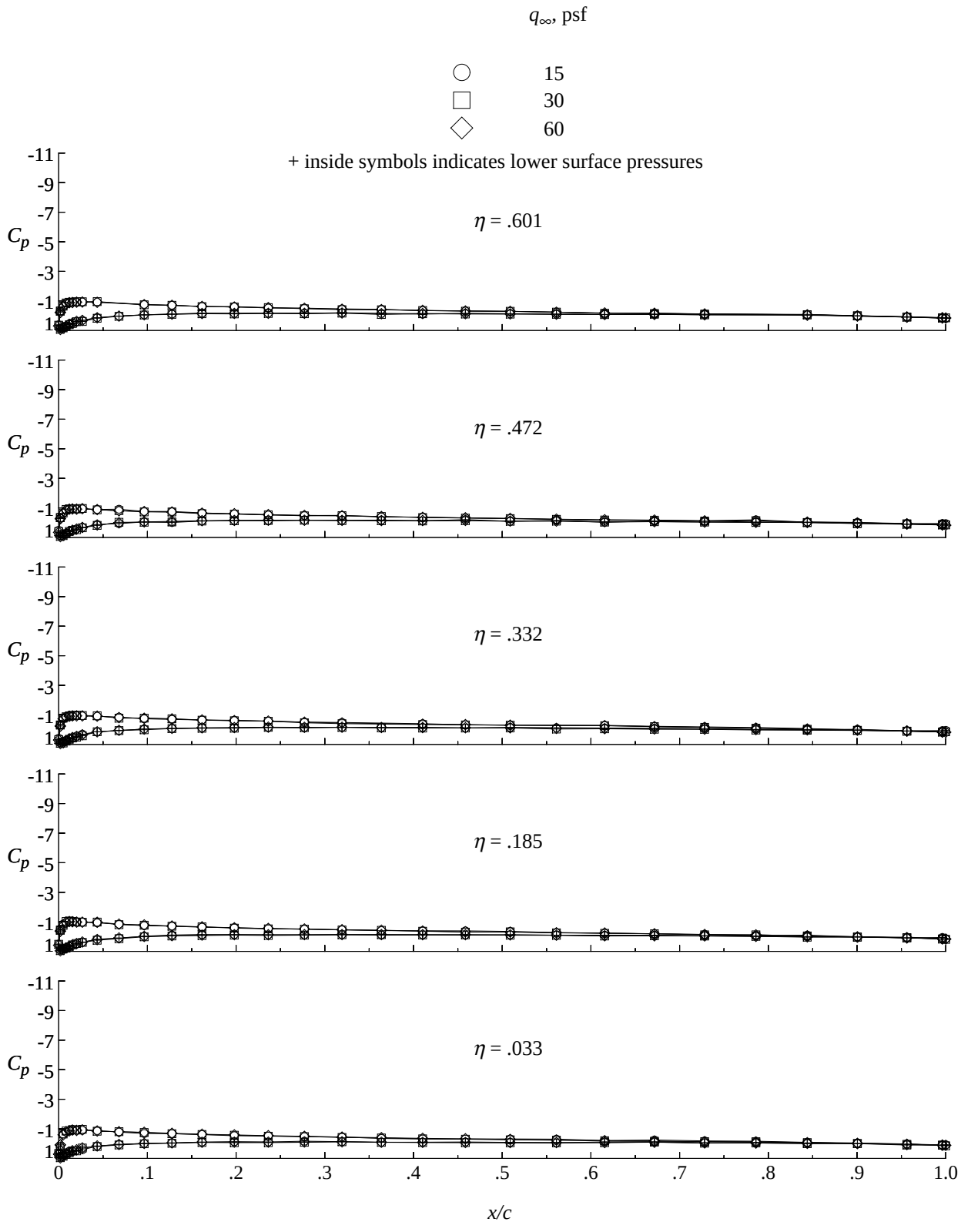


(e) $\alpha = 4°$.

Figure 5. Continued.

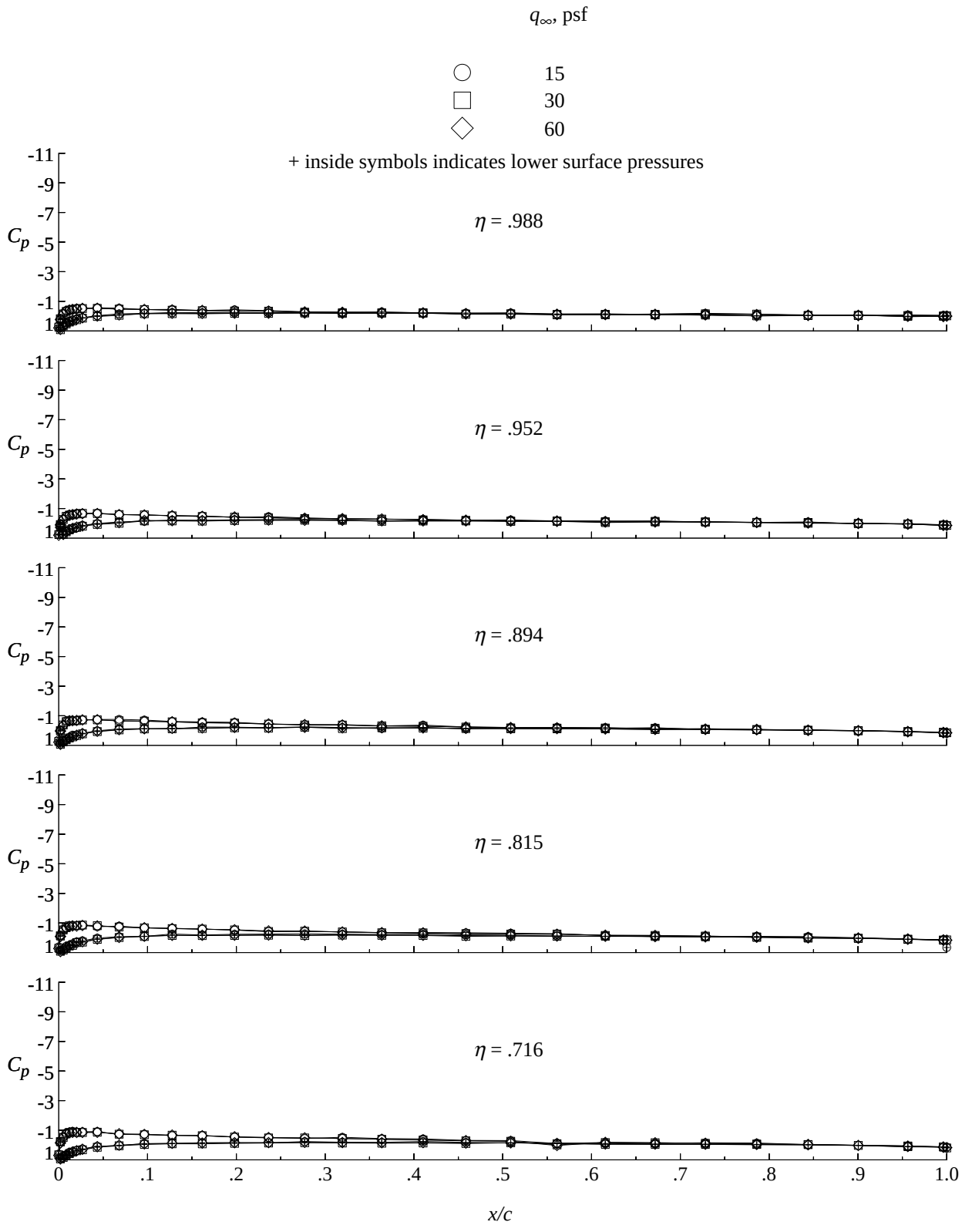


(e) Concluded.

Figure 5. Continued.

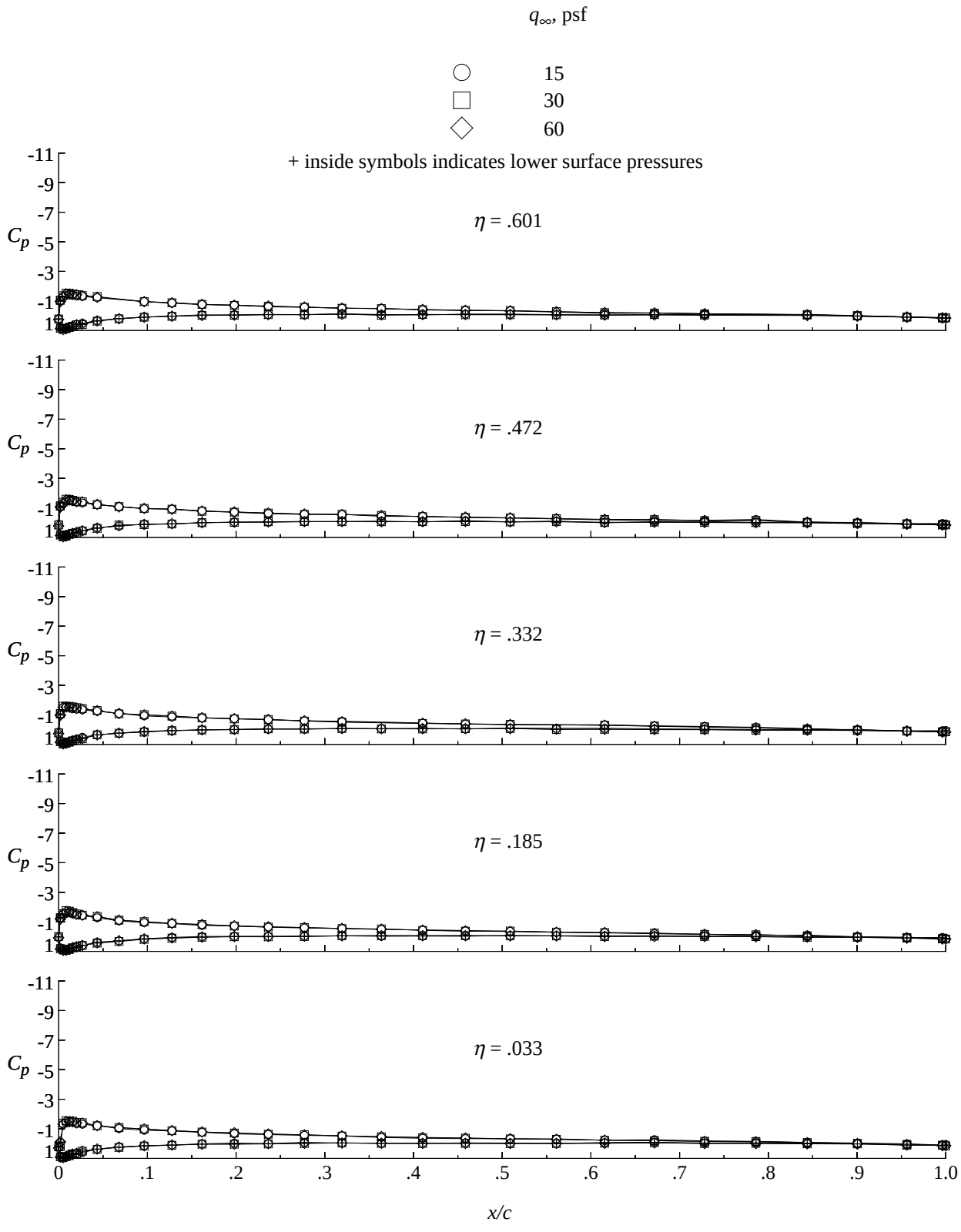


(f) $\alpha = 6°$.

Figure 5. Continued.

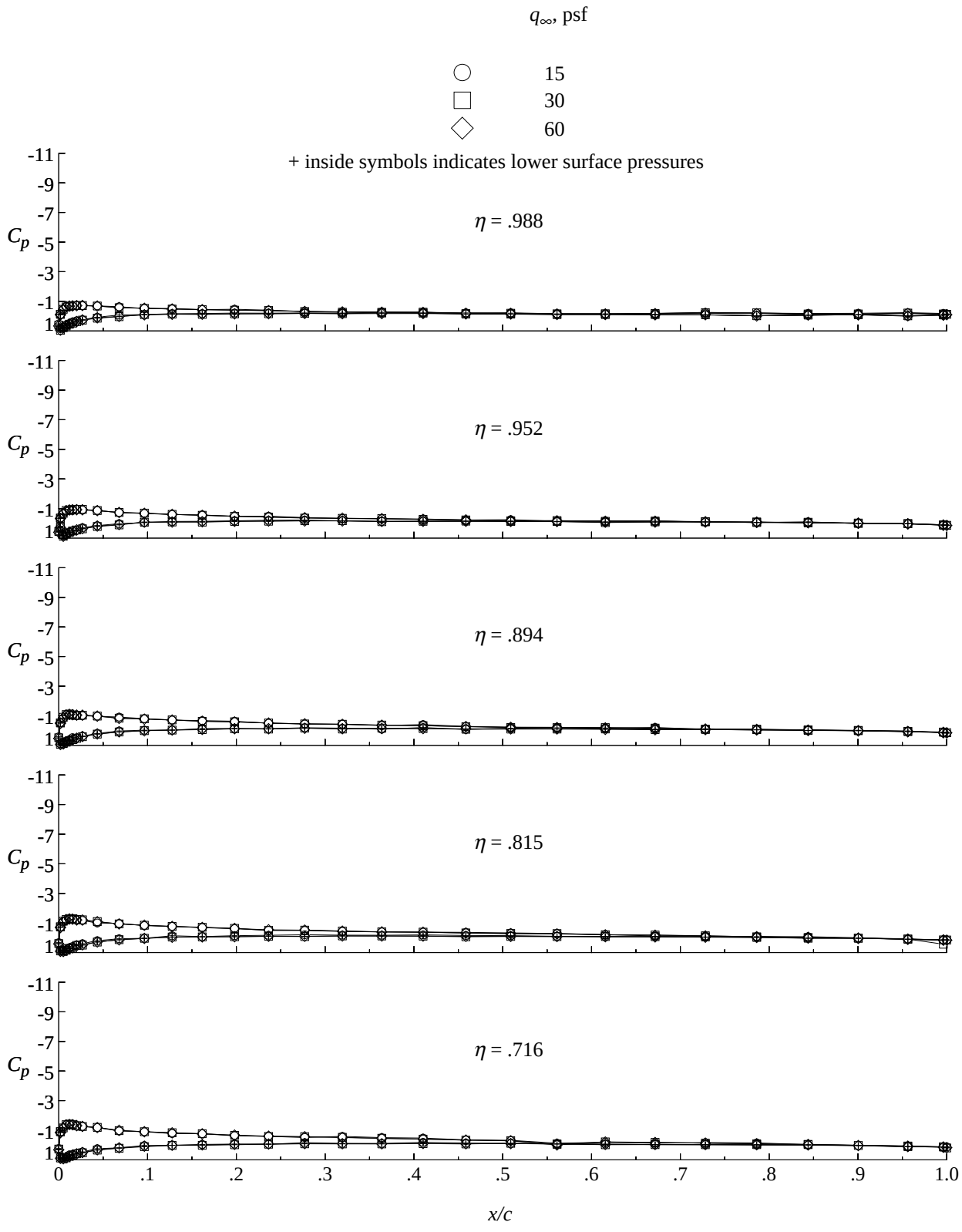


(f) Concluded.

Figure 5. Continued.

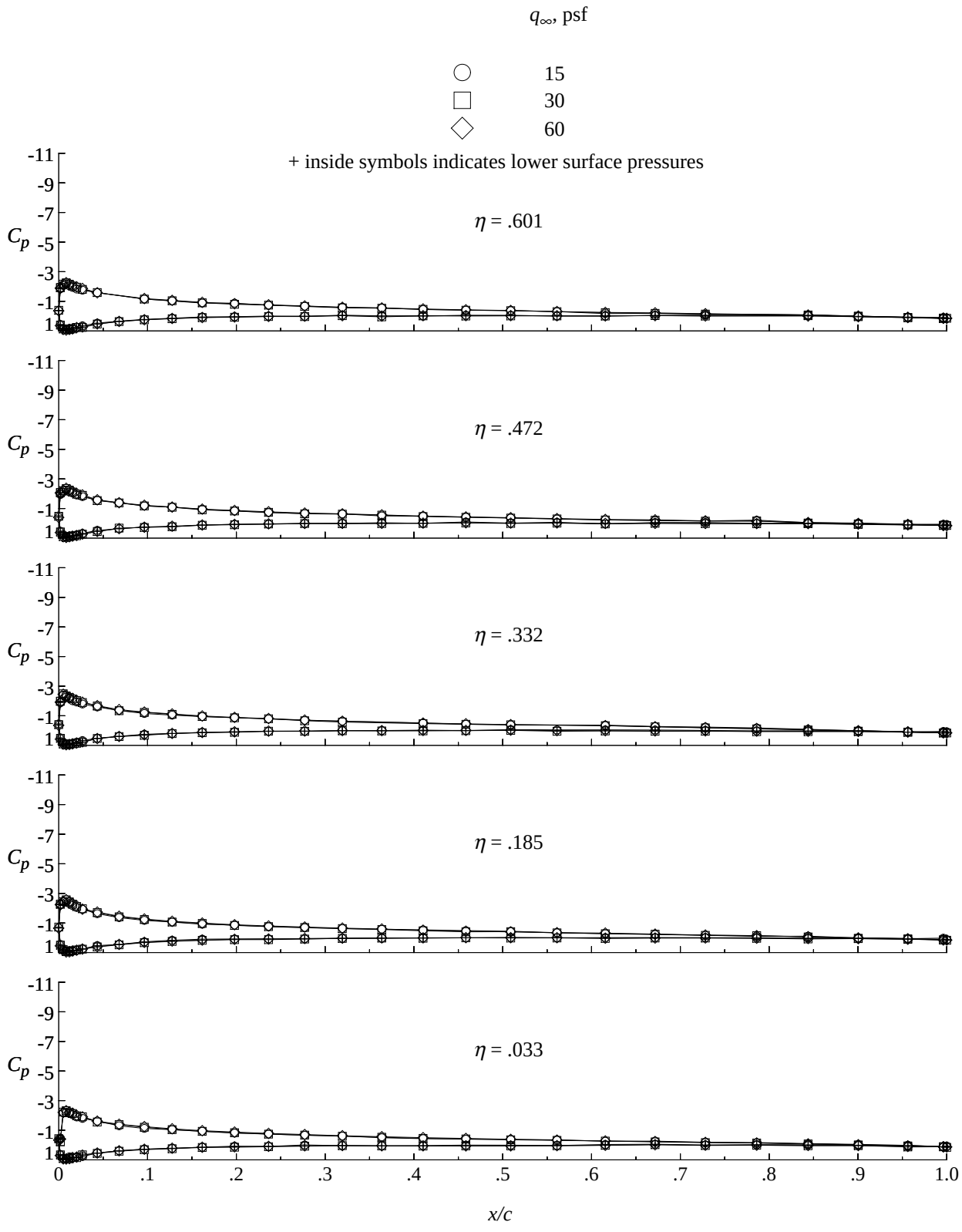


(g) $\alpha = 8°$.

Figure 5. Continued.

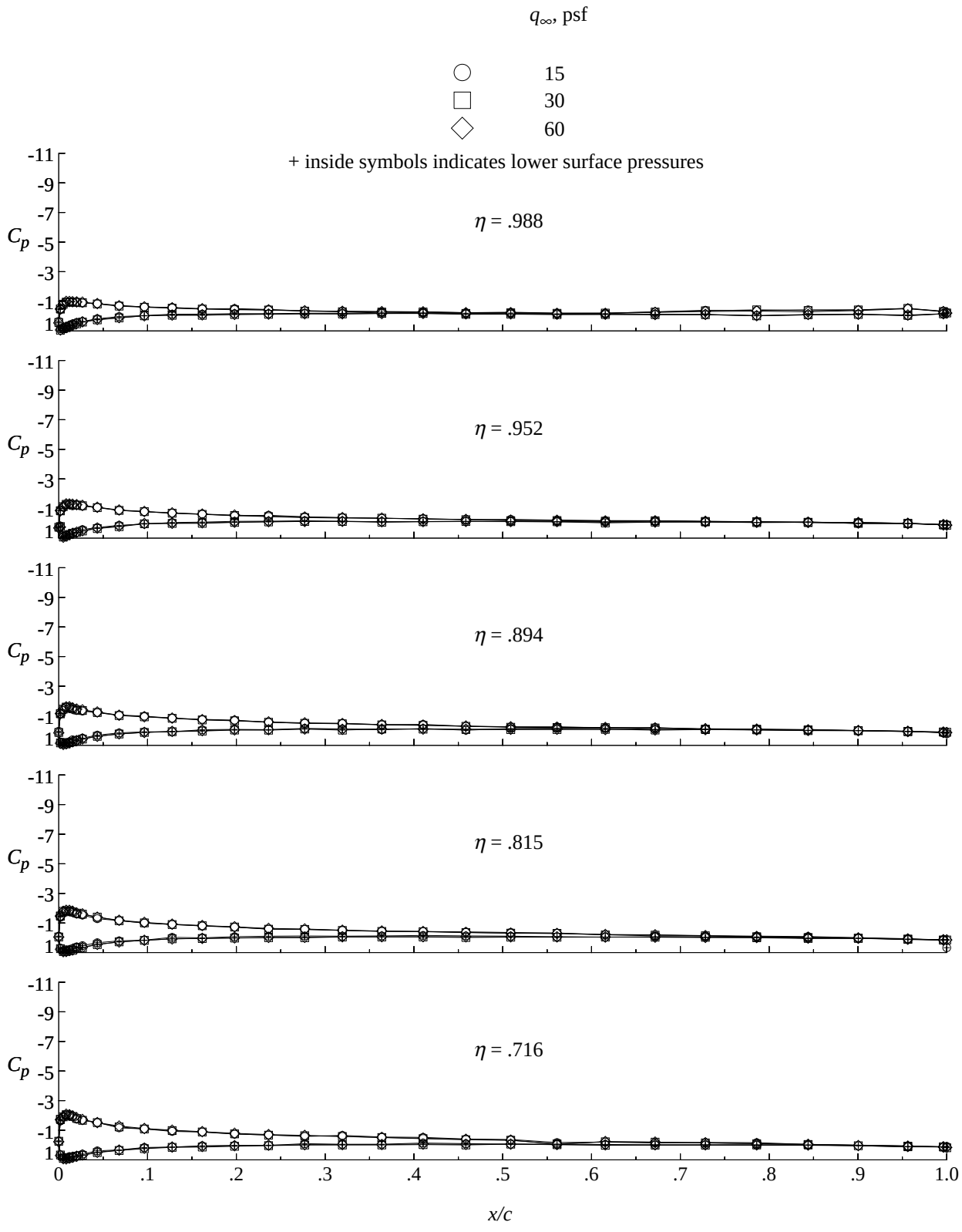


(g) Concluded.

Figure 5. Continued.

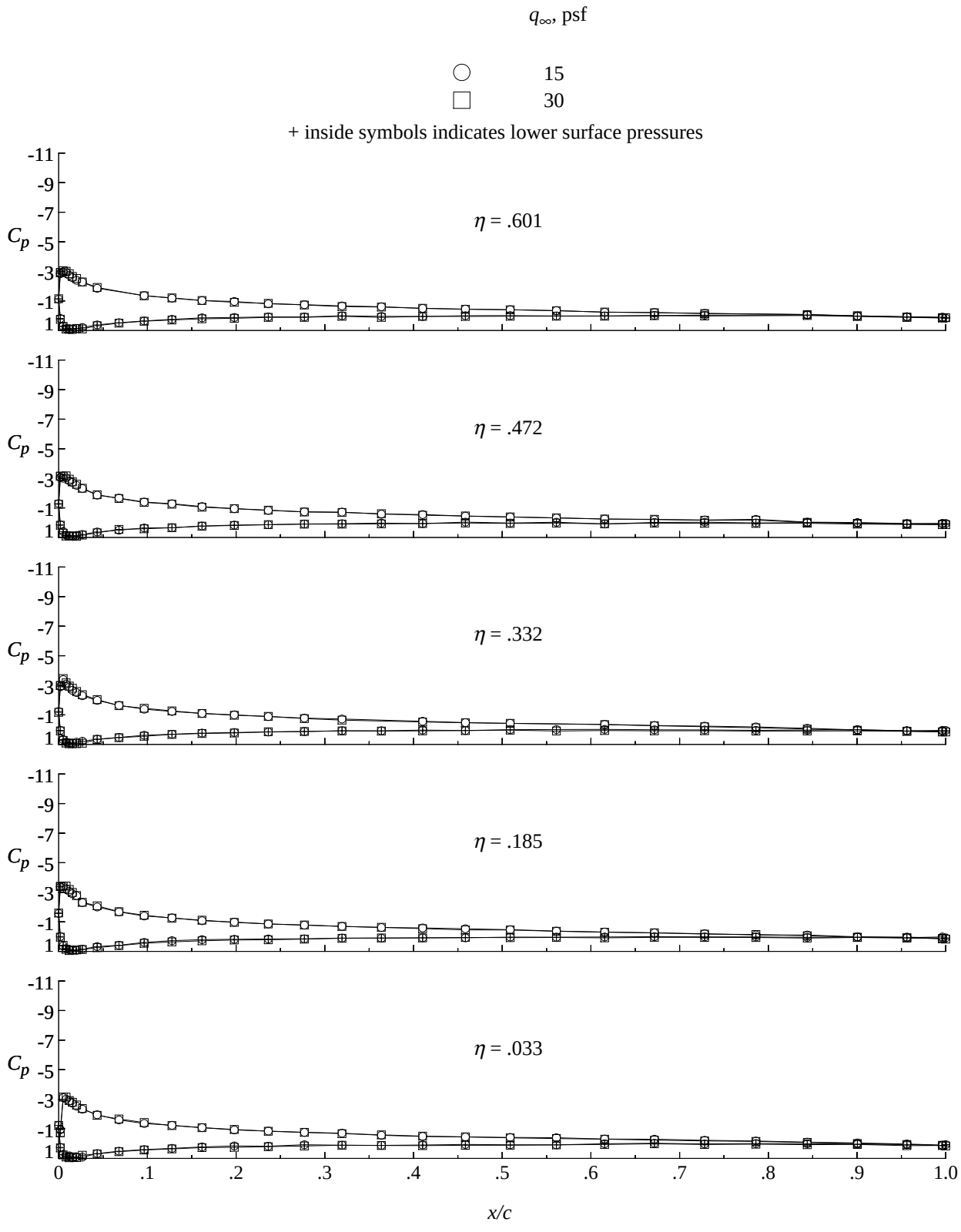


(h) $\alpha = 10°$.

Figure 5. Continued.

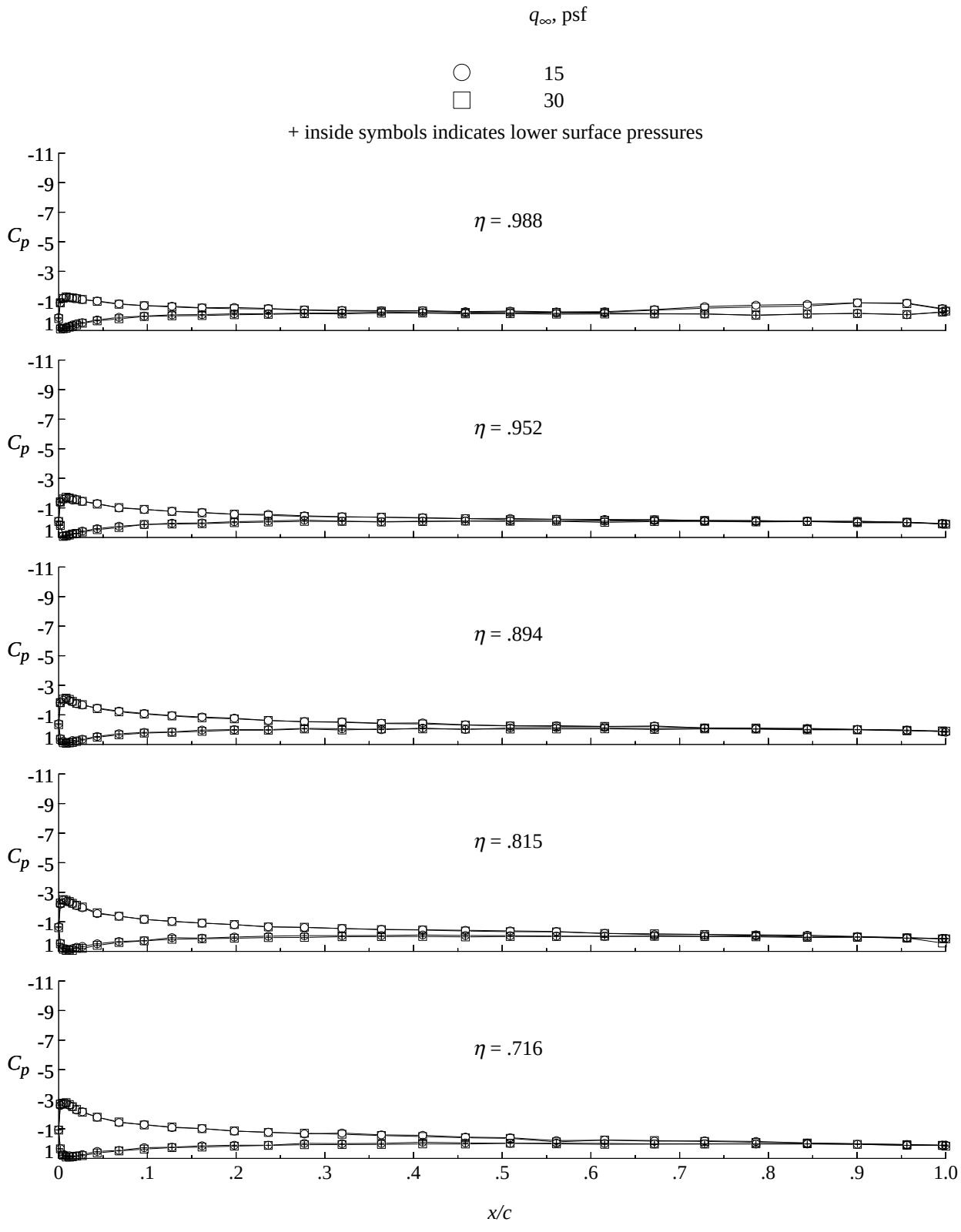


(h) Concluded.

Figure 5. Continued.

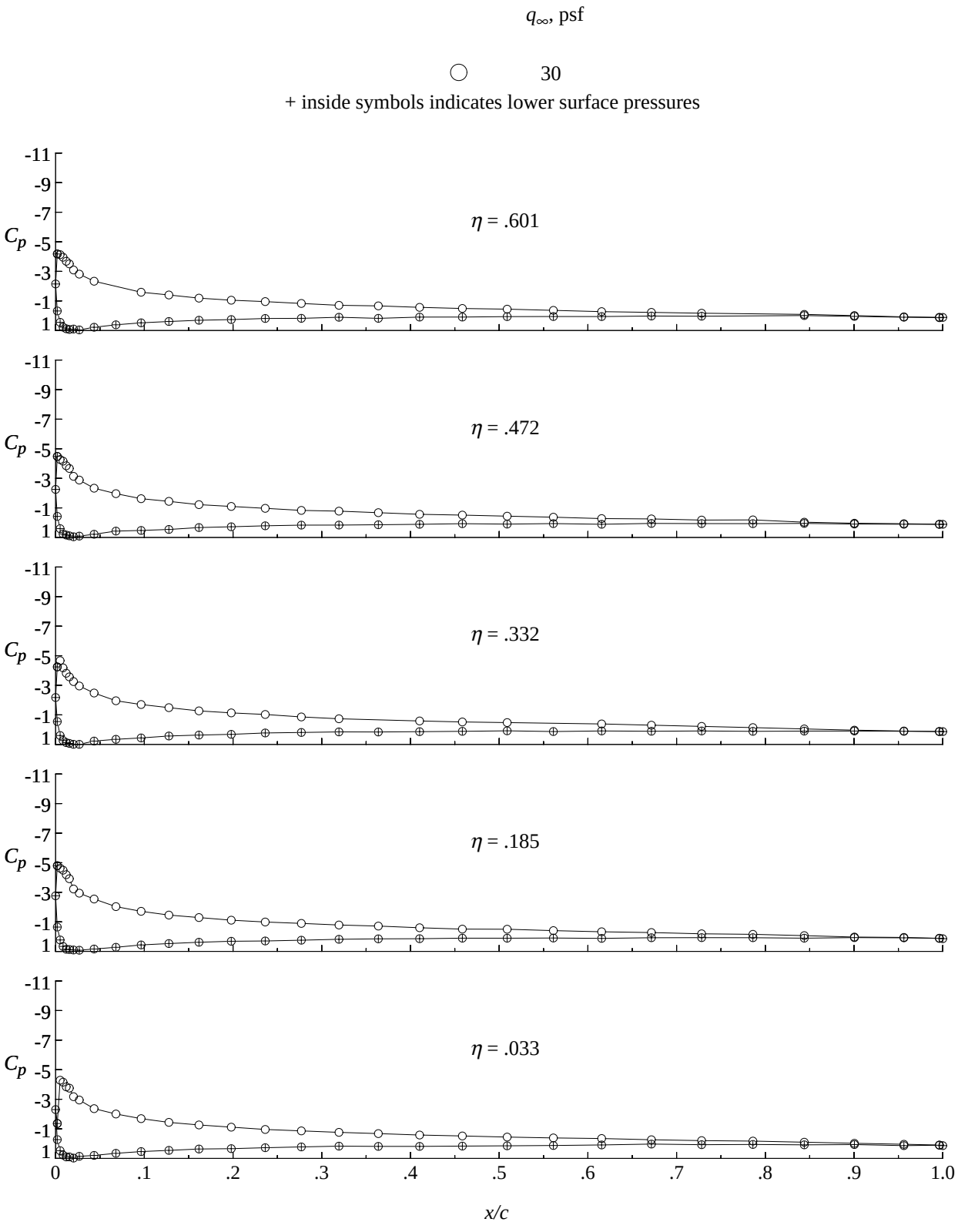


(i) $\alpha = 12°$.

Figure 5. Continued.

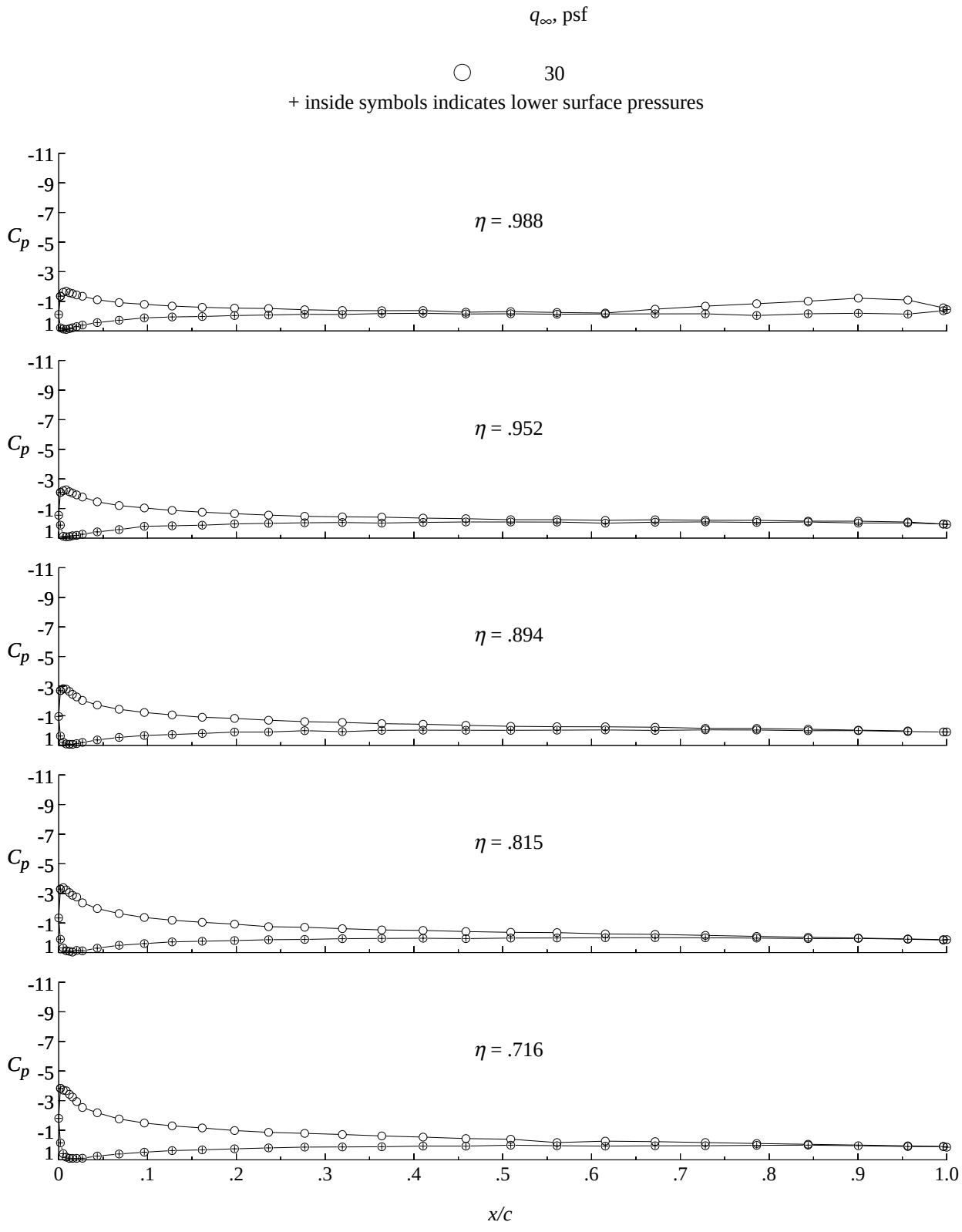


(i) Concluded.

Figure 5. Continued.

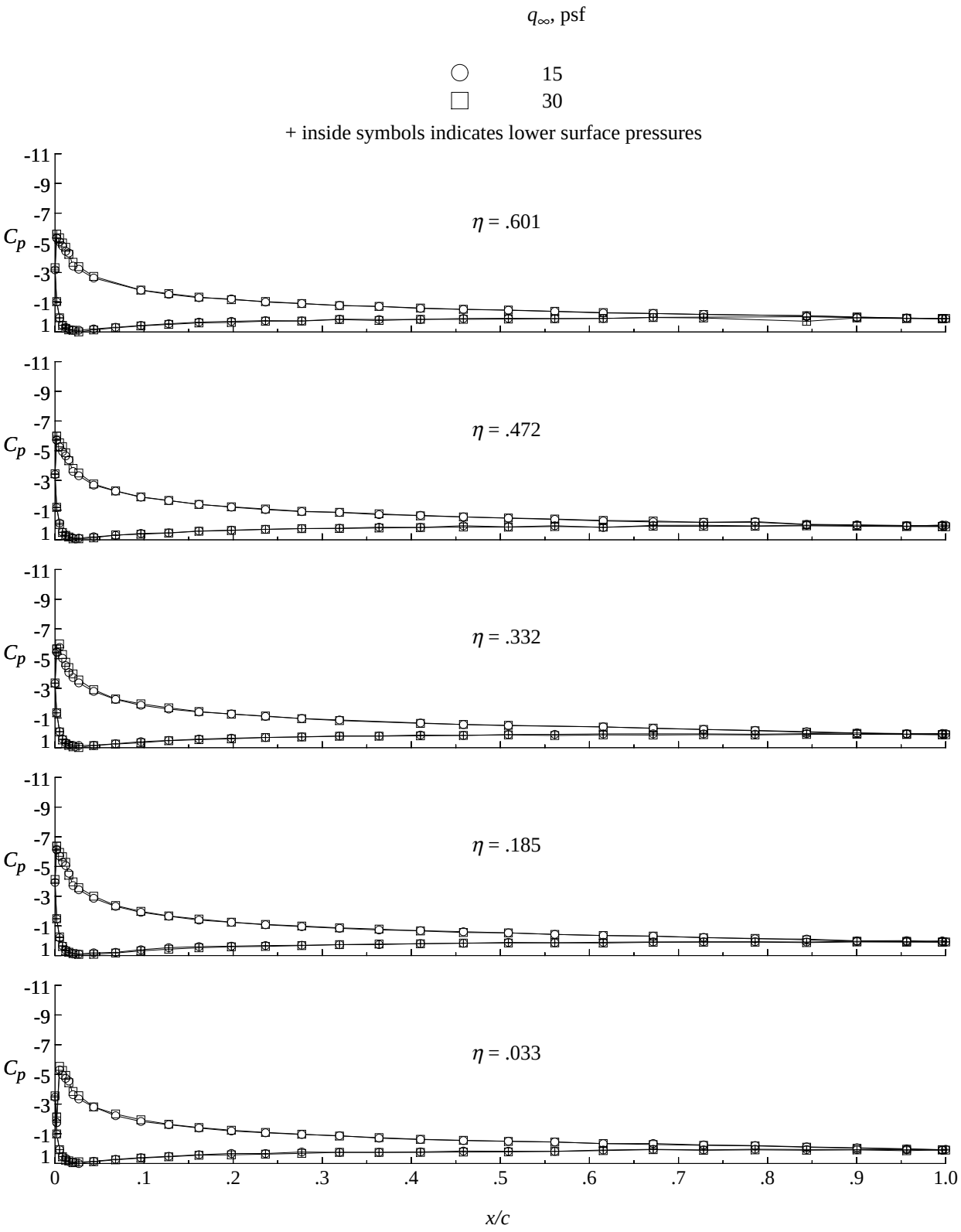


(j) $\alpha = 14°$.

Figure 5. Continued.

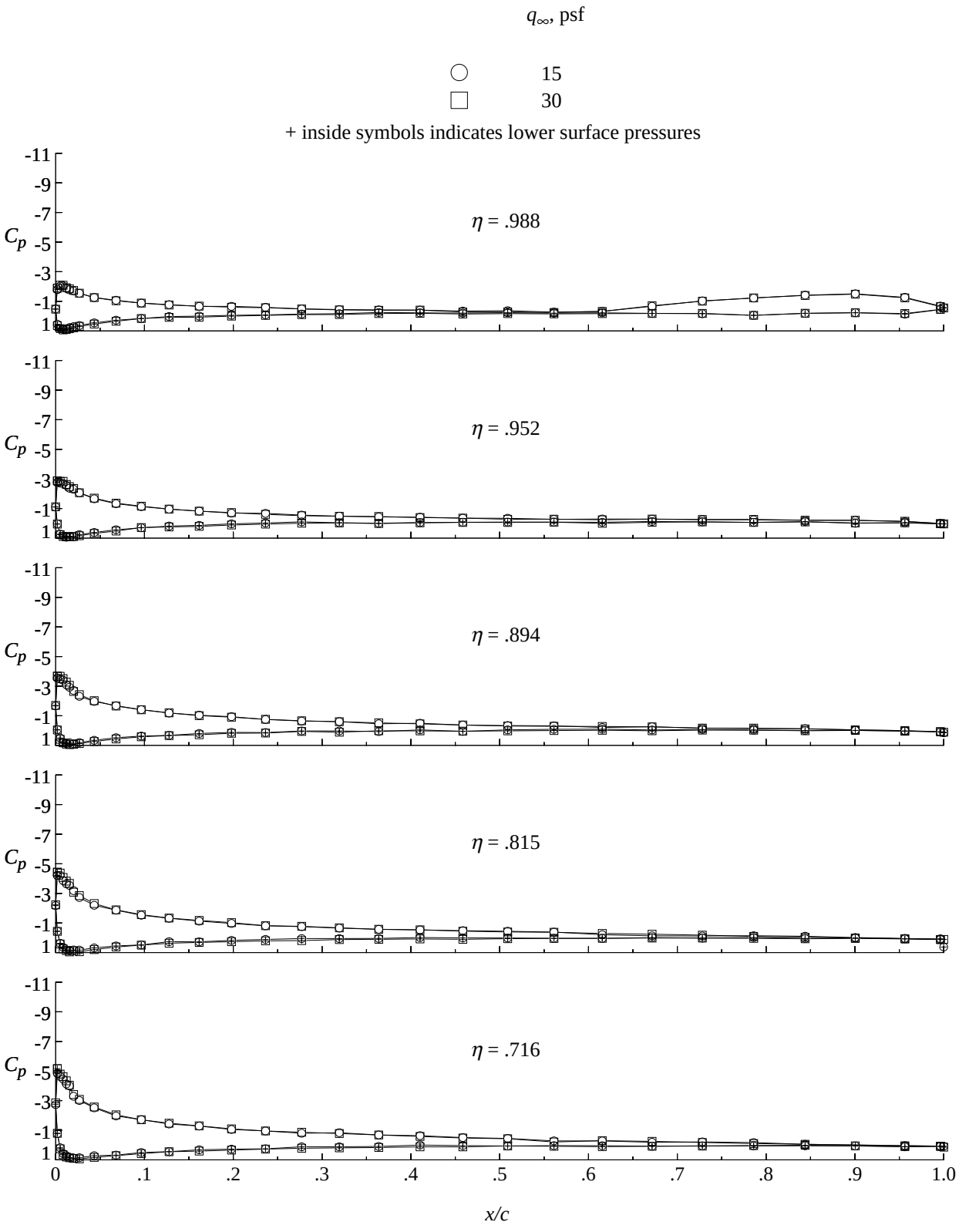


(j) Concluded.

Figure 5. Continued.

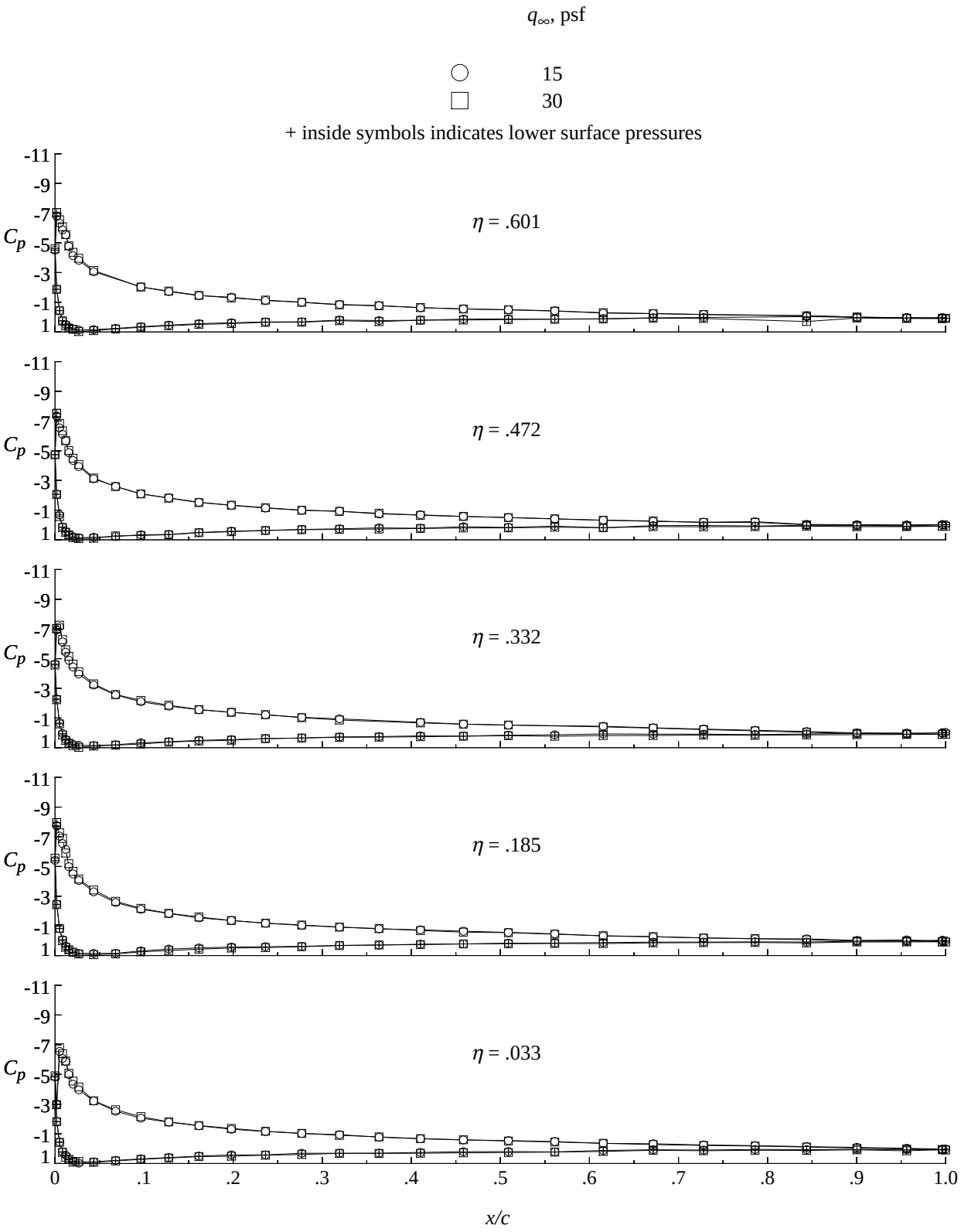


(k) $\alpha = 16°$.

Figure 5. Continued.

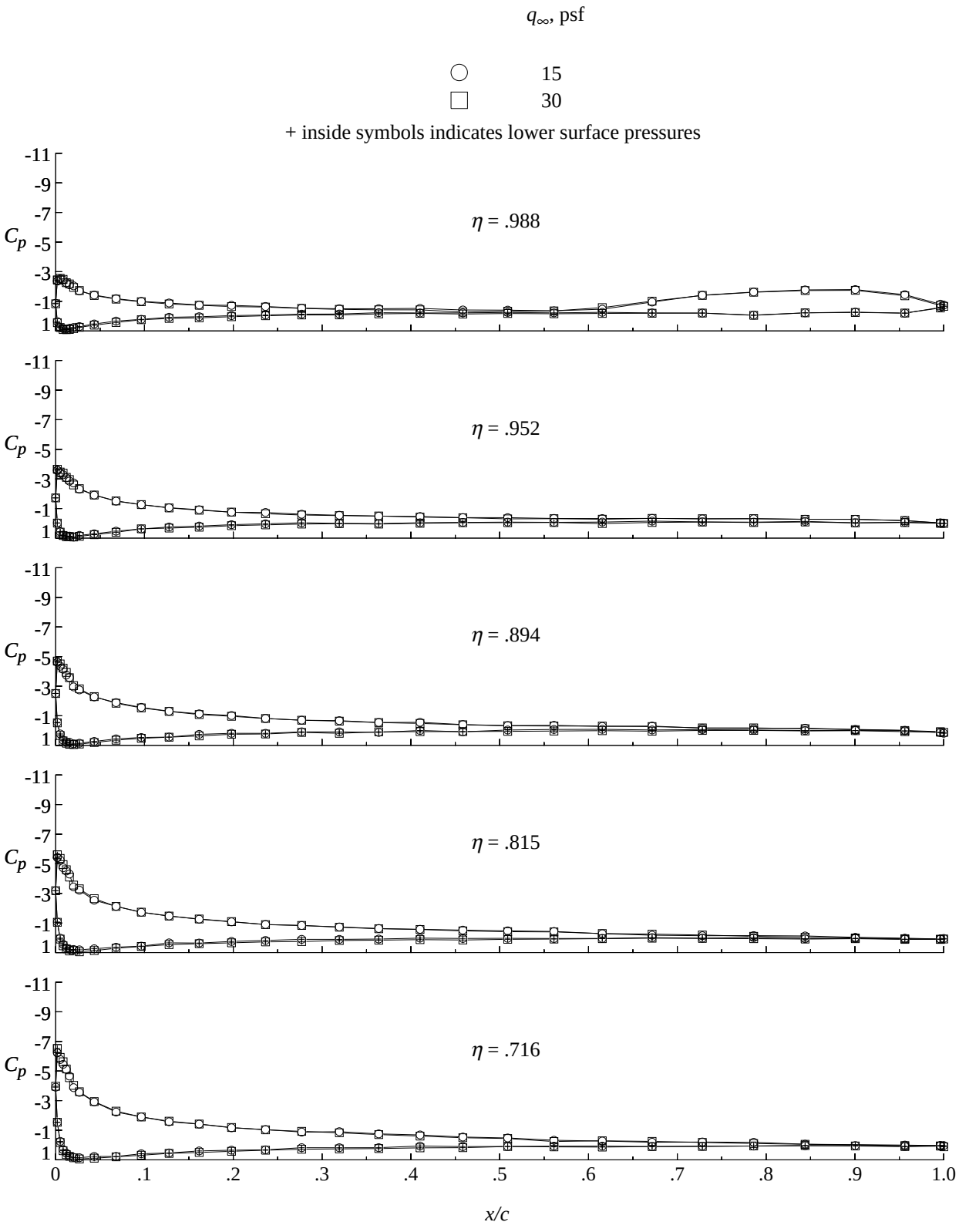


(k) Concluded.

Figure 5. Continued.

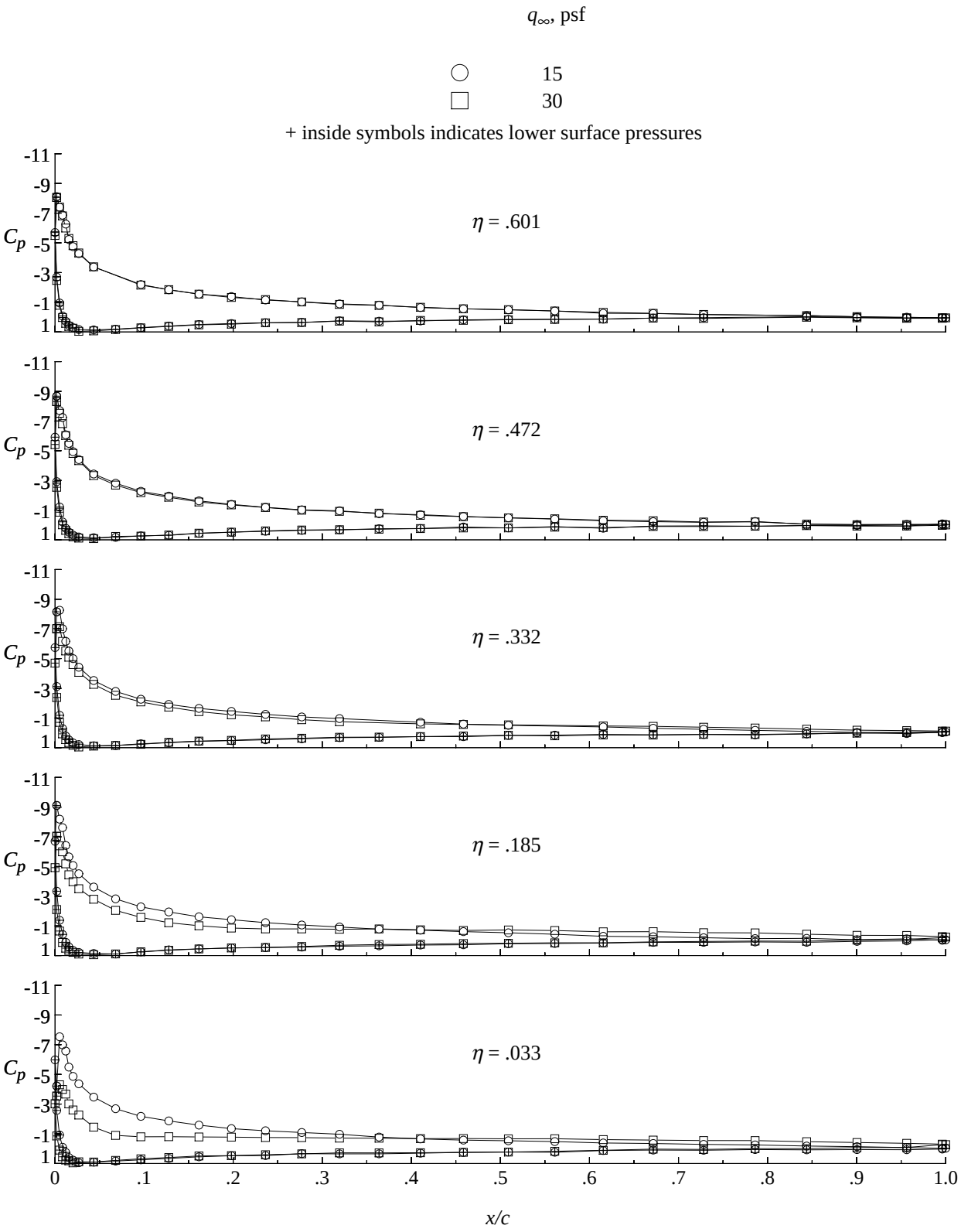


(l) $\alpha = 18°$.

Figure 5. Continued.

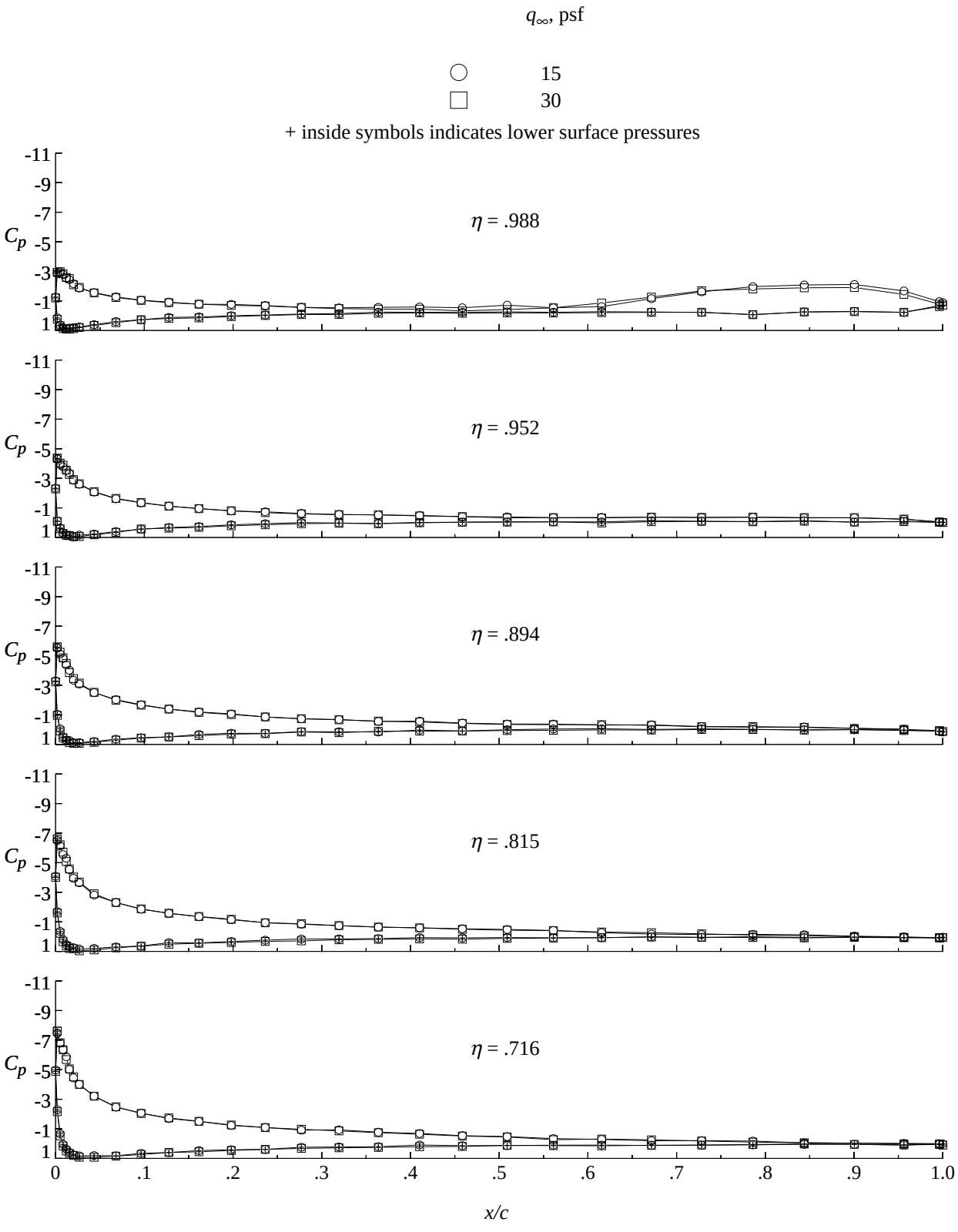


(l) Concluded.

Figure 5. Concluded.

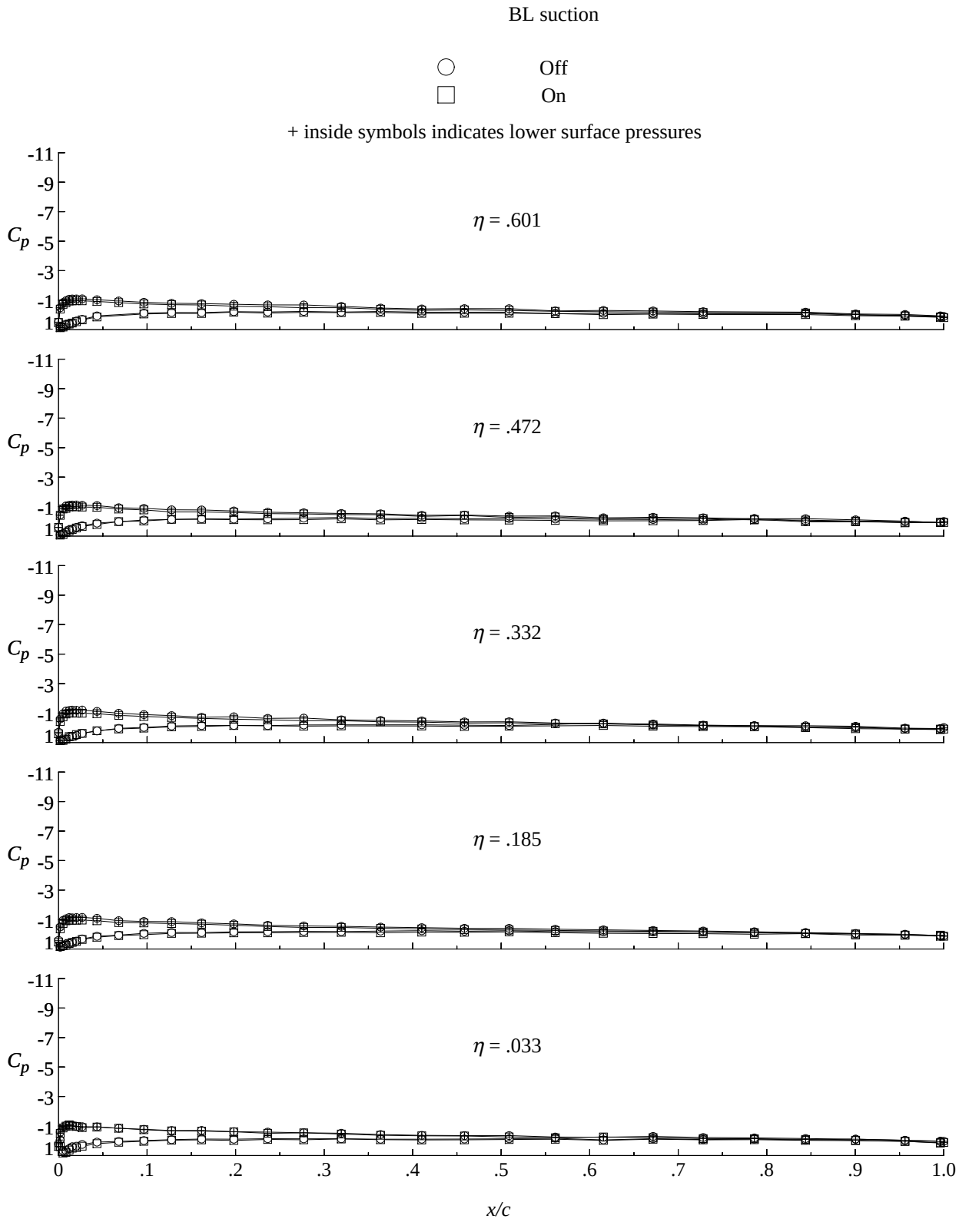


(a) $\alpha$ = - 4°.

Figure 6. Effect of tunnel floor boundary layer suction on cruise wing pressure distribution. $q_\infty$ = 15 psf.

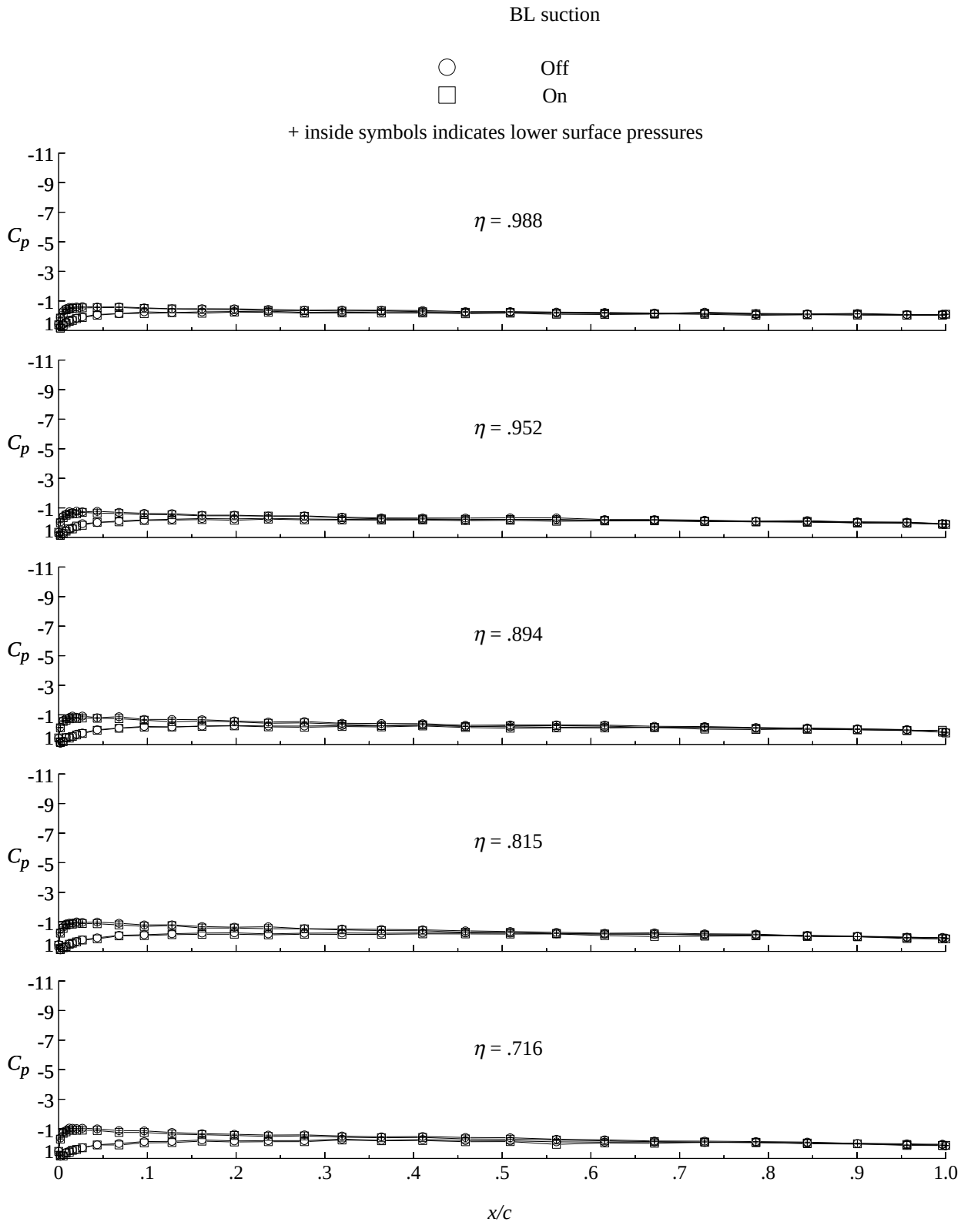


(a) Concluded.

Figure 6. Continued.

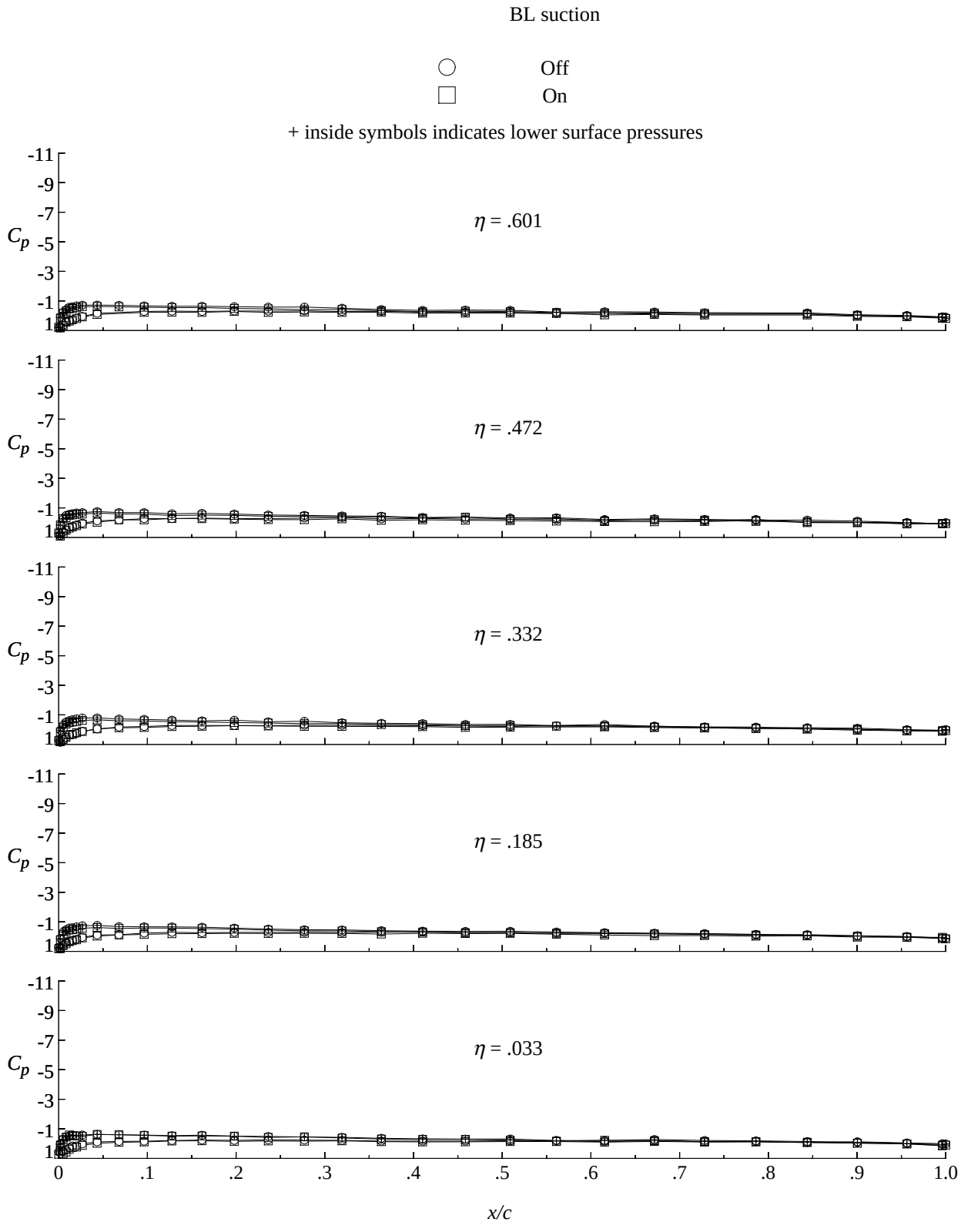


(b) $\alpha$ = - 2°.

Figure 6. Continued.

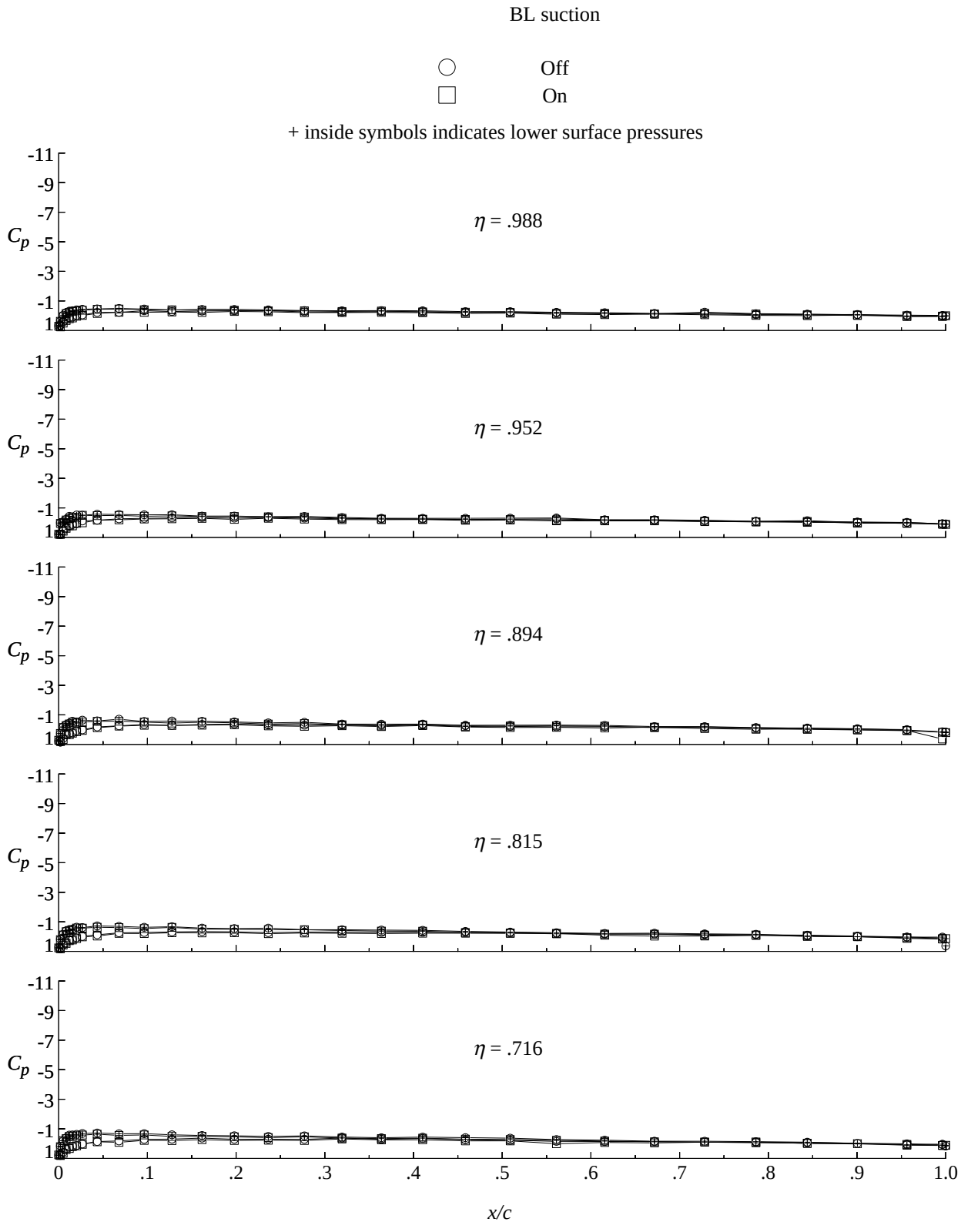


(b) Concluded.

Figure 6. Continued.

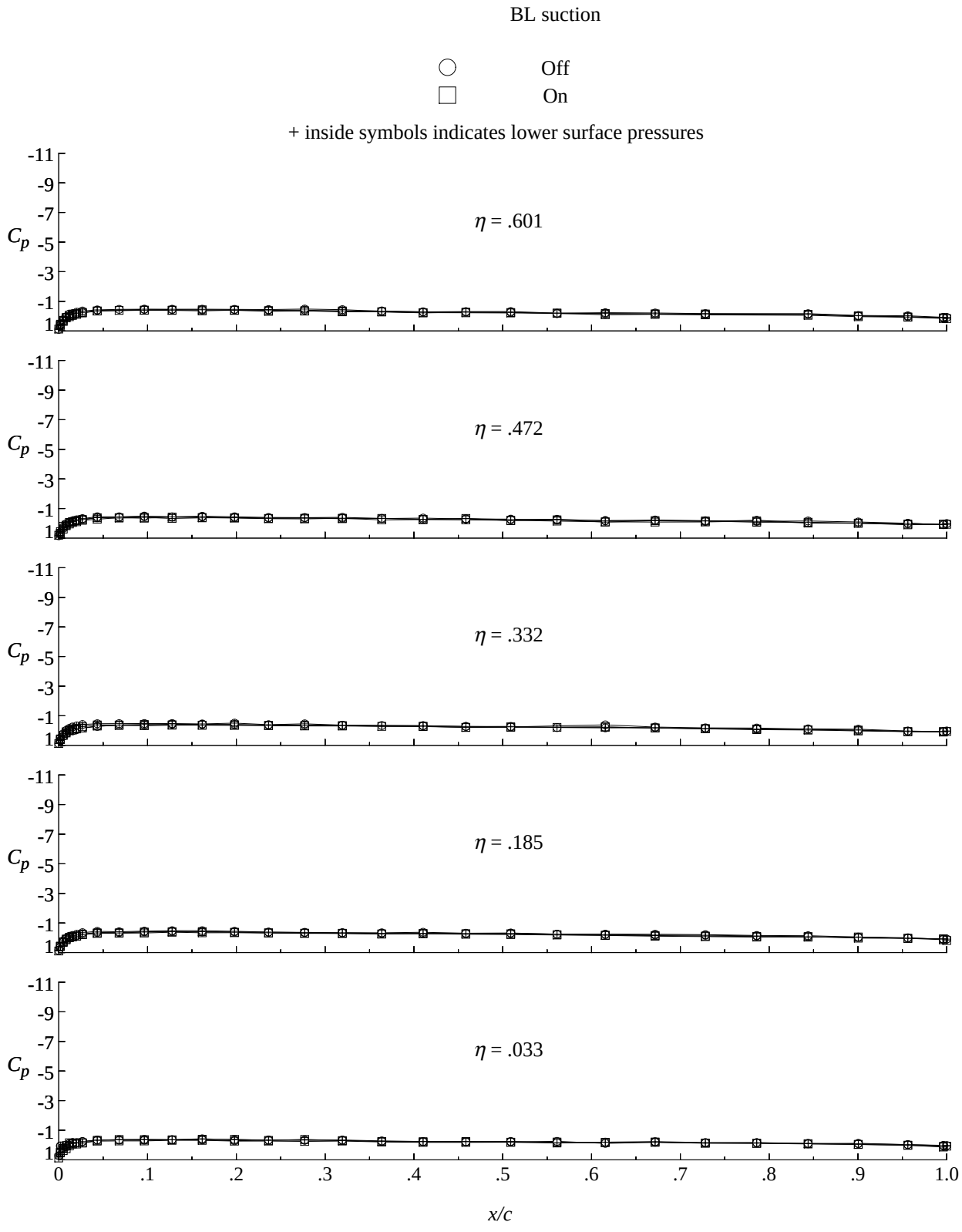


(c) $\alpha = 0°$.

Figure 6. Continued.

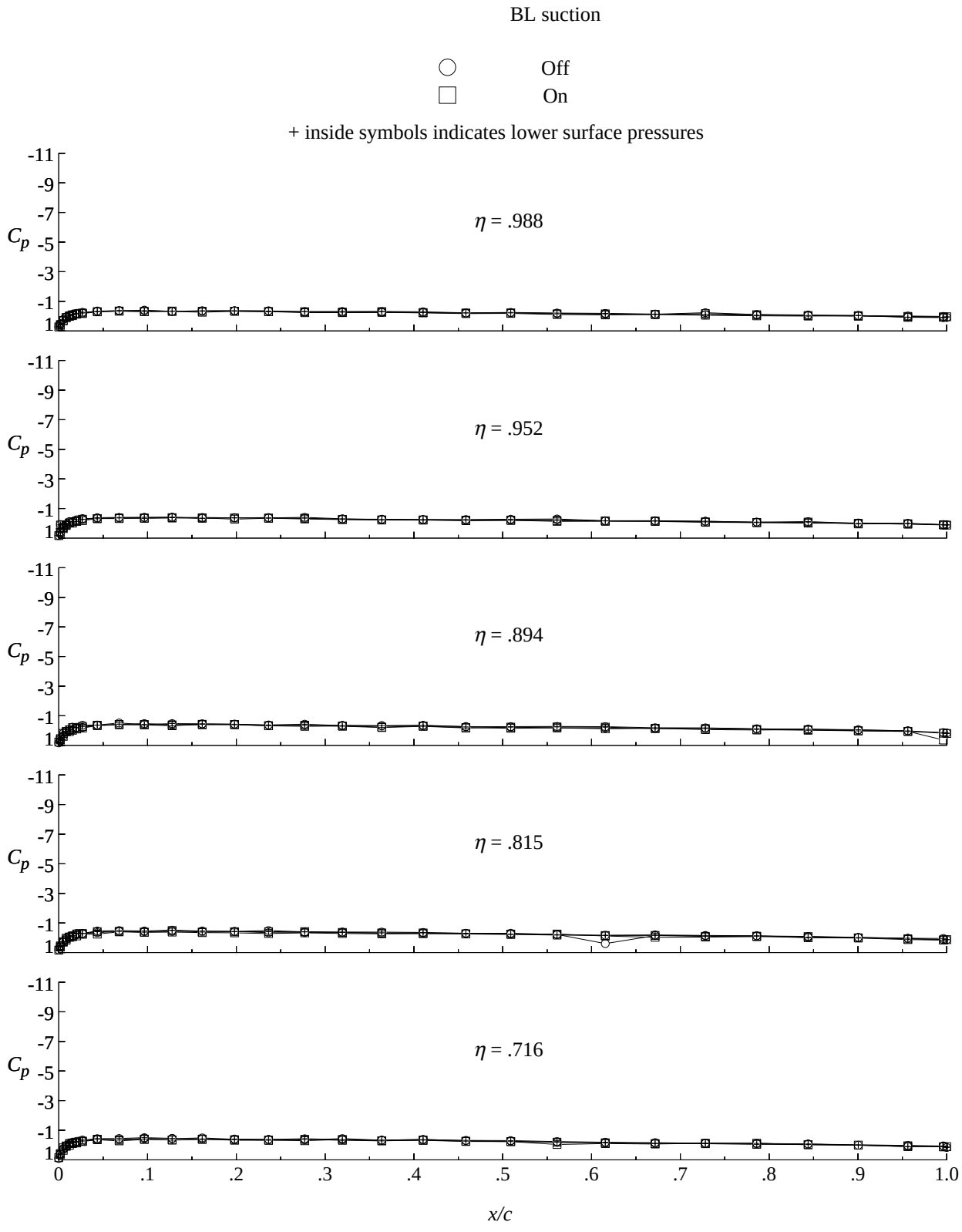


(c) Concluded.

Figure 6. Continued.

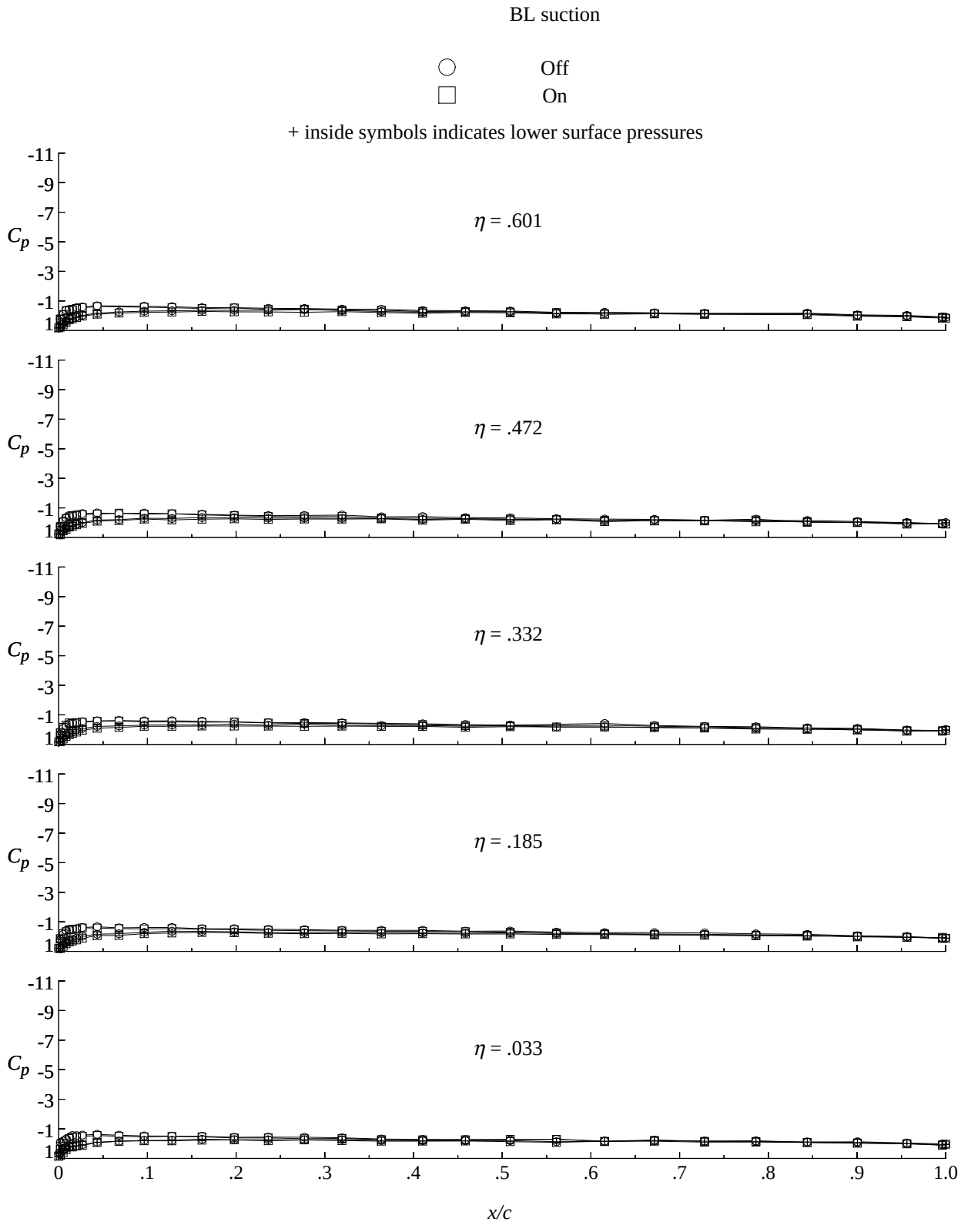


(d) $\alpha = 2°$.

Figure 6. Continued.

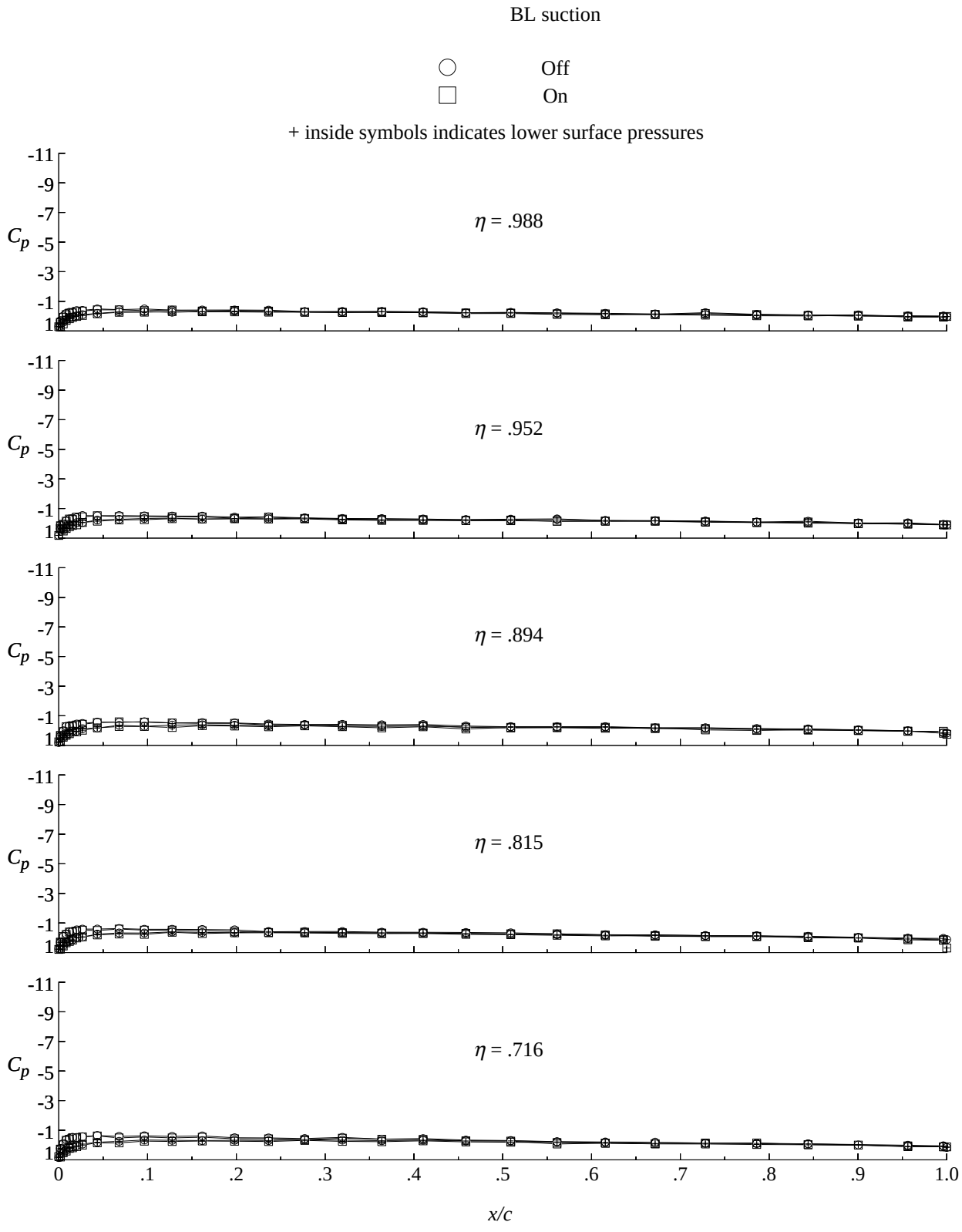


(d) Concluded.

Figure 6. Continued.

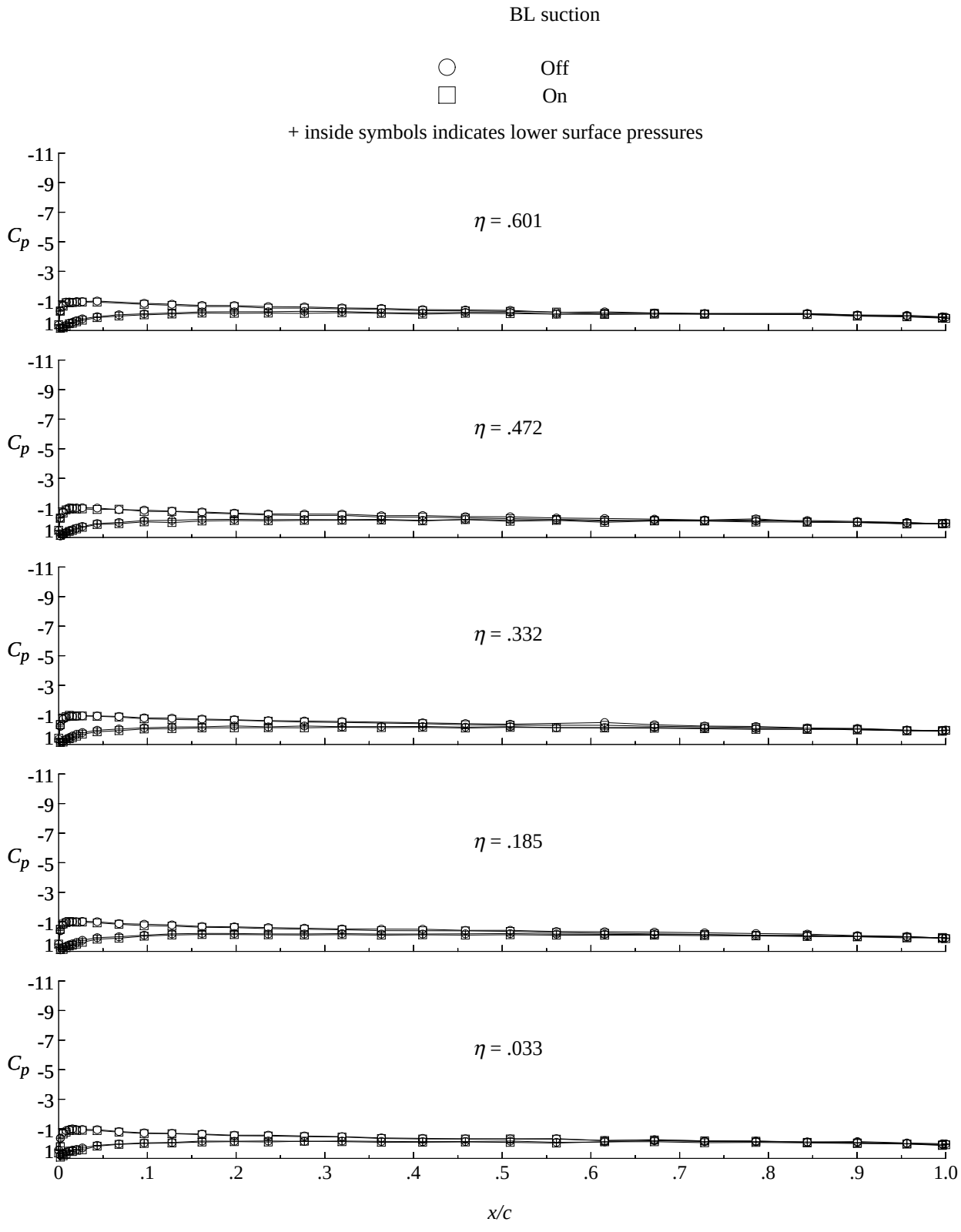


(e) $\alpha = 4°$.

Figure 6. Continued.

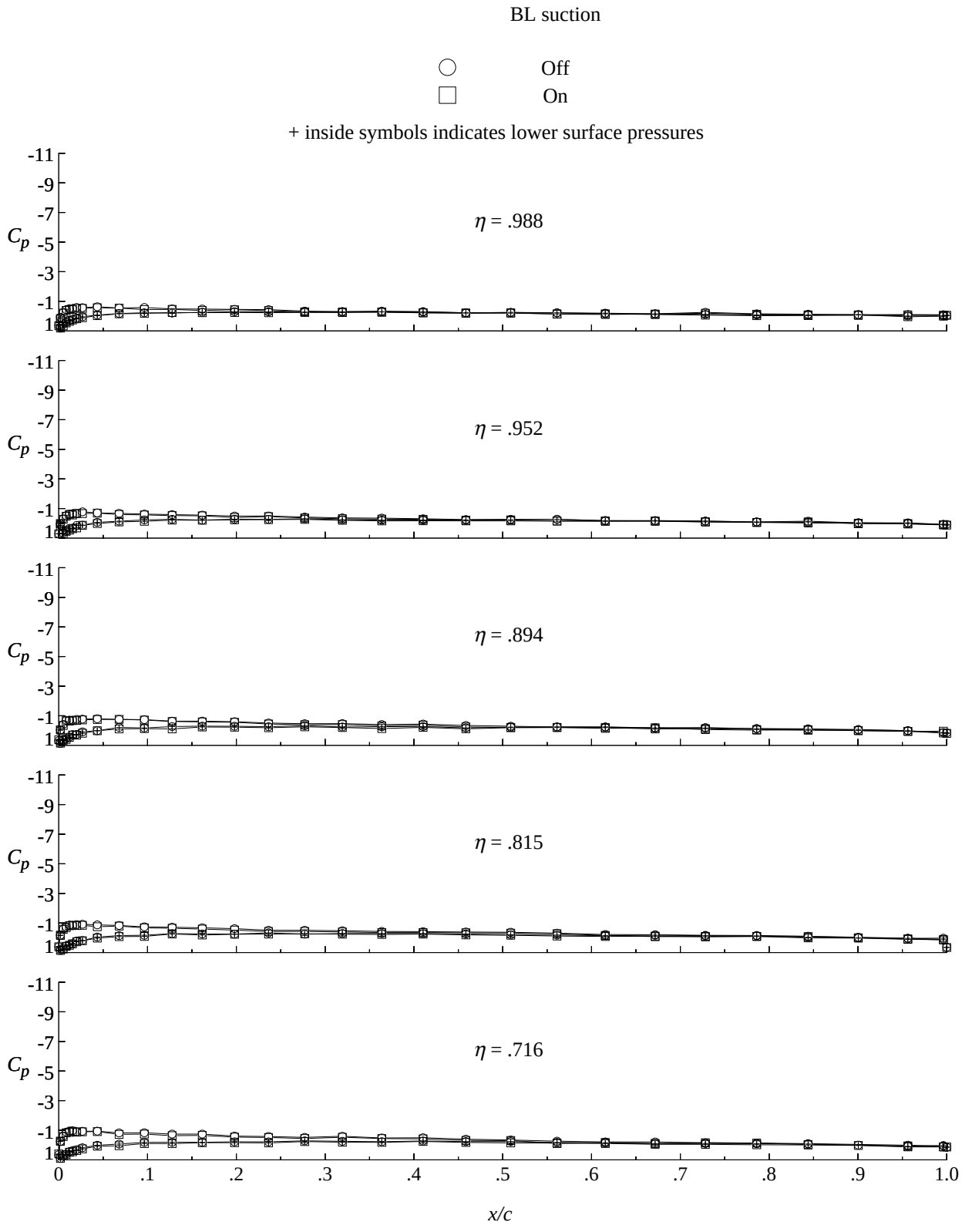


(e) Concluded.

Figure 6. Continued.

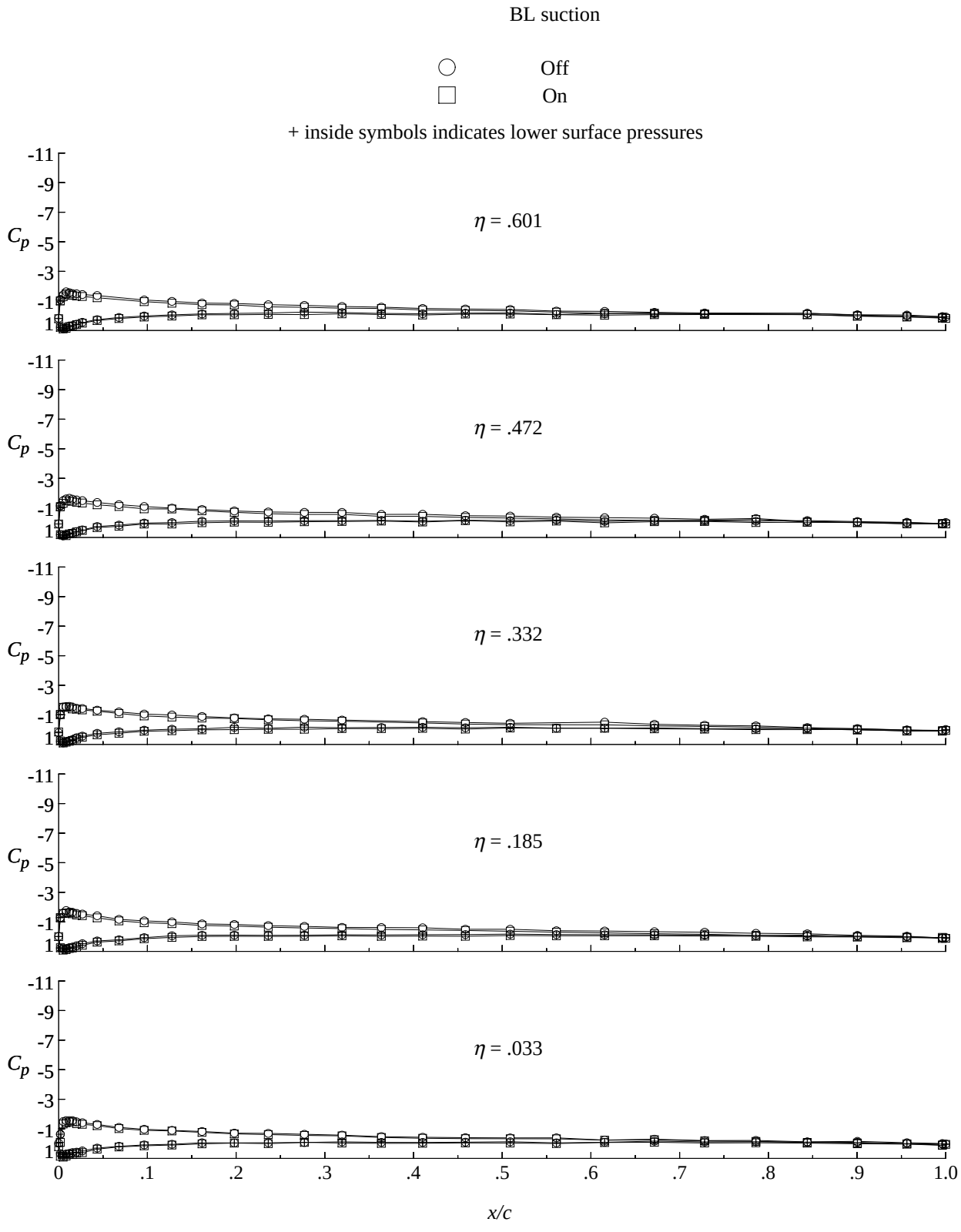


(f) $\alpha = 6°$.

Figure 6. Continued.

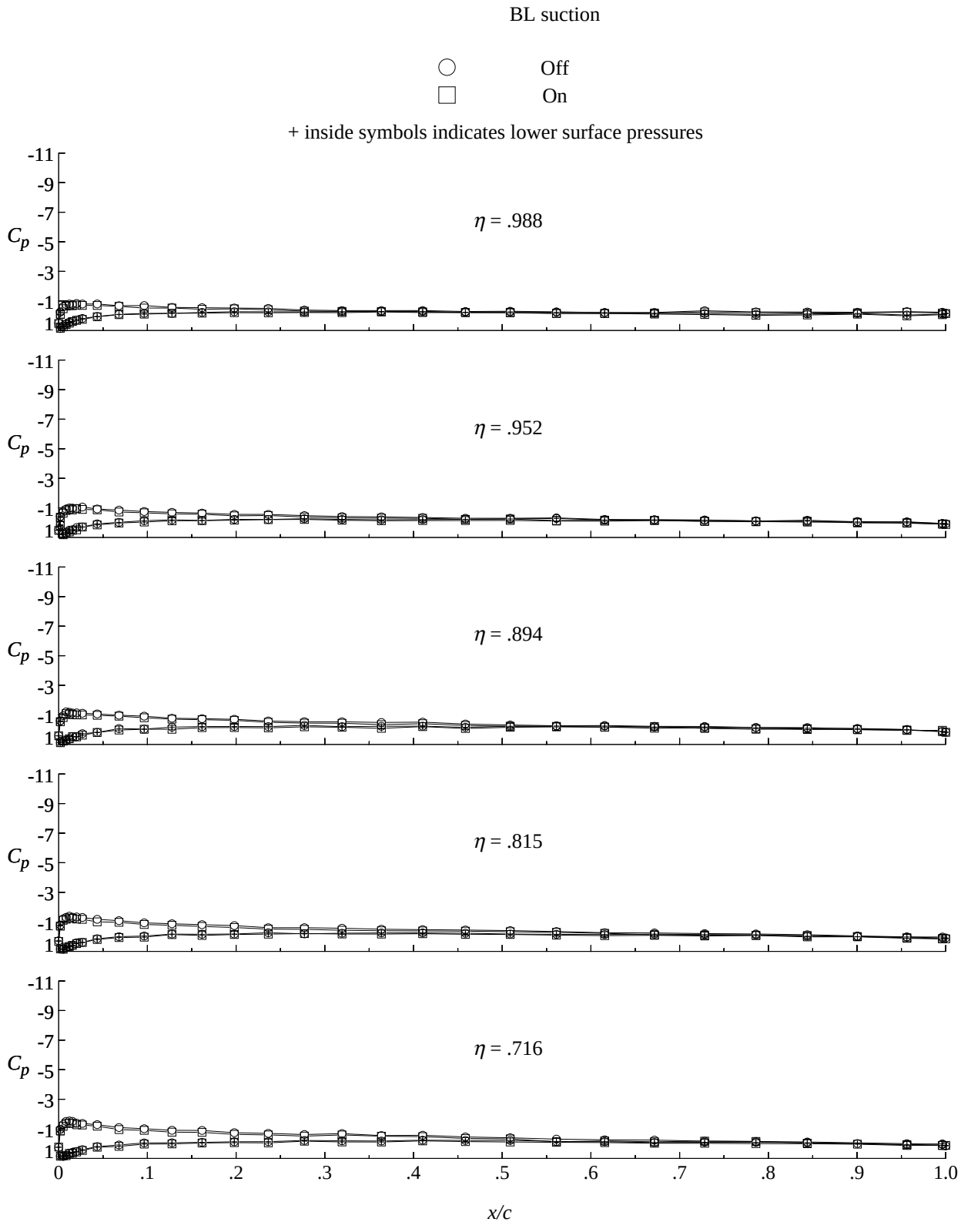


(f) Concluded.

Figure 6. Continued.

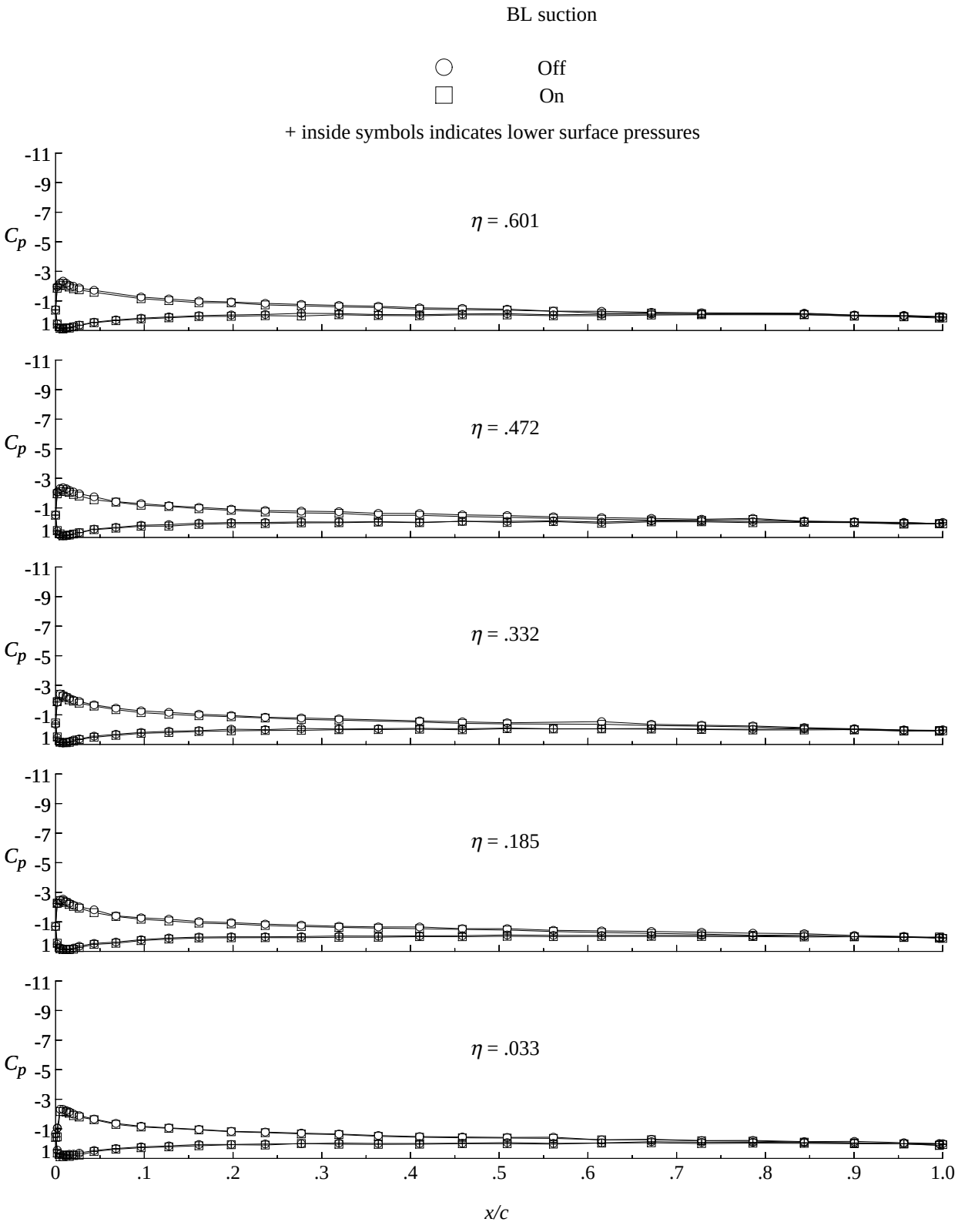


(g) $\alpha = 8°$.

Figure 6. Continued.

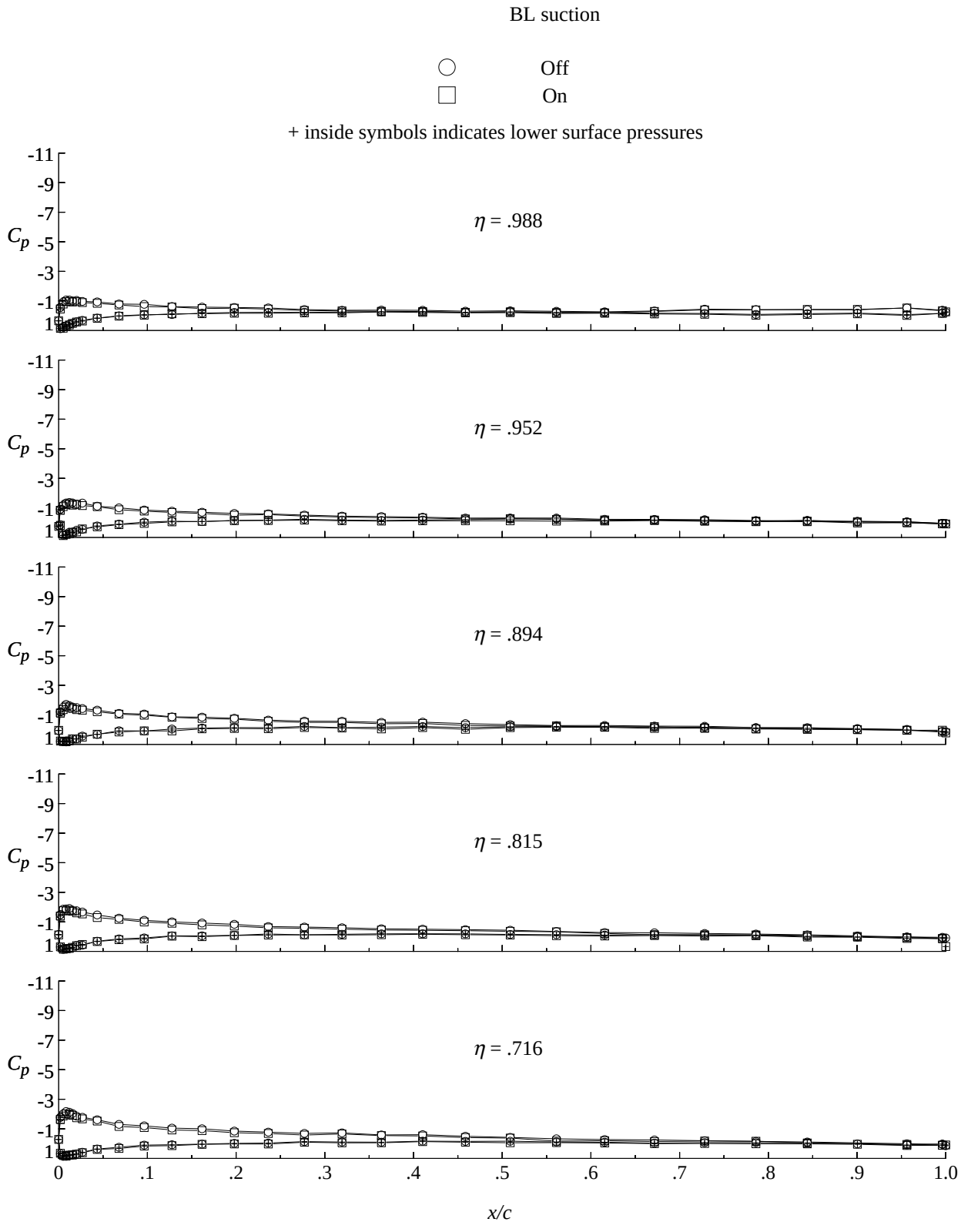


(g) Concluded.

Figure 6. Continued.

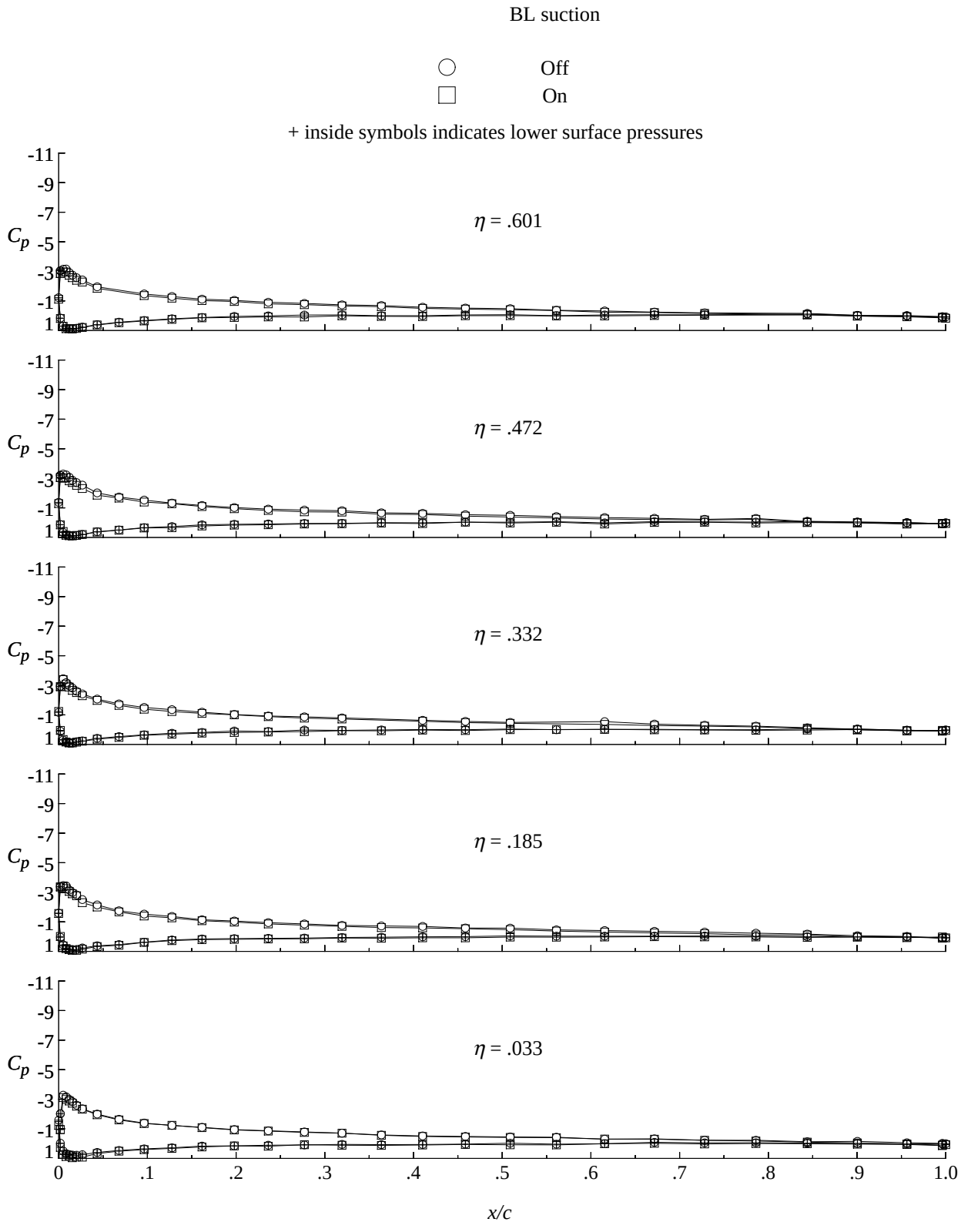


(h) $\alpha = 10°$.

Figure 6. Continued.

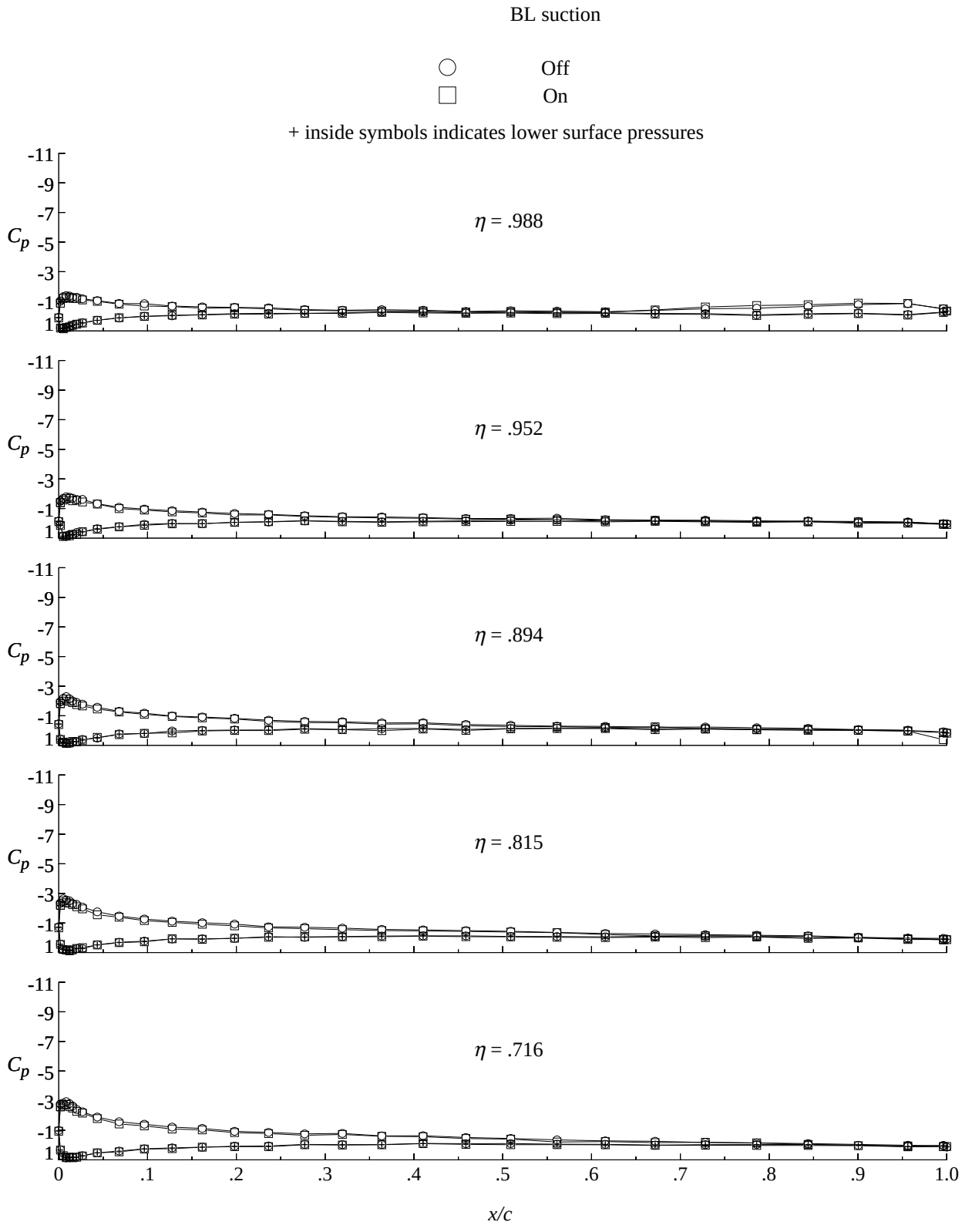


(h) Concluded.

Figure 6. Continued.

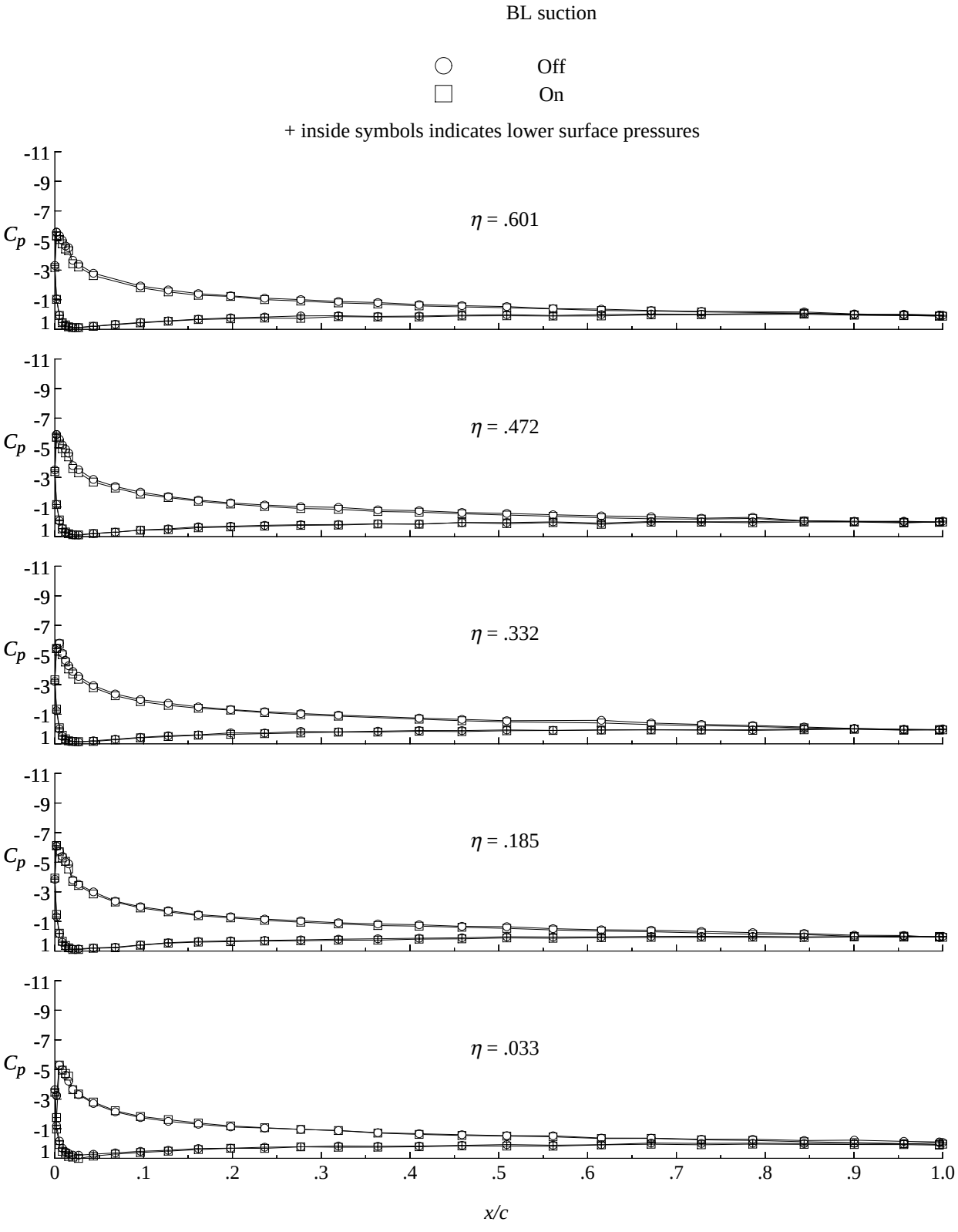


(i) $\alpha = 14°$.

Figure 6. Continued.

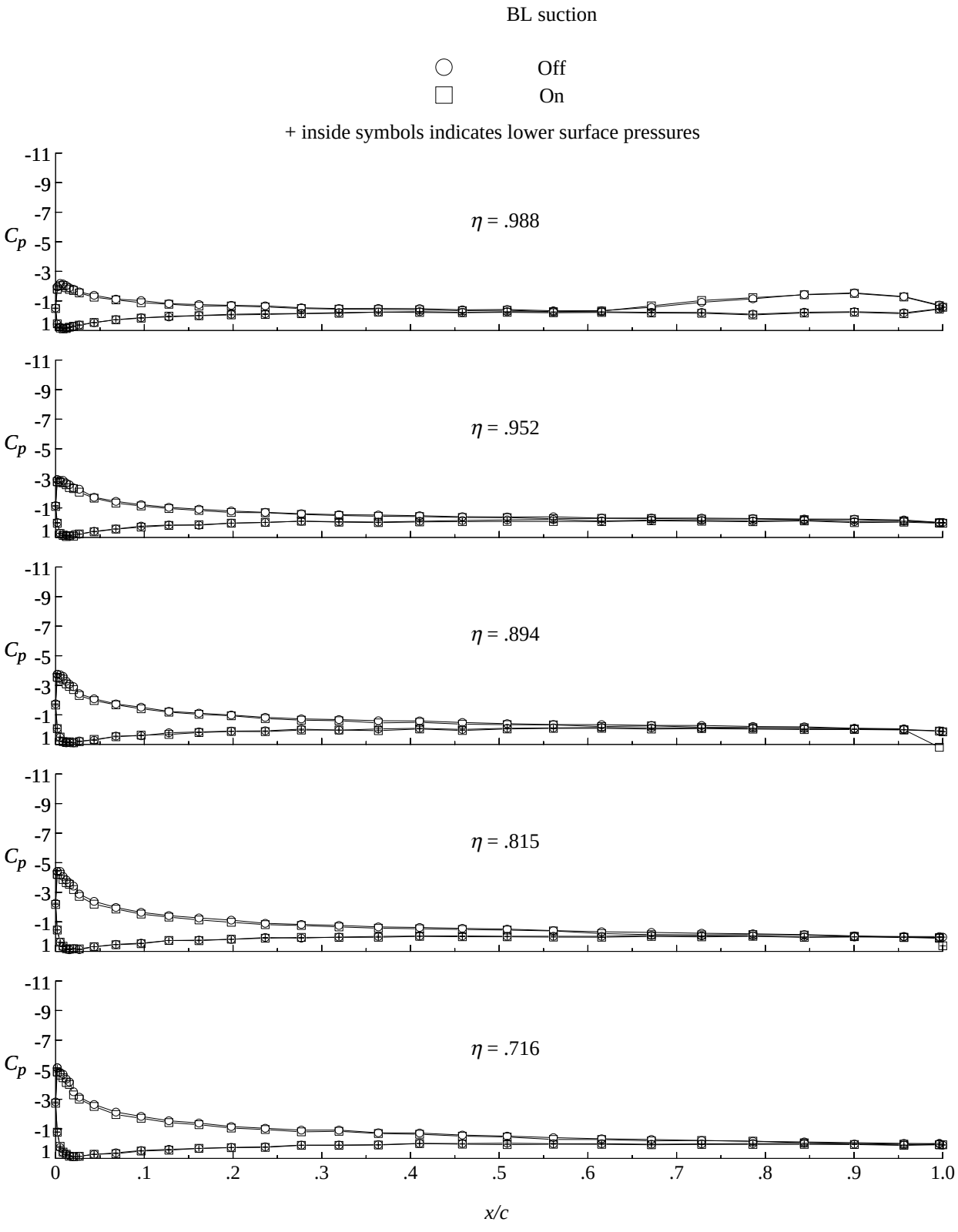


(i) Concluded.

Figure 6. Continued.

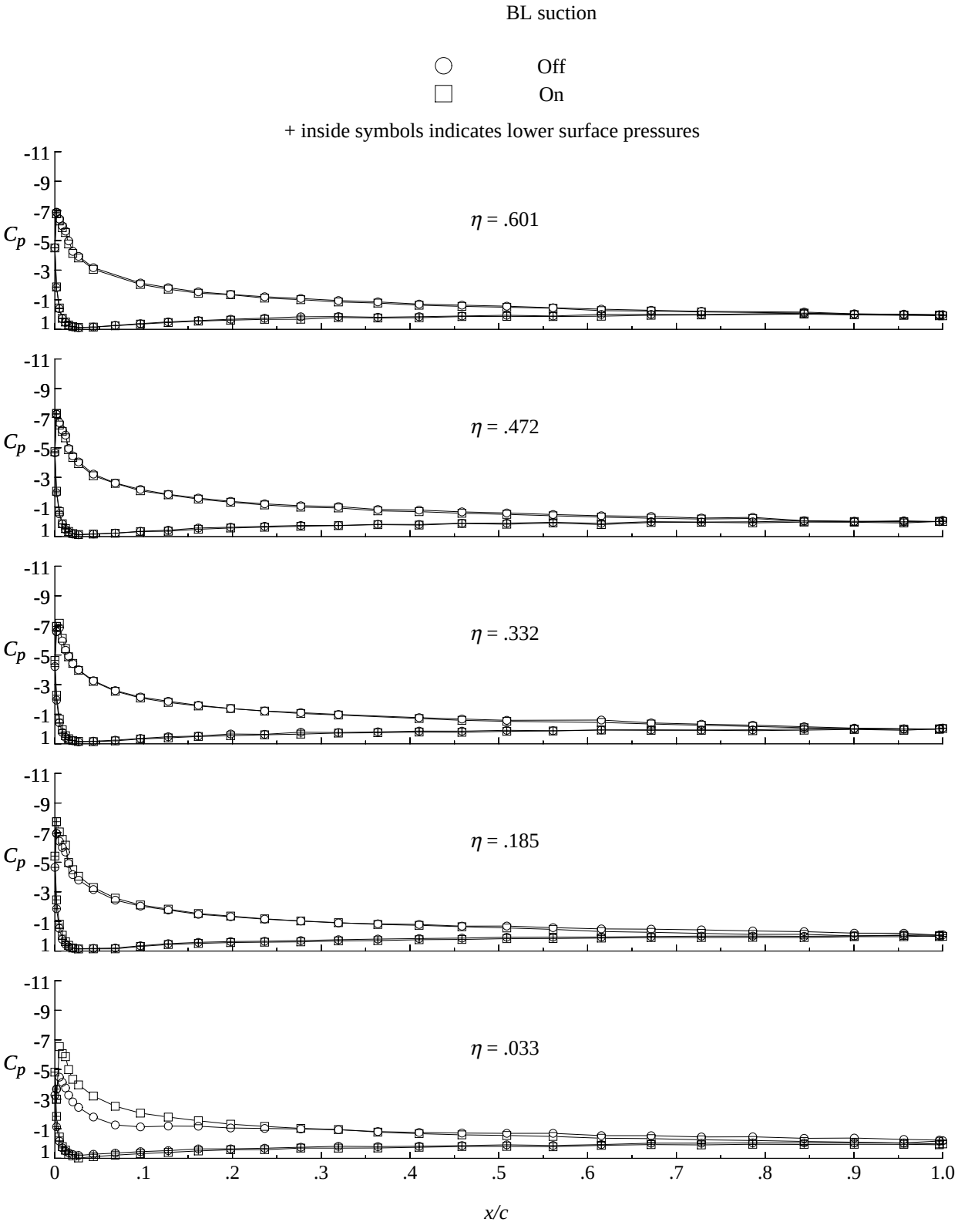


(j) $\alpha = 16°$.

Figure 6. Continued.

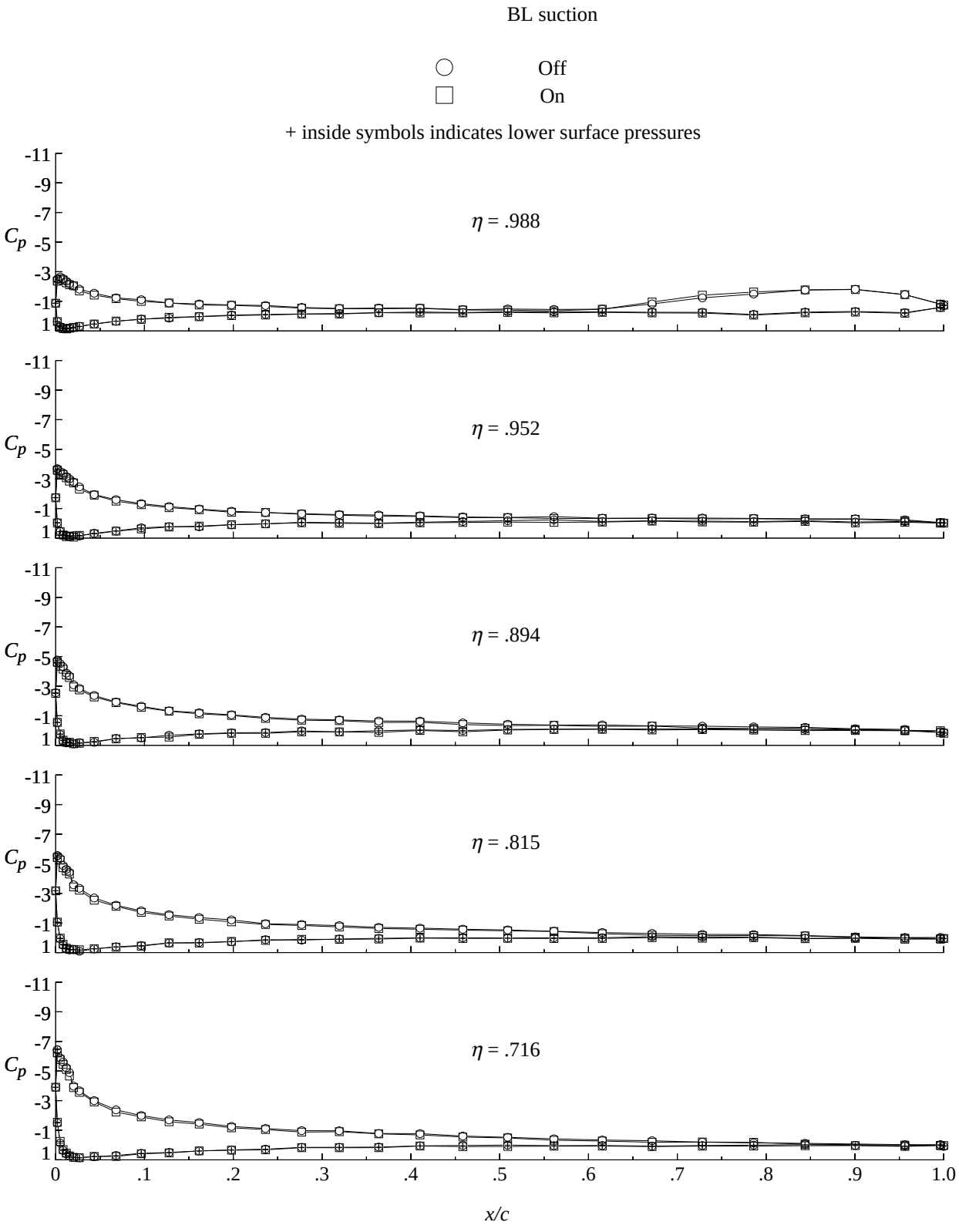


(j) Concluded.

Figure 6. Continued.

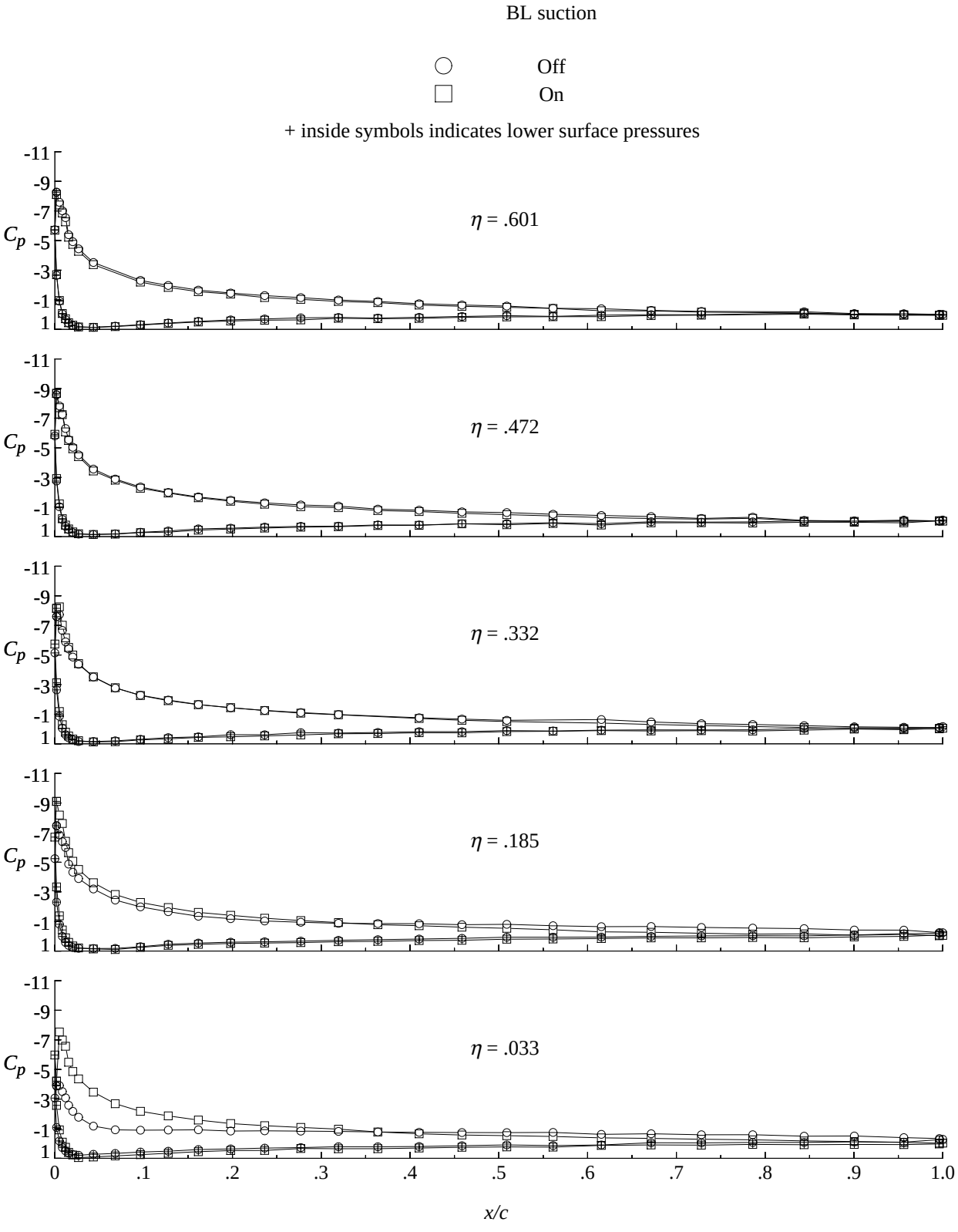


(k) $\alpha = 18°$.

Figure 6. Continued.

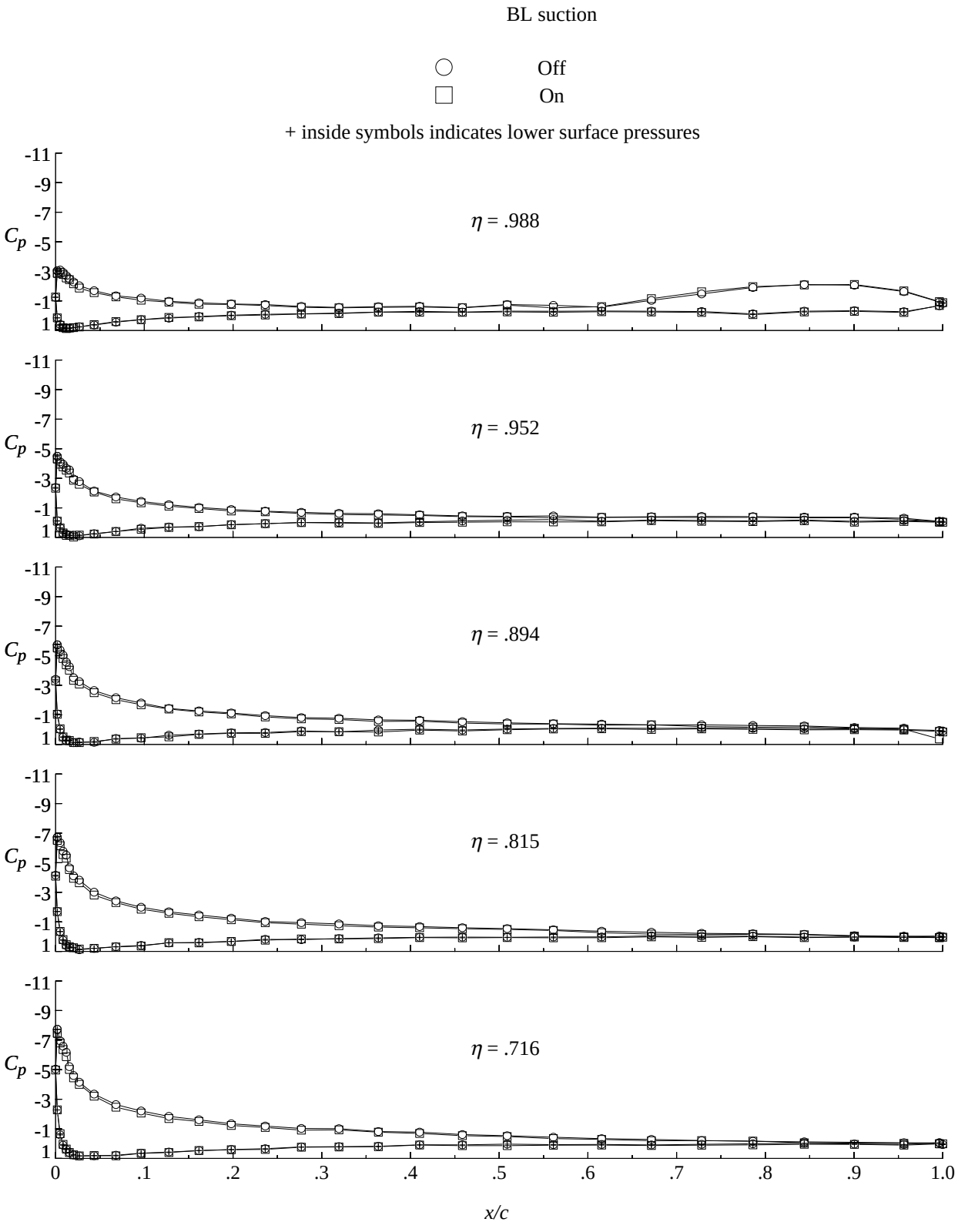


(k) Concluded.

Figure 6. Concluded.

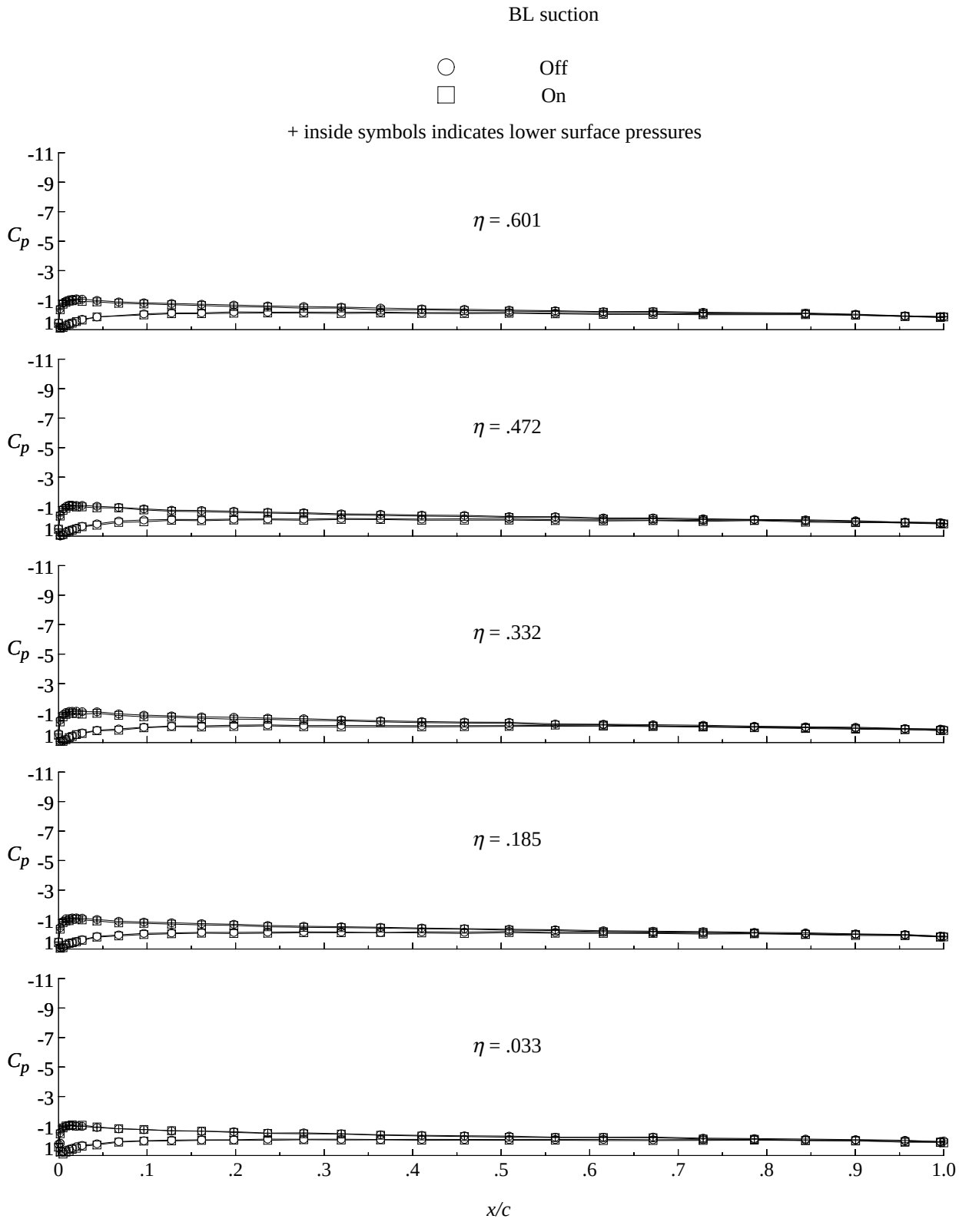


(a) $\alpha$ = - 4°.

Figure 7. Effect of tunnel floor boundary layer suction on cruise wing pressure distribution. $q_\infty$ = 30 psf.

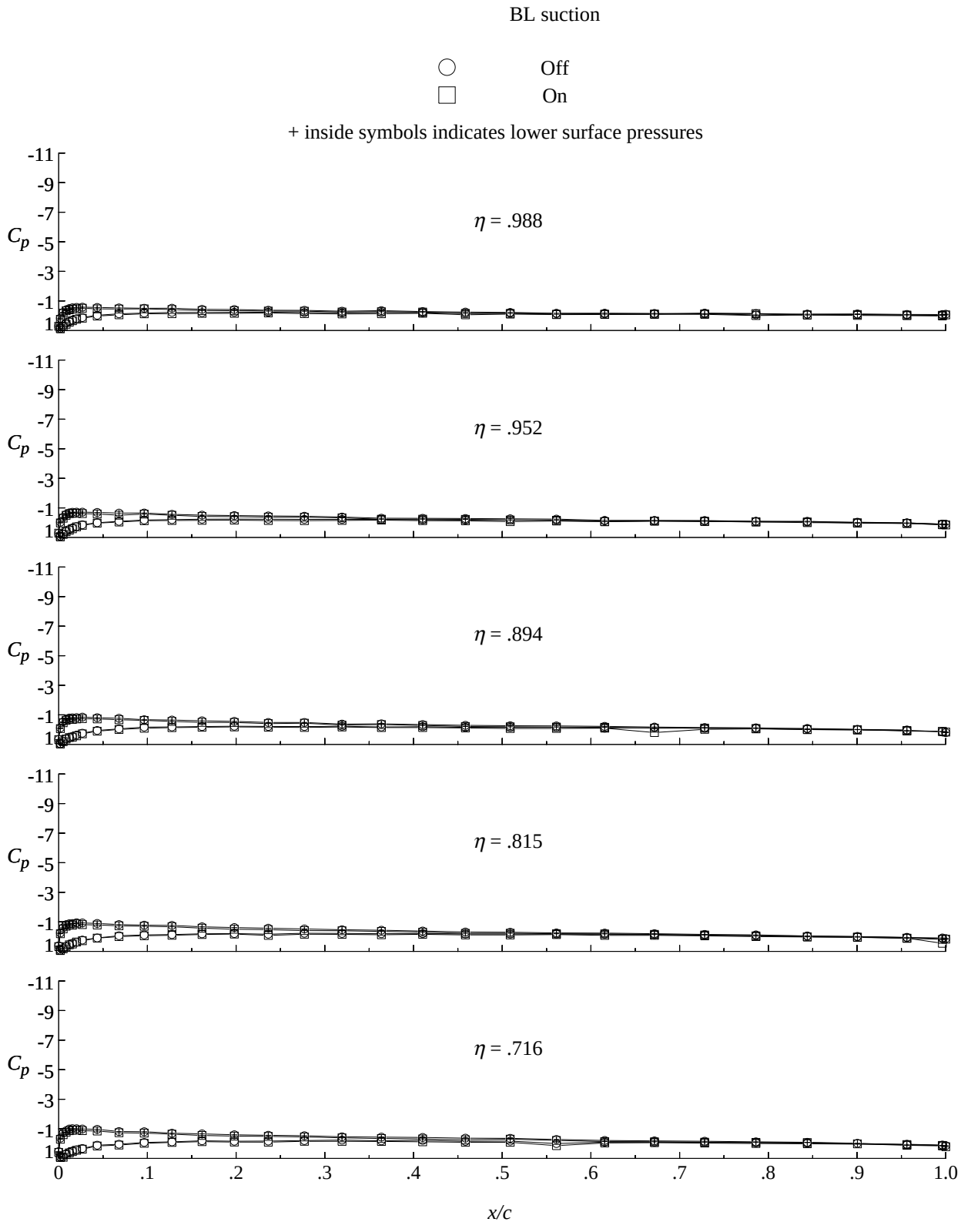


(a) Concluded.

Figure 7. Continued.

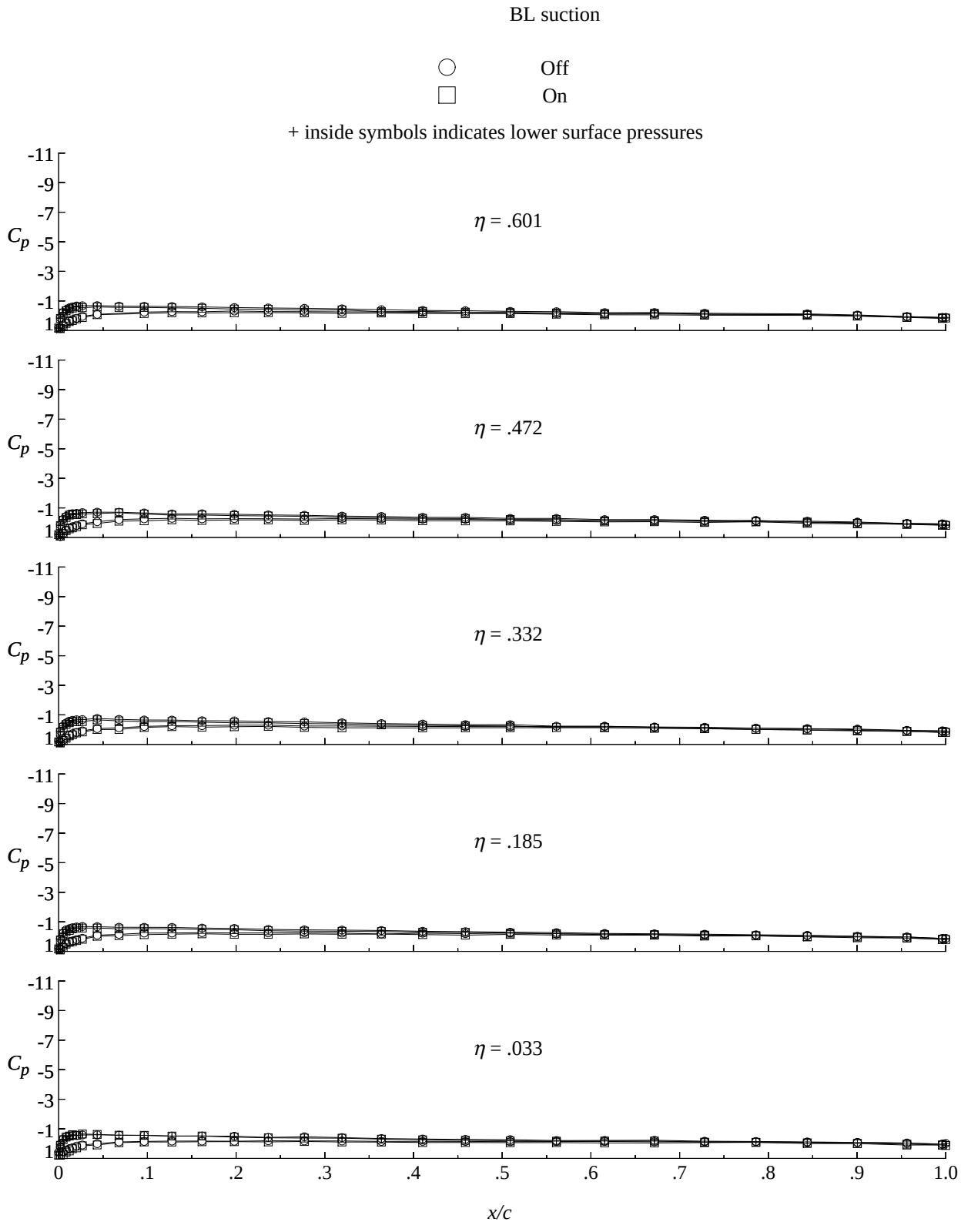


(b) $\alpha$ = - 2°.

Figure 7. Continued.

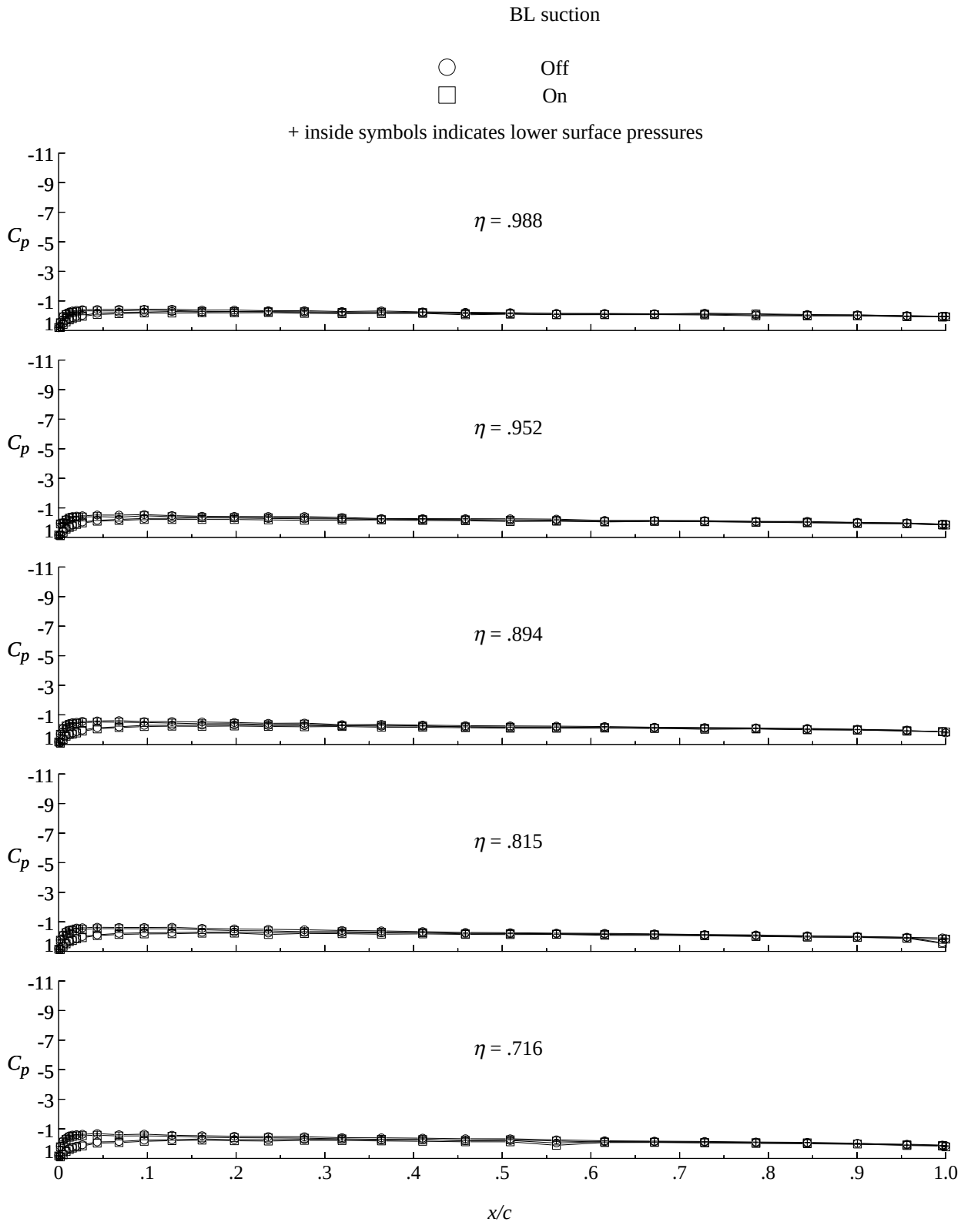


(b) Concluded.

Figure 7. Continued.

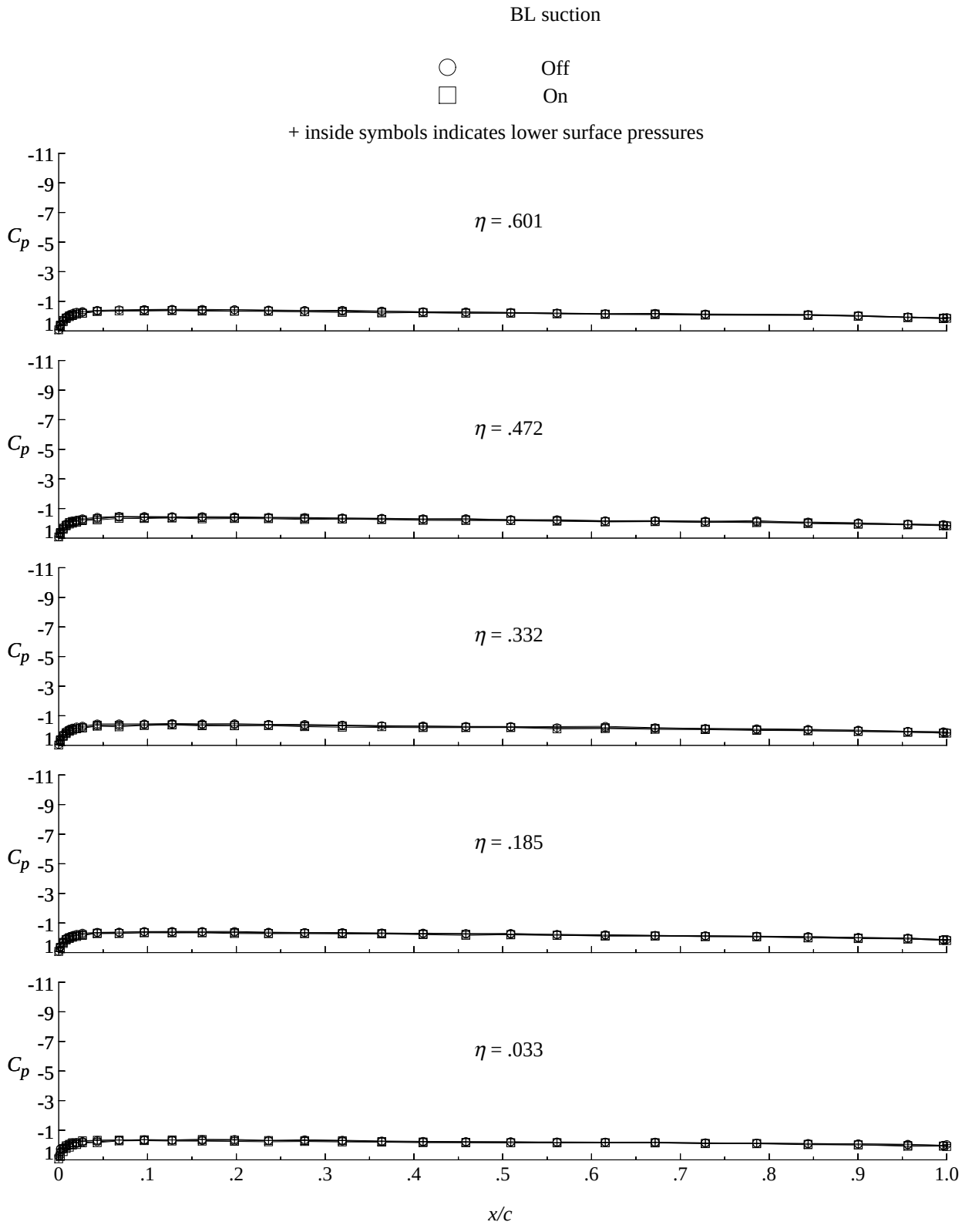


(c) $\alpha = 0°$.

Figure 7. Continued.

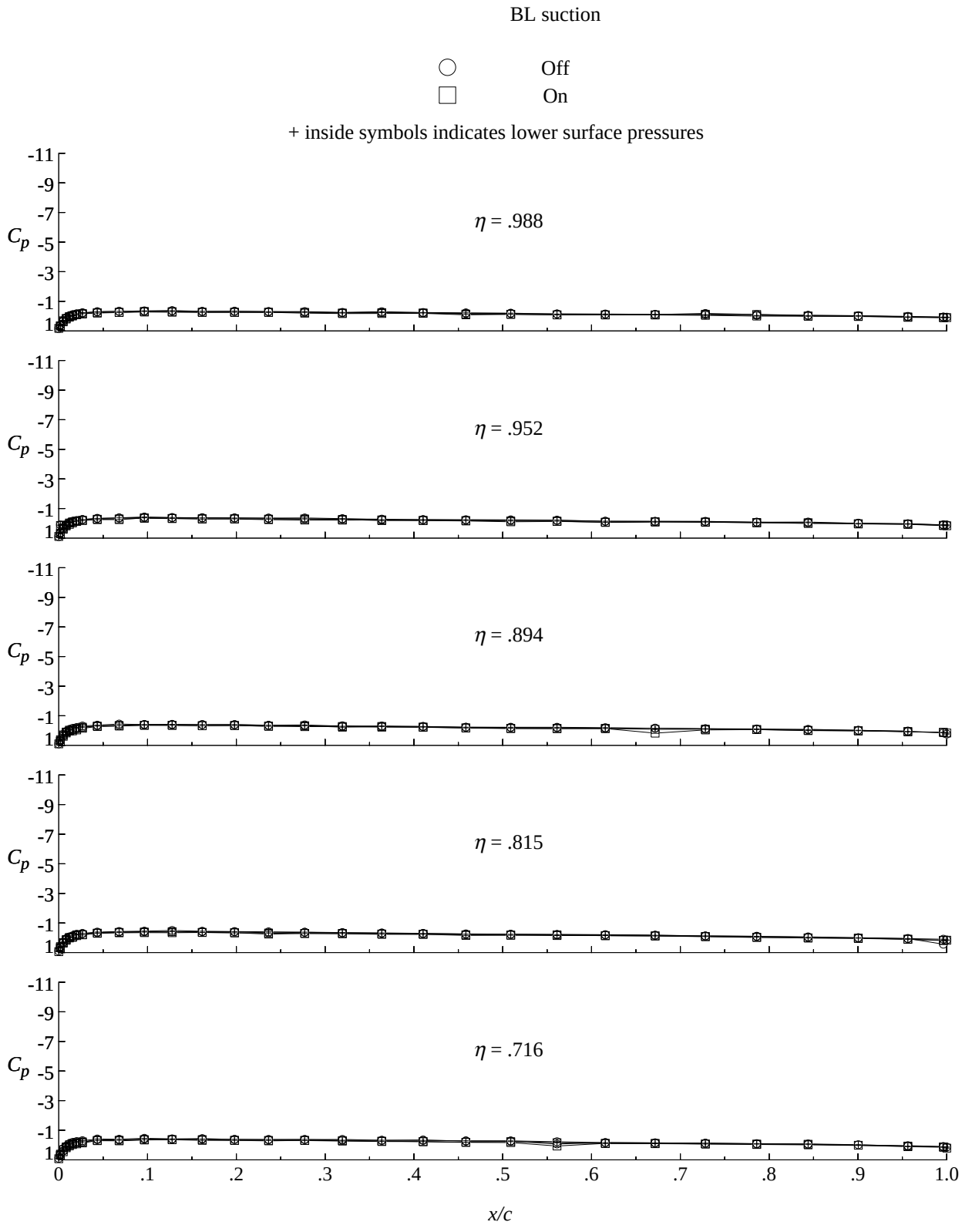


(c) Concluded.

Figure 7. Continued.

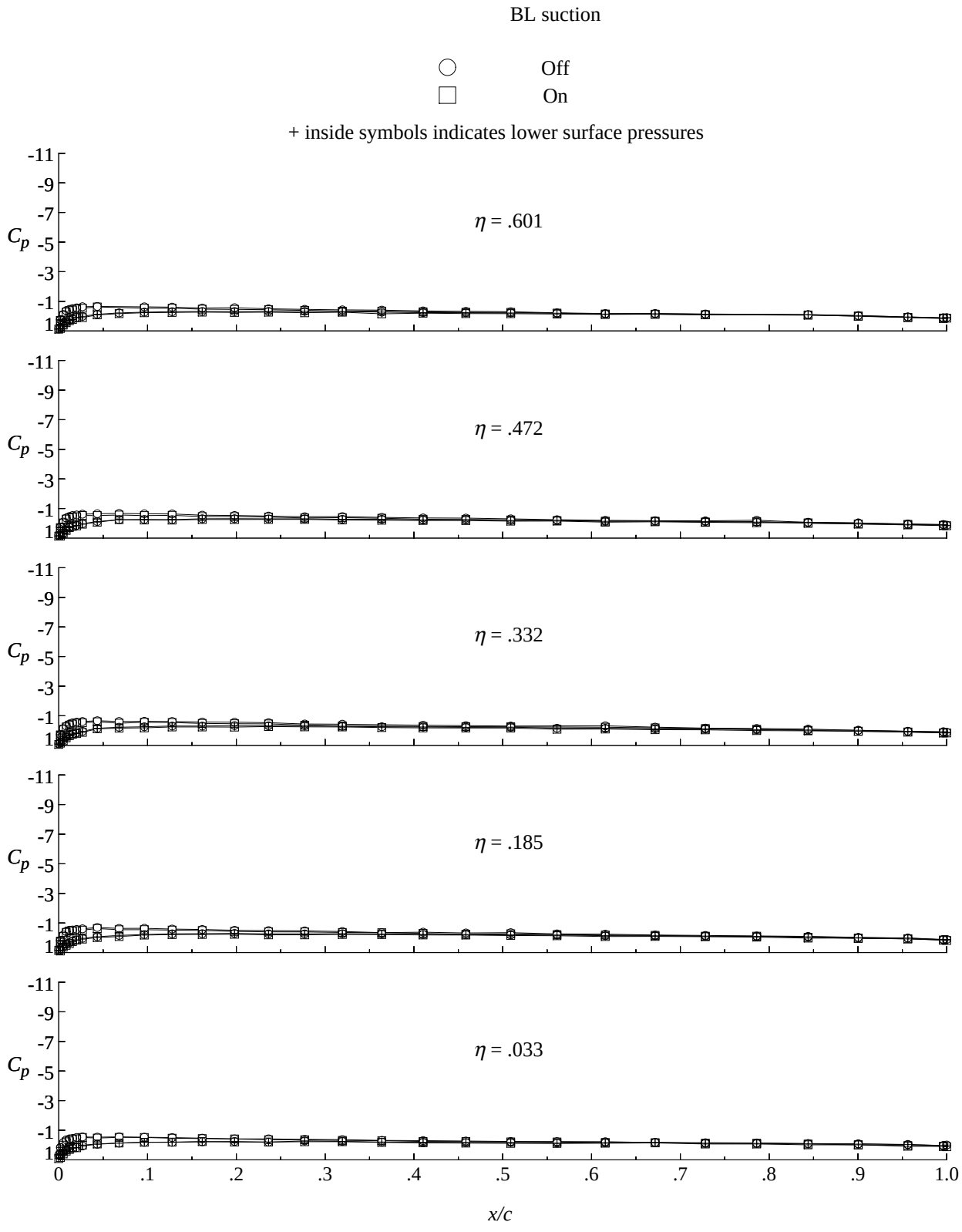


(d) $\alpha = 2°$.

Figure 7. Continued.

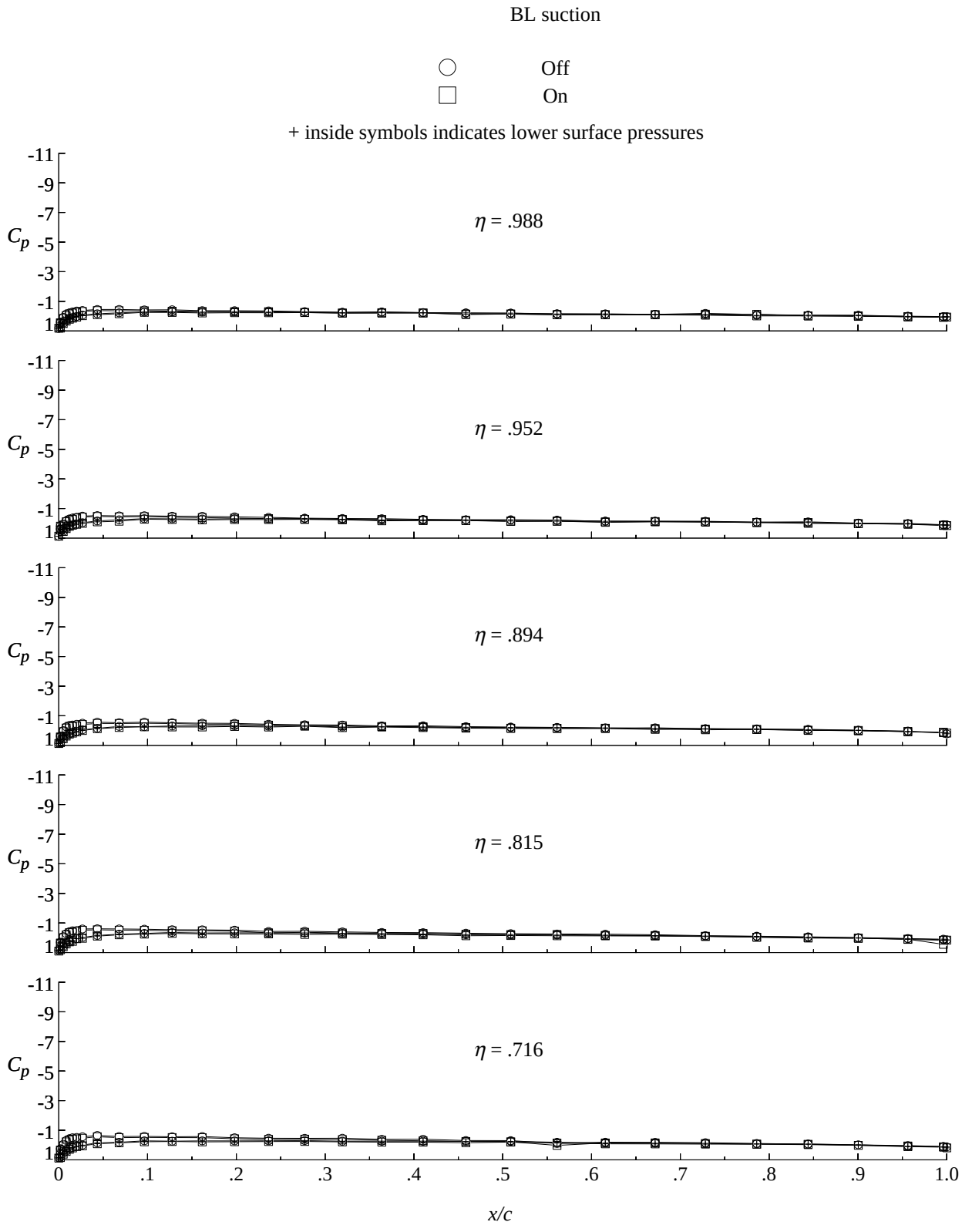


(d) Concluded.

Figure 7. Continued.

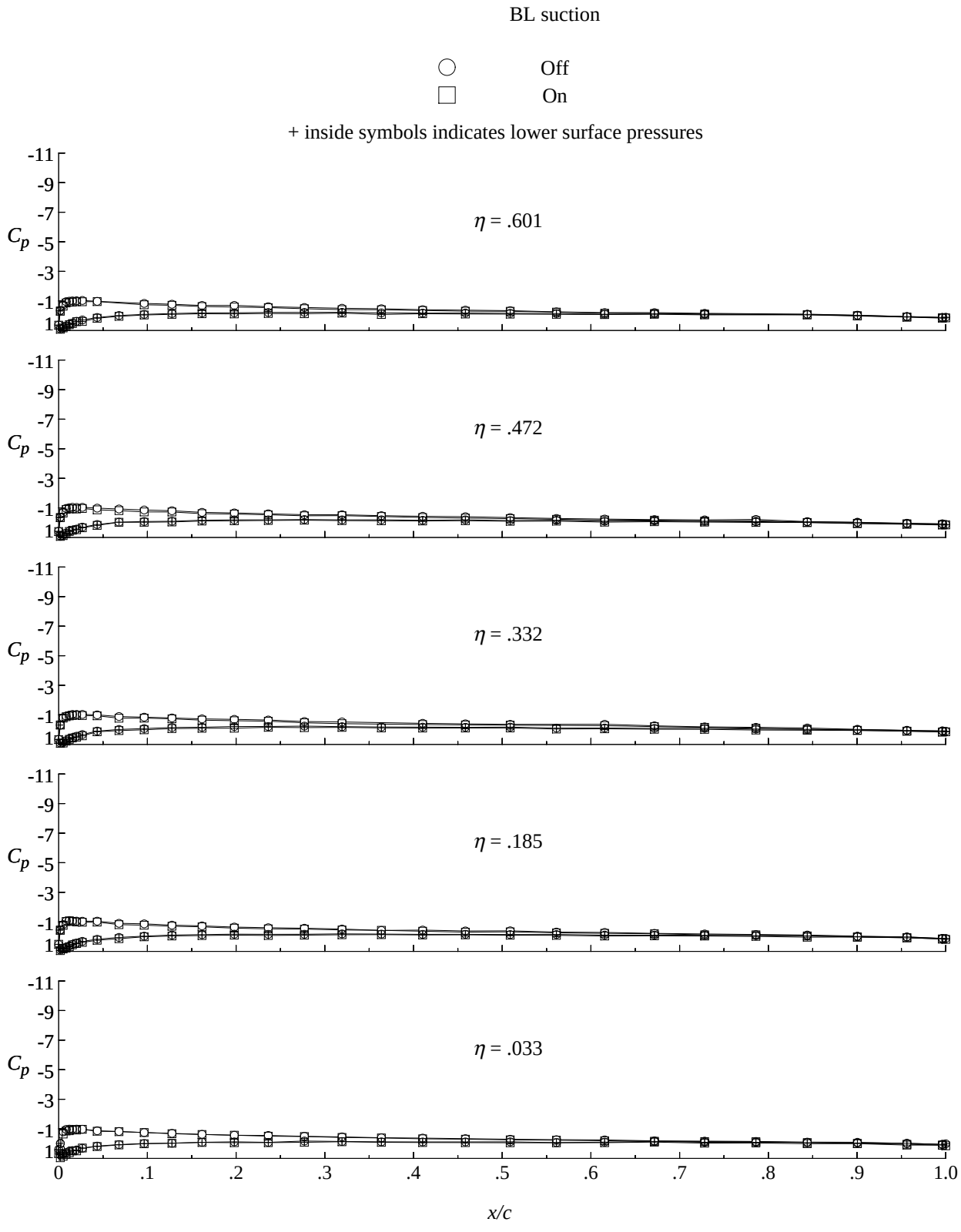


(e) $\alpha = 4°$.

Figure 7. Continued.

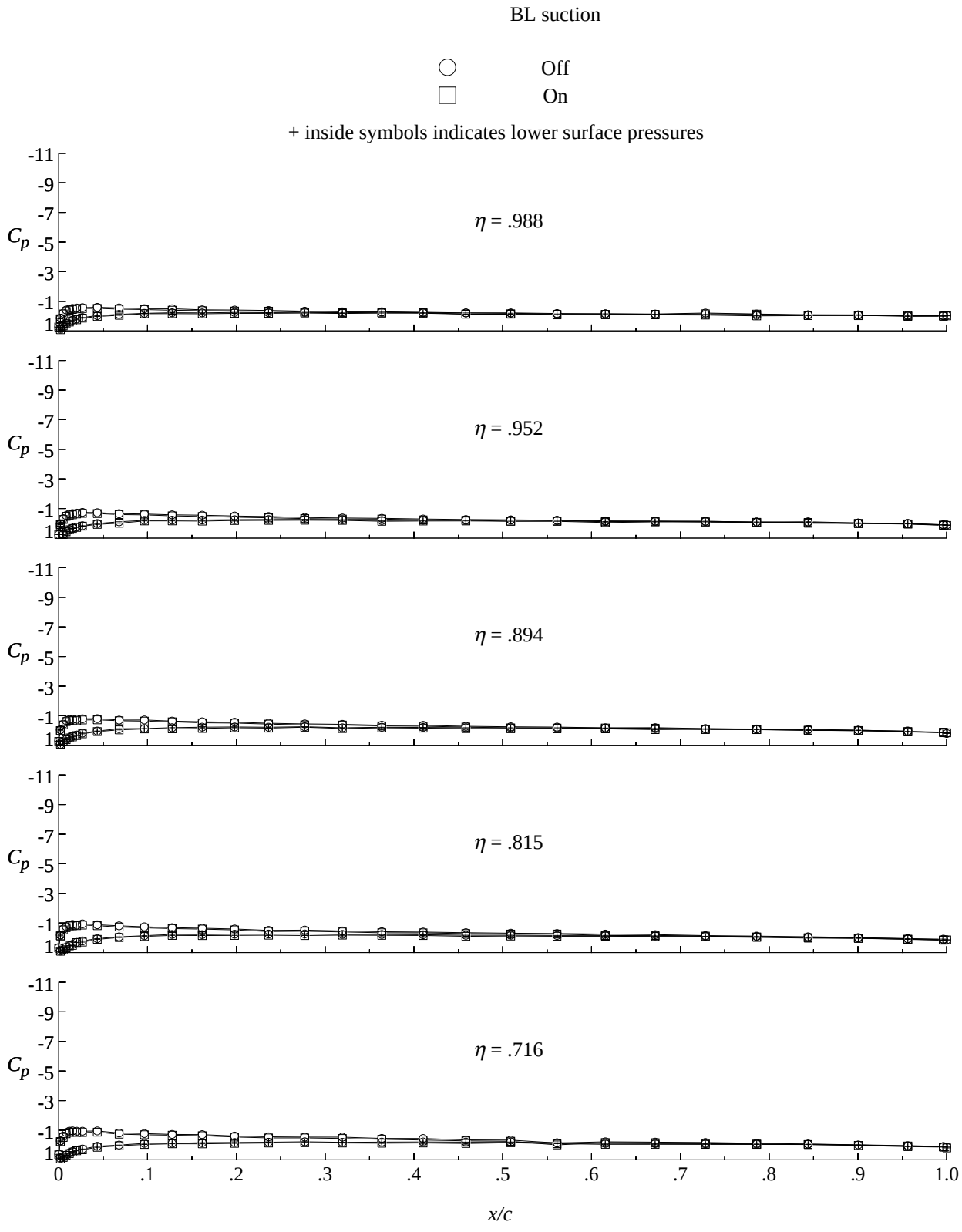


(e) Concluded.

Figure 7. Continued.

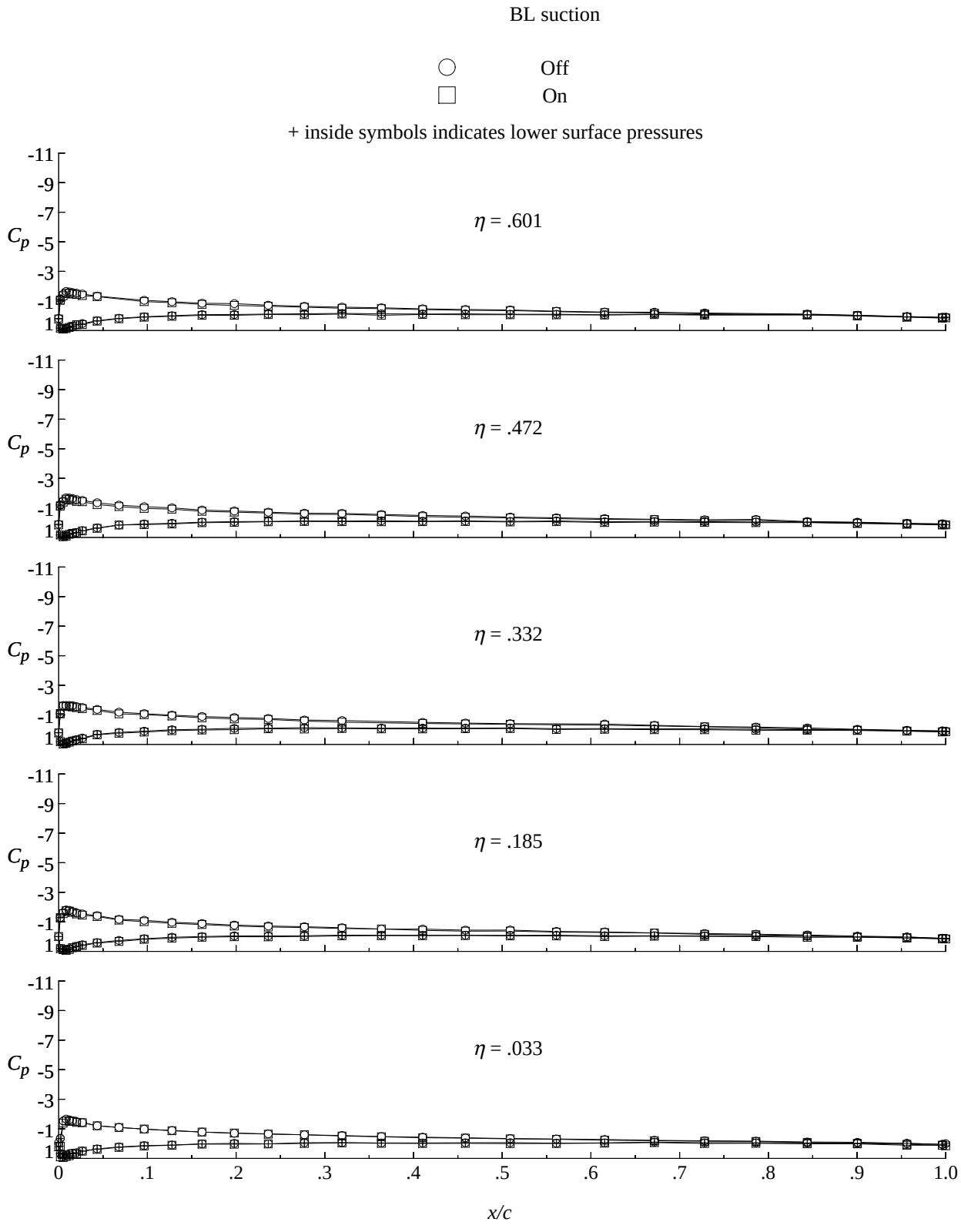


(f) $\alpha = 6°$.

Figure 7. Continued.

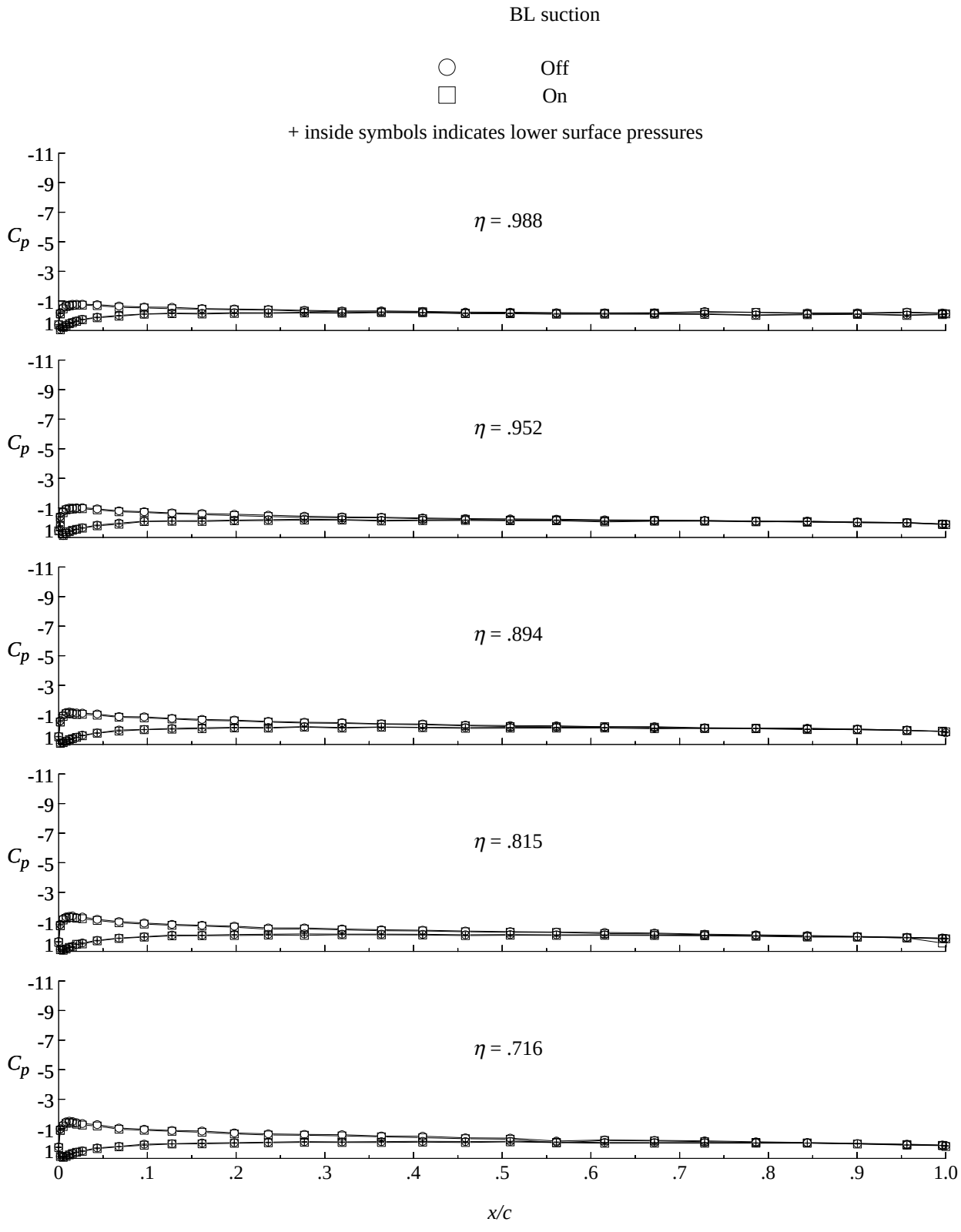


(f) Concluded.

Figure 7. Continued.

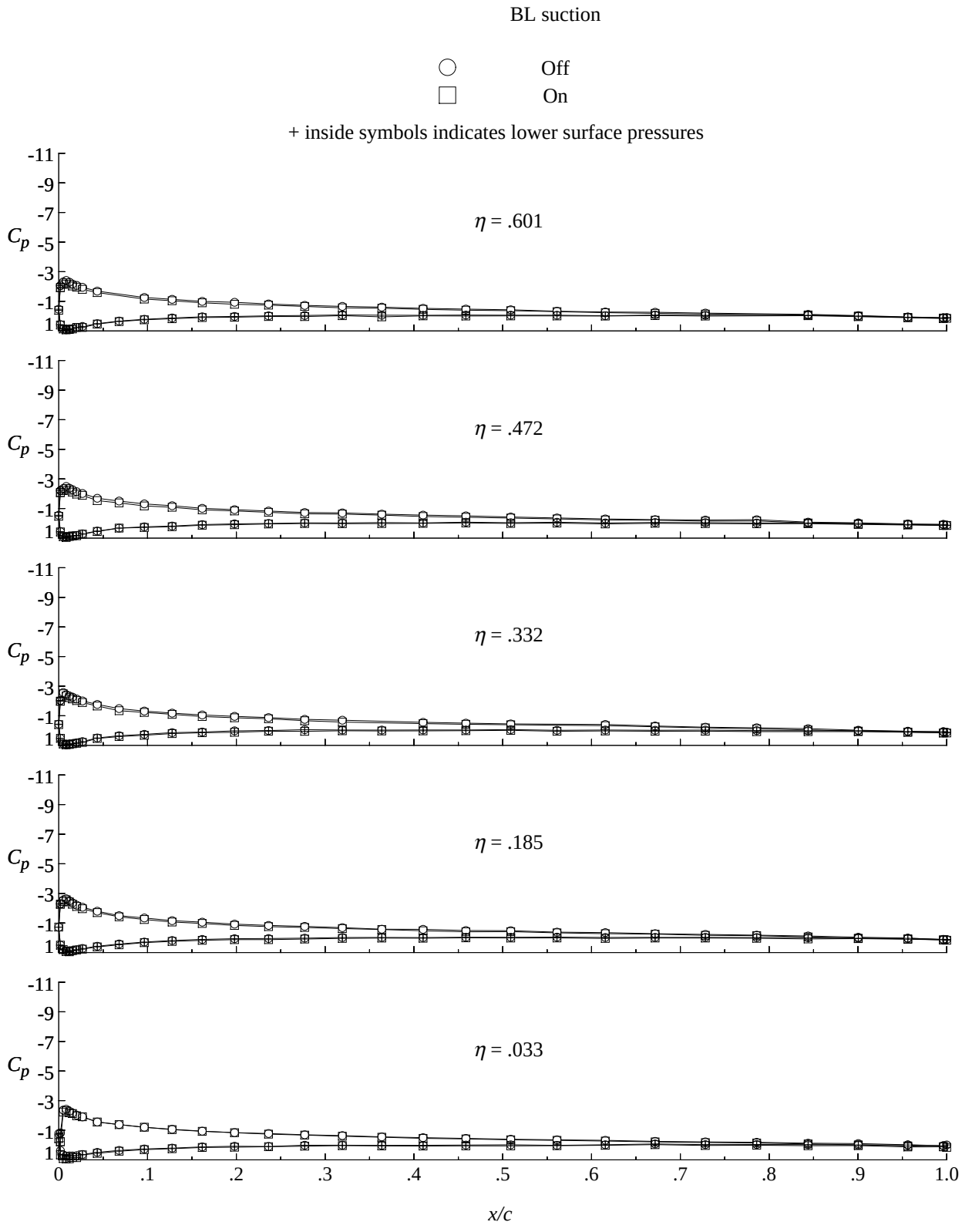


(g) $\alpha = 8°$.

Figure 7. Continued.

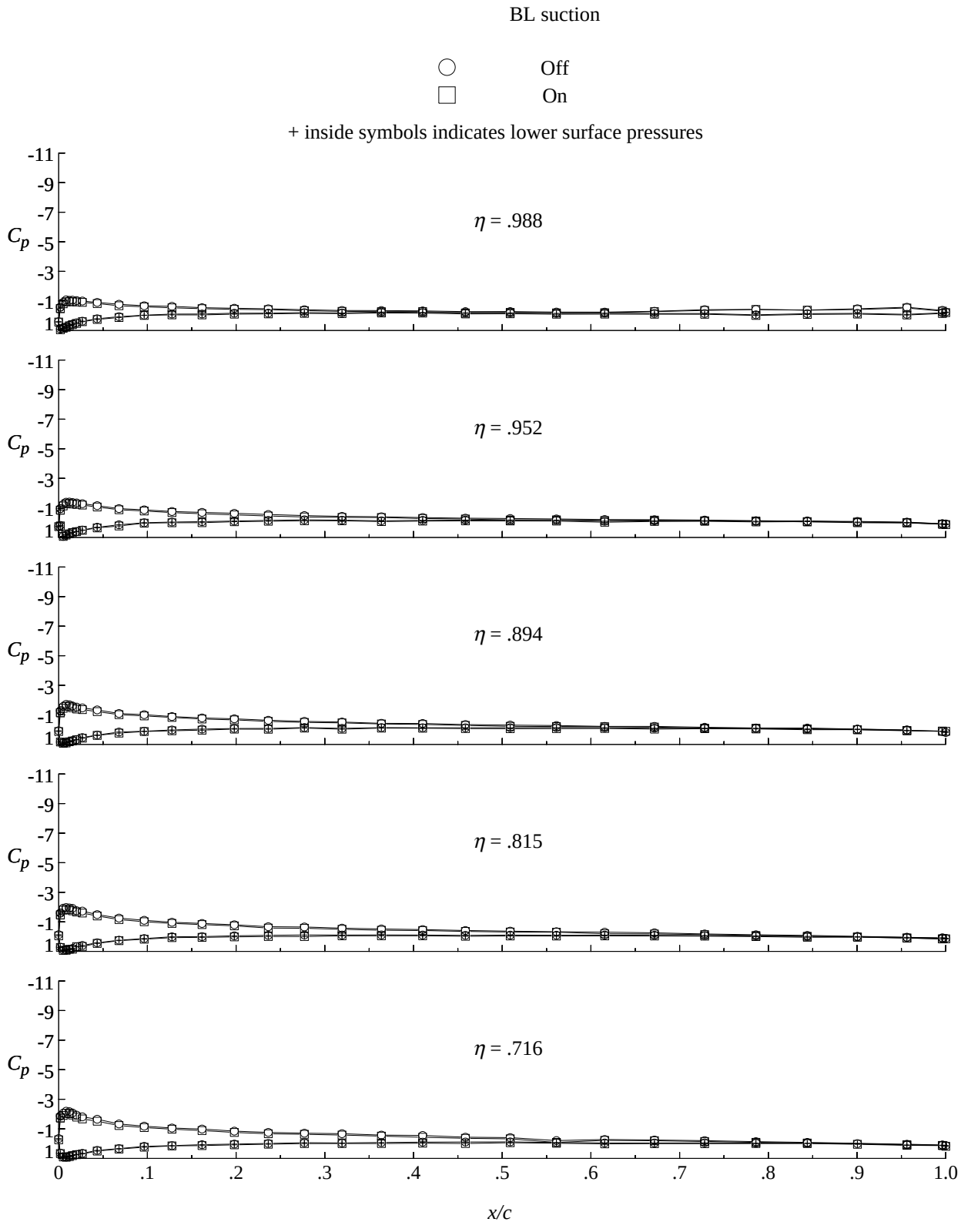


(g) Concluded.

Figure 7. Continued.

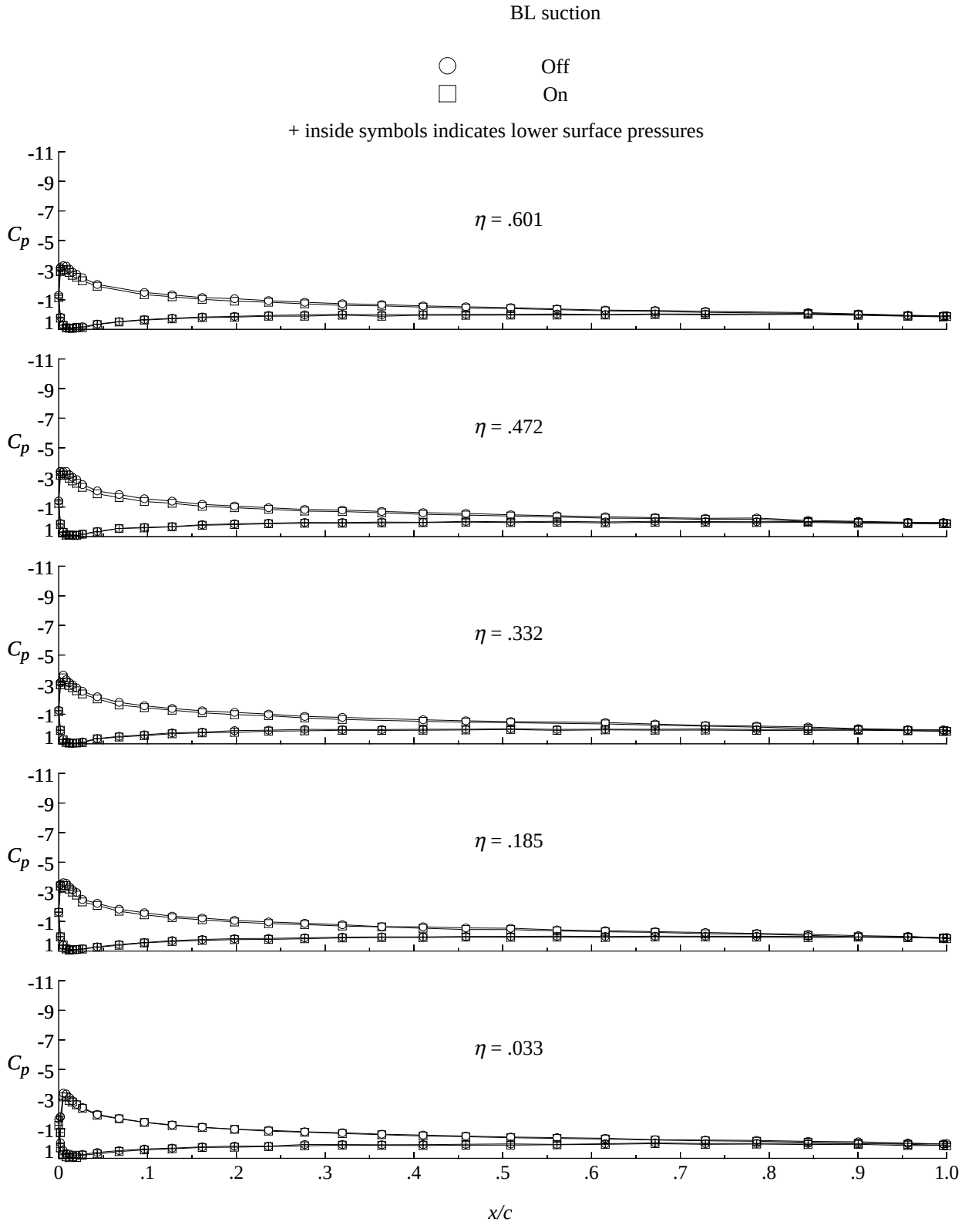


(h) $\alpha = 10°$.

Figure 7. Continued.

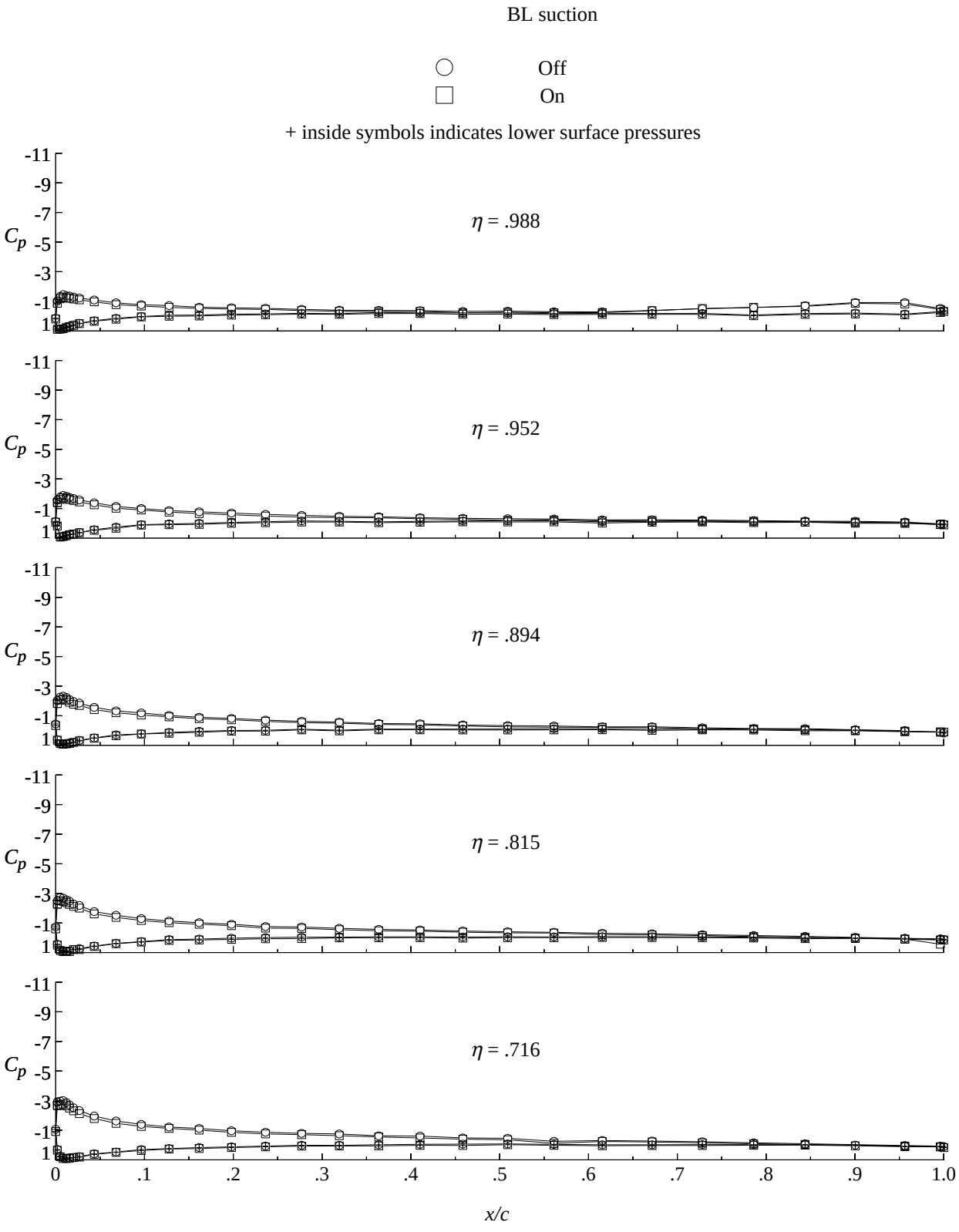


(h) Concluded.

Figure 7. Continued.

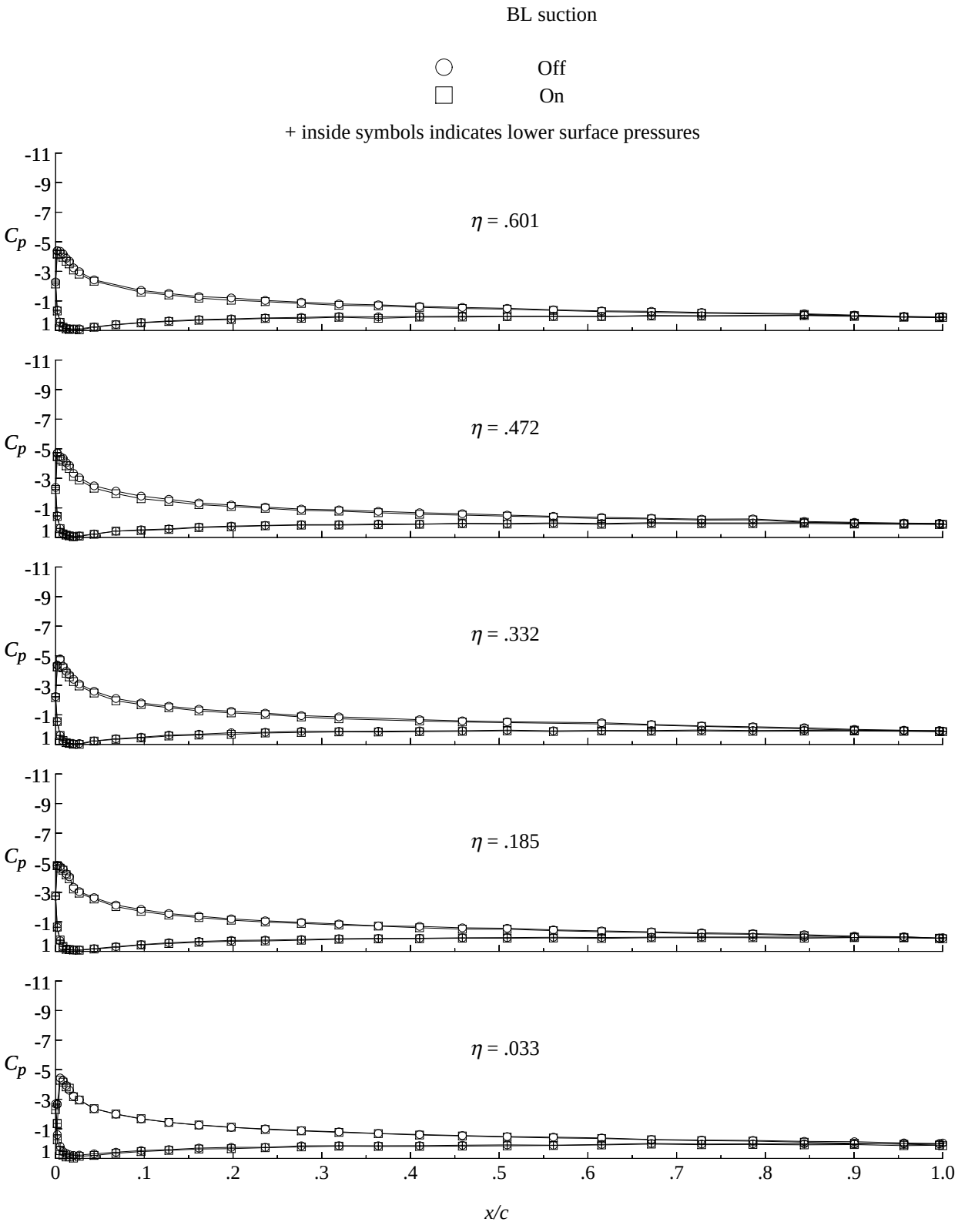


(i) $\alpha = 12°$.

Figure 7. Continued.

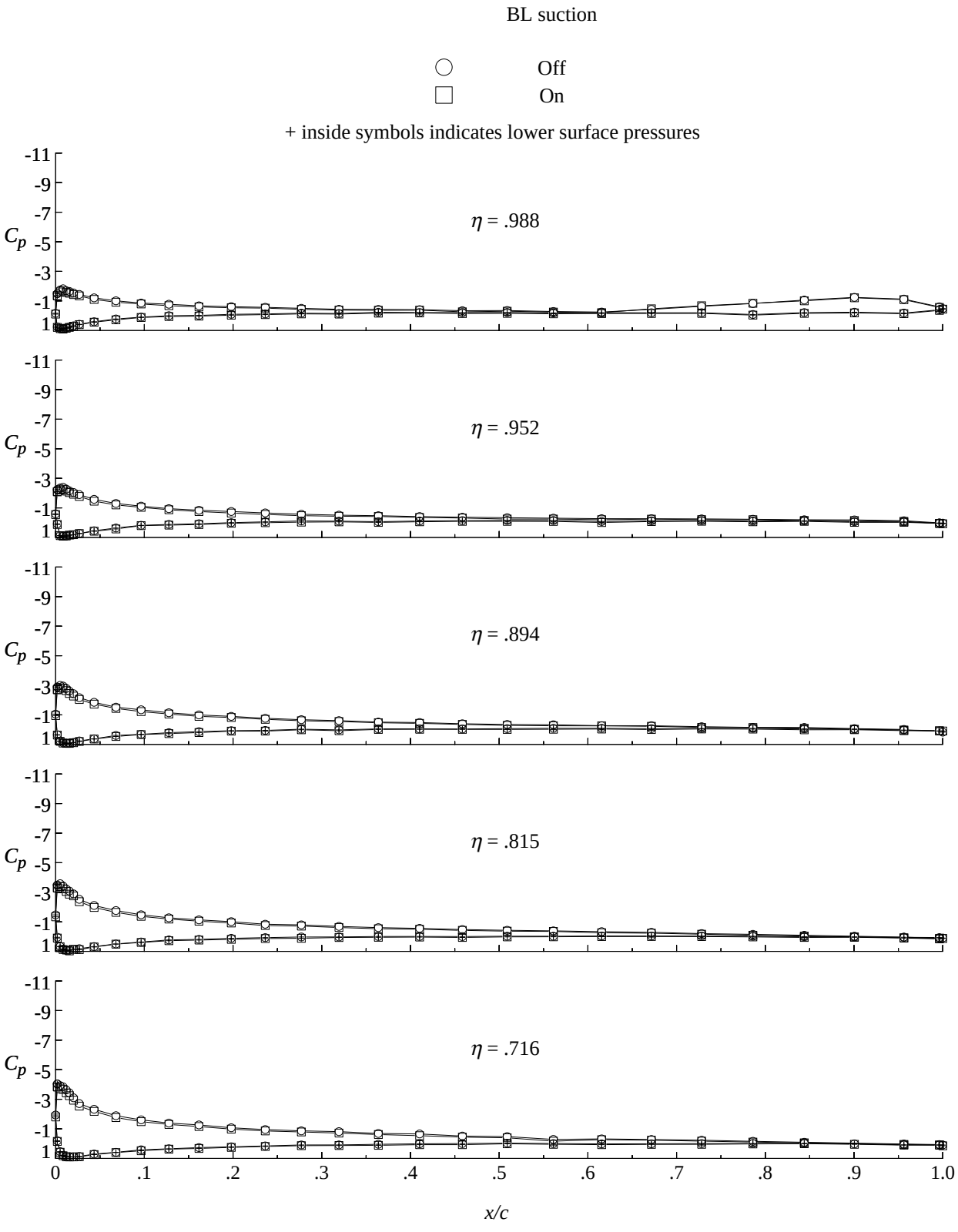


(i) Concluded.

Figure 7. Continued.

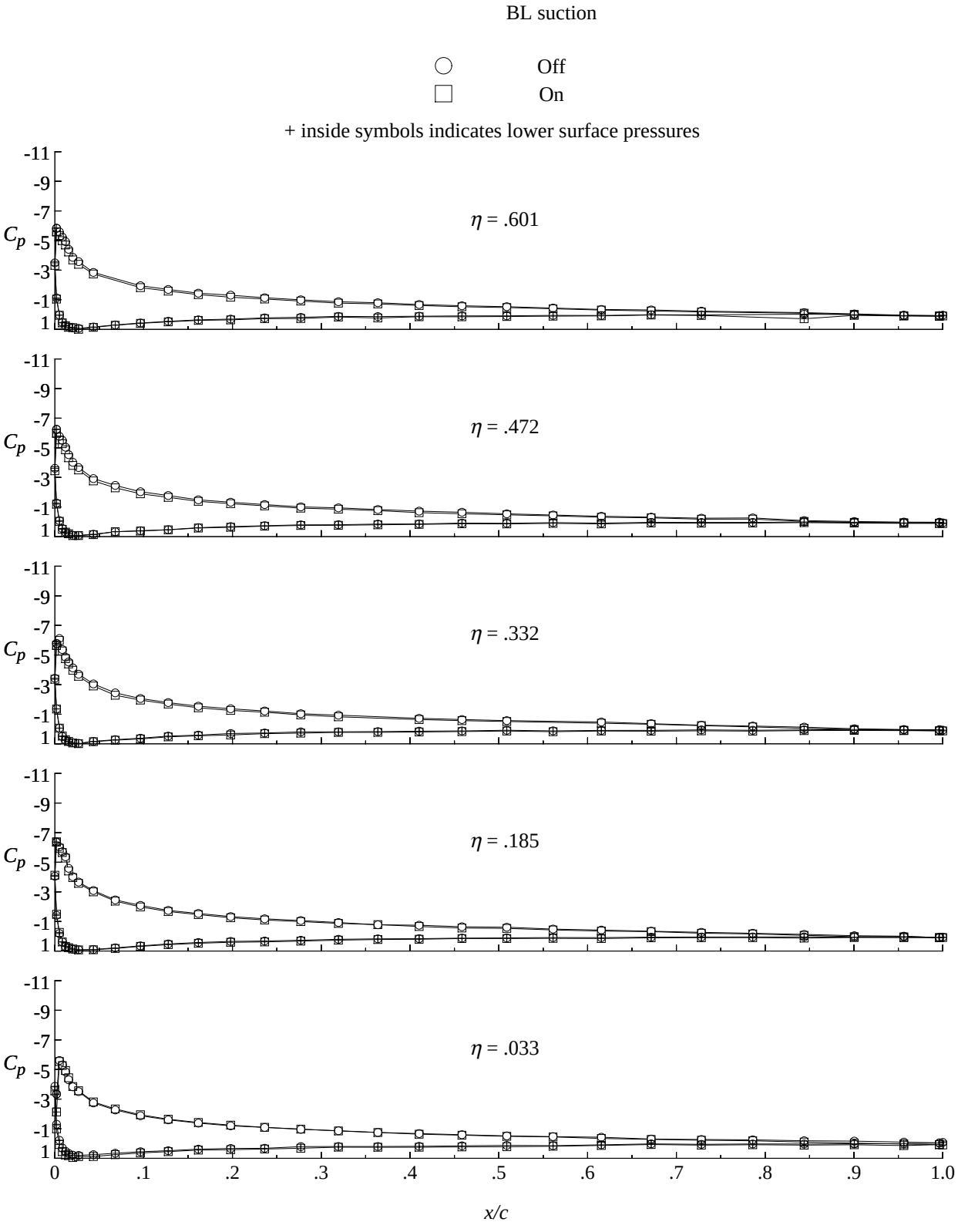


(j) $\alpha = 14°$.

Figure 7. Continued.

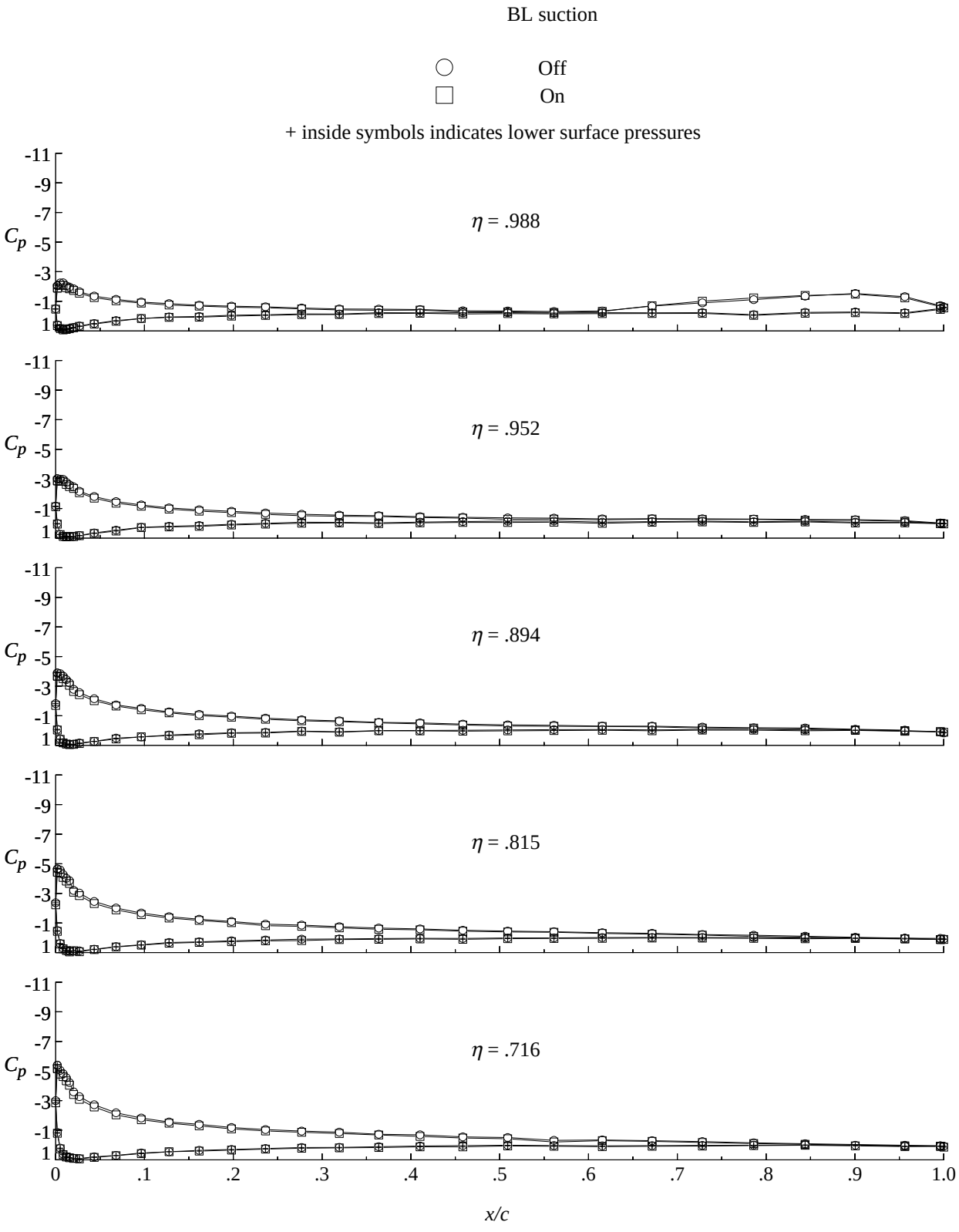


(j) Concluded.

Figure 7. Continued.

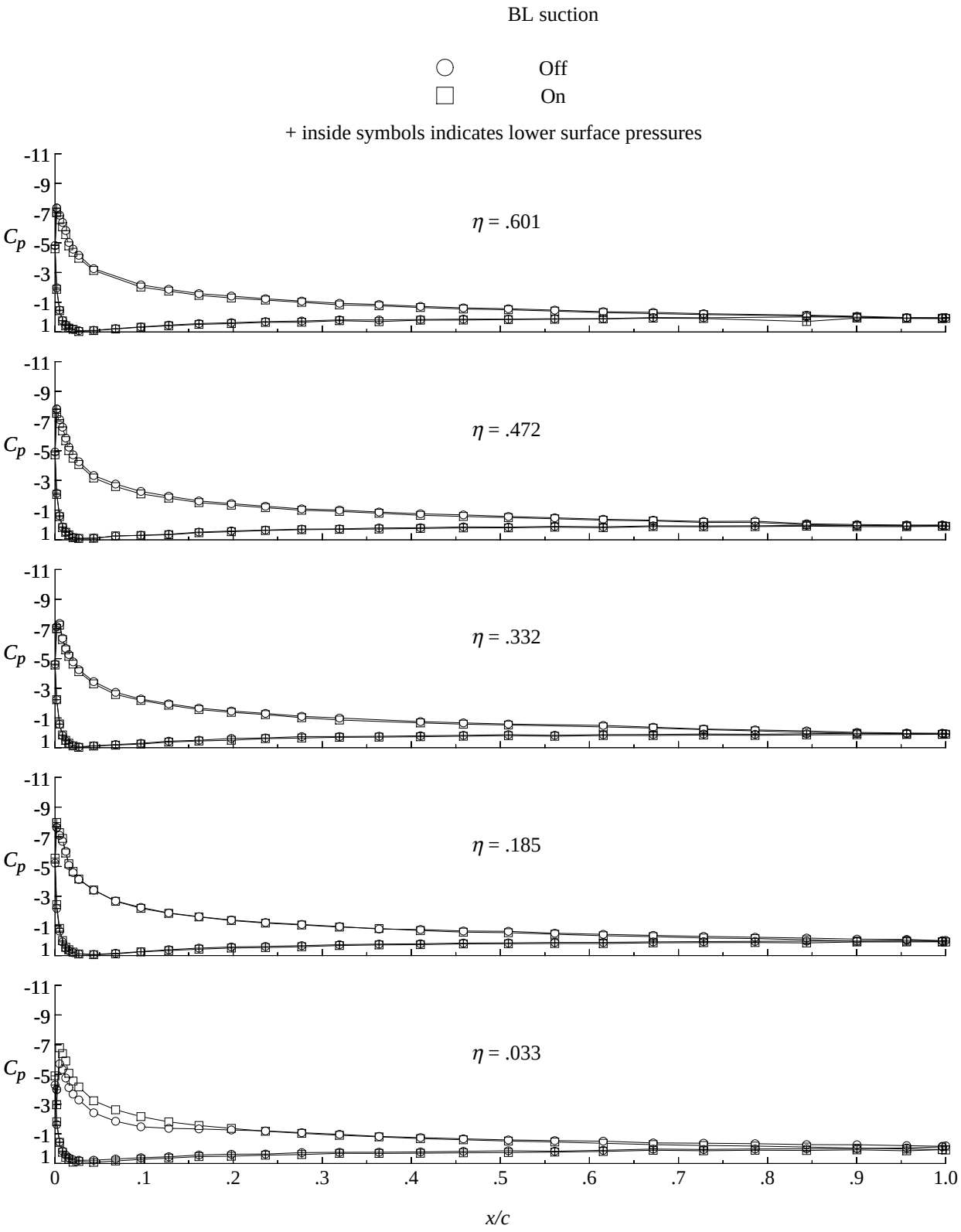


(k) $\alpha = 16°$.

Figure 7. Continued.

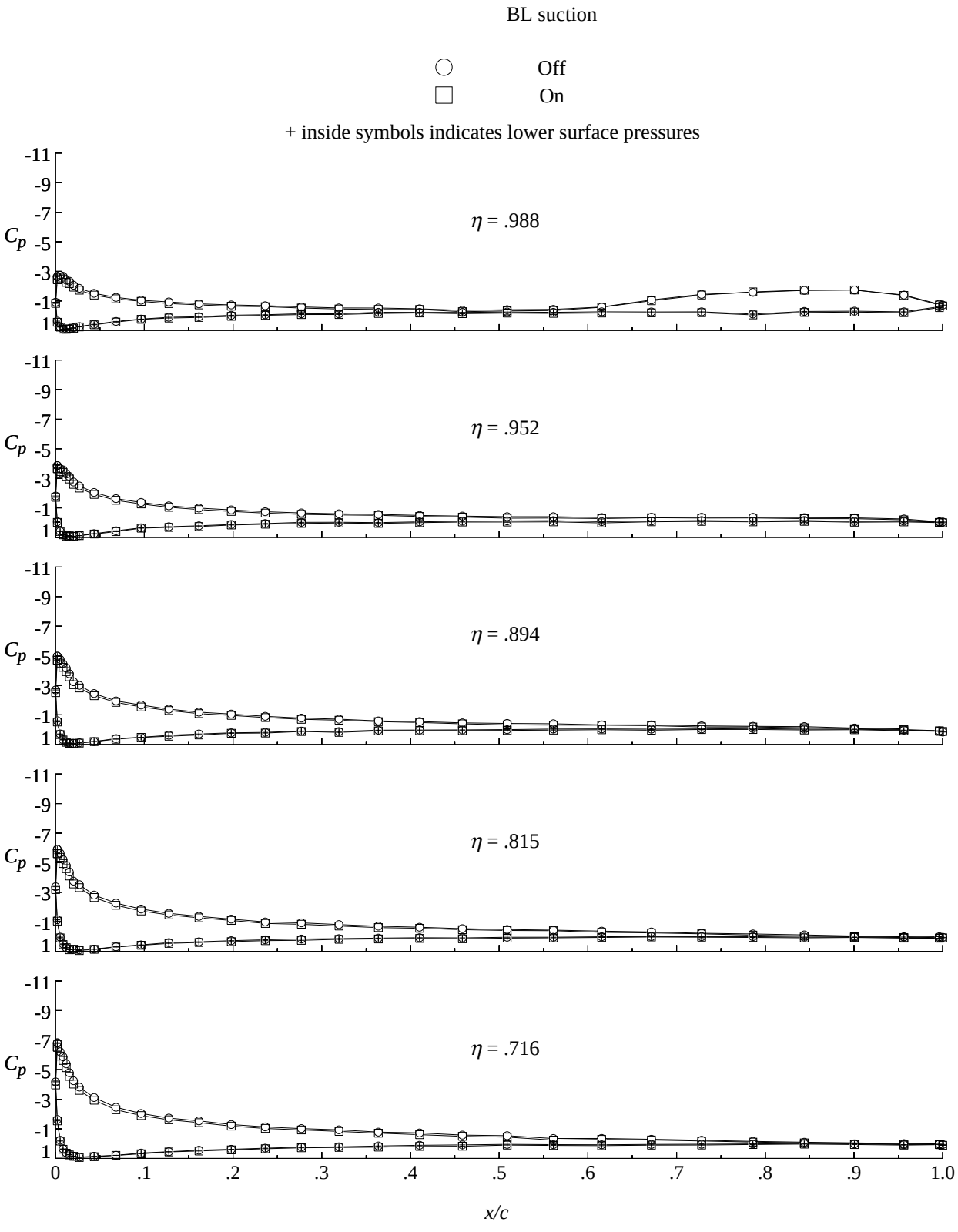


(k) Concluded.

Figure 7. Continued.

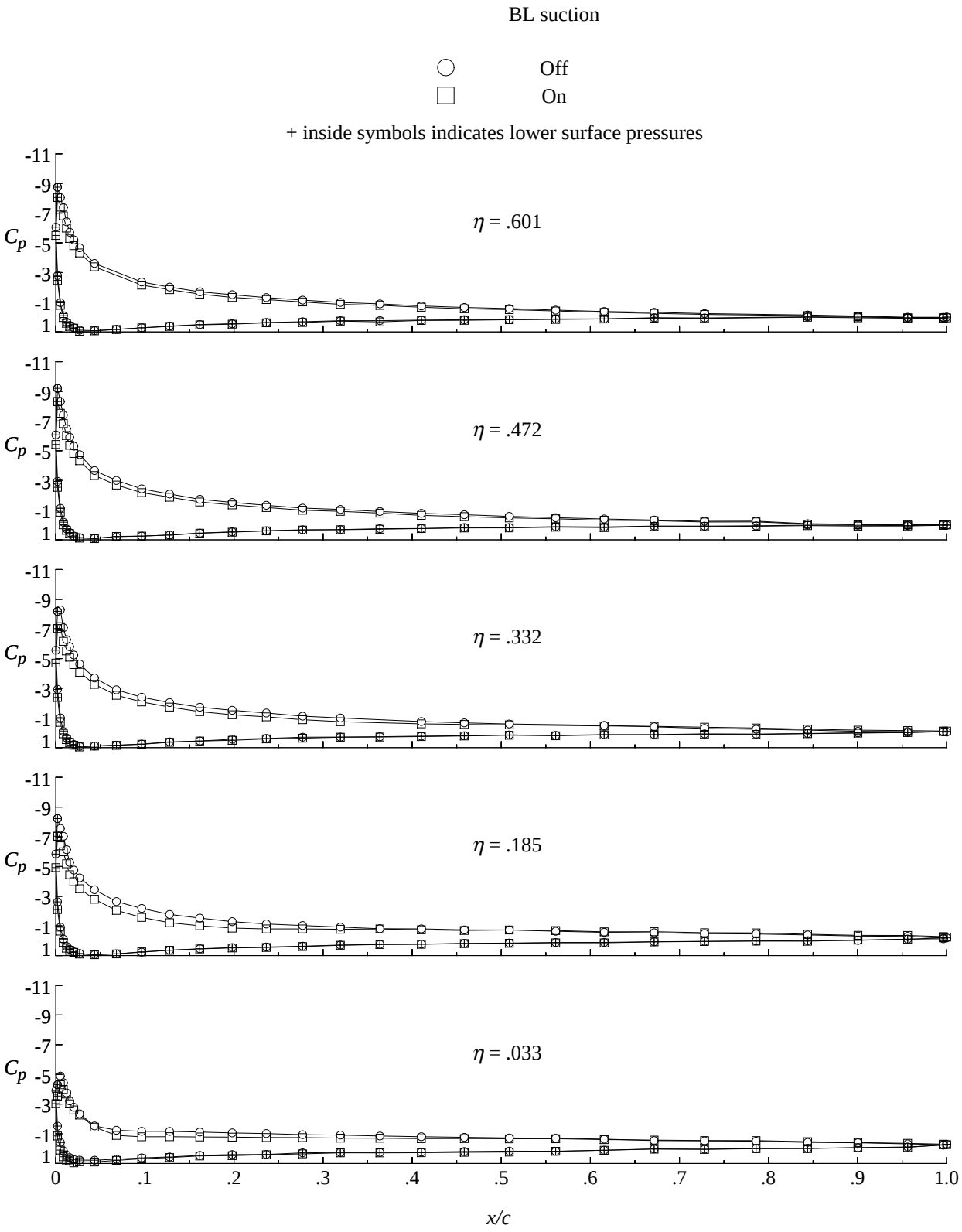


(l) $\alpha = 18°$.

Figure 7. Continued.

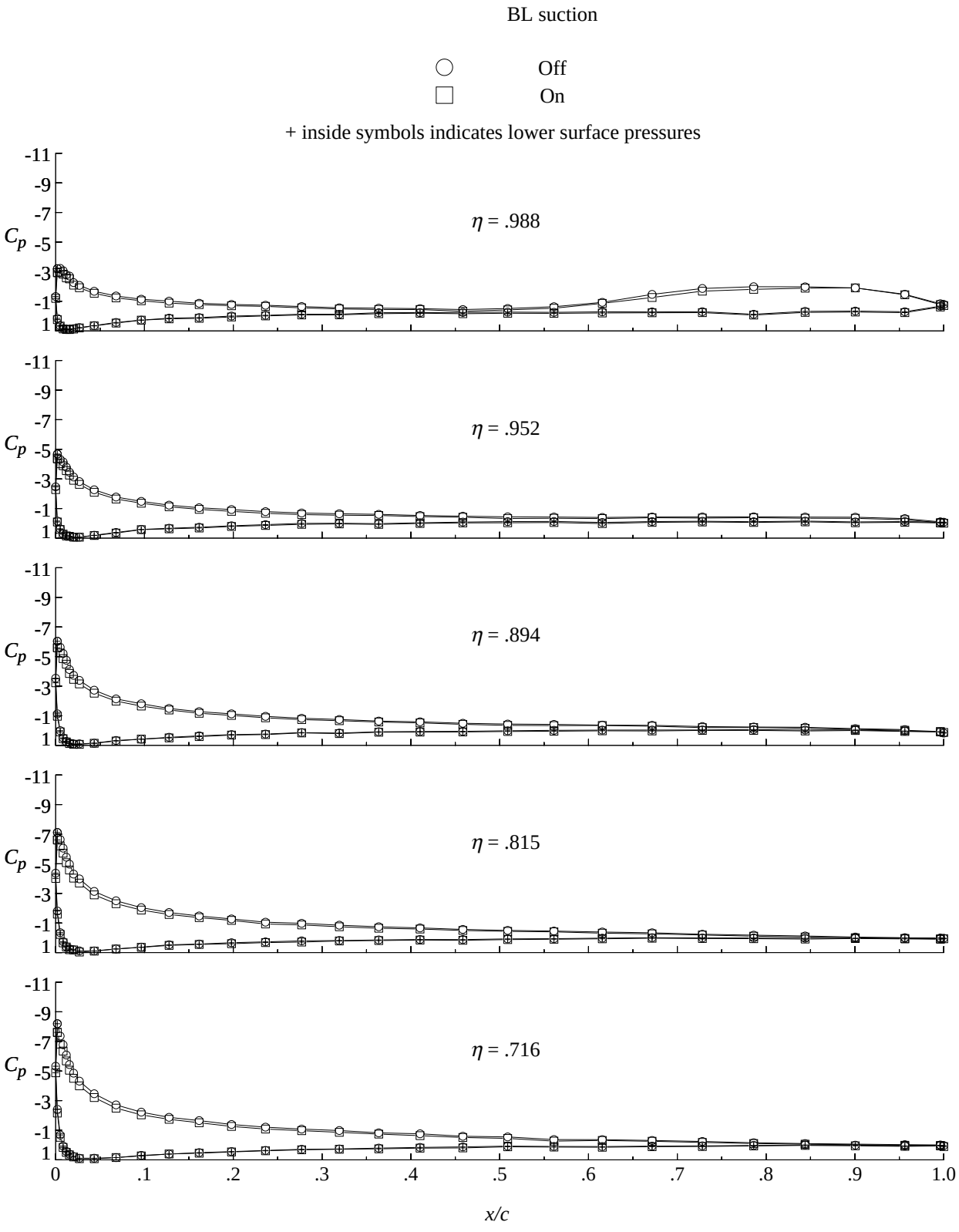


(l) Concluded.

Figure 7. Concluded.

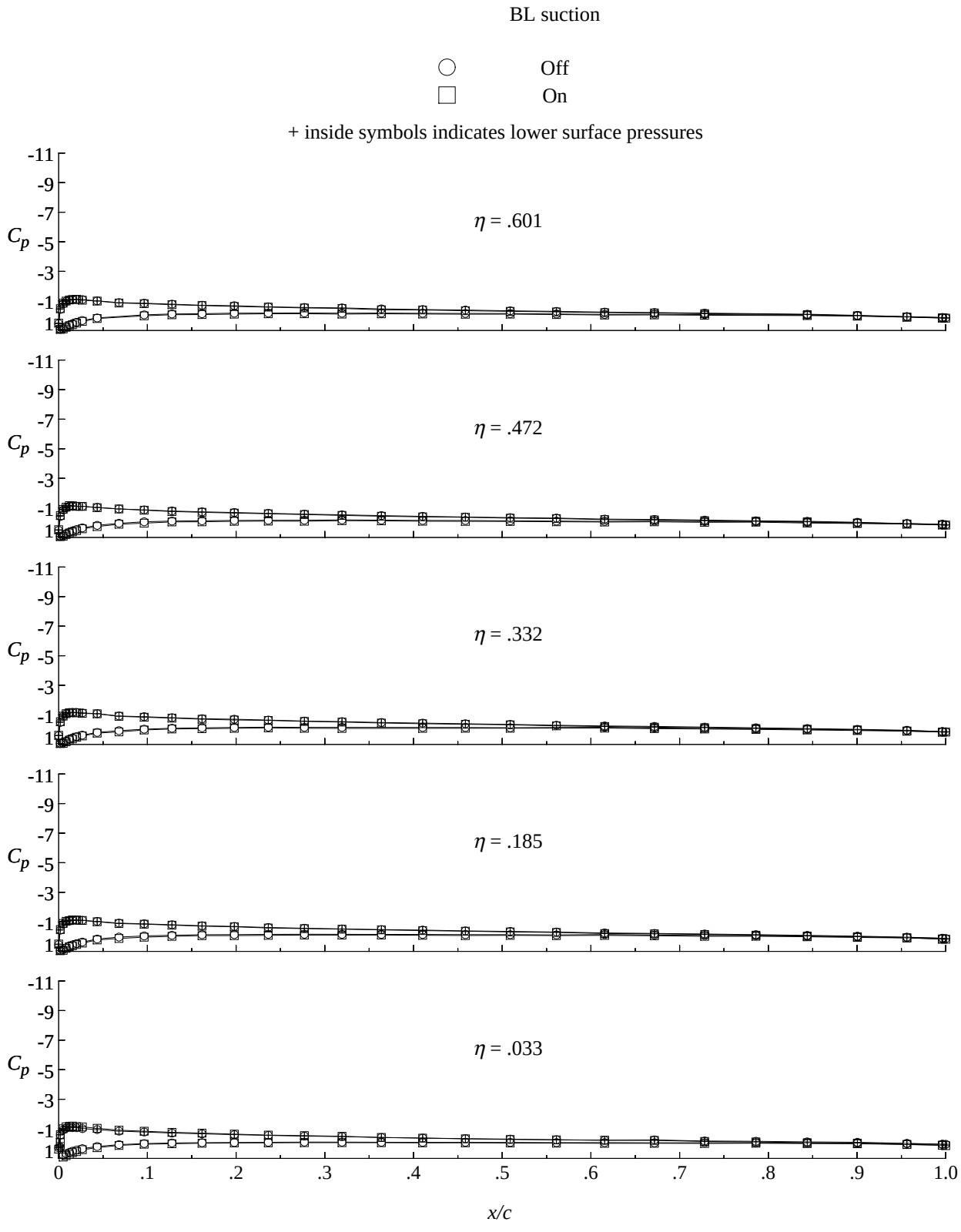


(a) $\alpha$ = - 4°.

Figure 8. Effect of tunnel floor boundary layer suction on cruise wing pressure distribution. $q_\infty$ = 60 psf.

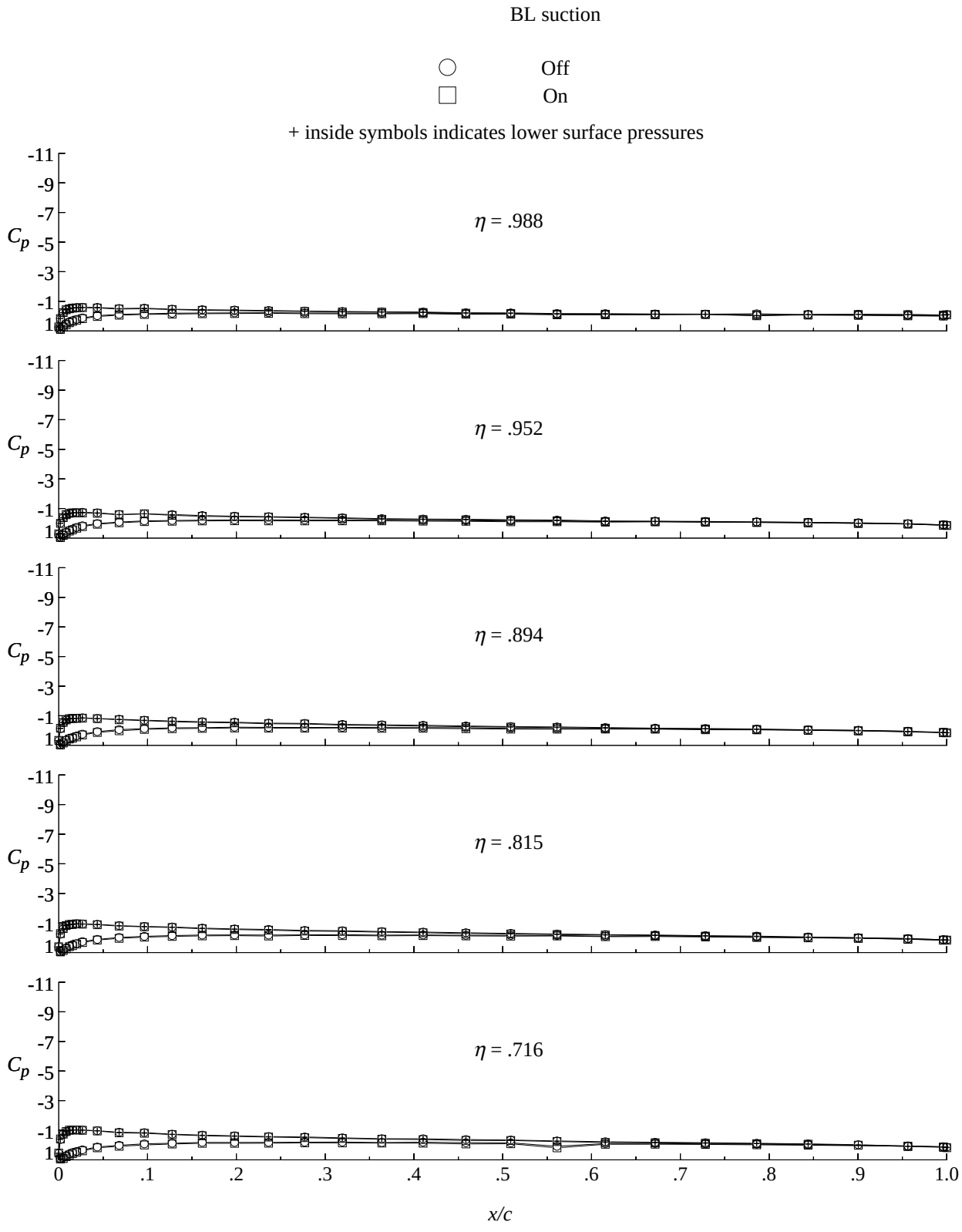


(a) Concluded.

Figure 8. Continued.

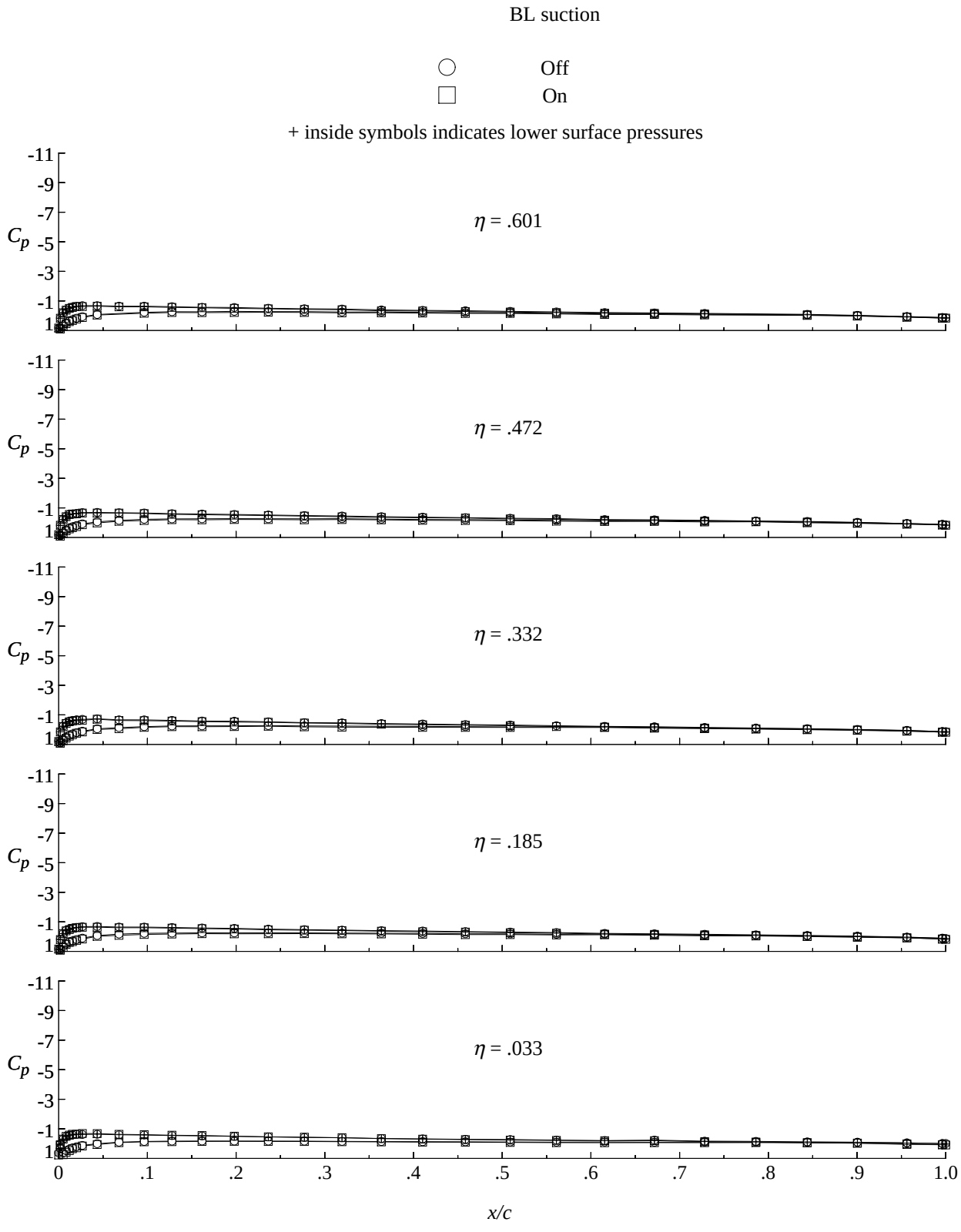


(b) $\alpha$ = - 2°.

Figure 8. Continued.

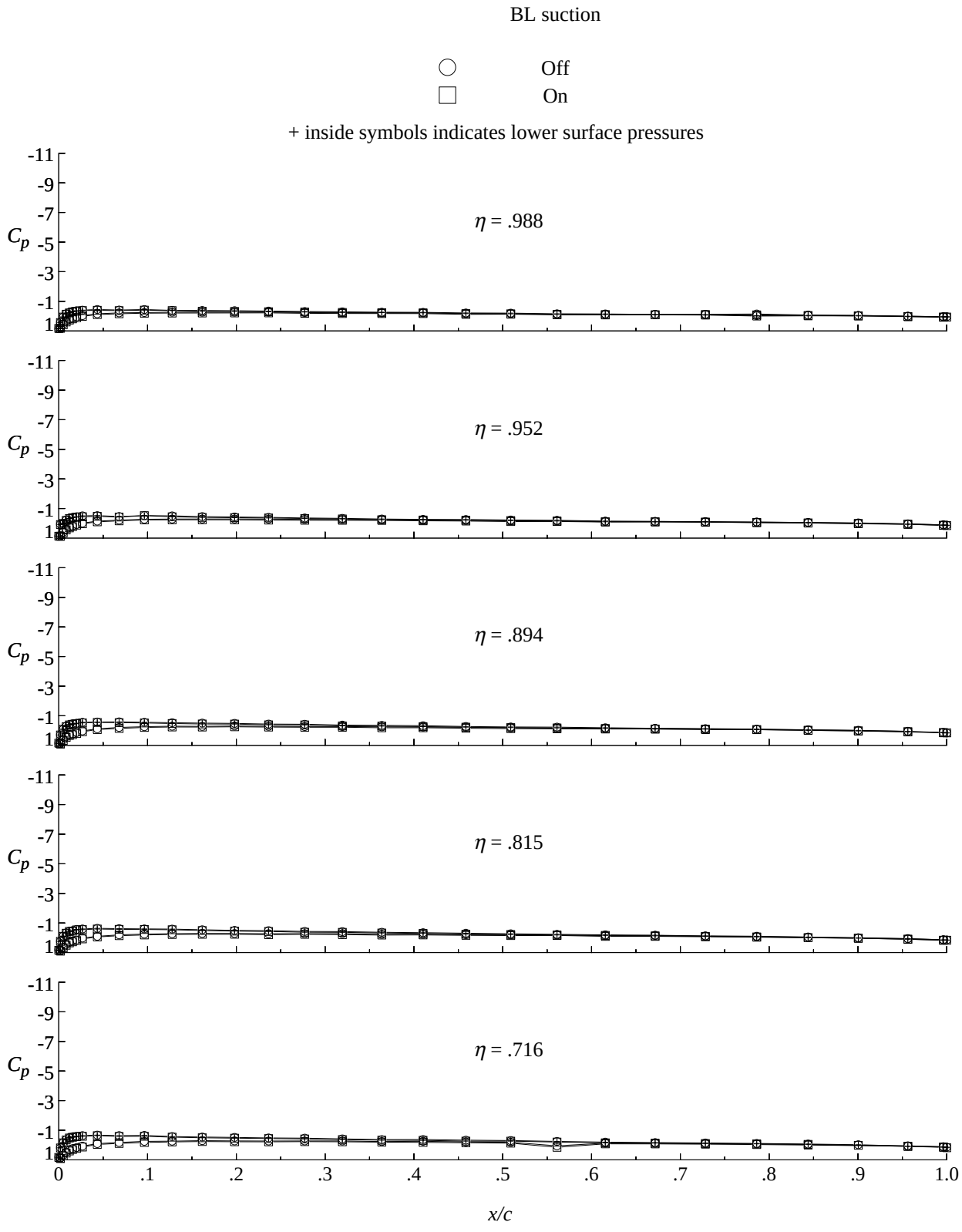


(b) Concluded.

Figure 8. Continued.

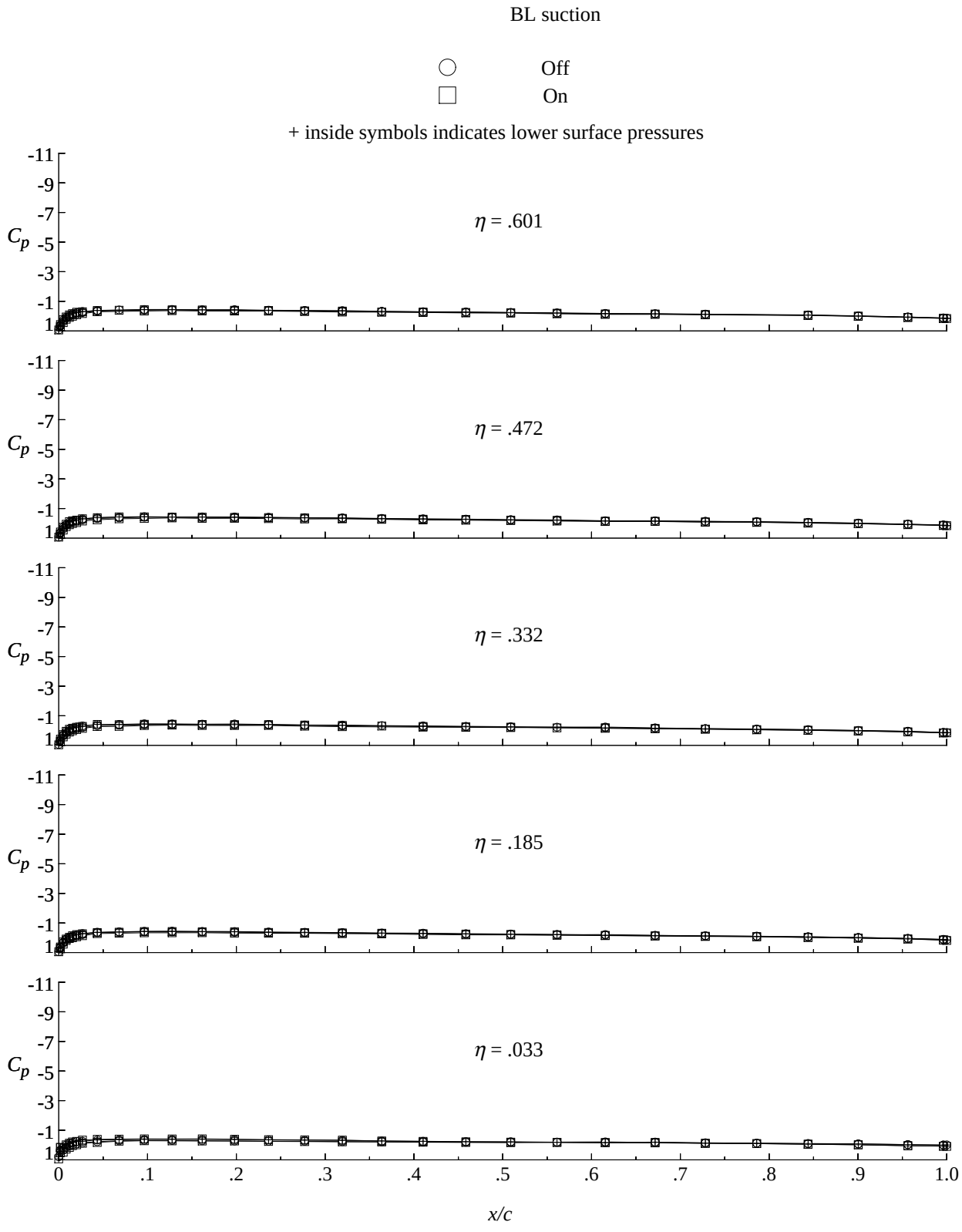


(c) $\alpha = 0°$.

Figure 8. Continued.

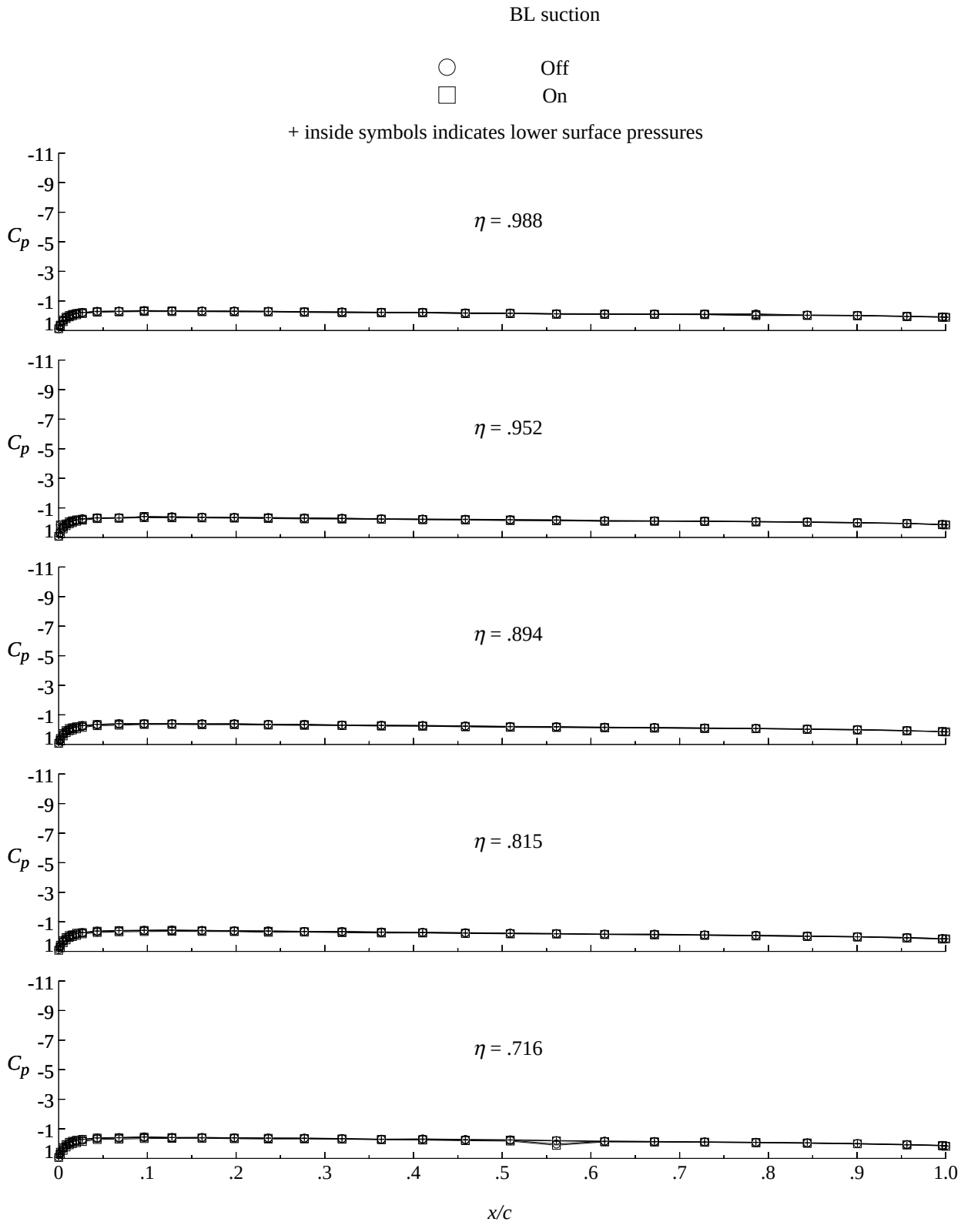


(c) Concluded.

Figure 8. Continued.

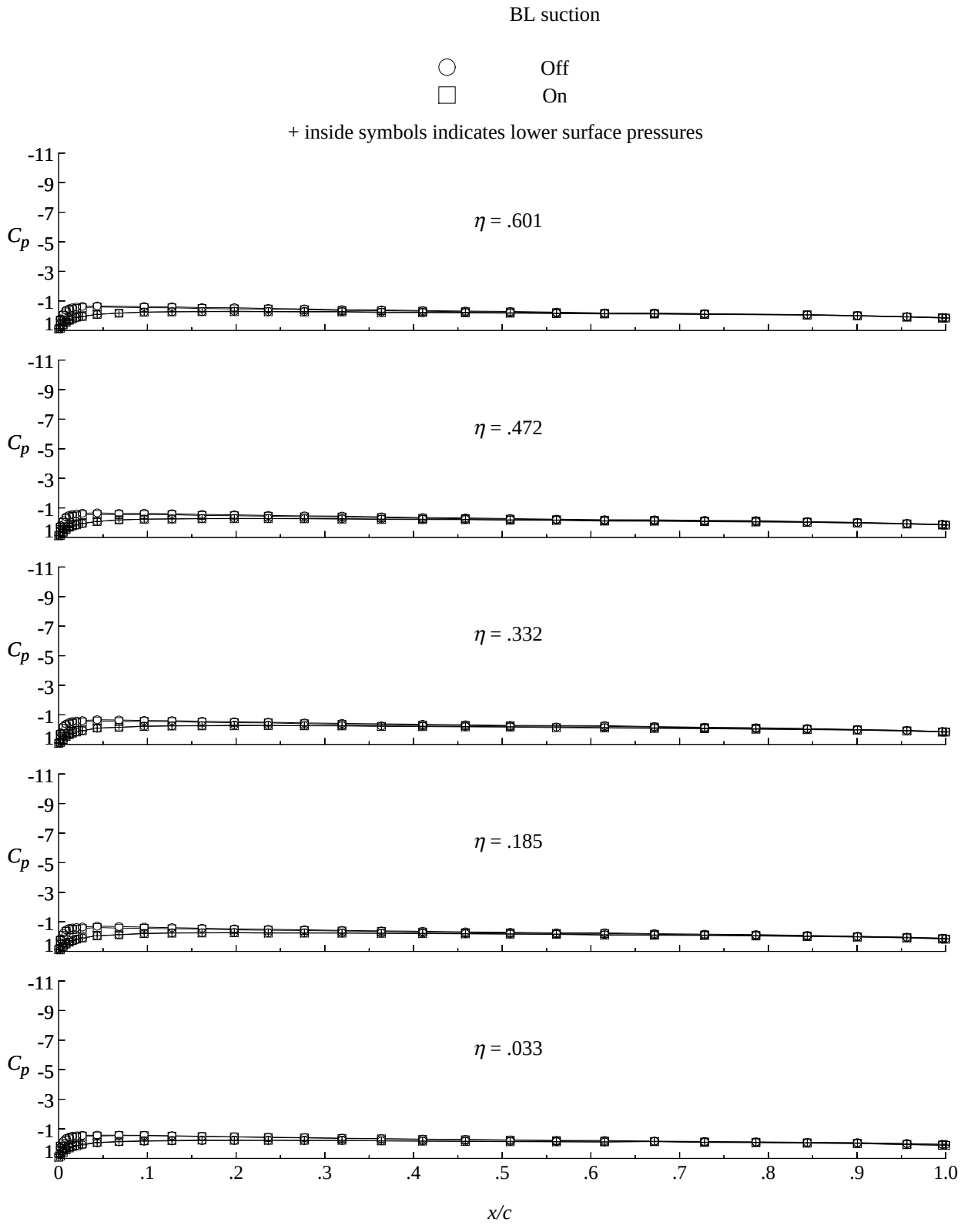


(d) $\alpha = 2°$.

Figure 8. Continued.

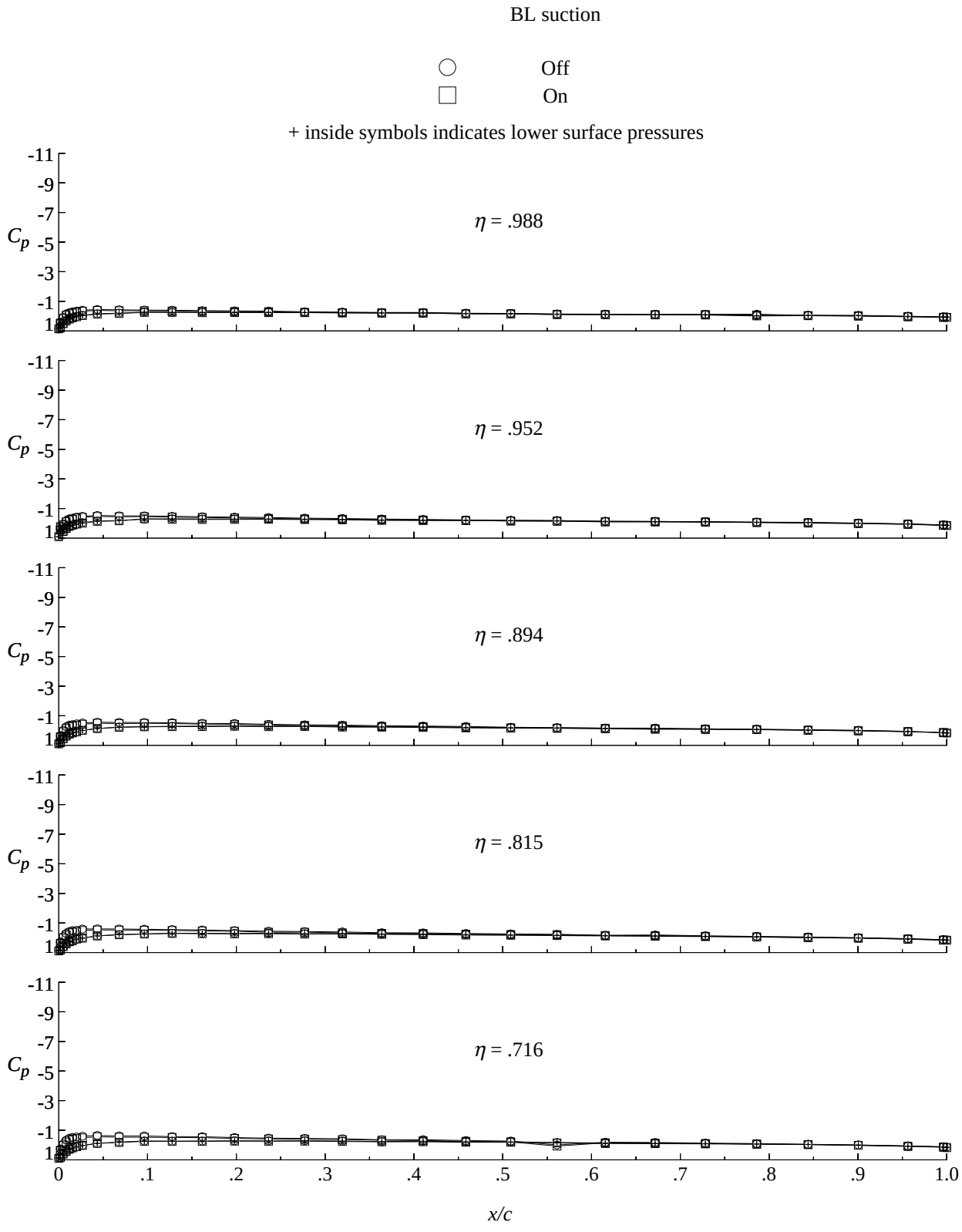


(d) Concluded.

Figure 8. Continued.

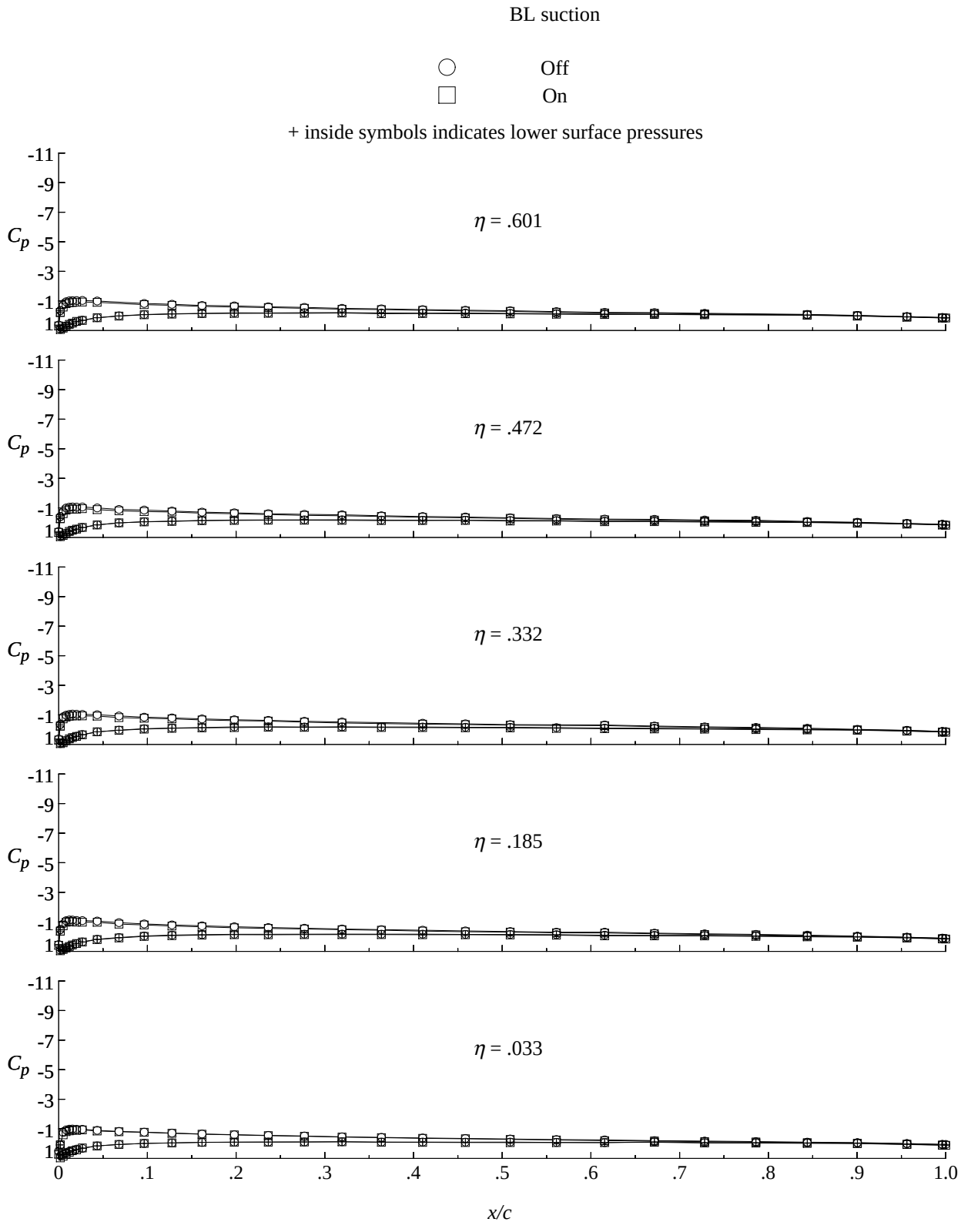


(e) $\alpha = 4°$.

Figure 8. Continued.

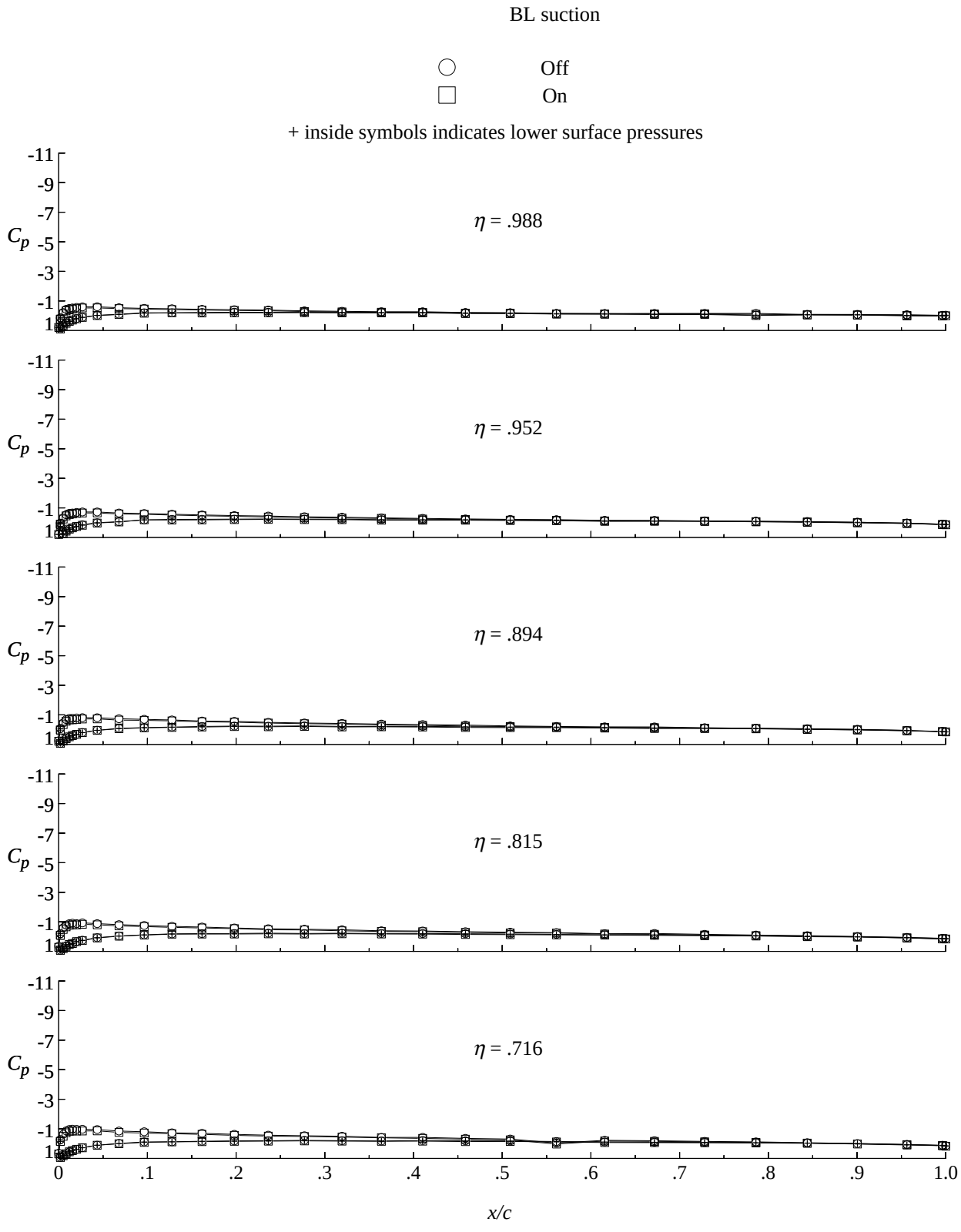


(e) Concluded.

Figure 8. Continued.

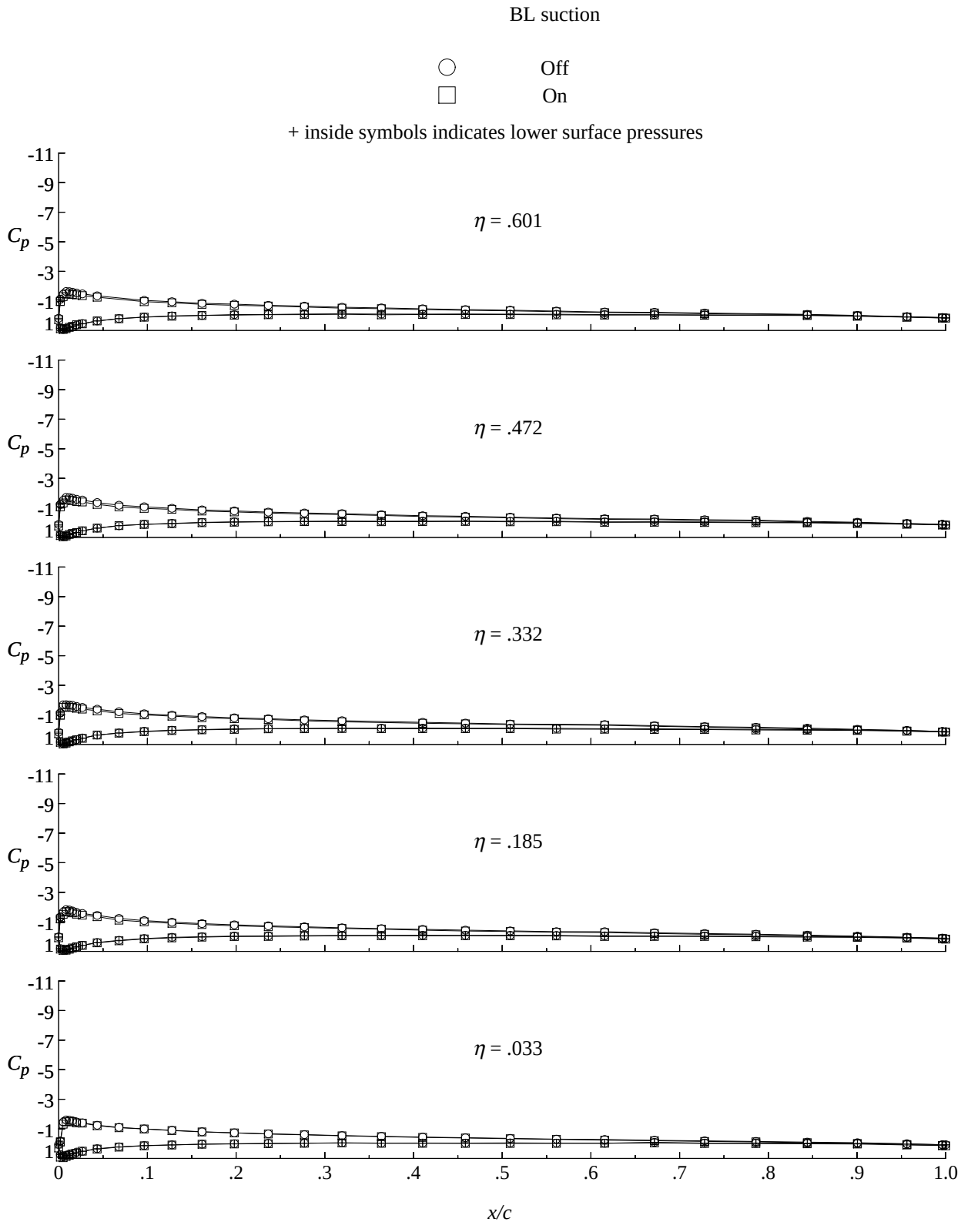


(f) $\alpha = 6°$.

Figure 8. Continued.

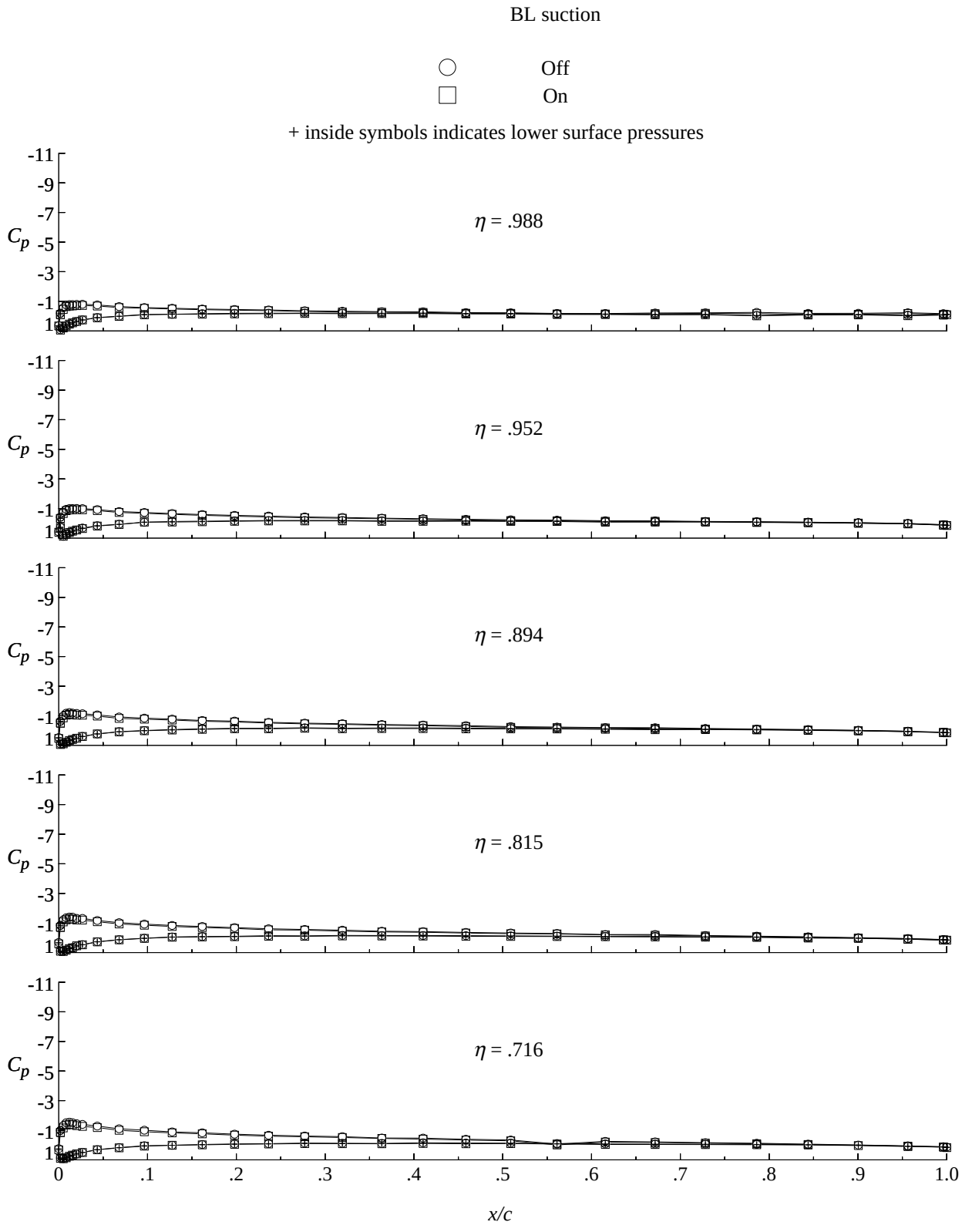


(f) Concluded.

Figure 8. Continued.

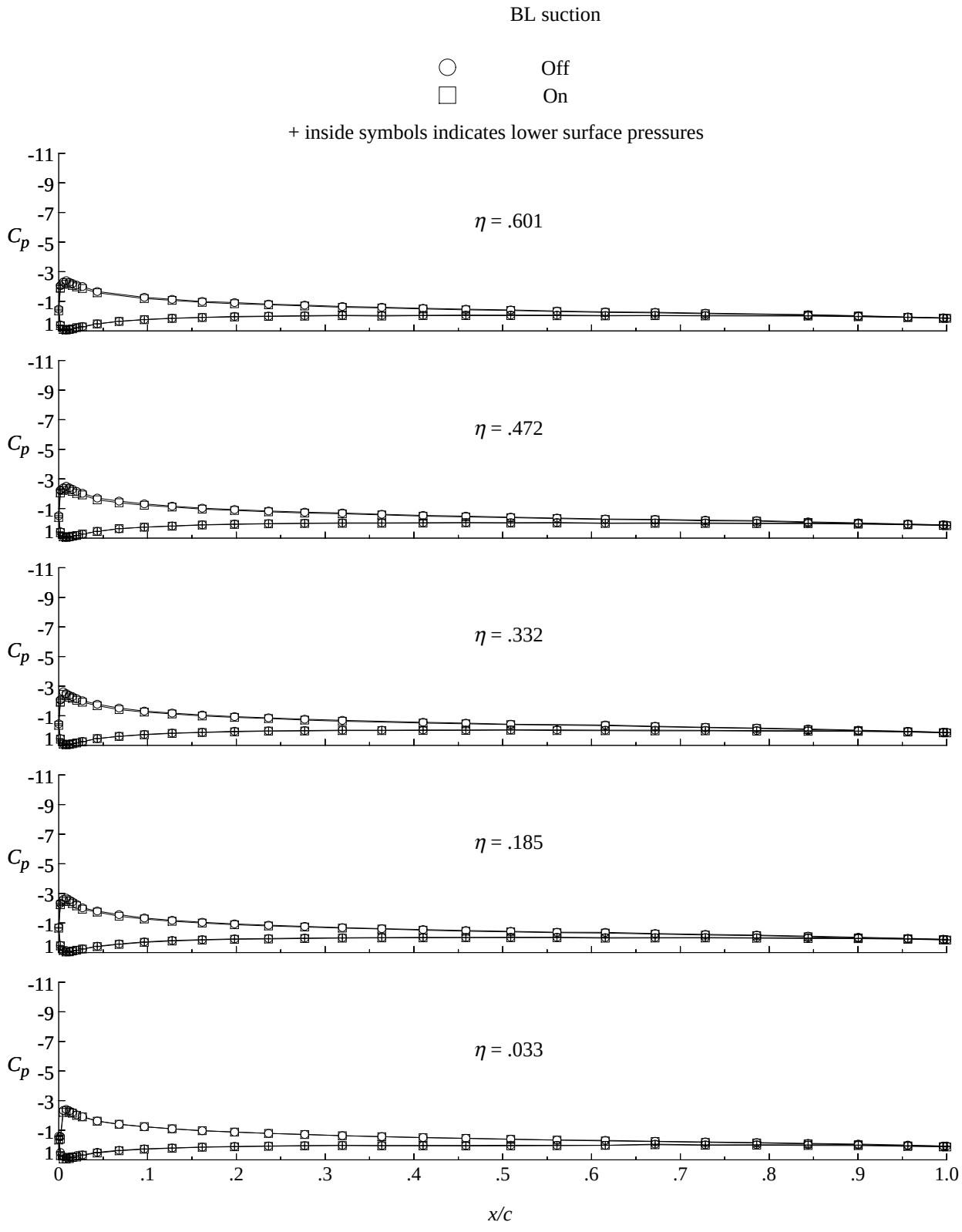


(g) $\alpha = 8°$.

Figure 8. Continued.

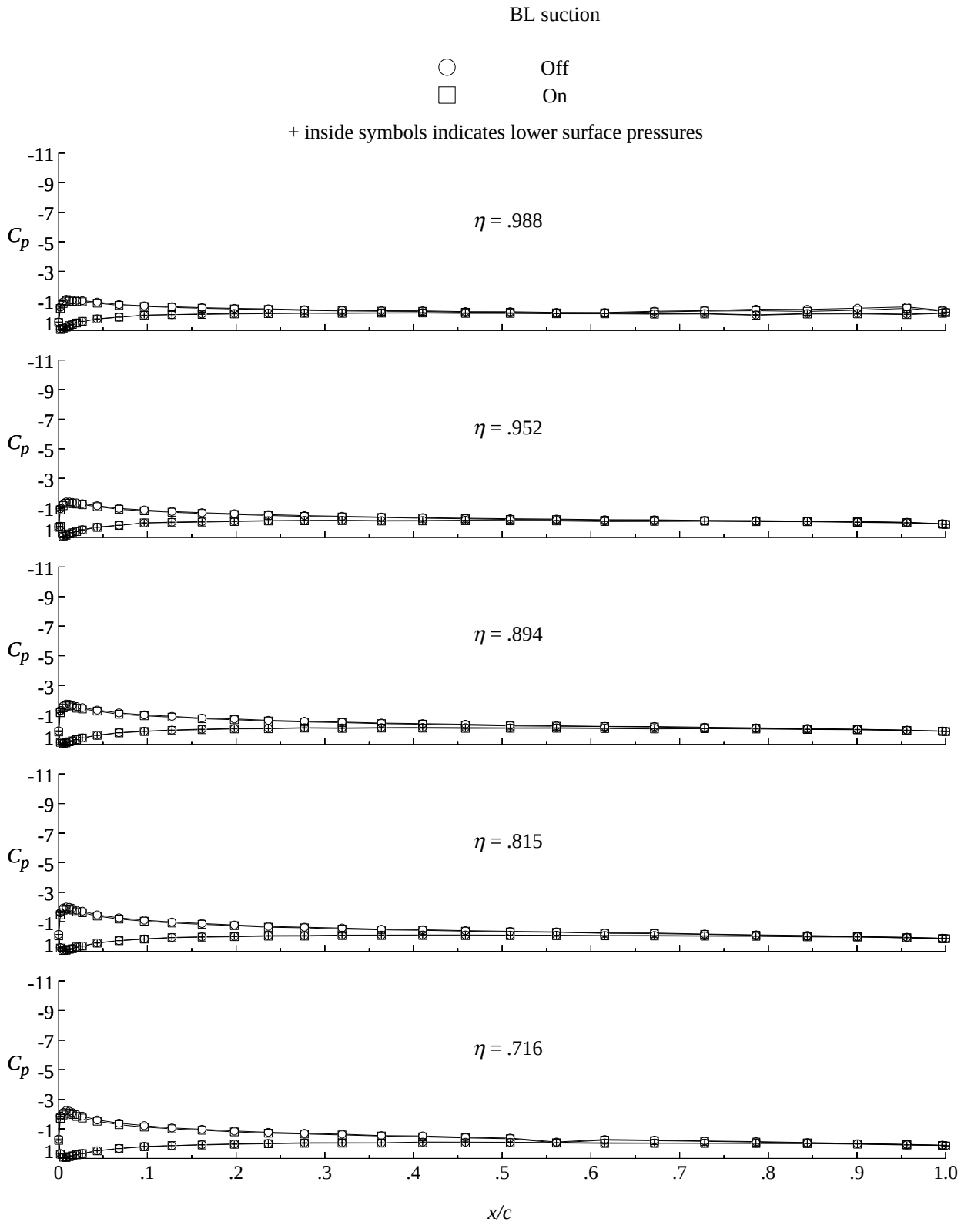


(g) Concluded.

Figure 8. Concluded.

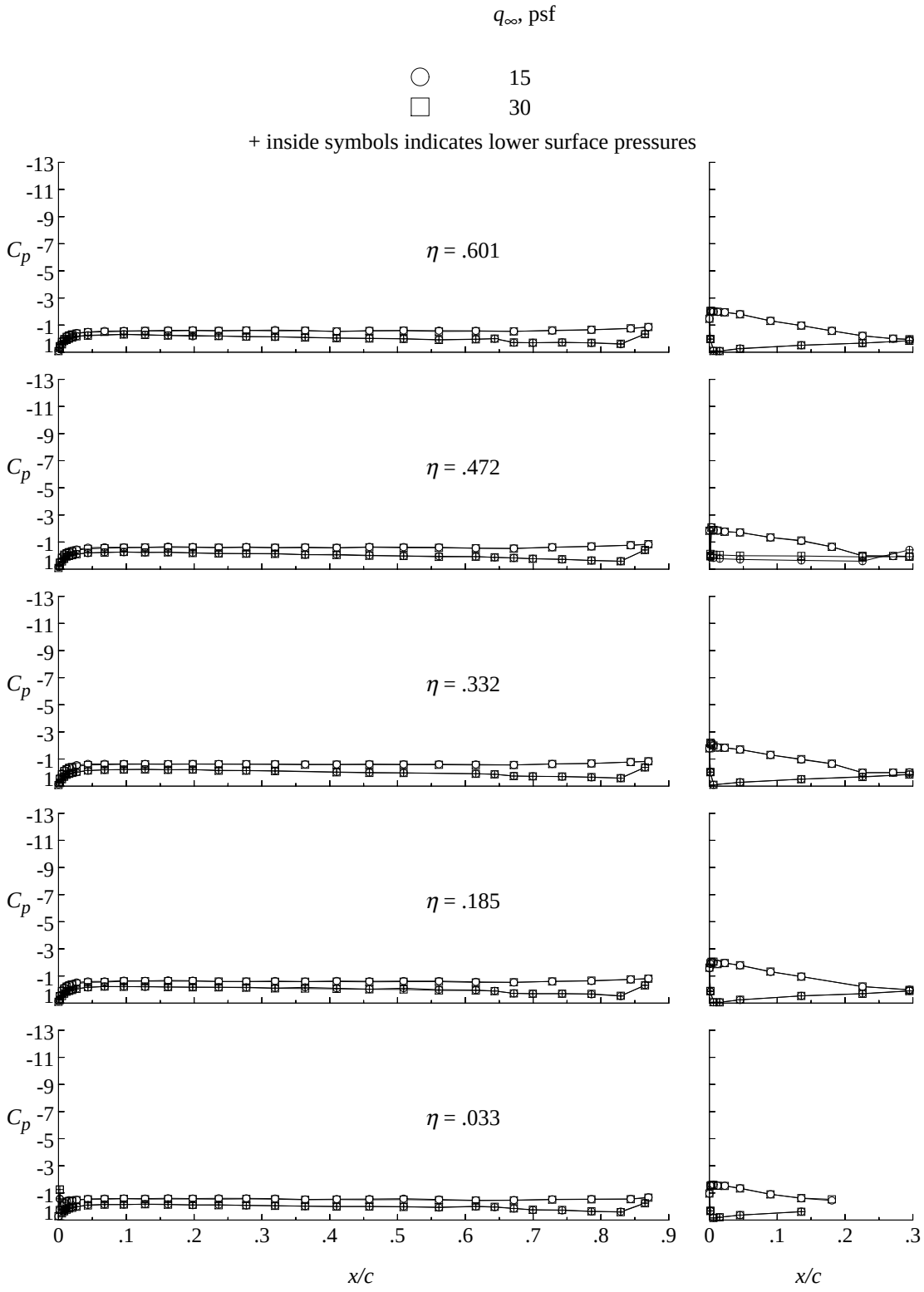


(a) $\alpha$ = - 4°.

Figure 9. Free-stream speed effect on trailing-edge-flap-only wing pressure distribution. Tunnel floor boundary layer suction on.

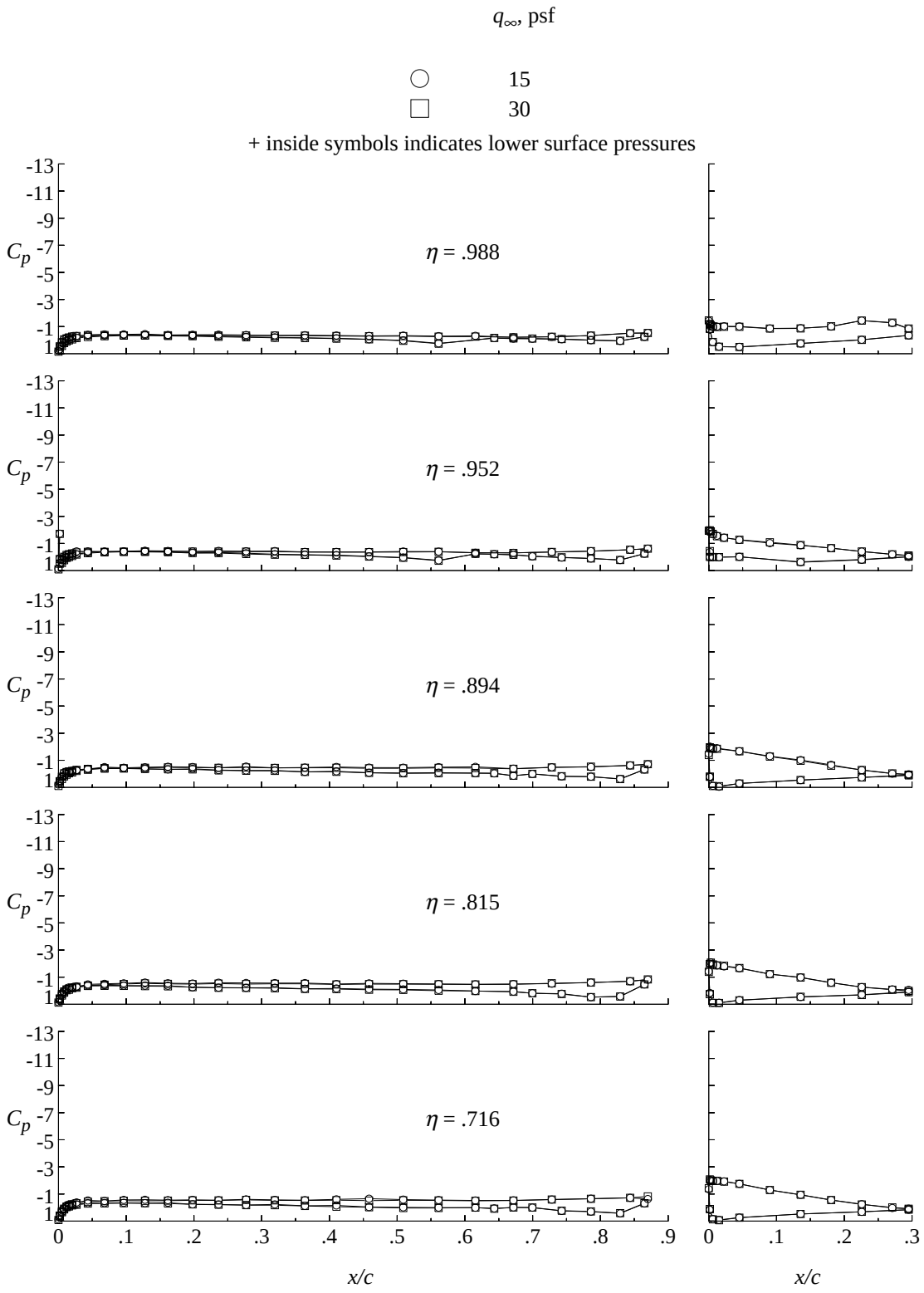


(a) Concluded.

Figure 9. Continued.

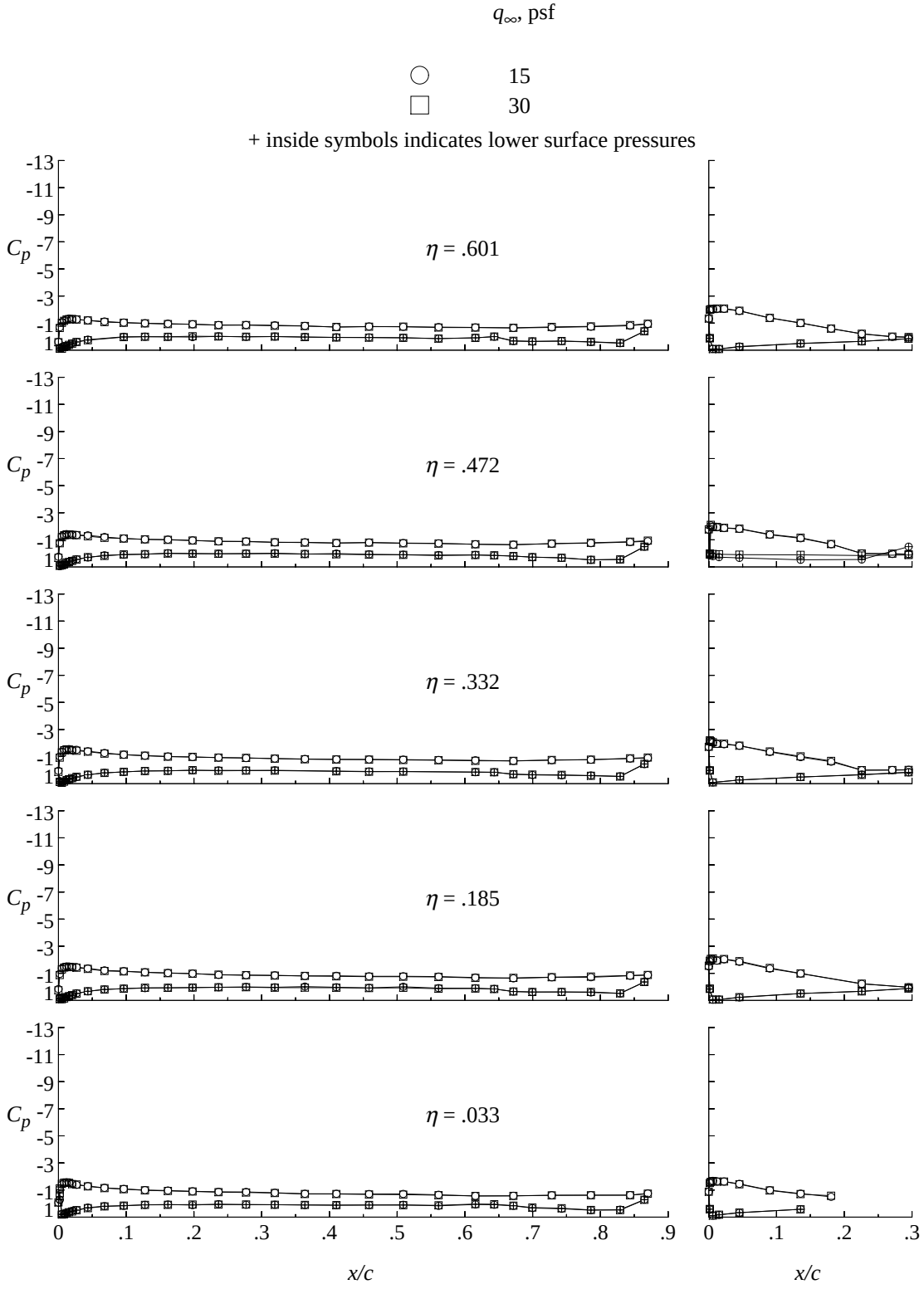


(b) $\alpha = 0°$.

Figure 9. Continued.

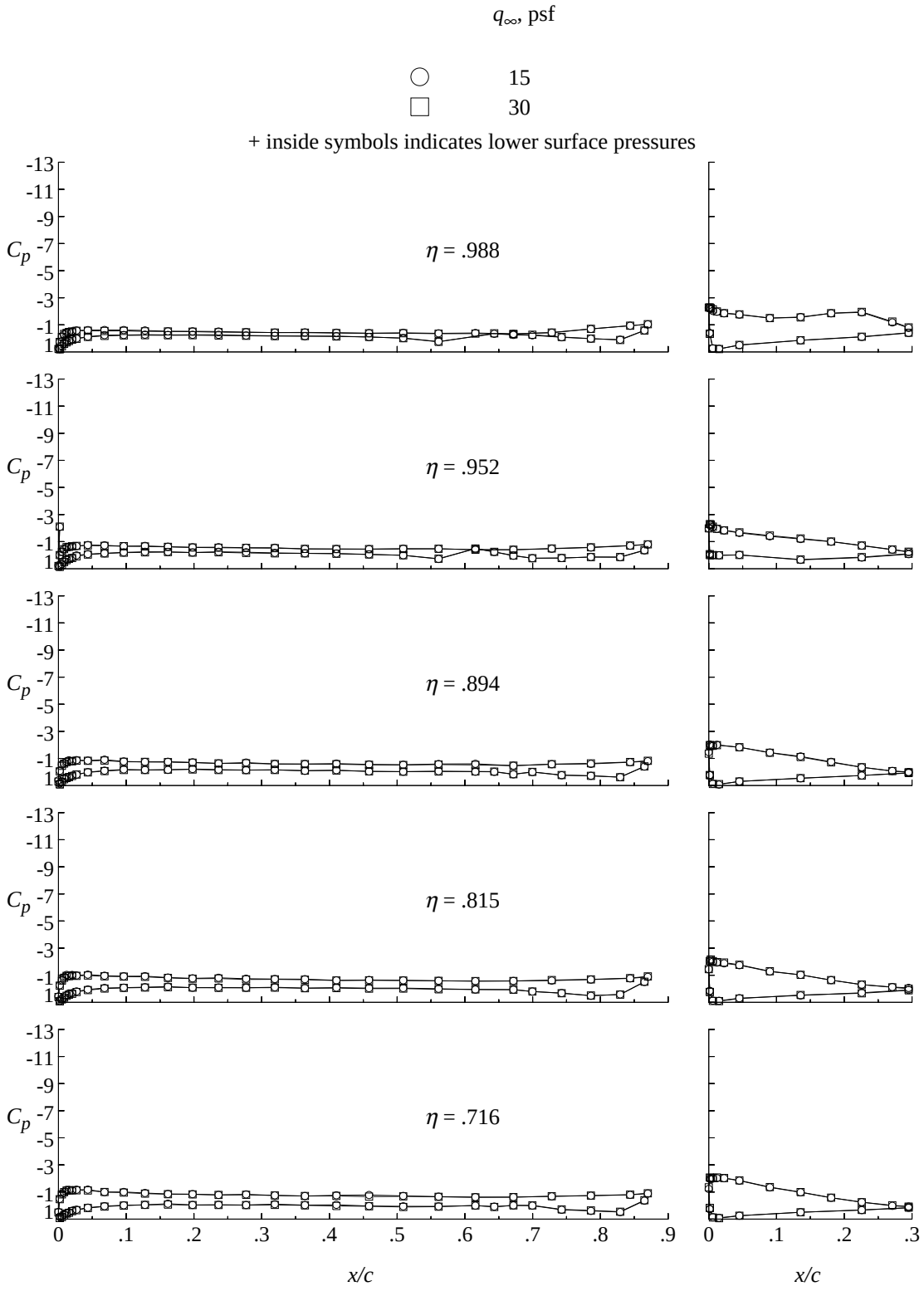


(b) Concluded.

Figure 9. Continued.

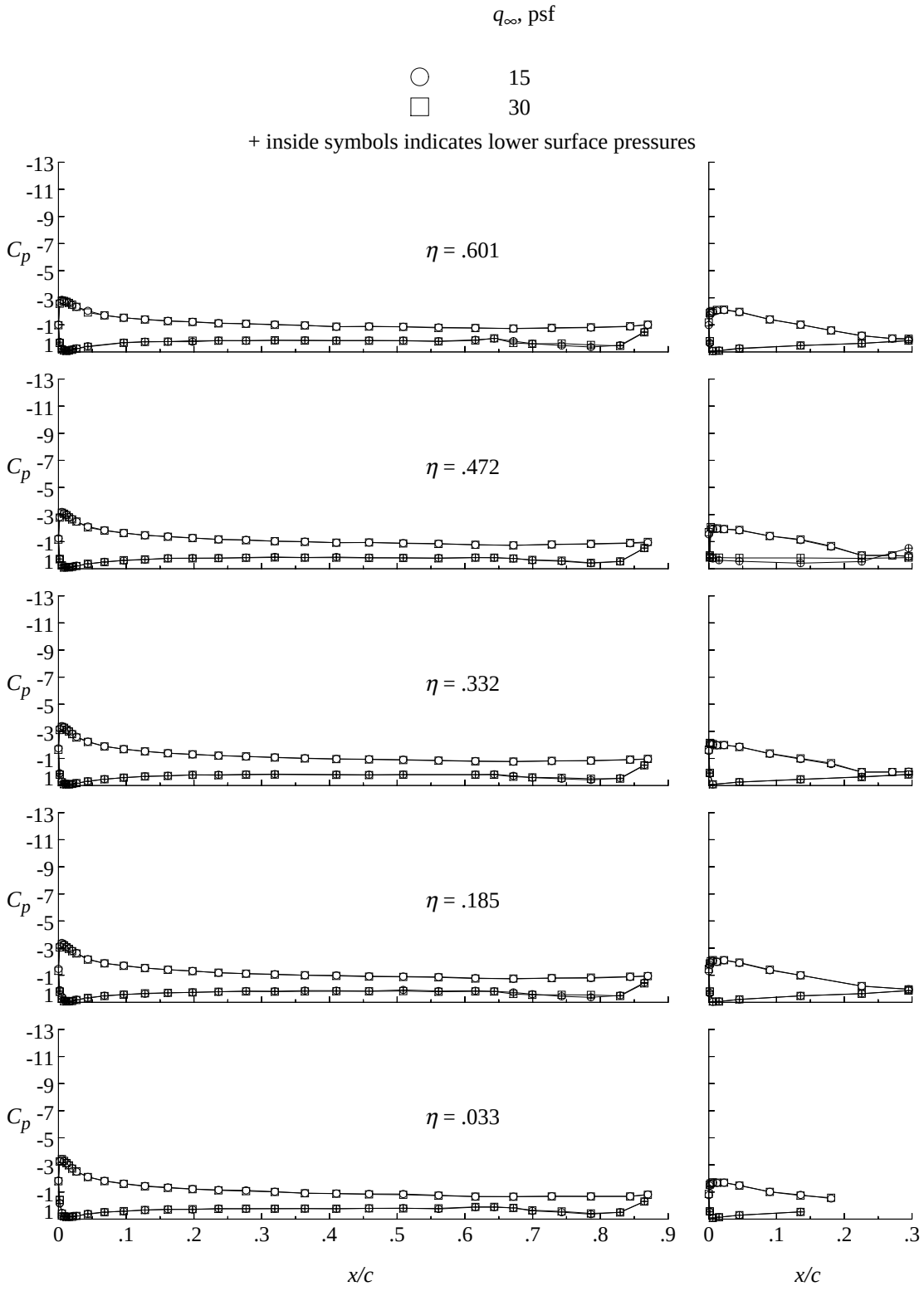


(c) $\alpha = 4°$.

Figure 9. Continued.

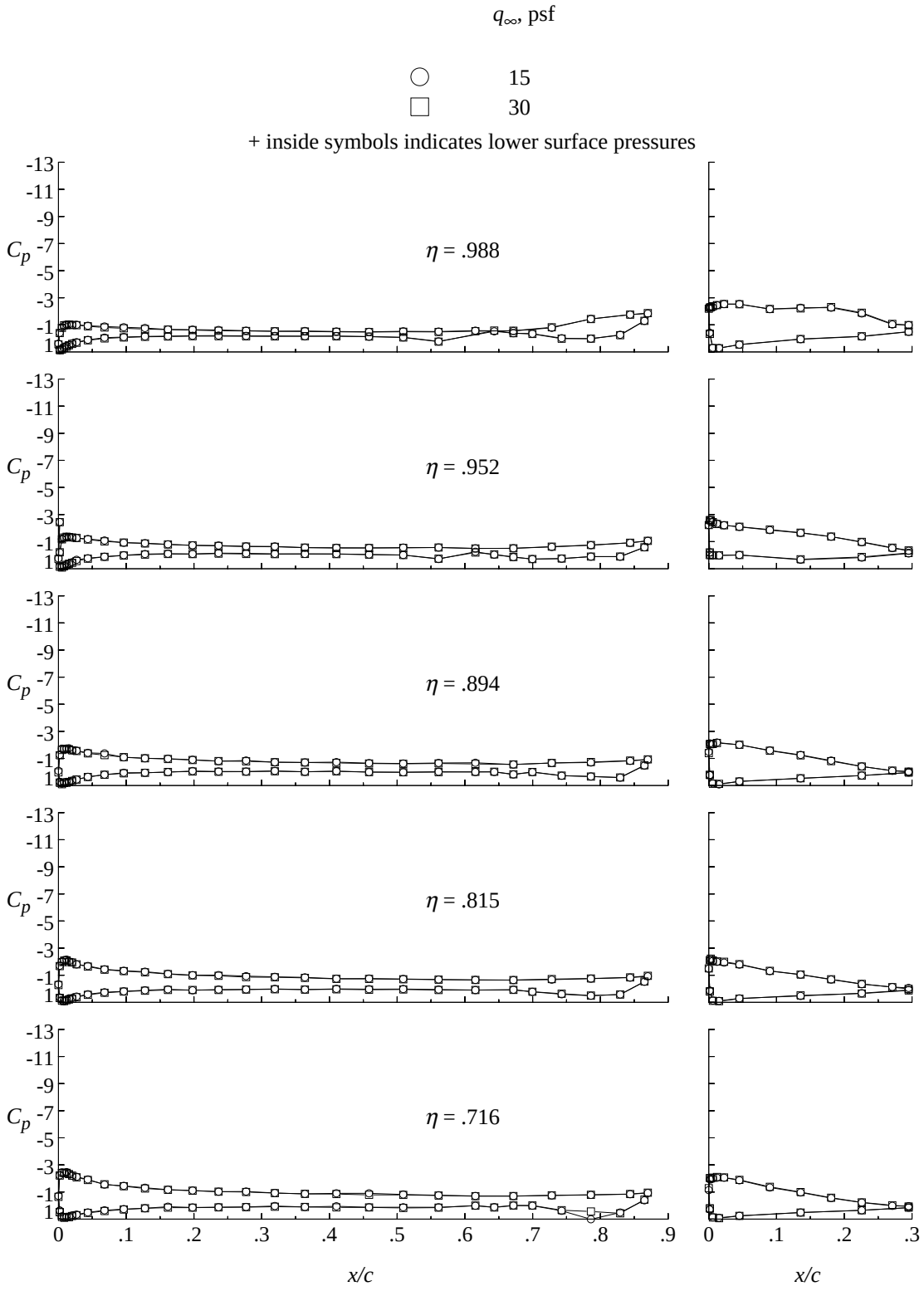


(c) Concluded.

Figure 9. Continued.

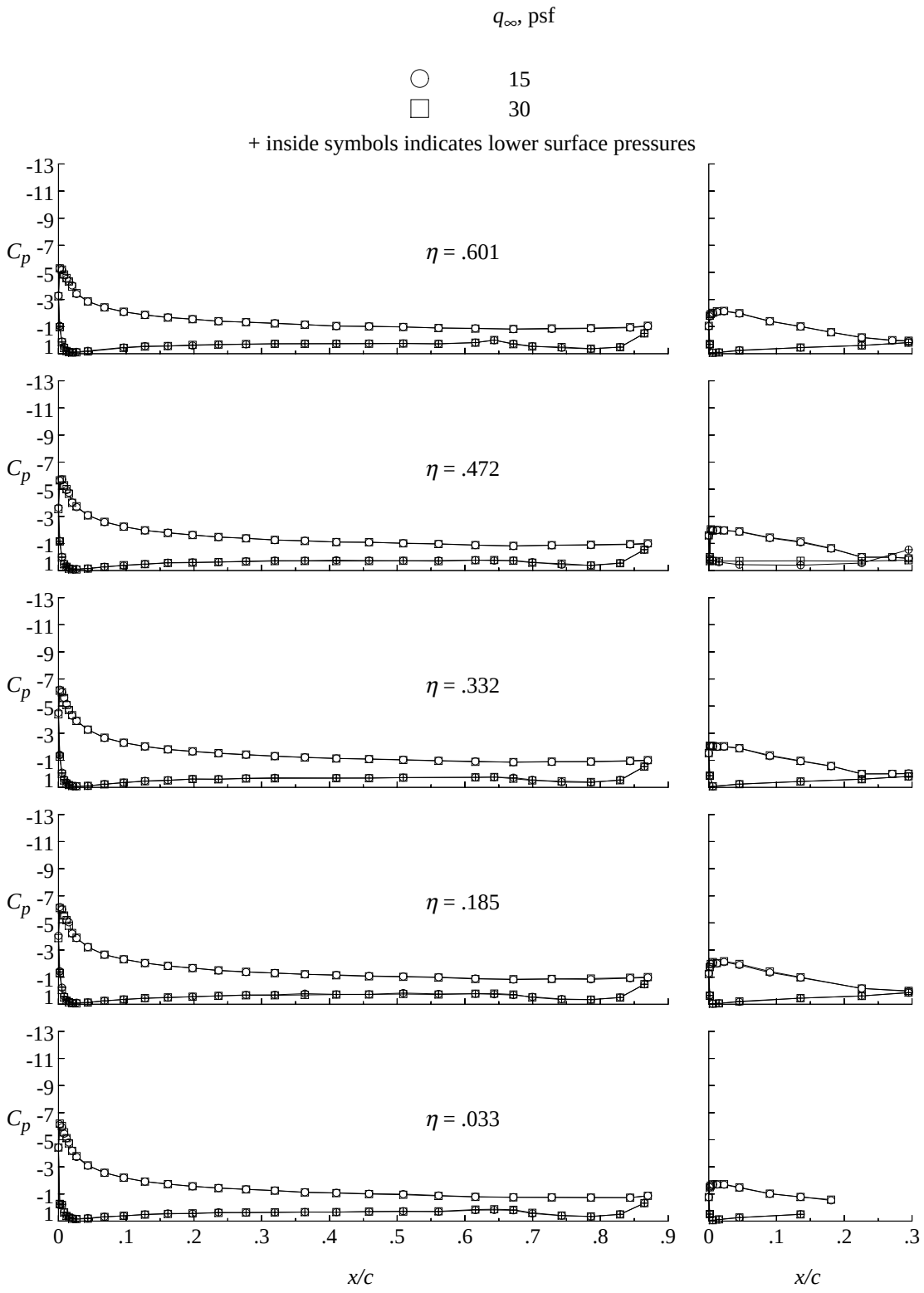


(d) $\alpha = 8°$.

Figure 9. Continued.

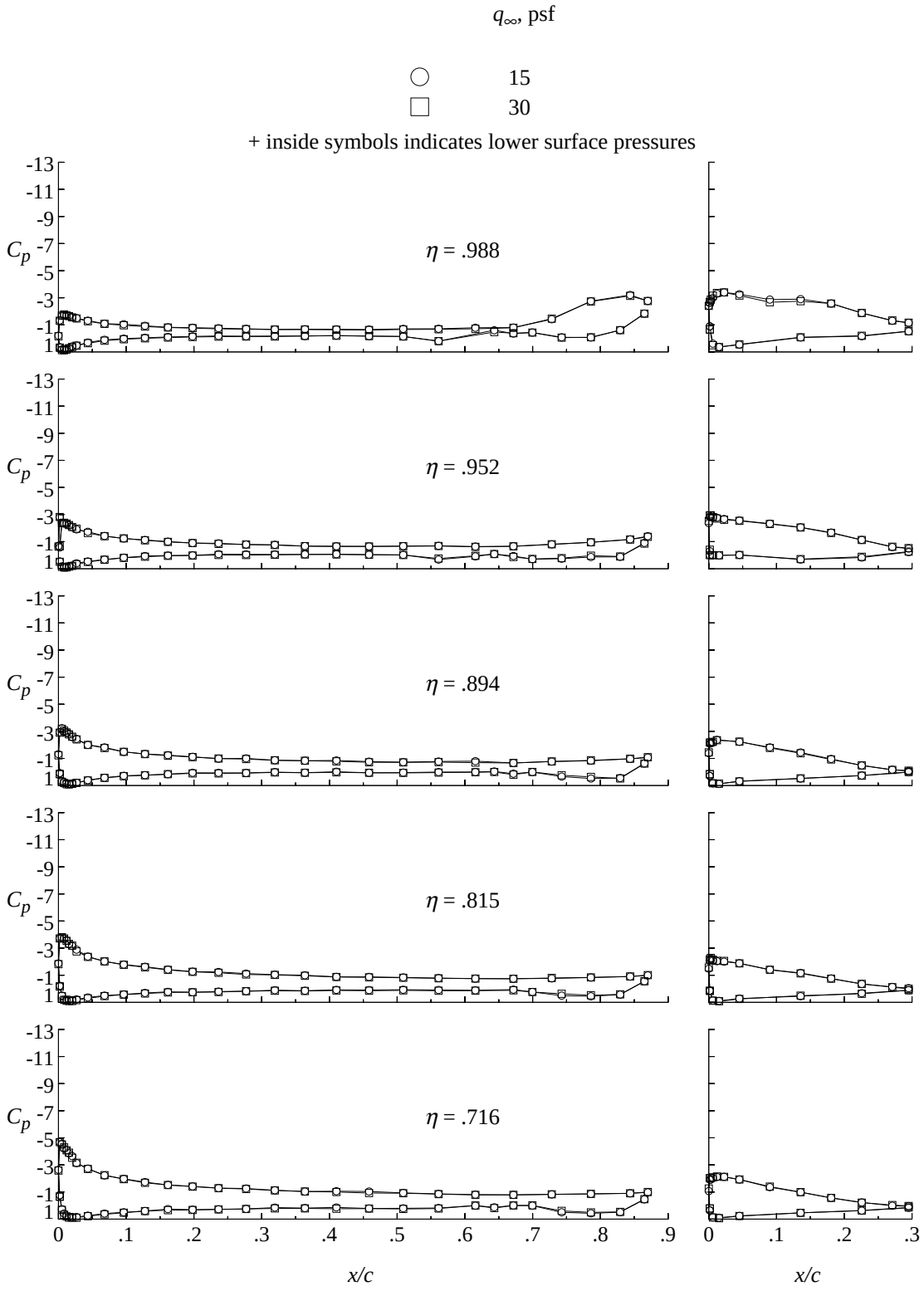


(d) Concluded.

Figure 9. Concluded.

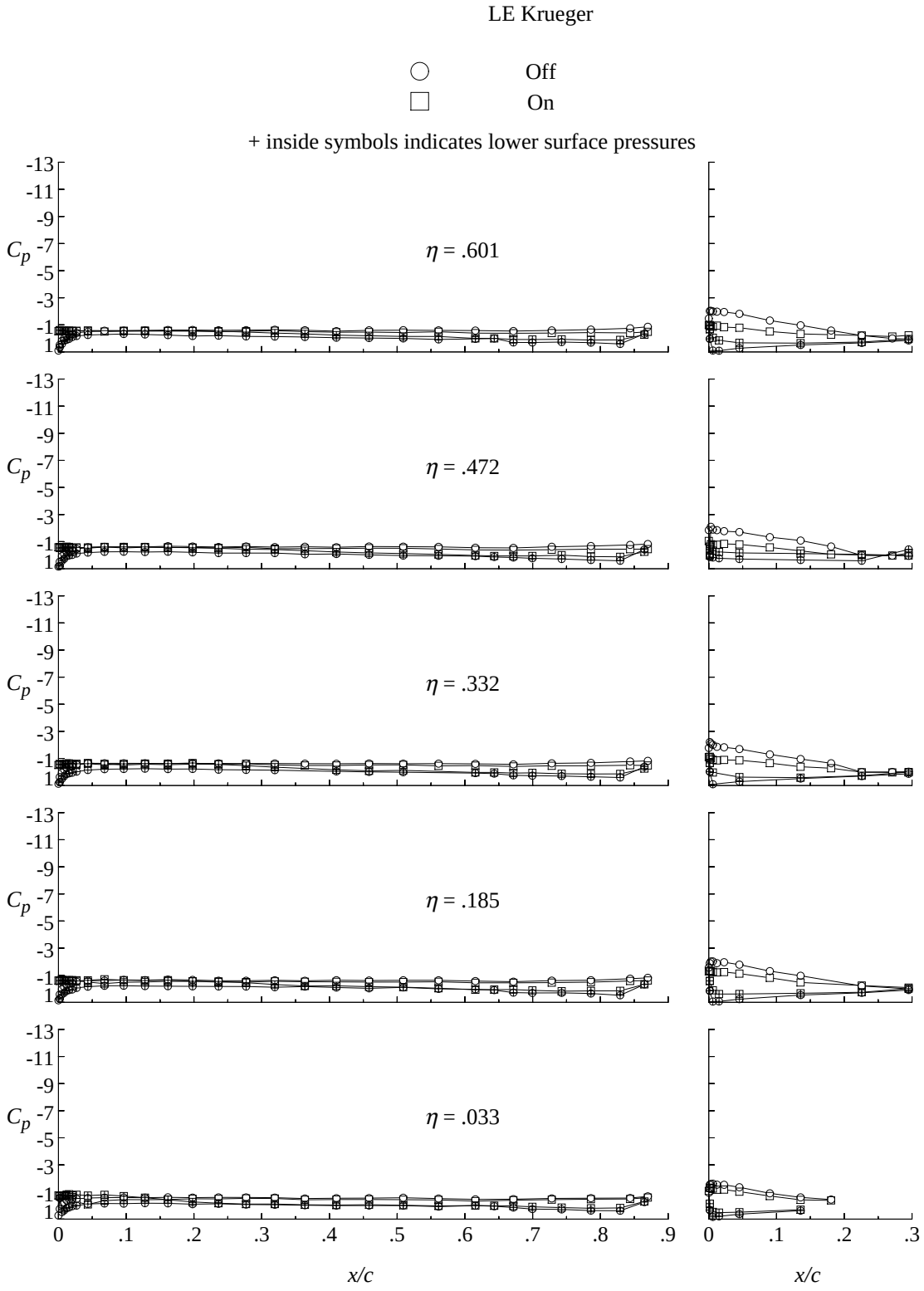


(a) $\alpha$ = - 4°.

Figure 10. Effect of leading-edge Krueger flap on wing pressure distribution. Tunnel floor boundary layer suction on, $q_\infty$ = 15 psf.

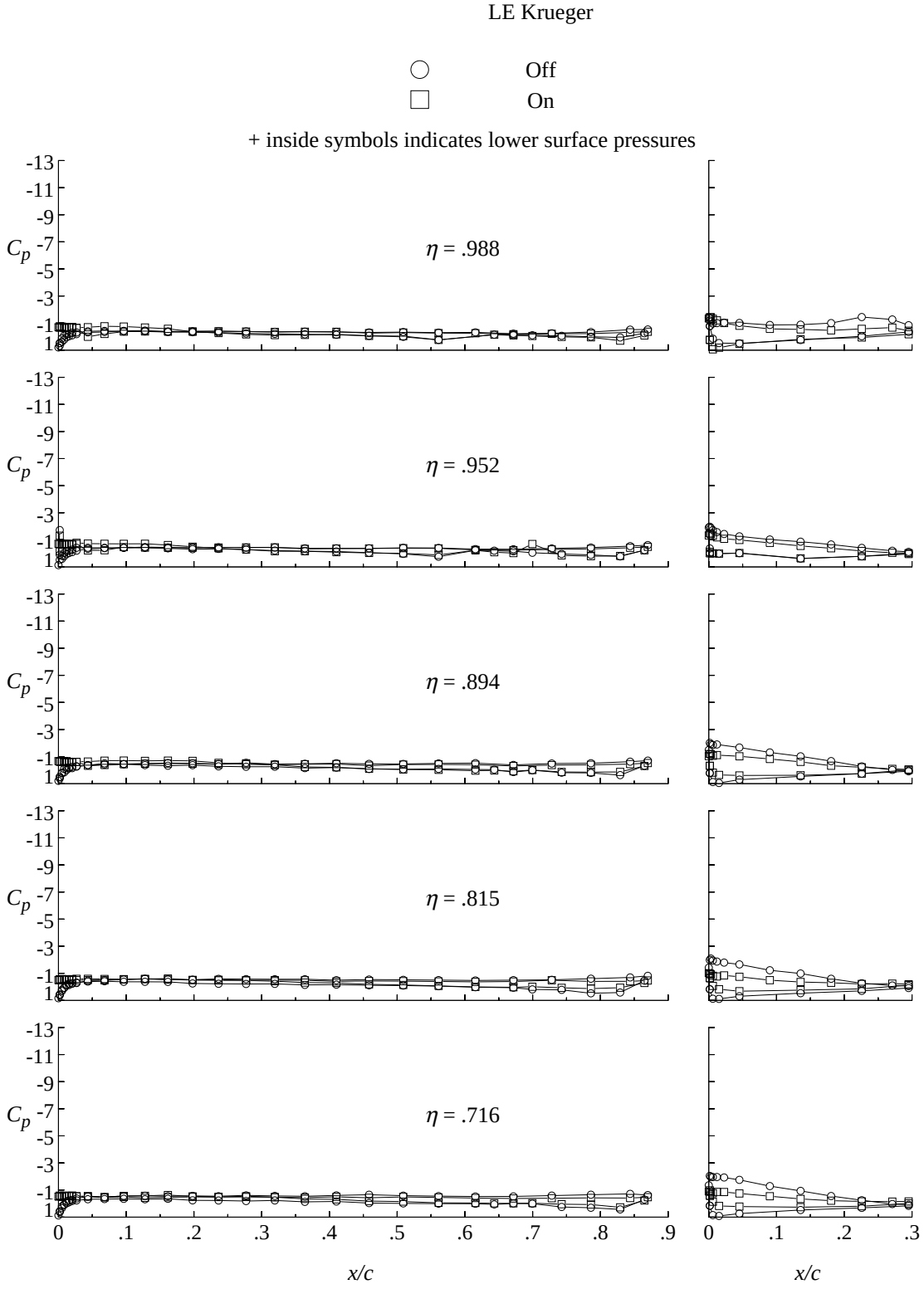


(a) Concluded.

Figure 10. Continued.

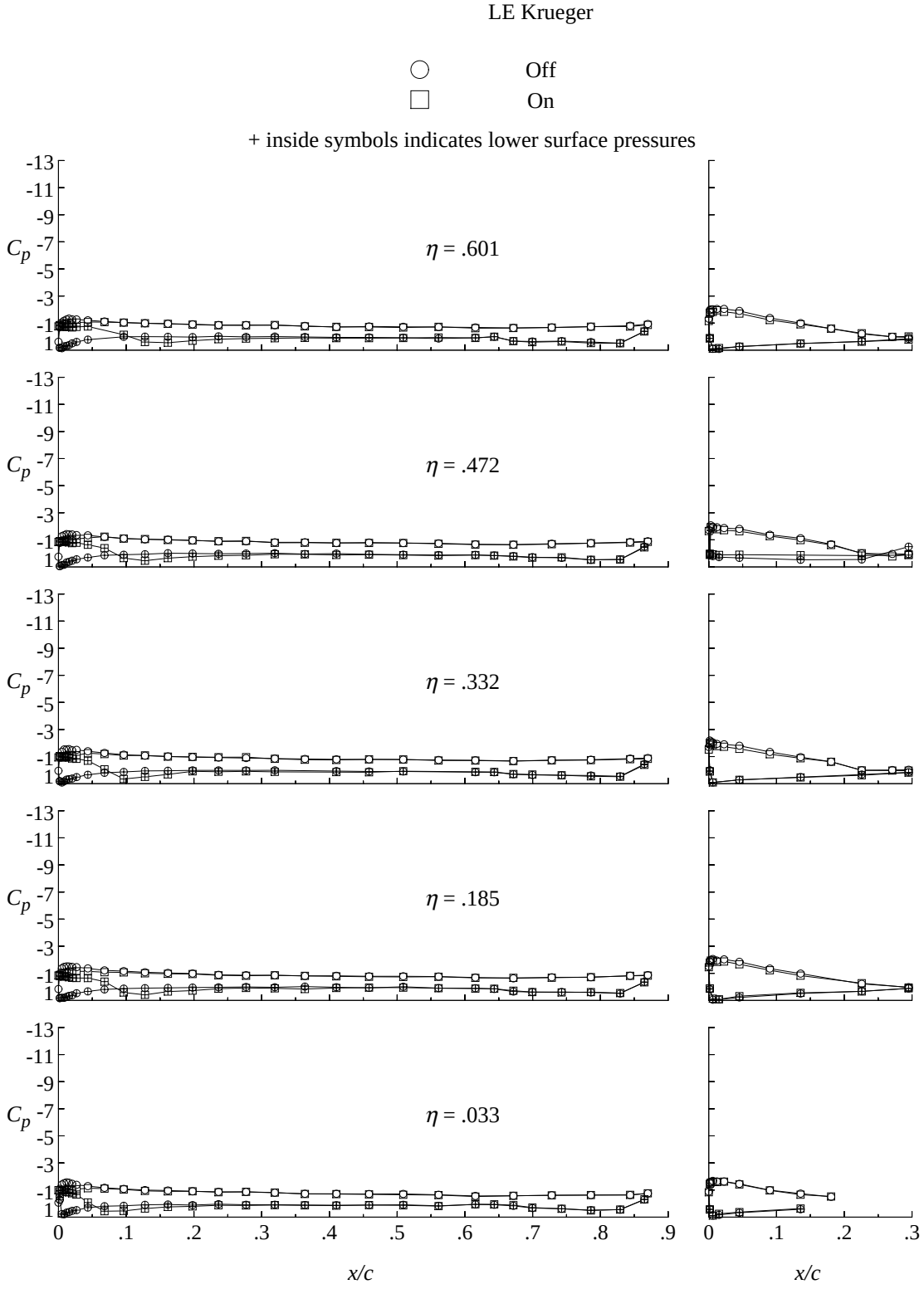


(b) $\alpha = 0°$.

Figure 10. Continued.

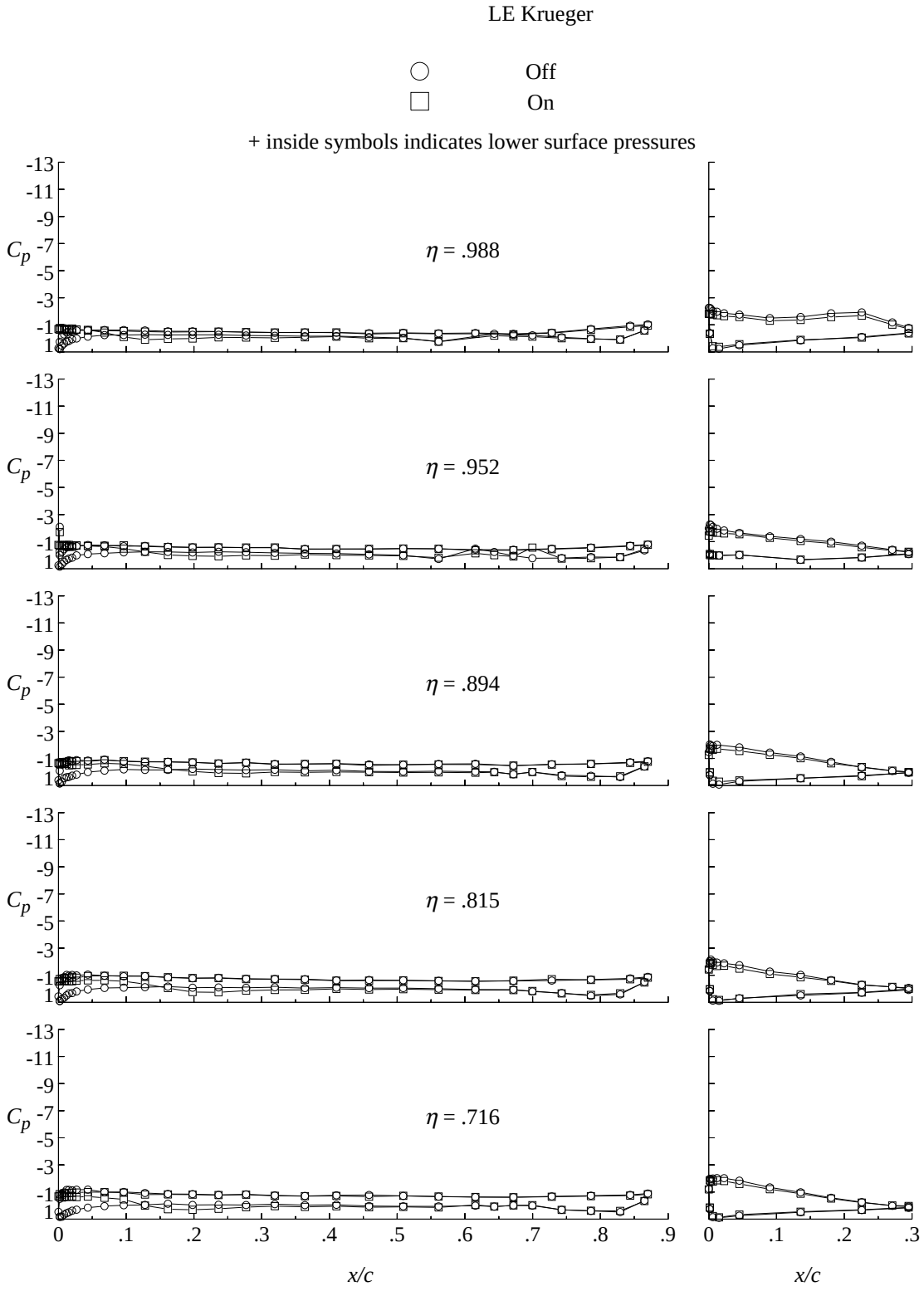


(b) Concluded.

Figure 10. Continued.

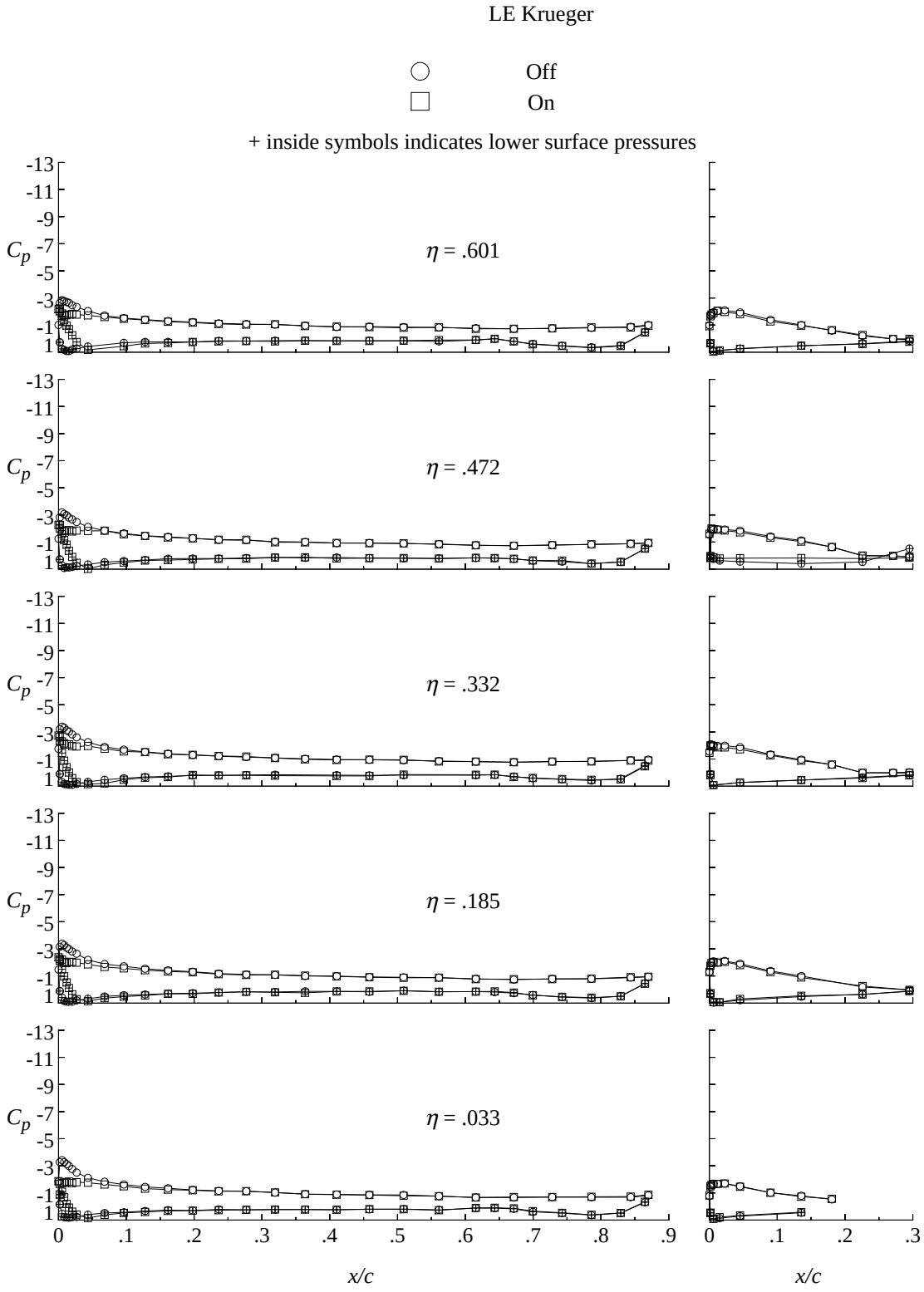


(c) $\alpha = 4°$.

Figure 10. Continued.

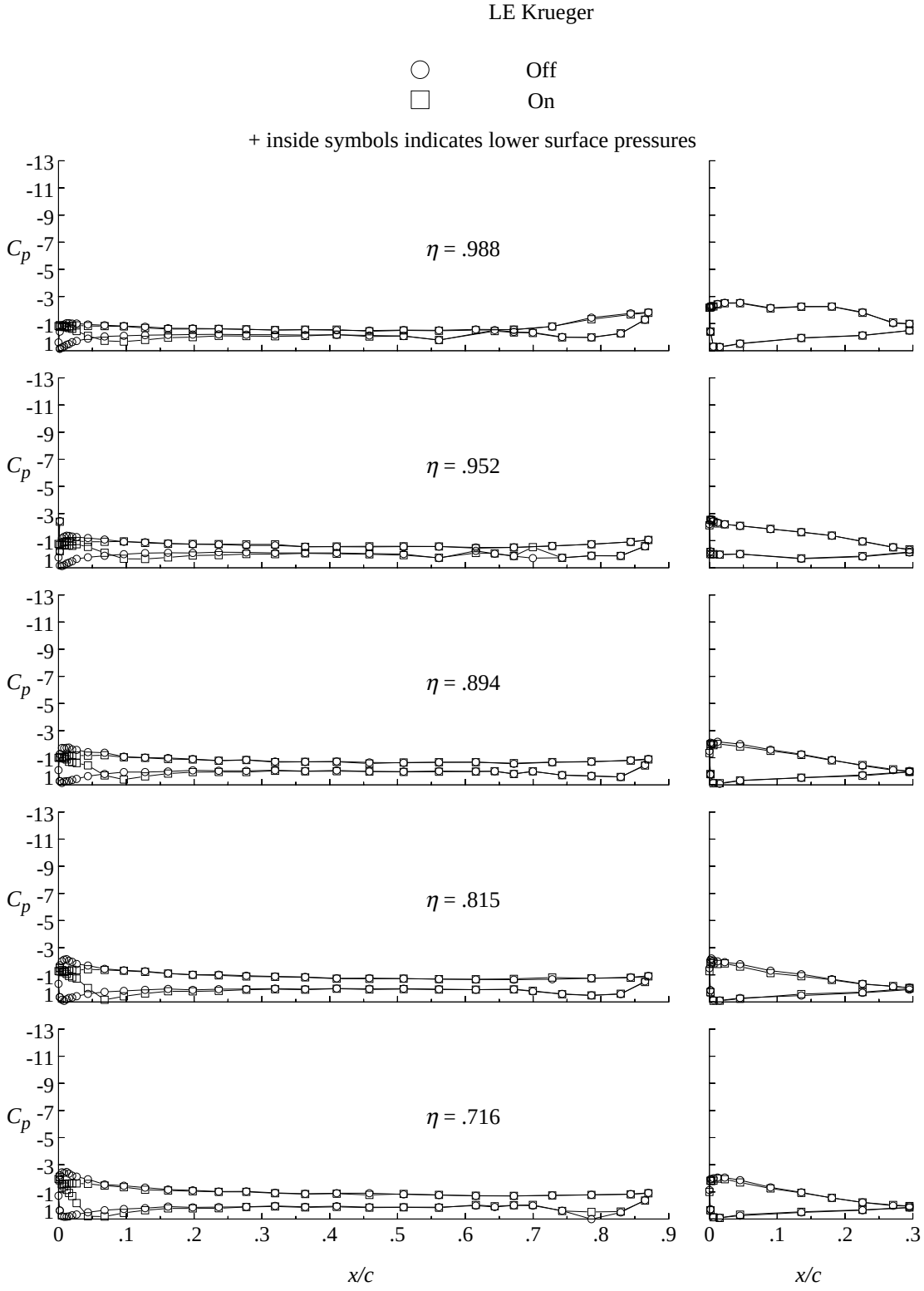


(c) Concluded.

Figure 10. Continued.

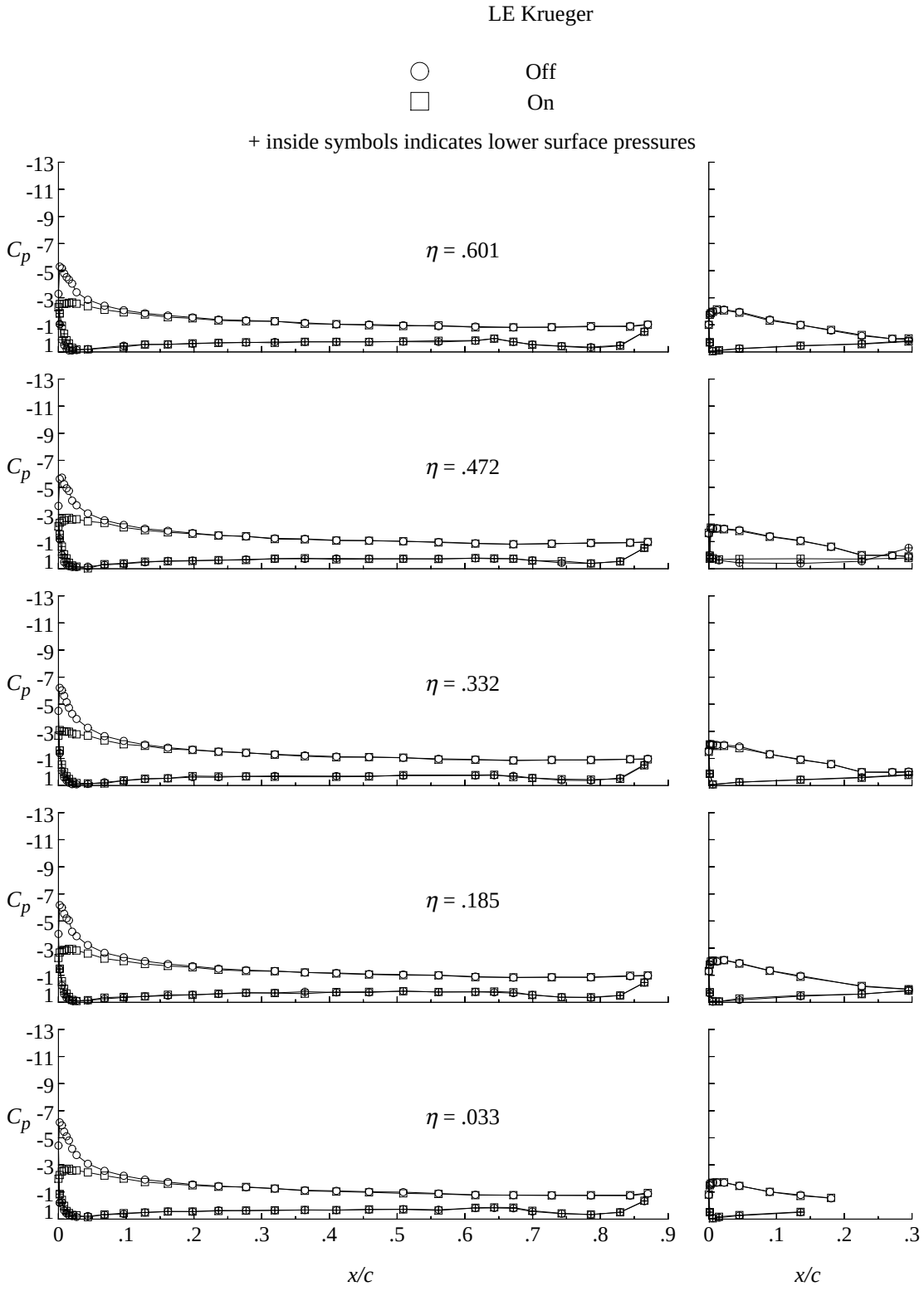


(d) $\alpha = 8°$.

Figure 10. Continued.

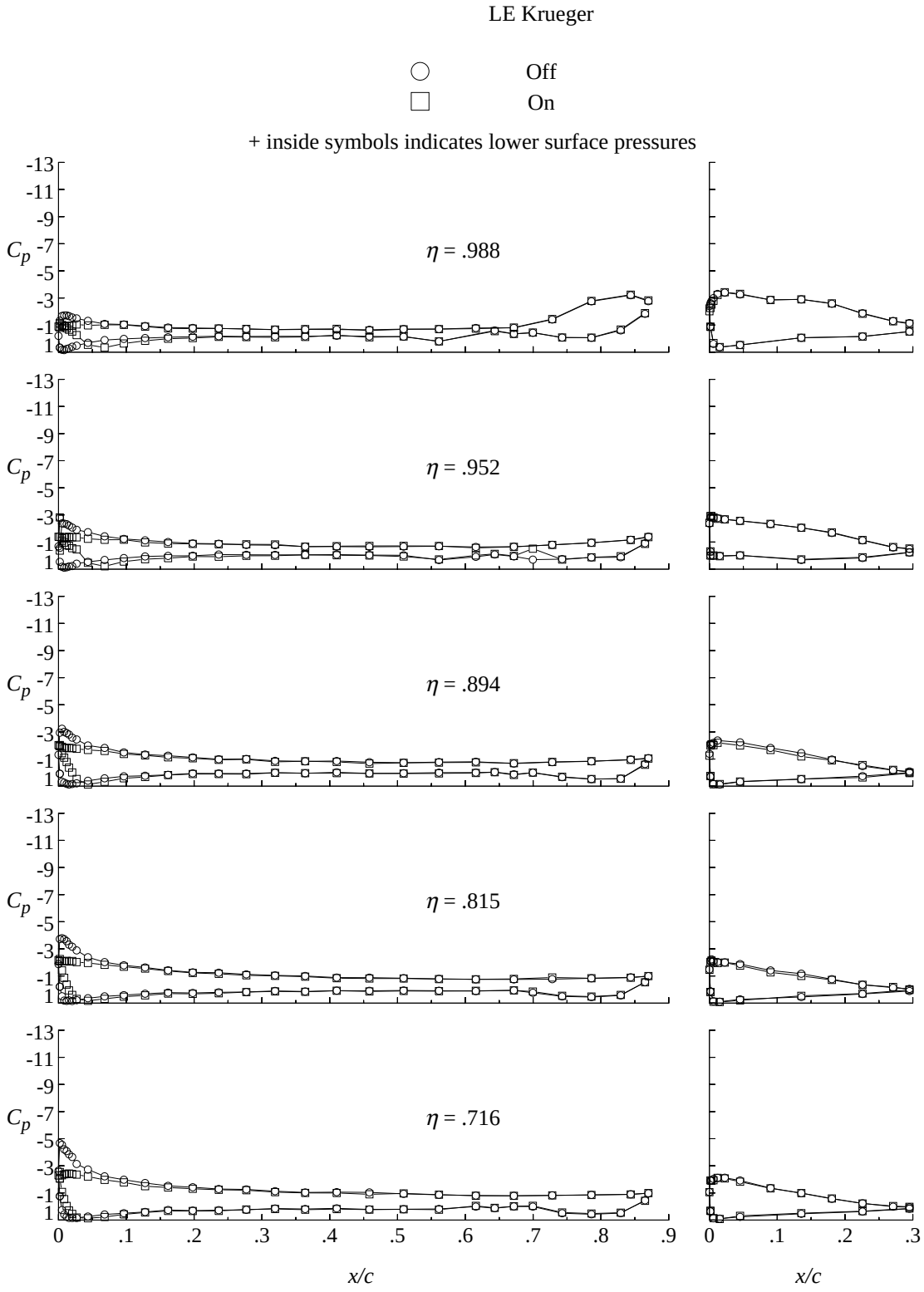


(d) Concluded.

Figure 10. Continued.

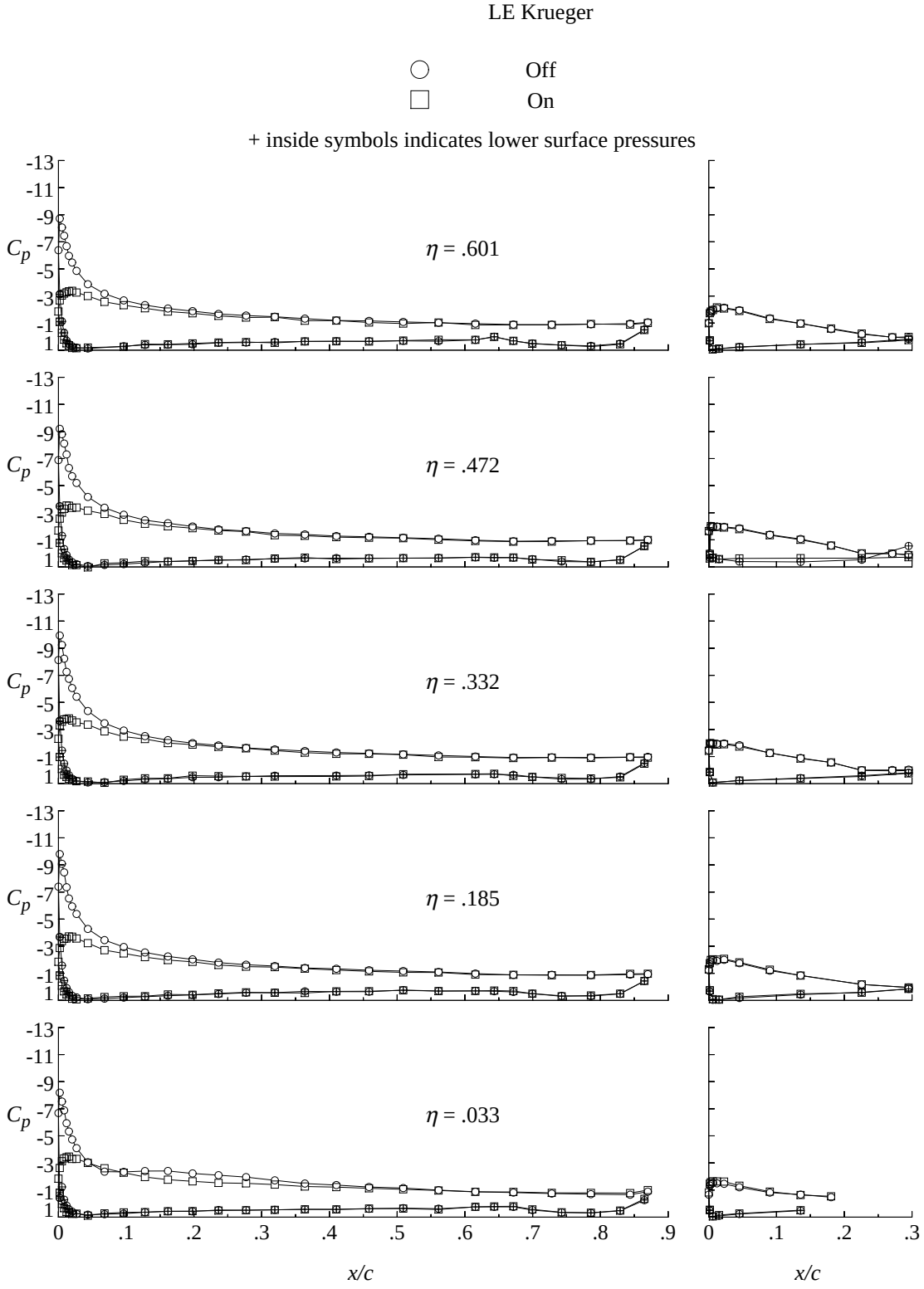


(e) $\alpha = 12°$.

Figure 10. Continued.

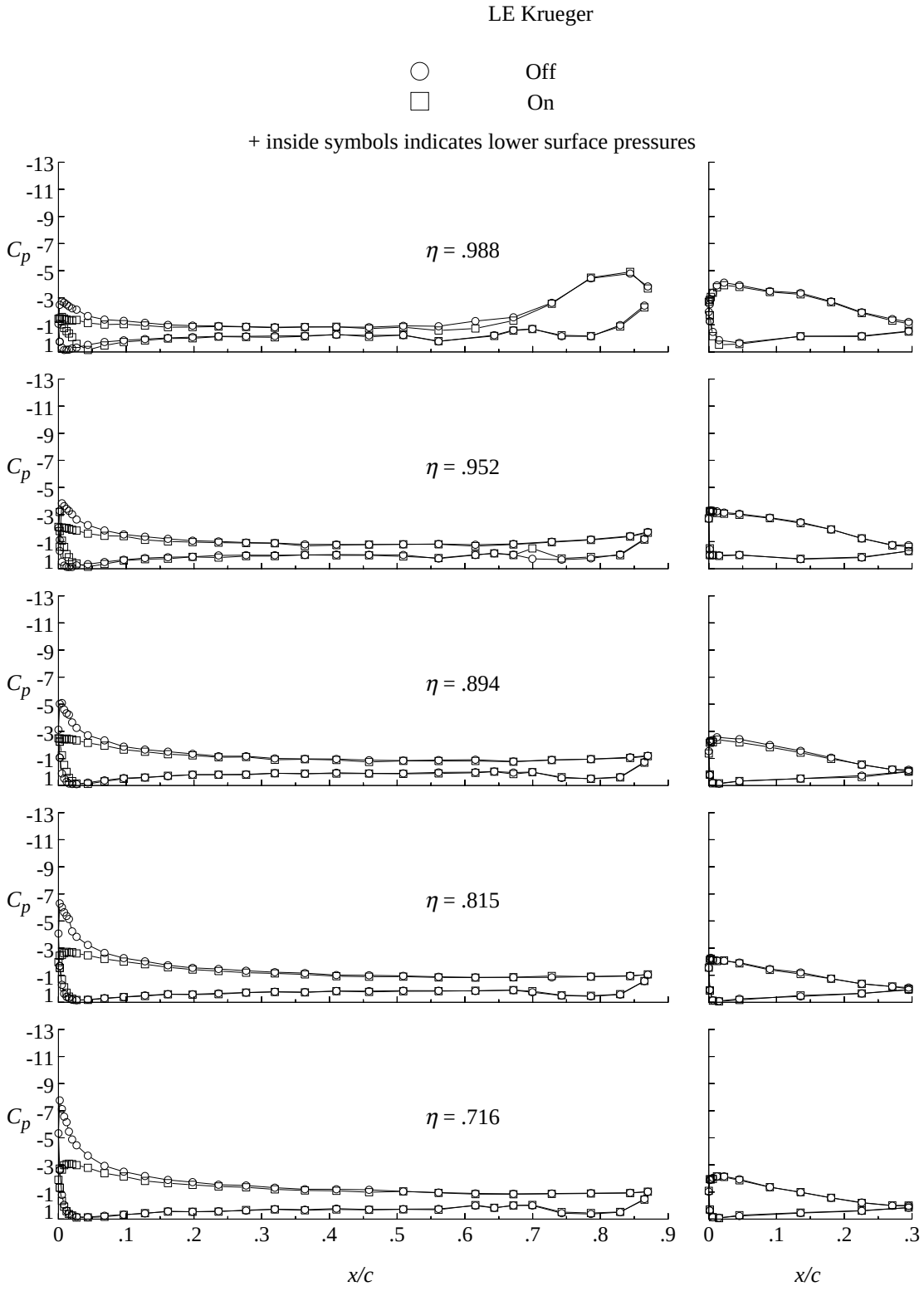


(e) Concluded.

Figure 10. Continued.

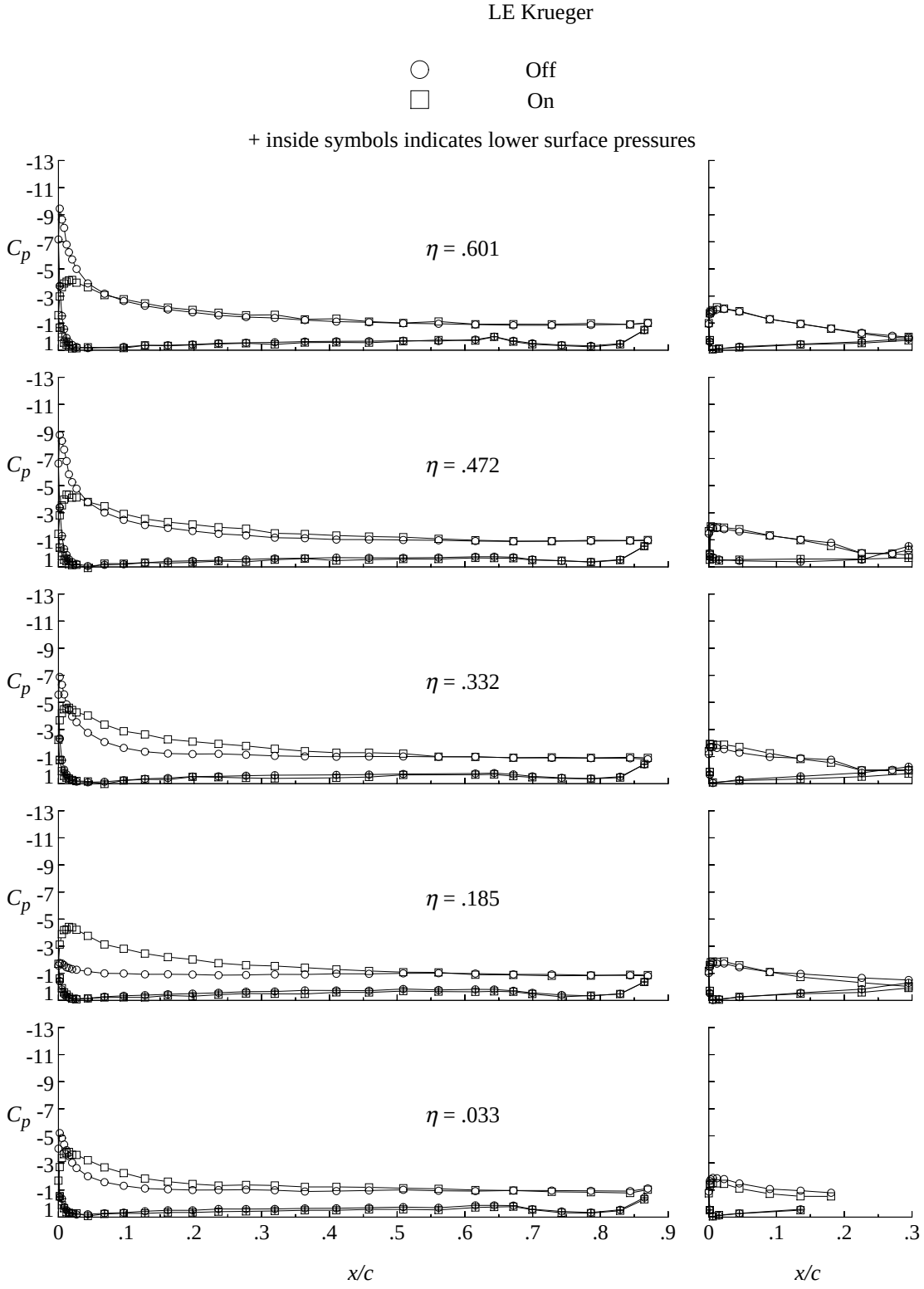


(f) $\alpha = 16°$.

Figure 10. Continued.

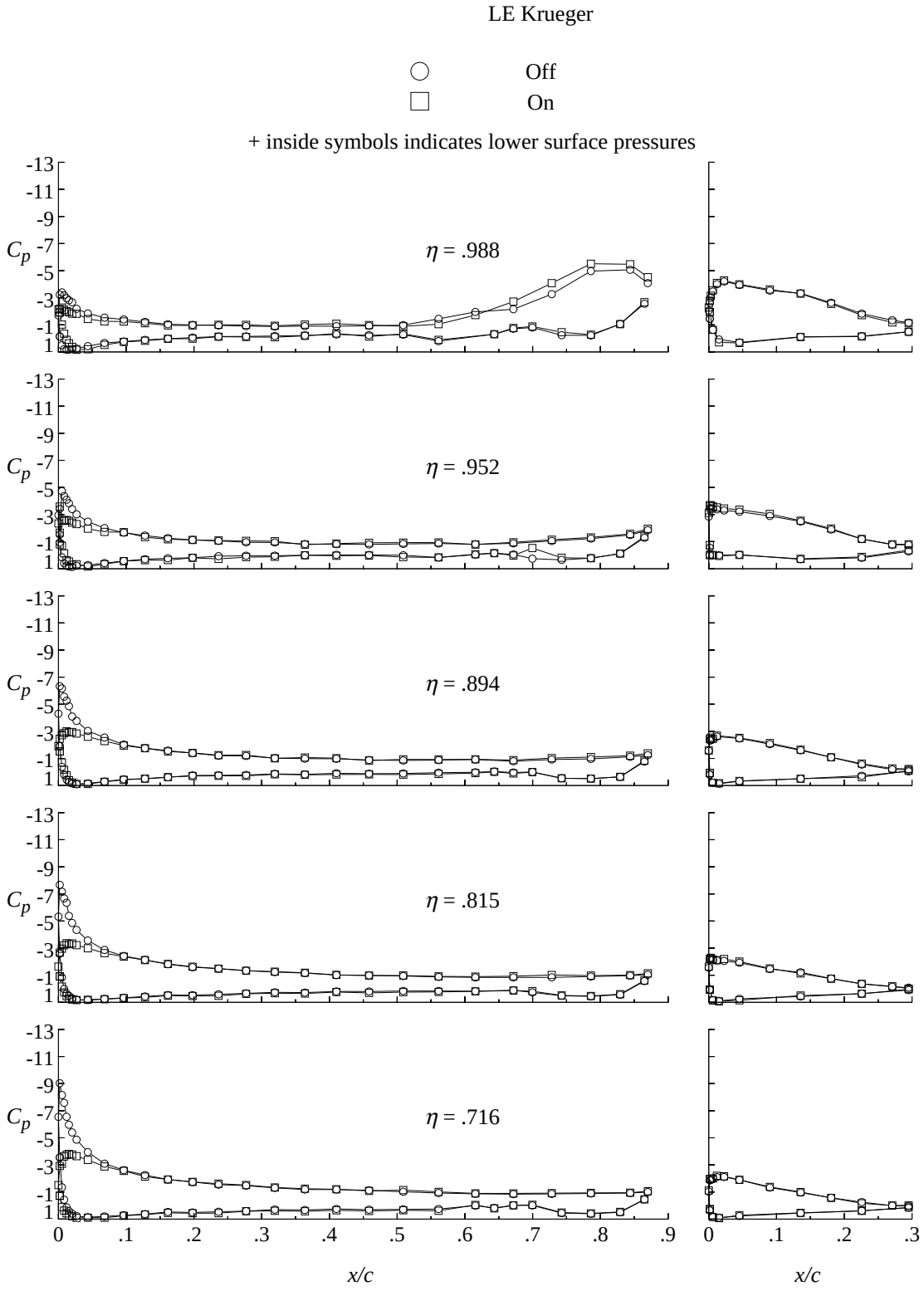


(f) Concluded.

Figure 10. Continued.

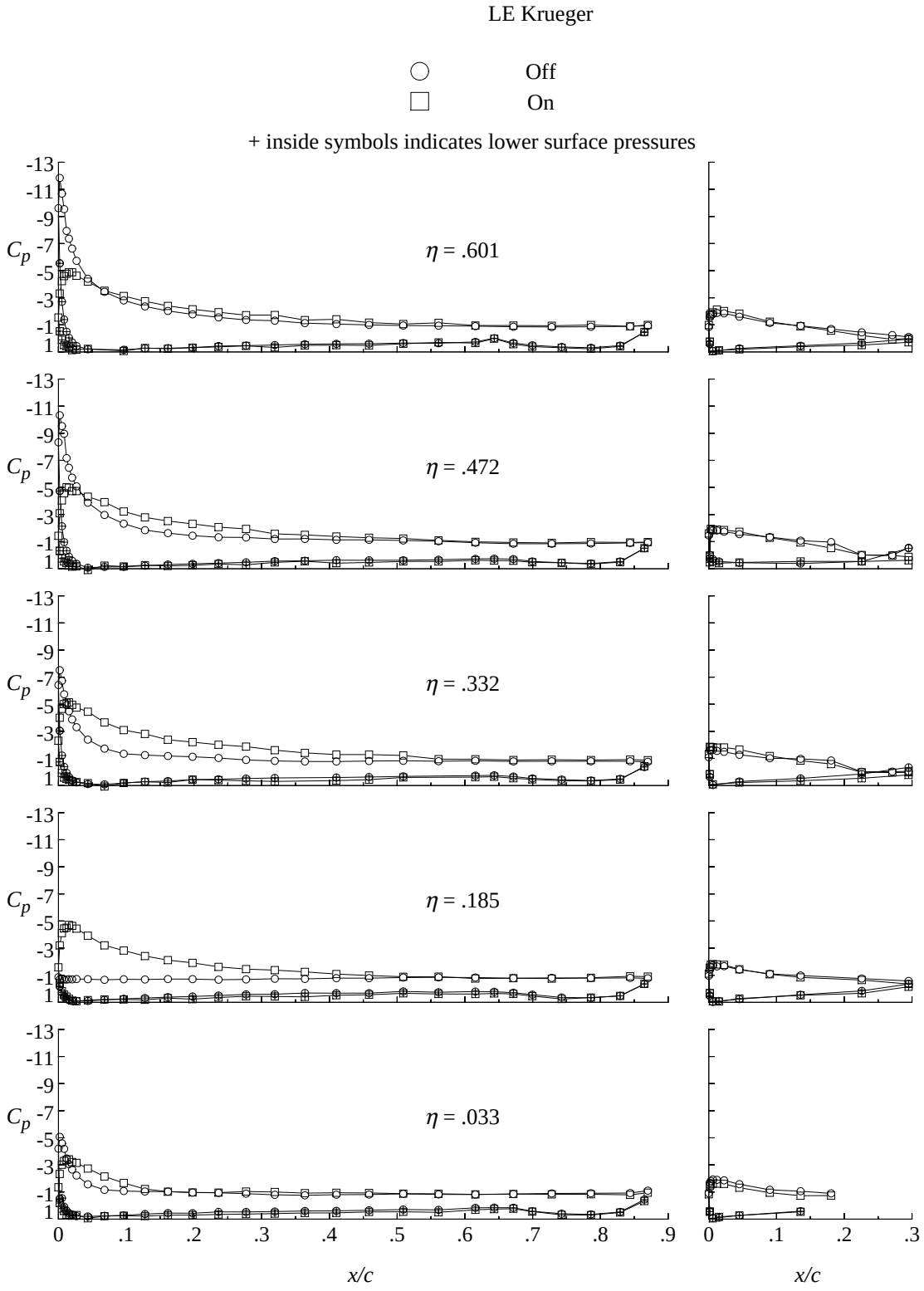


(g) $\alpha = 20°$.

Figure 10. Continued.

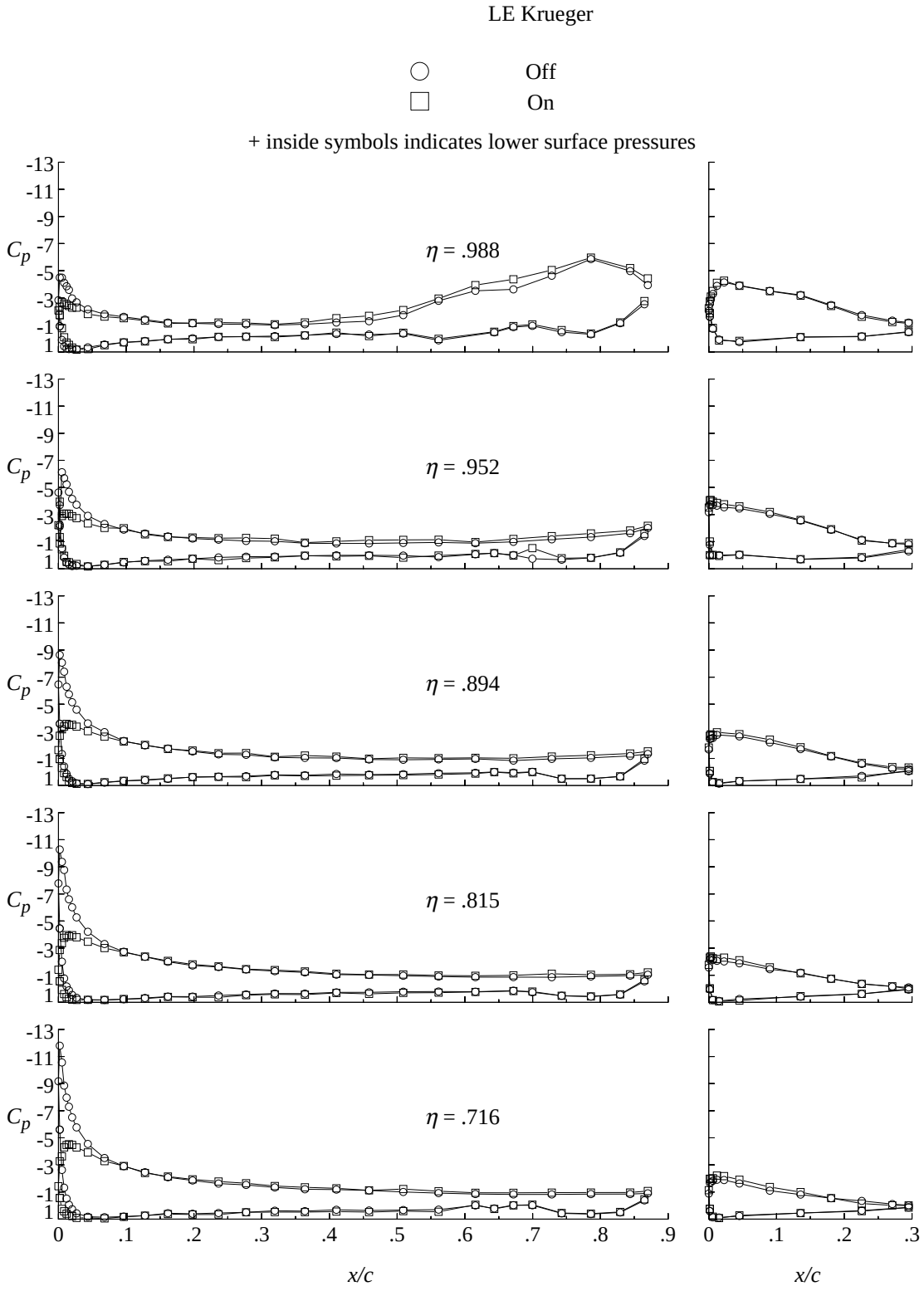


(g) Concluded.

Figure 10. Concluded.

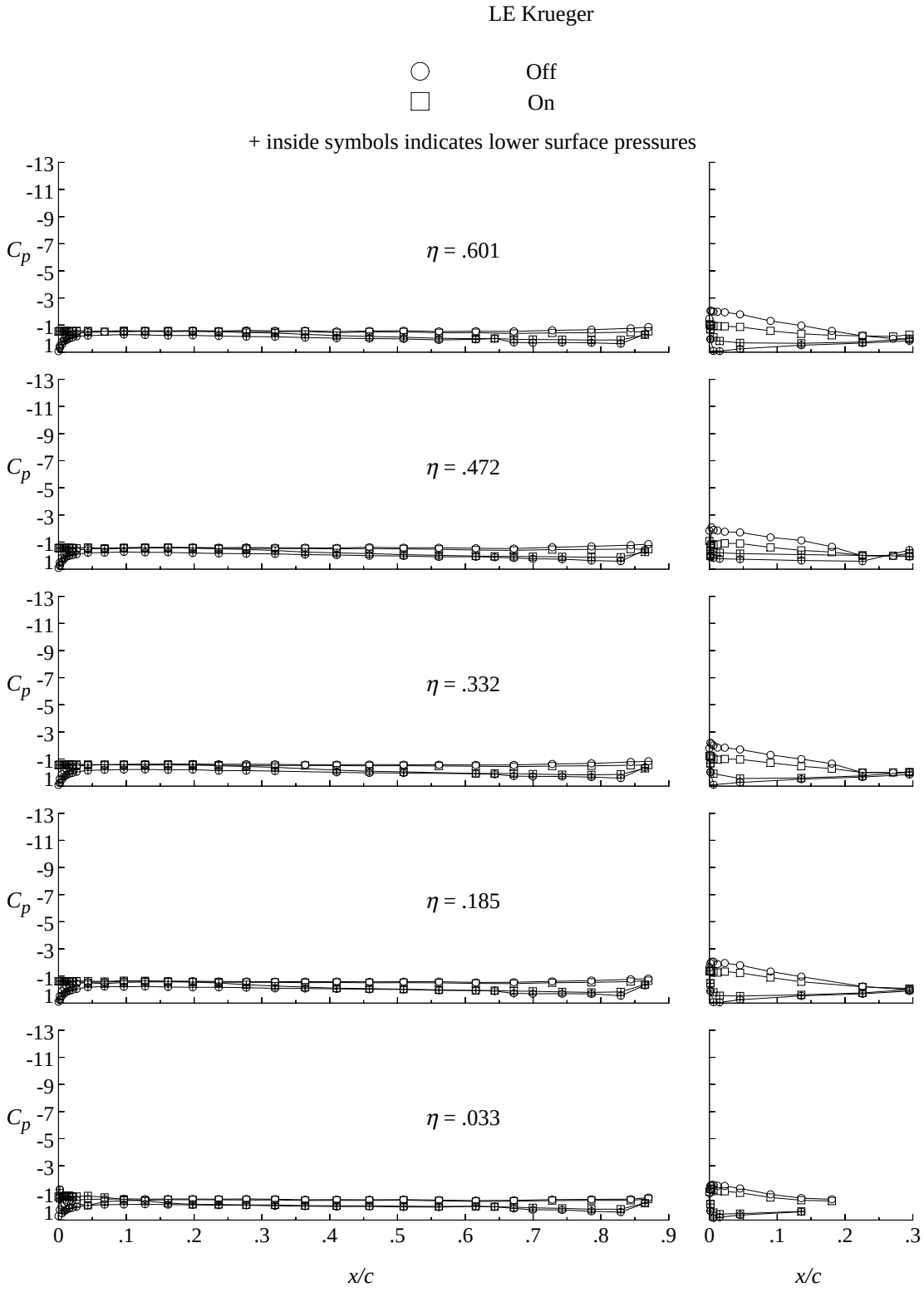


(a) $\alpha$ = - 4°.

Figure 11. Effect of leading-edge Krueger flap on wing pressure distribution. Tunnel floor boundary layer suction on, $q_\infty$ = 30 psf.

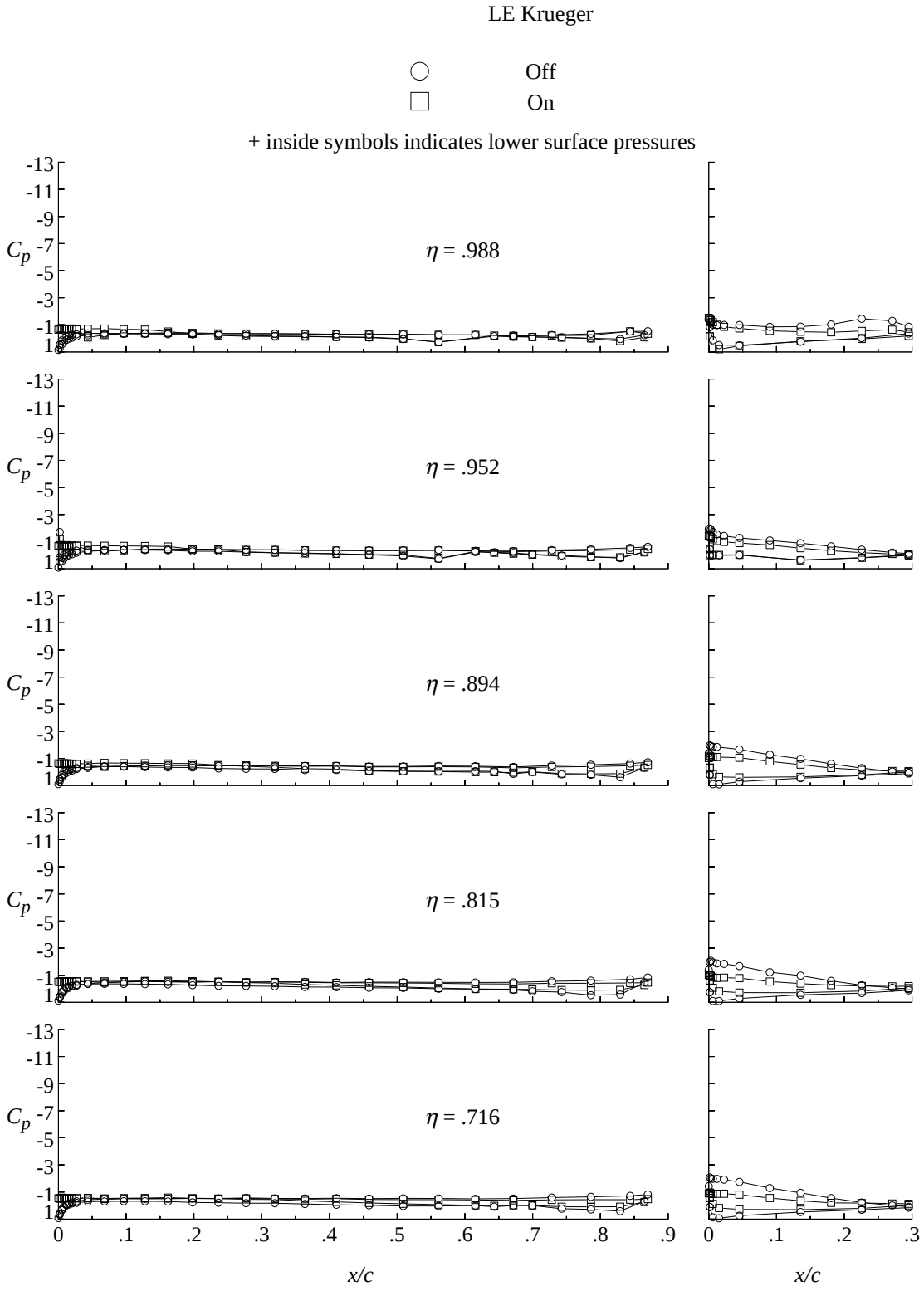


(a) Concluded.

Figure 11. Continued.

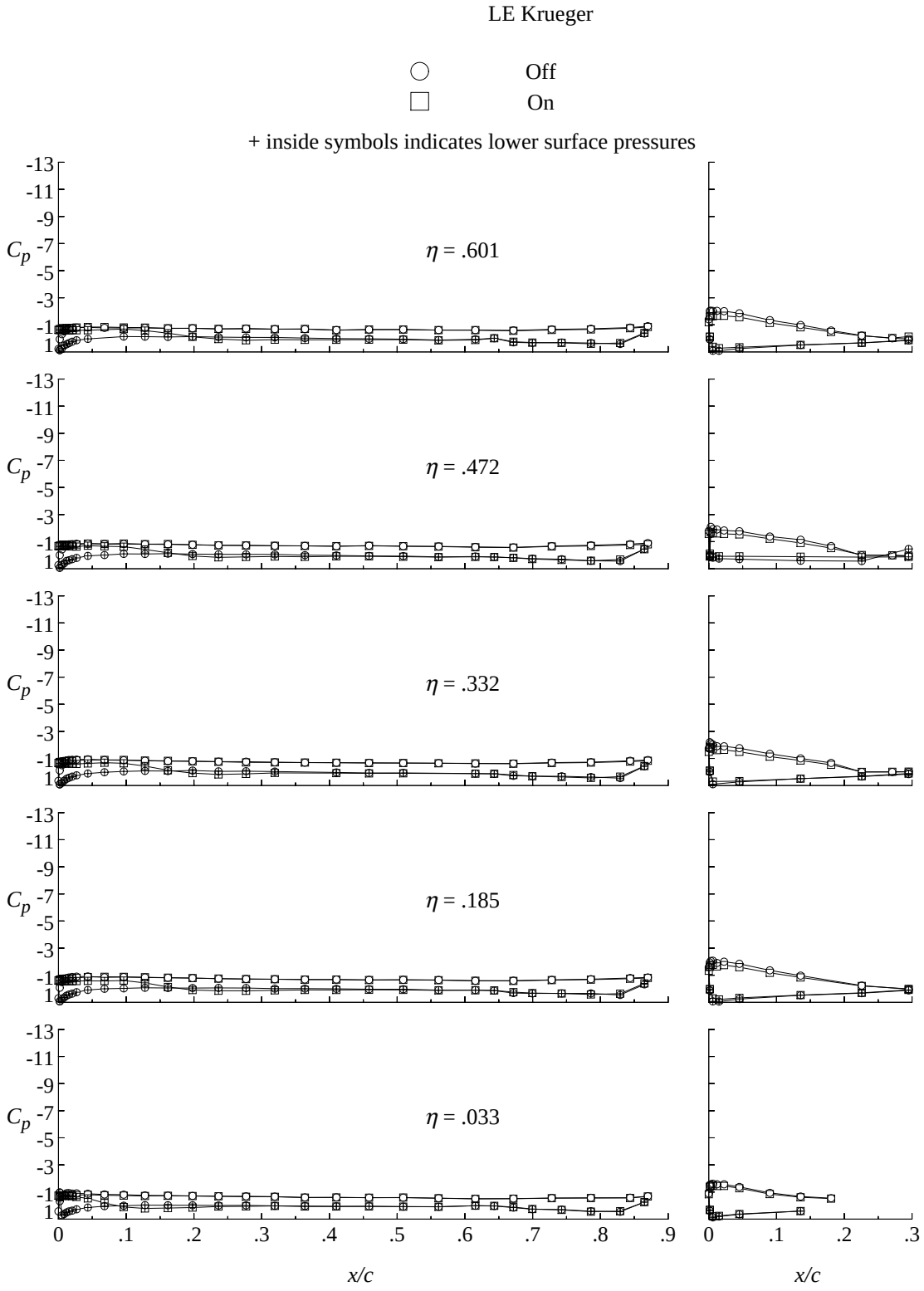


(b) $\alpha$ = - 2°.

Figure 11. Continued.

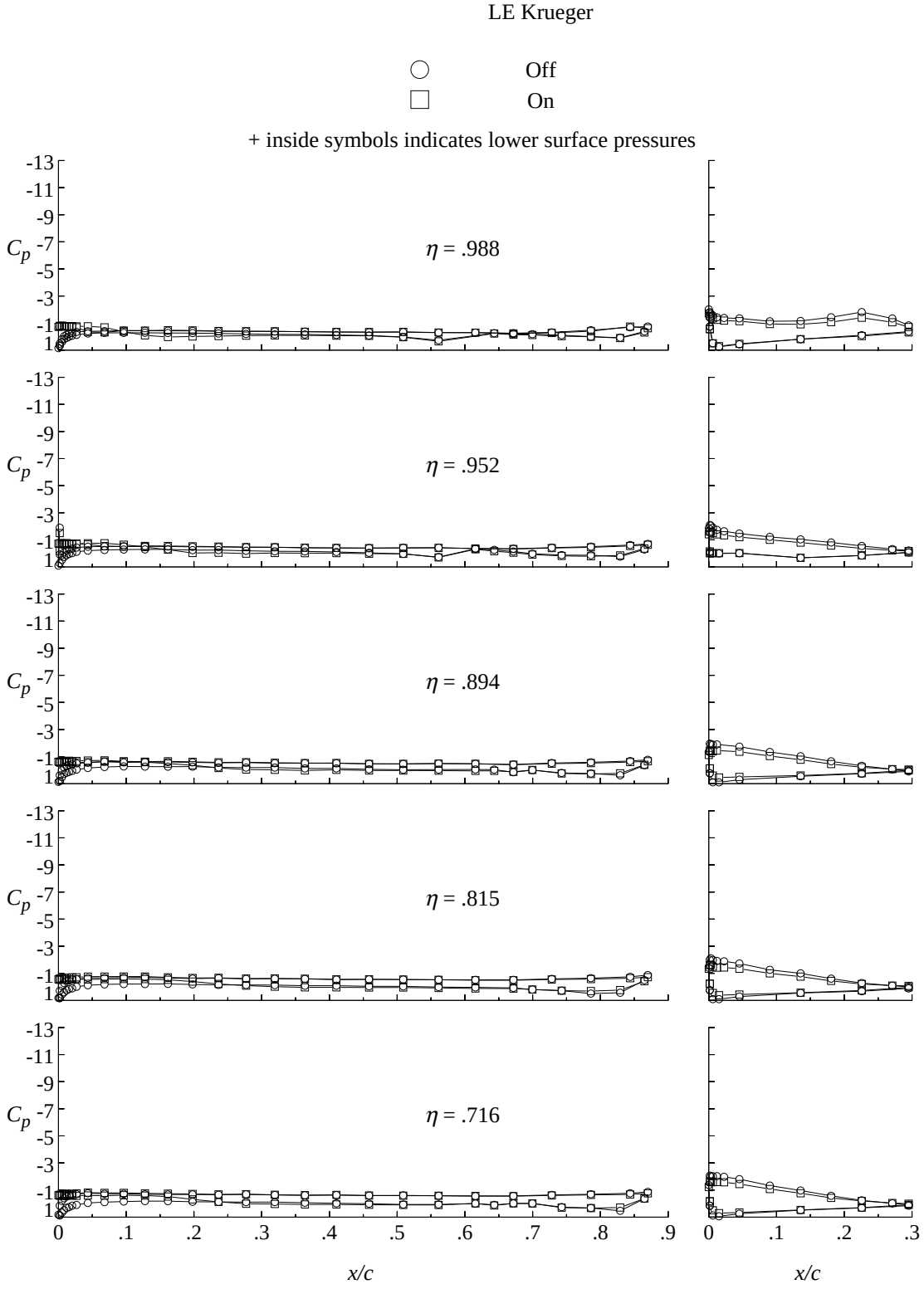


(b) Concluded.

Figure 11. Continued.

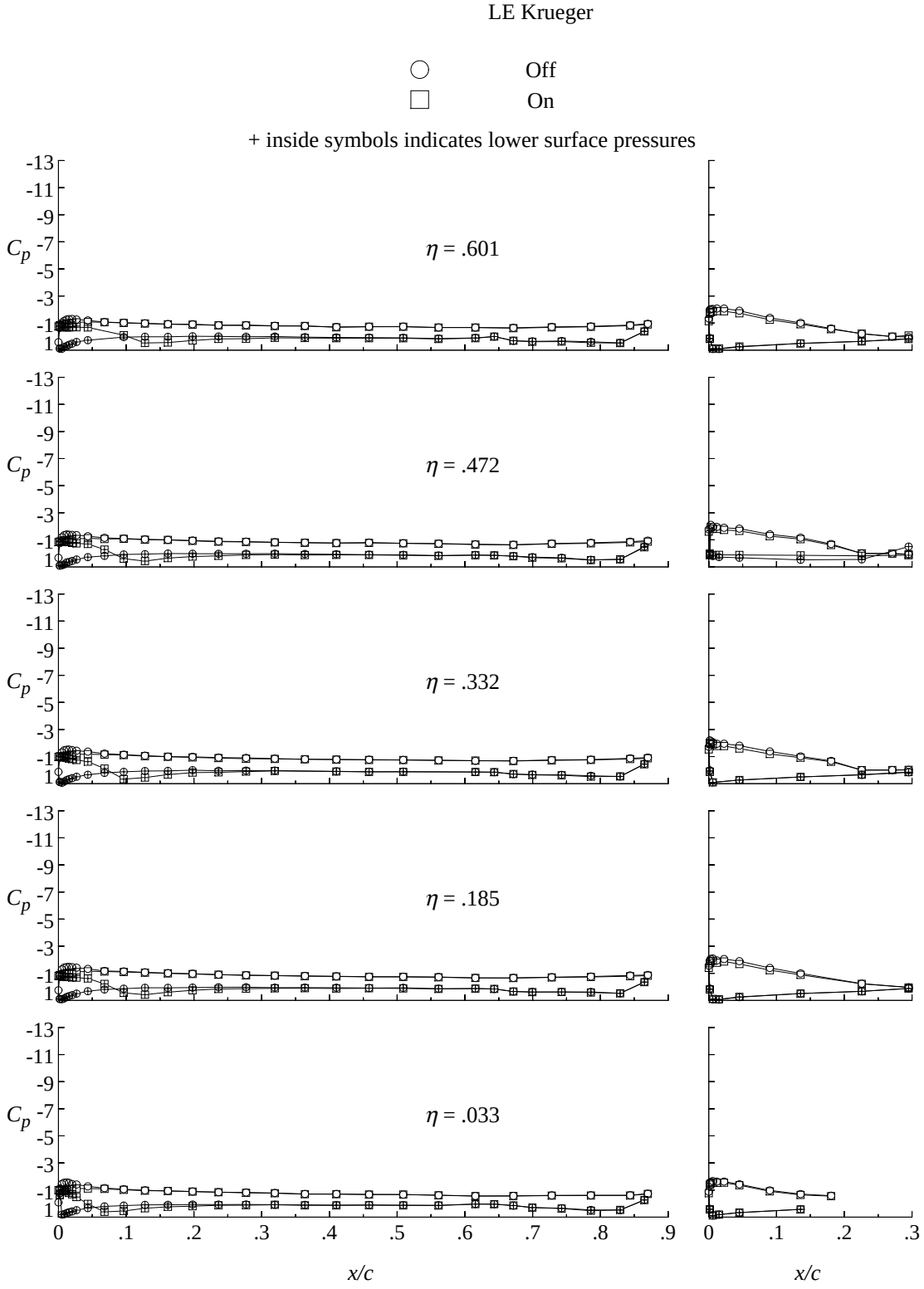


(c) $\alpha = 0°$.

Figure 11. Continued.

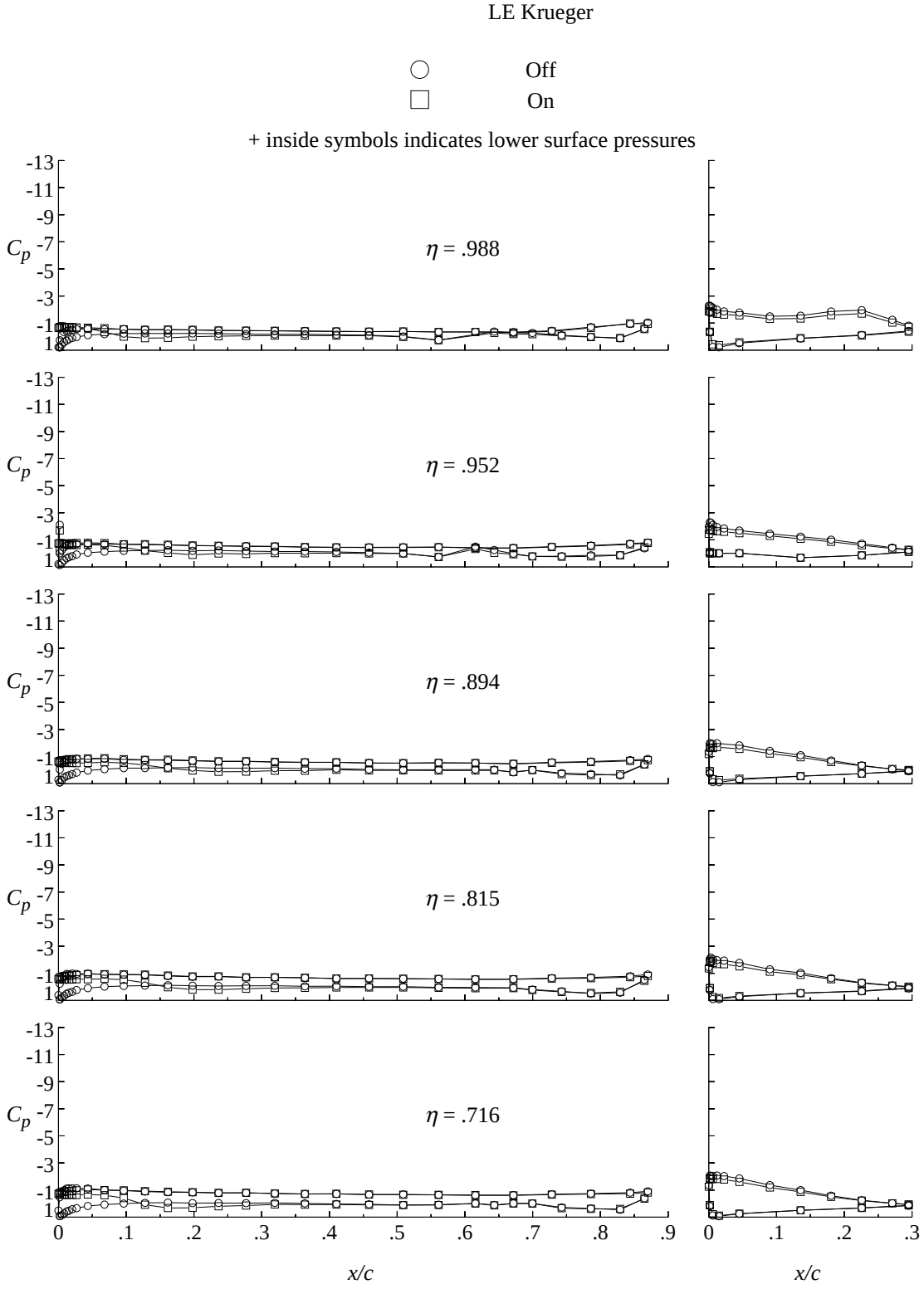


(c) Concluded.

Figure 11. Continued.

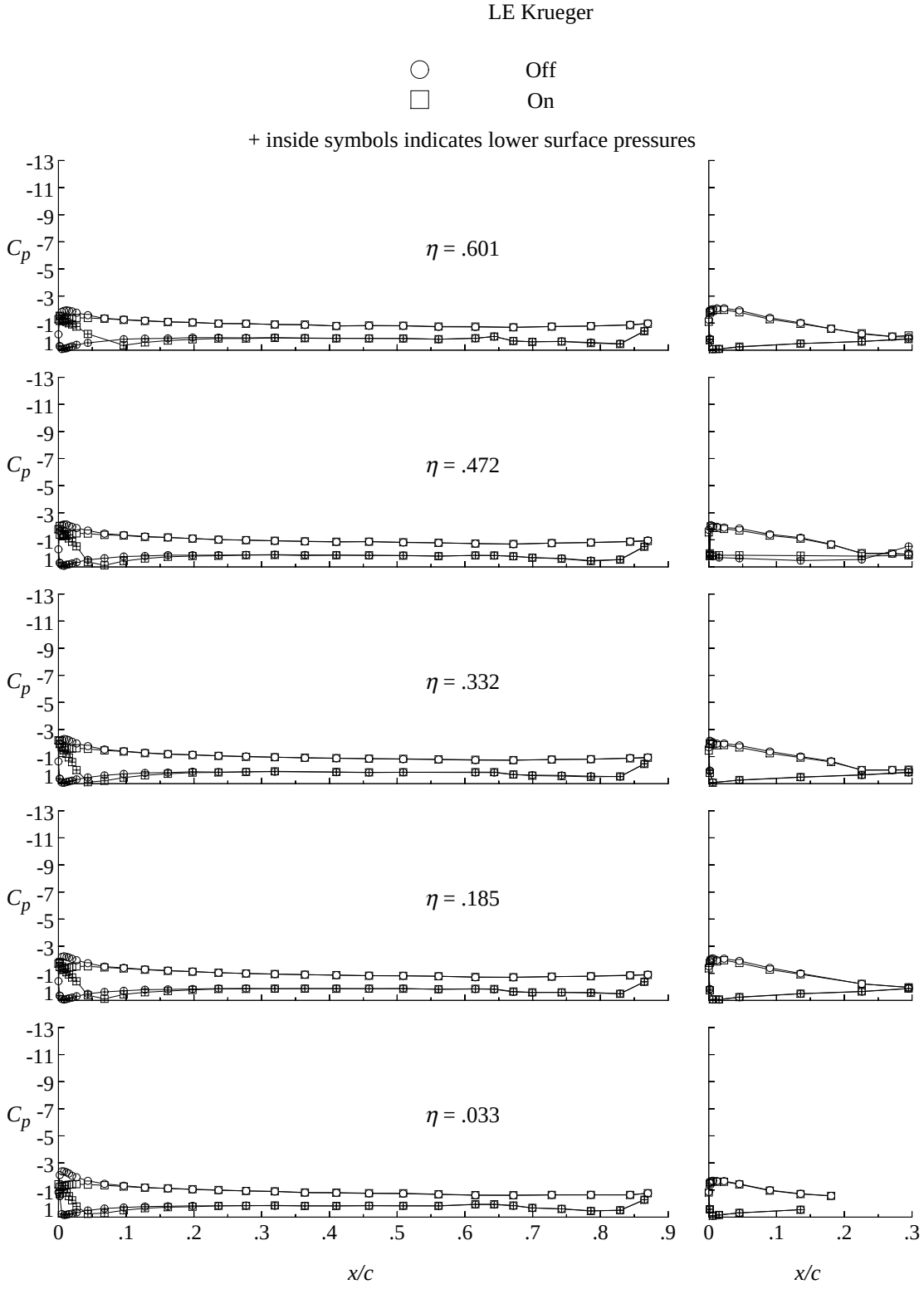


(d) $\alpha = 2°$.

Figure 11. Continued.

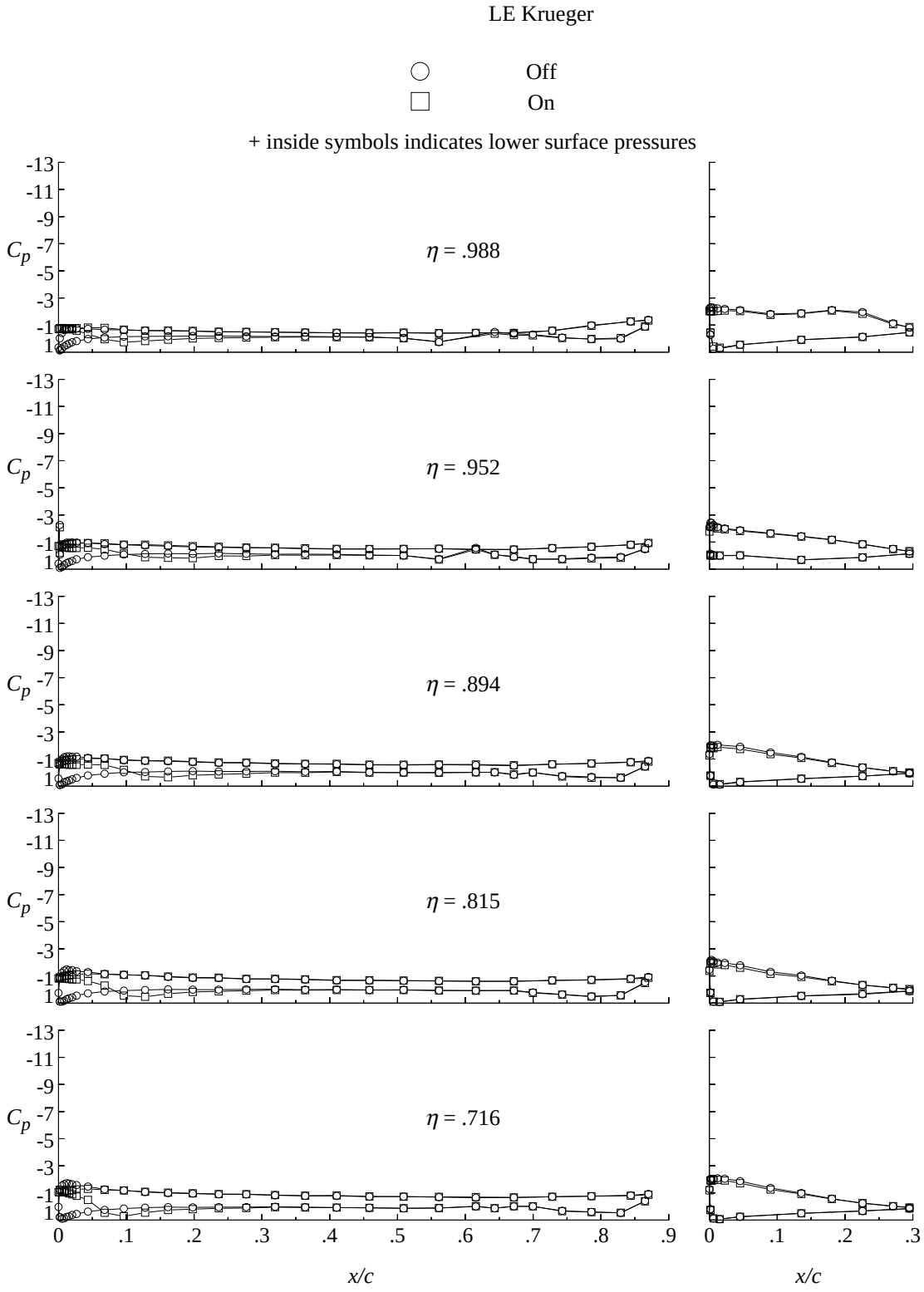


(d) Concluded.

Figure 11. Continued.

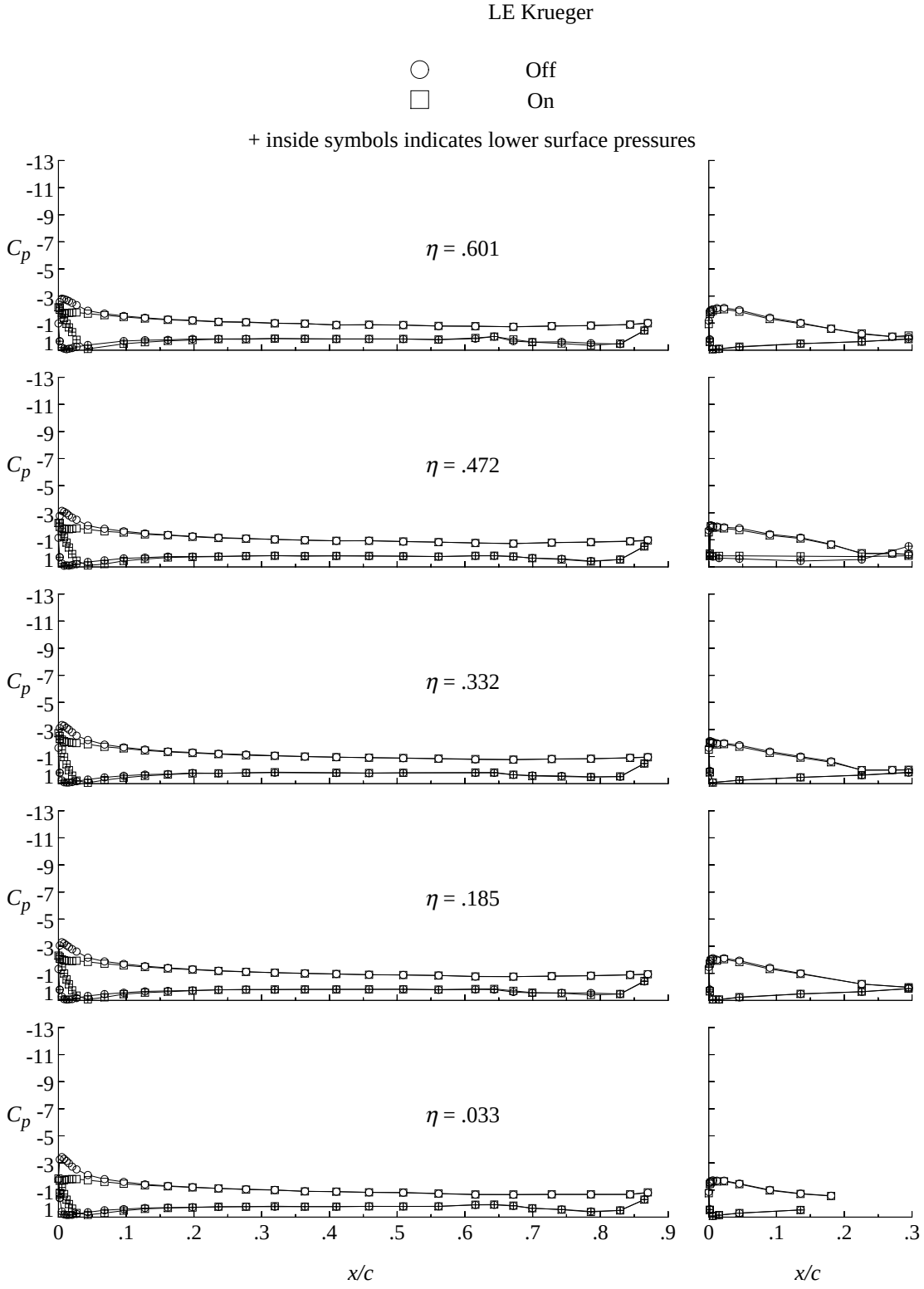


(e) $\alpha = 4°$.

Figure 11. Continued.

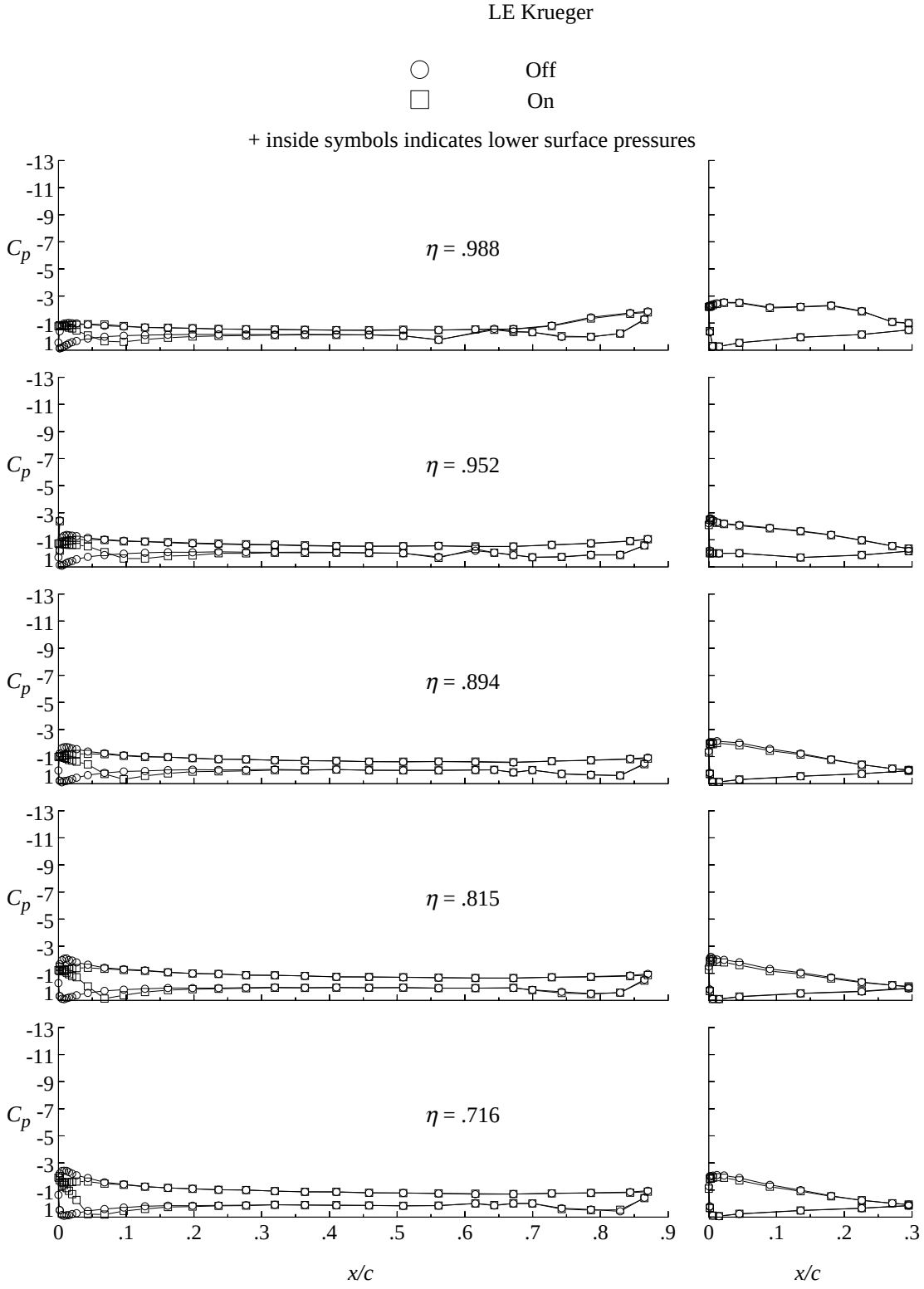


(e) Concluded.

Figure 11. Continued.

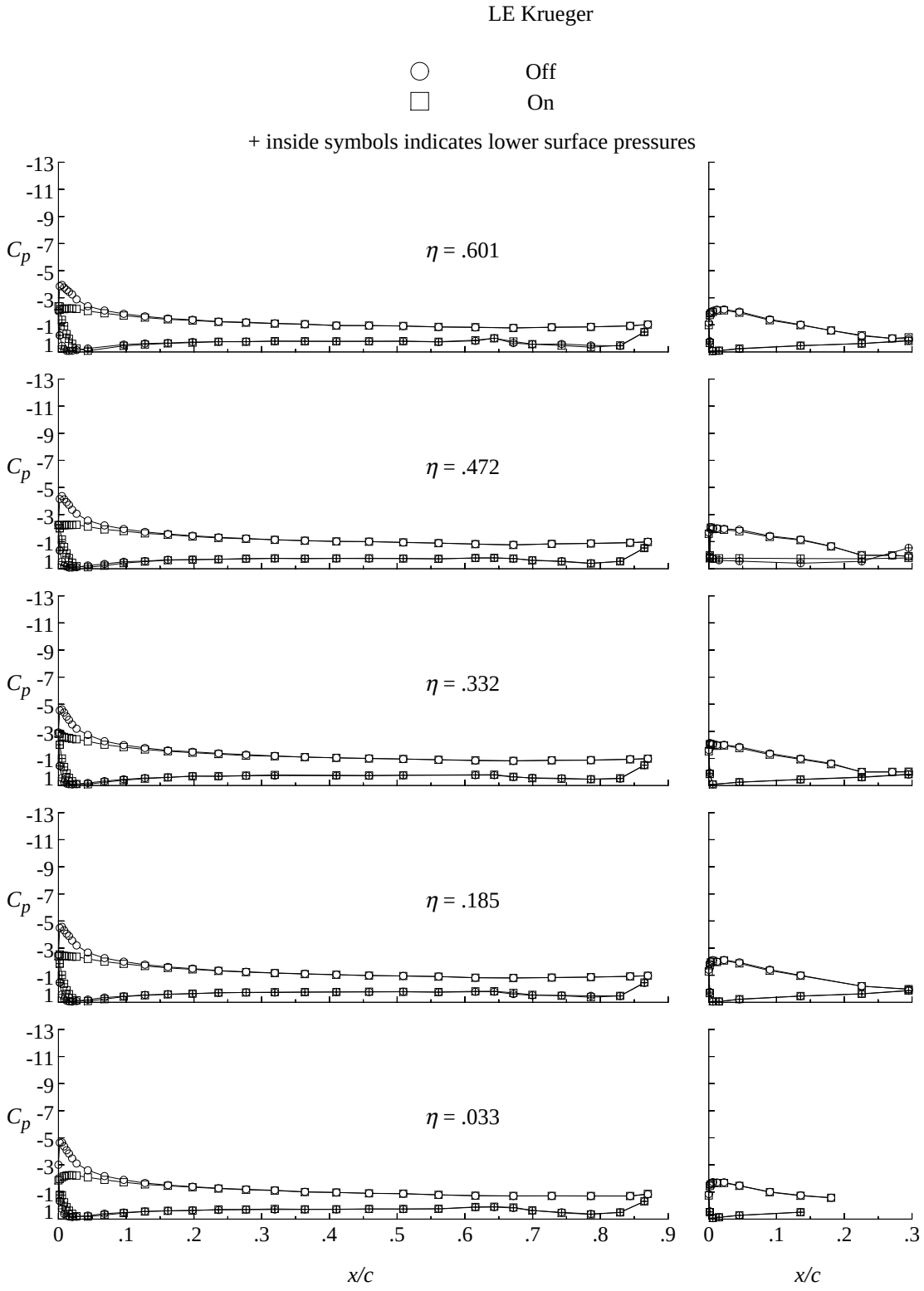


(f) $\alpha = 6°$.

Figure 11. Continued.

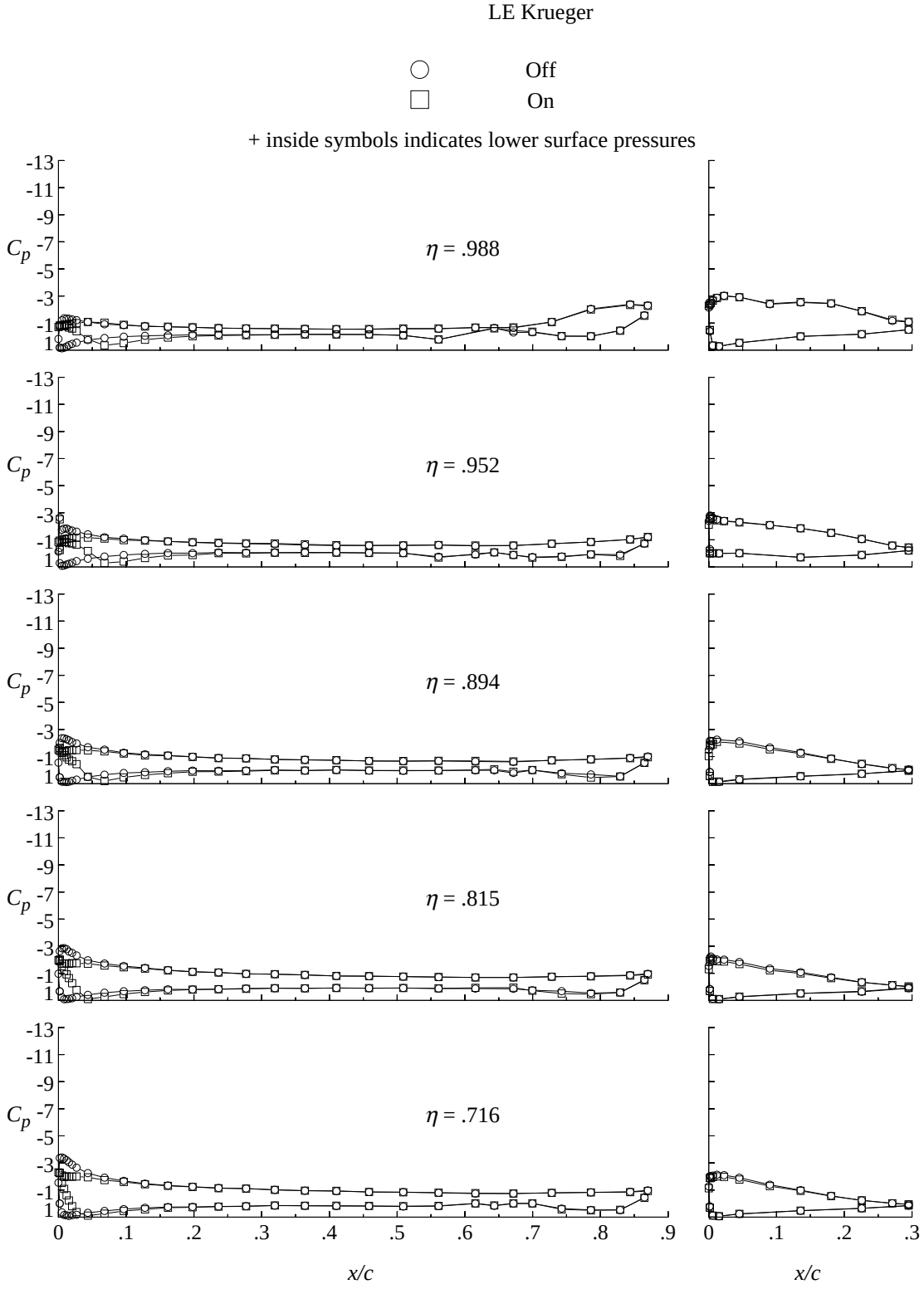


(f) Concluded.

Figure 11. Continued.

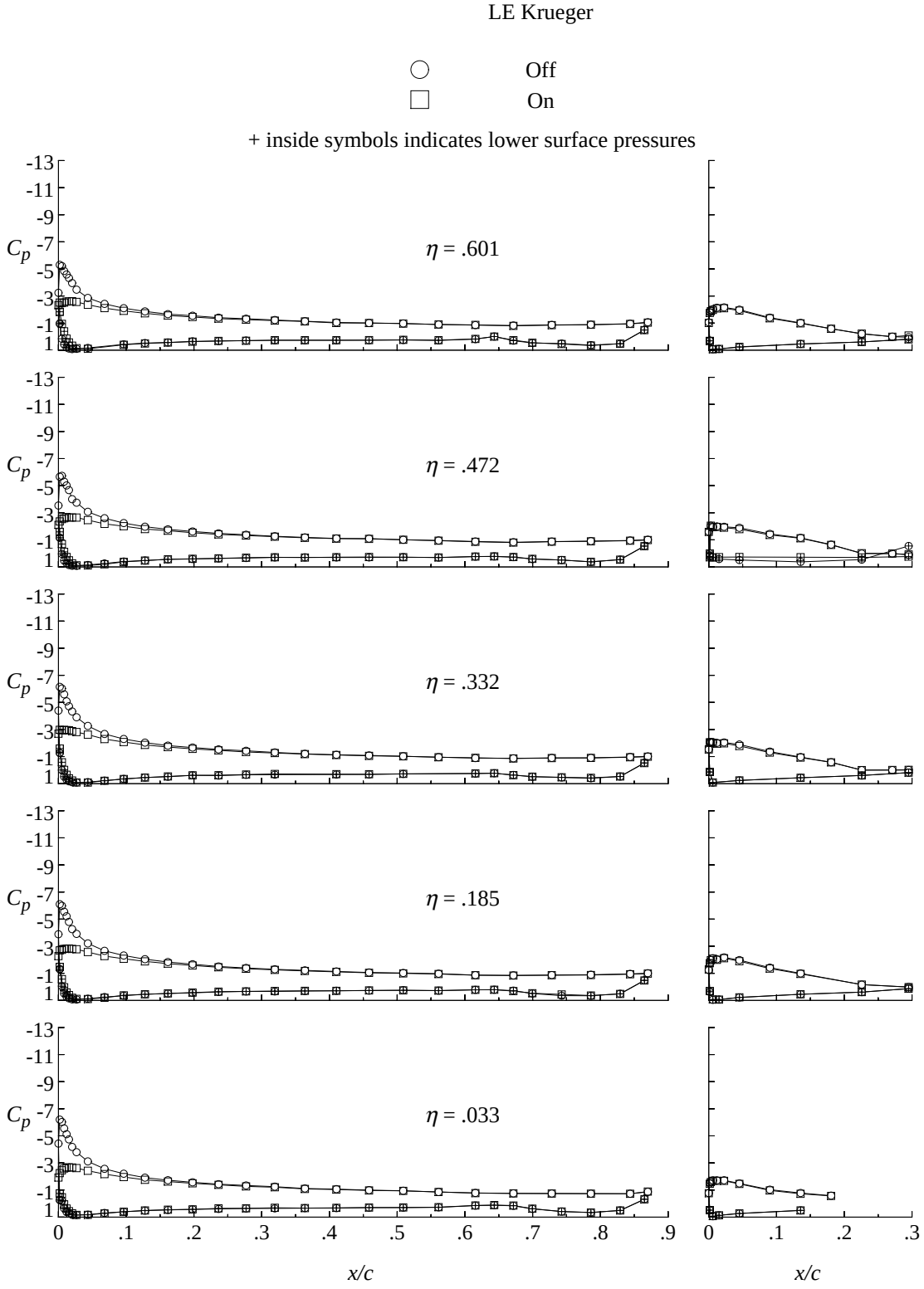


(g) $\alpha = 8°$.

Figure 11. Continued.

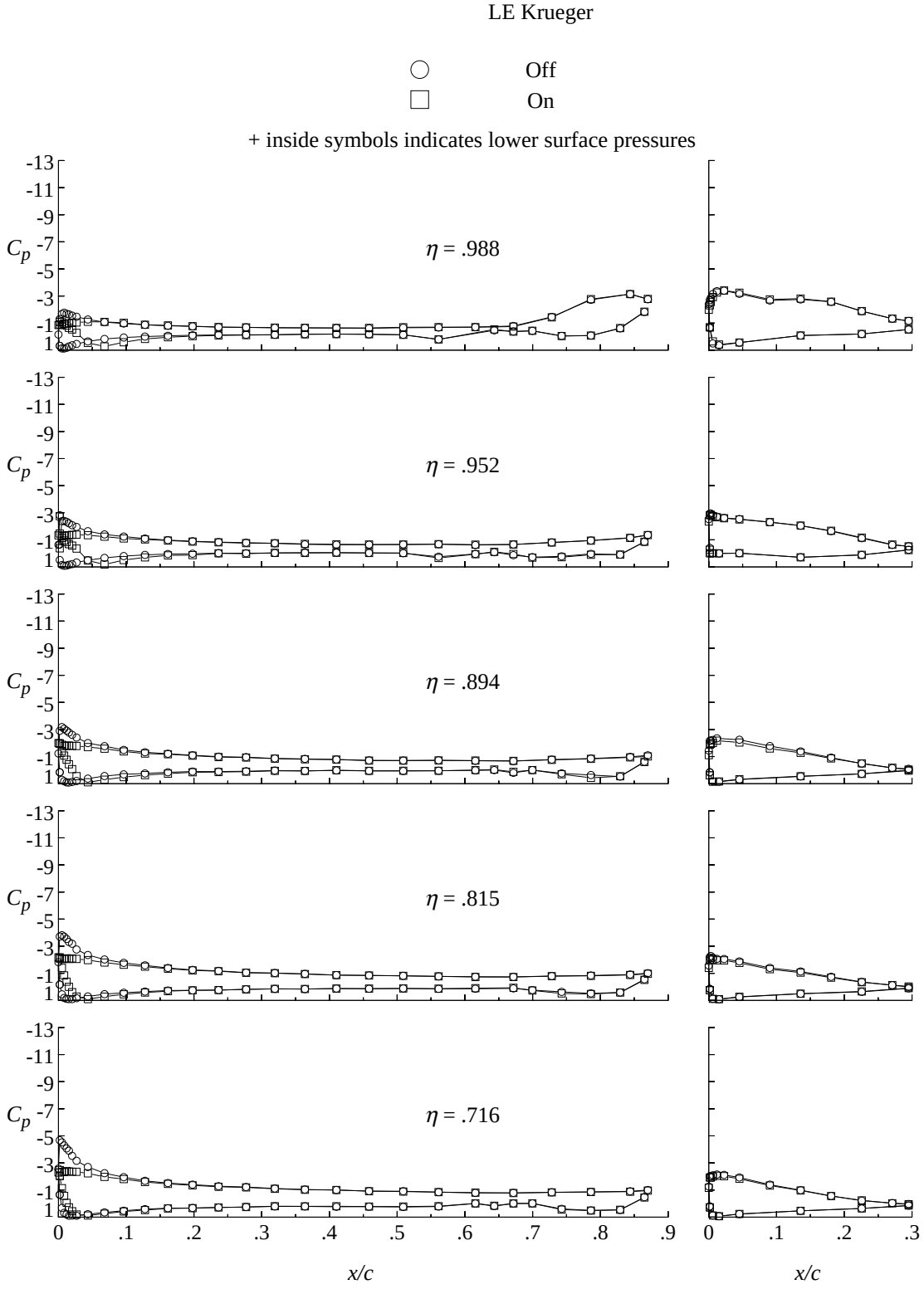


(g) Concluded.

Figure 11. Concluded.

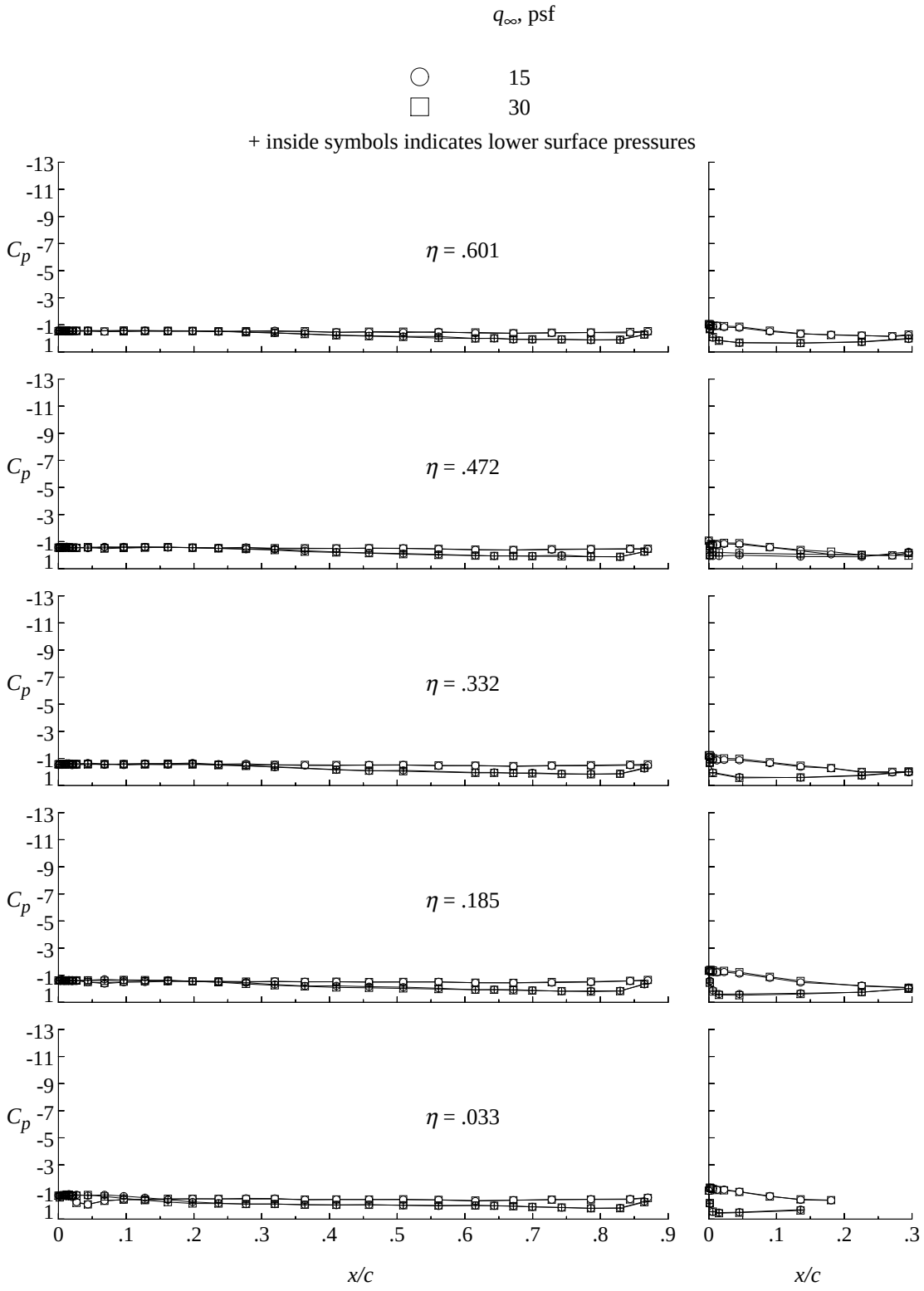


(a) $\alpha$ = - 4°.

Figure 12. Free-stream speed effect on high-lift wing pressure distribution. Tunnel floor boundary layer suction on.

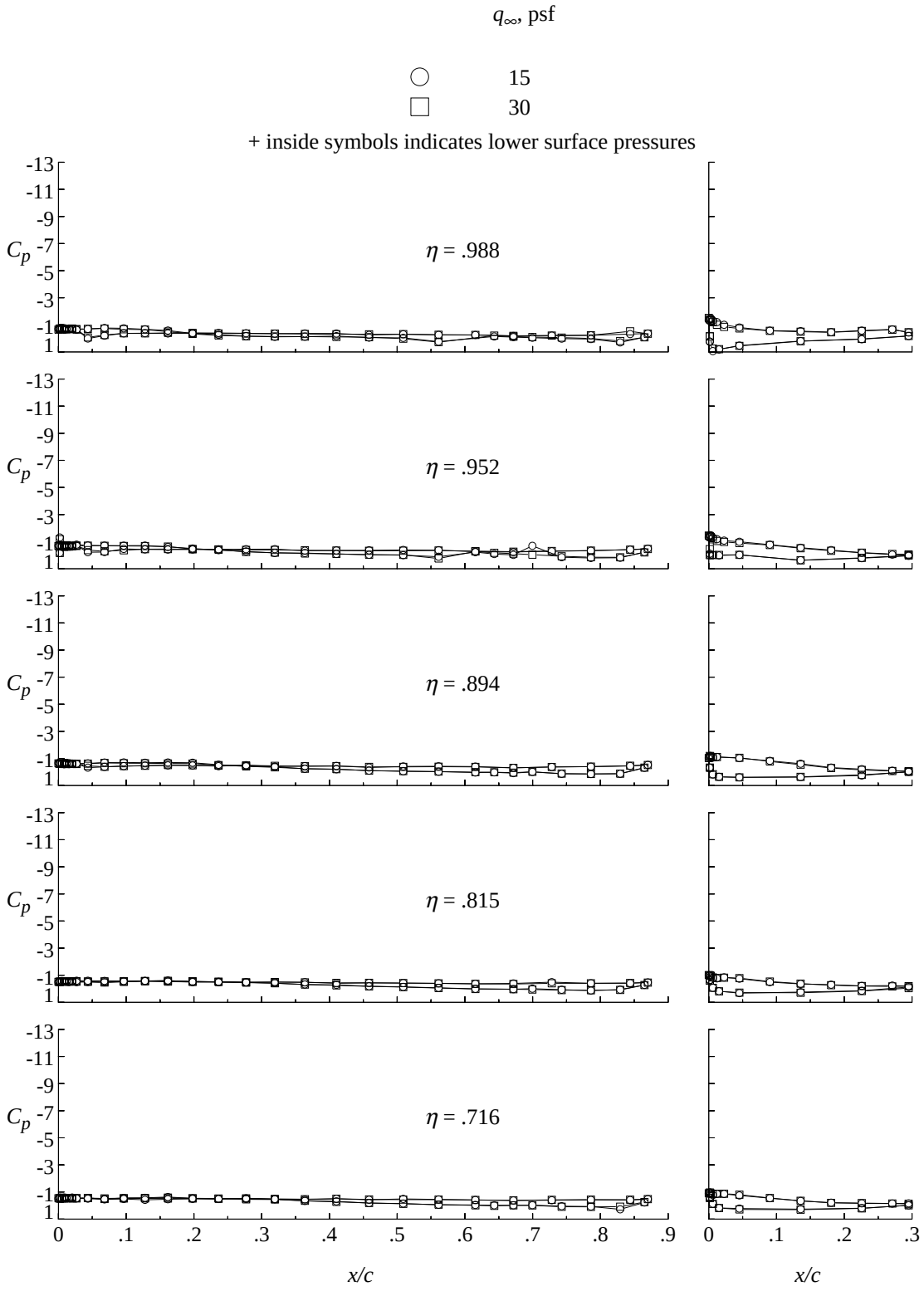


(a) Concluded.

Figure 12. Continued.

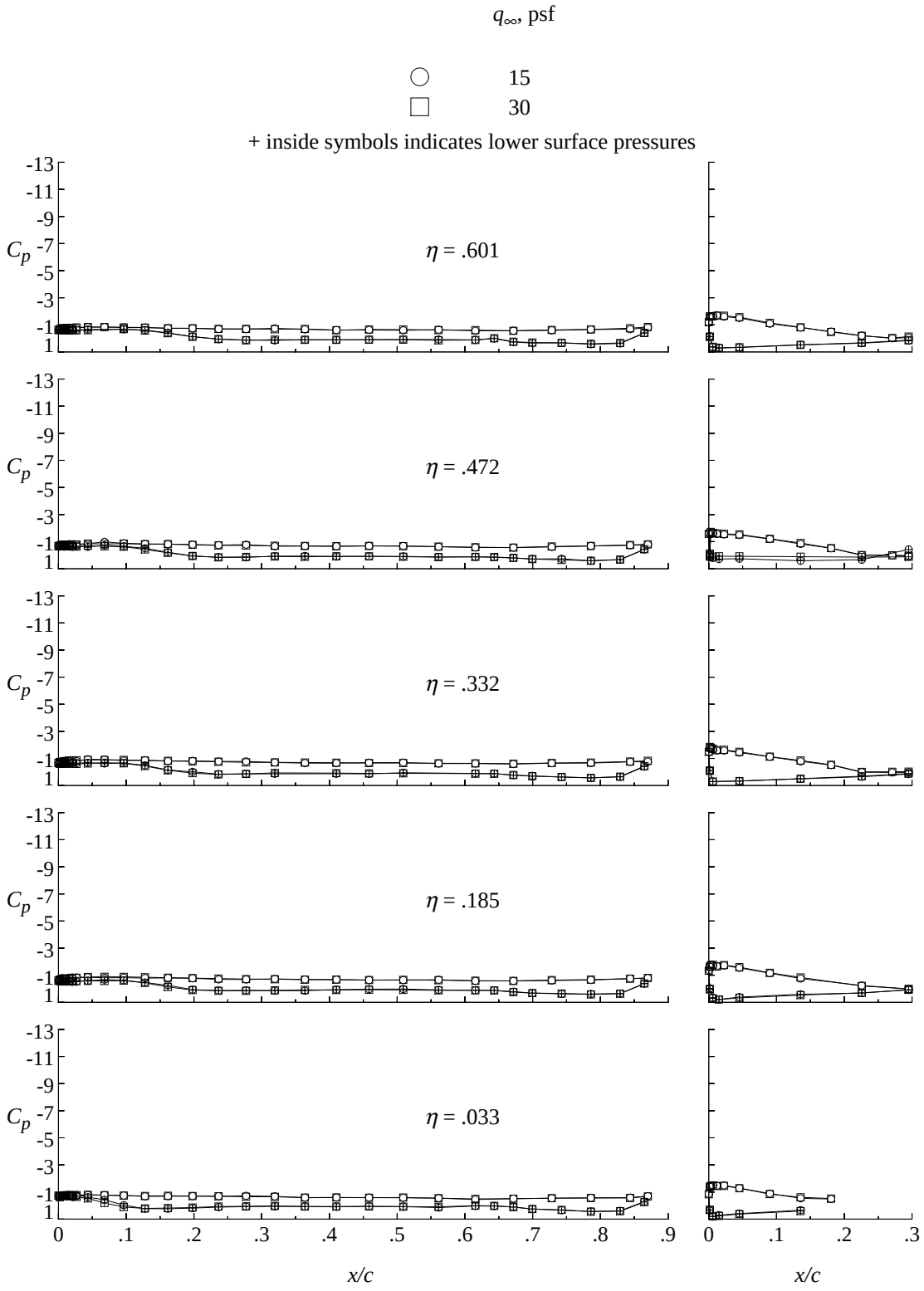


(b) $\alpha$ = - 2°.

Figure 12. Continued.

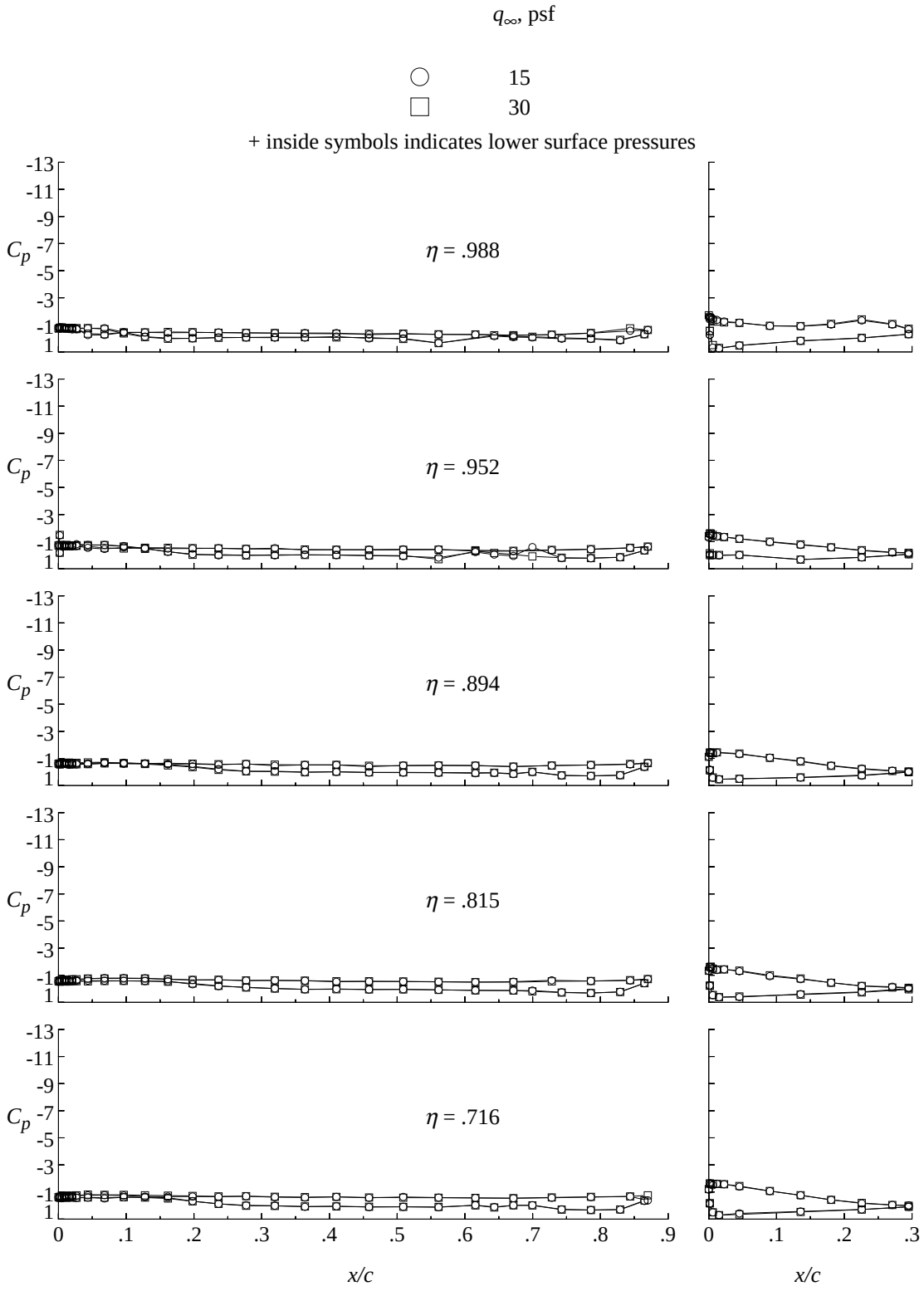


(b) Concluded.

Figure 12. Continued.

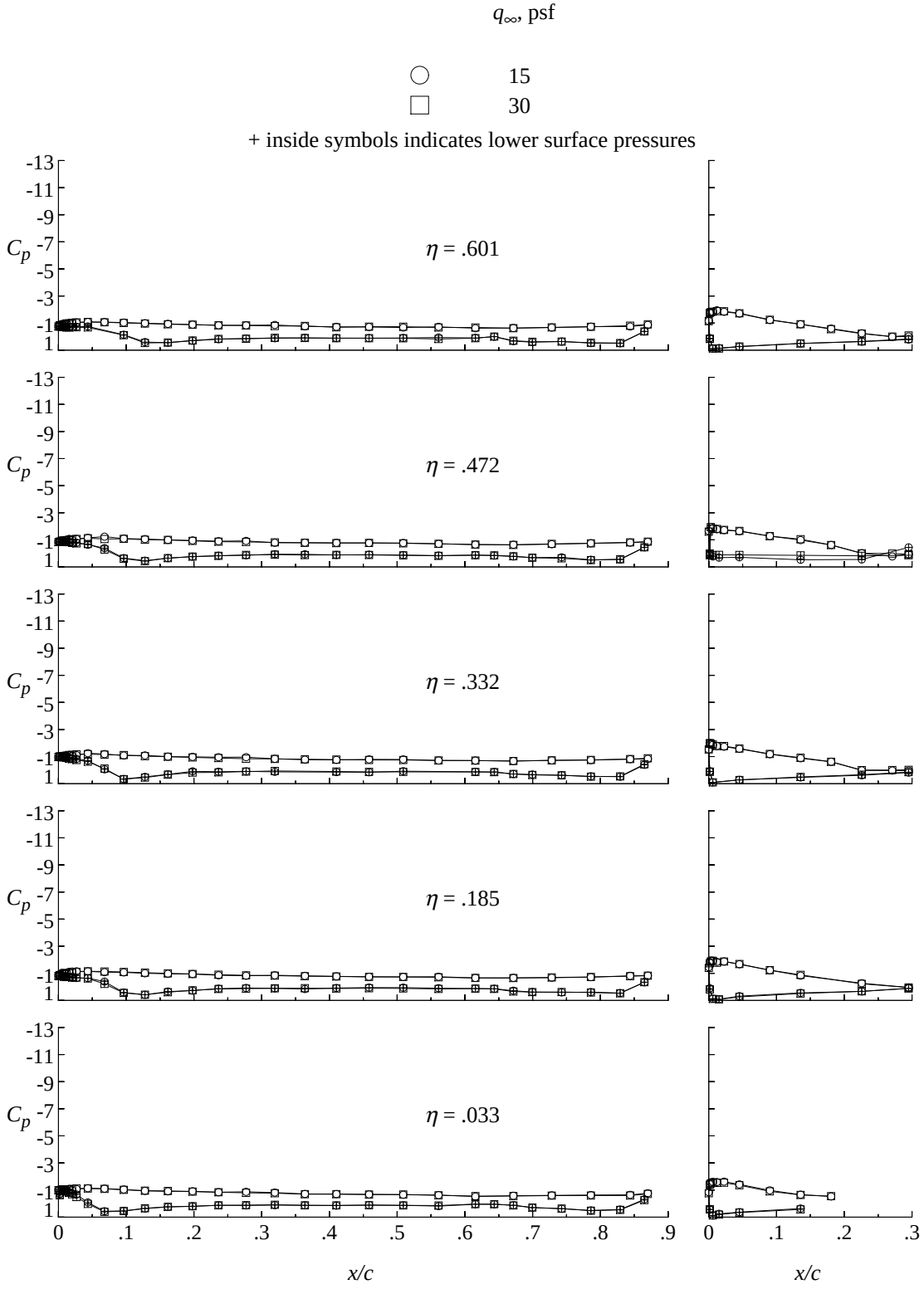


(c) $\alpha = 0°$.

Figure 12. Continued.

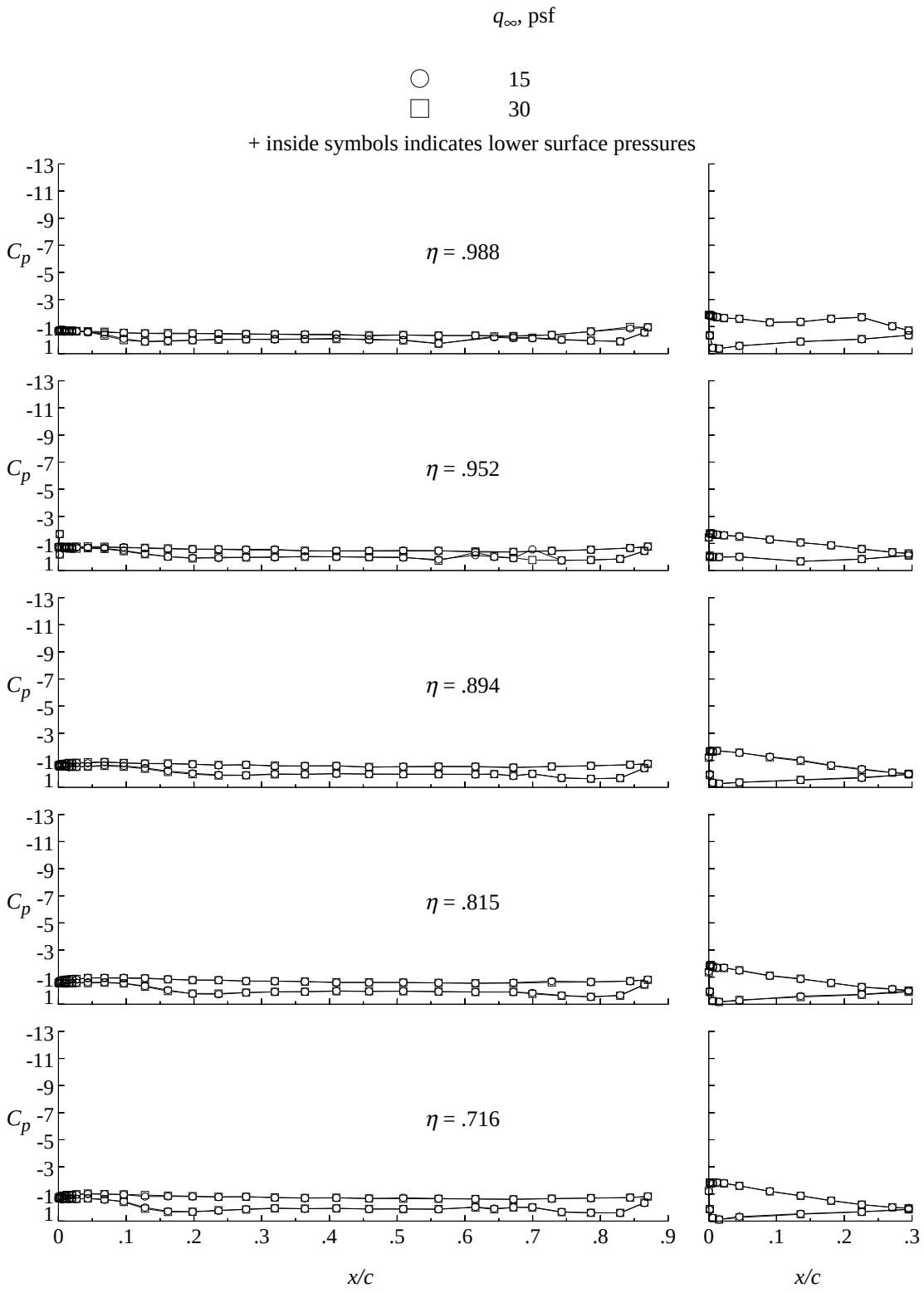


(c) Concluded.

Figure 12. Continued.

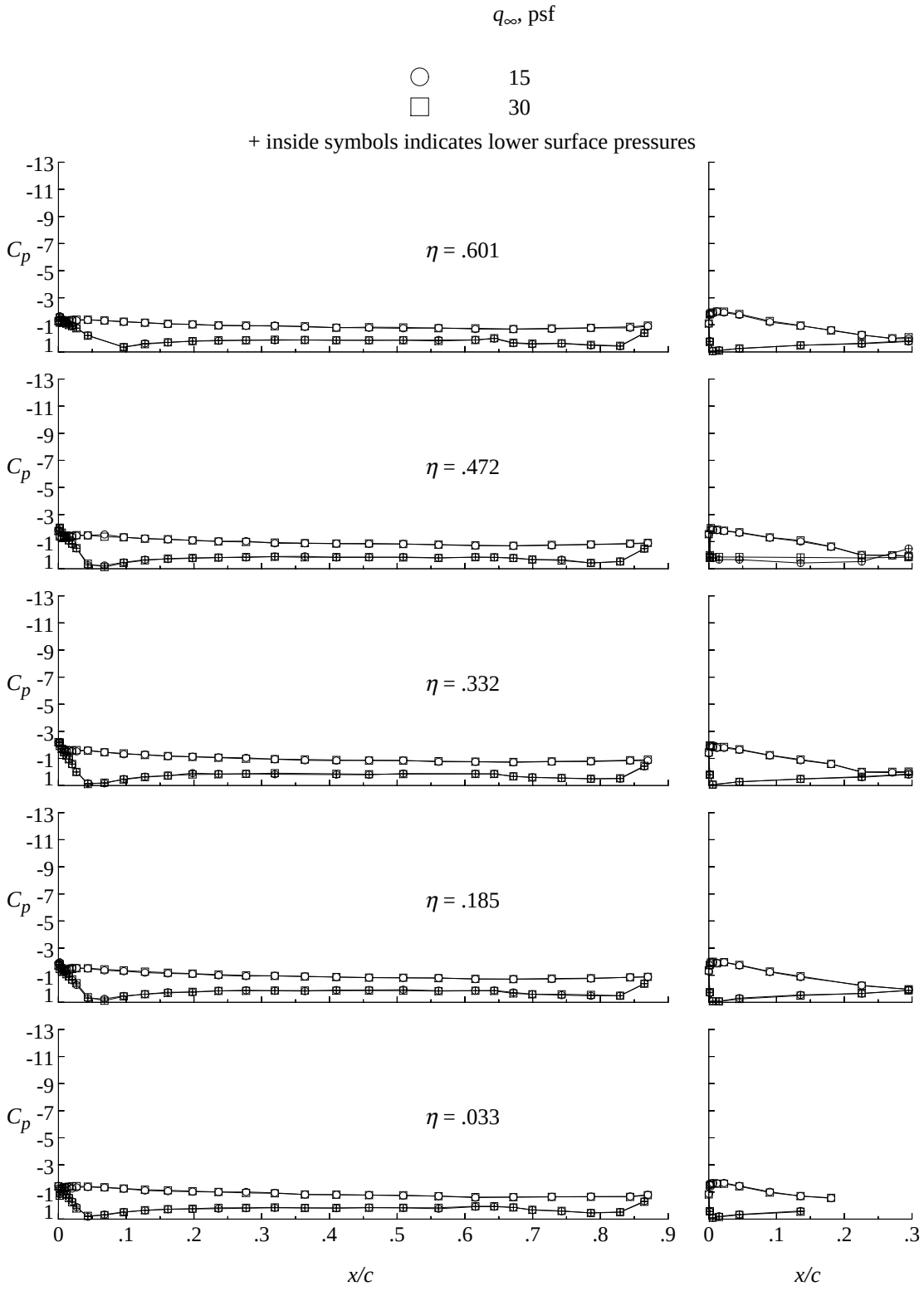


(d) $\alpha = 2°$.

Figure 12. Continued.

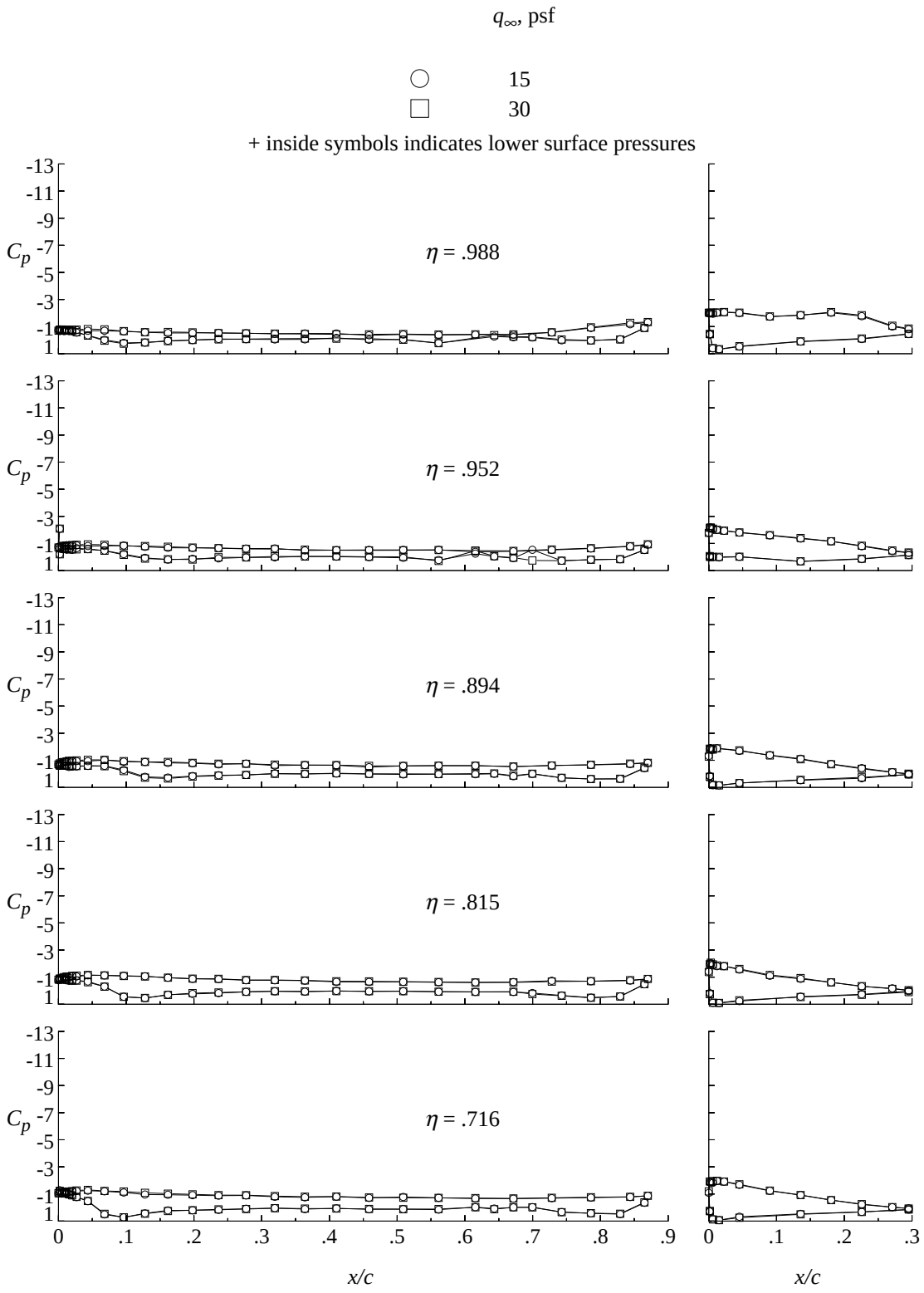


(d) Concluded.

Figure 12. Continued.

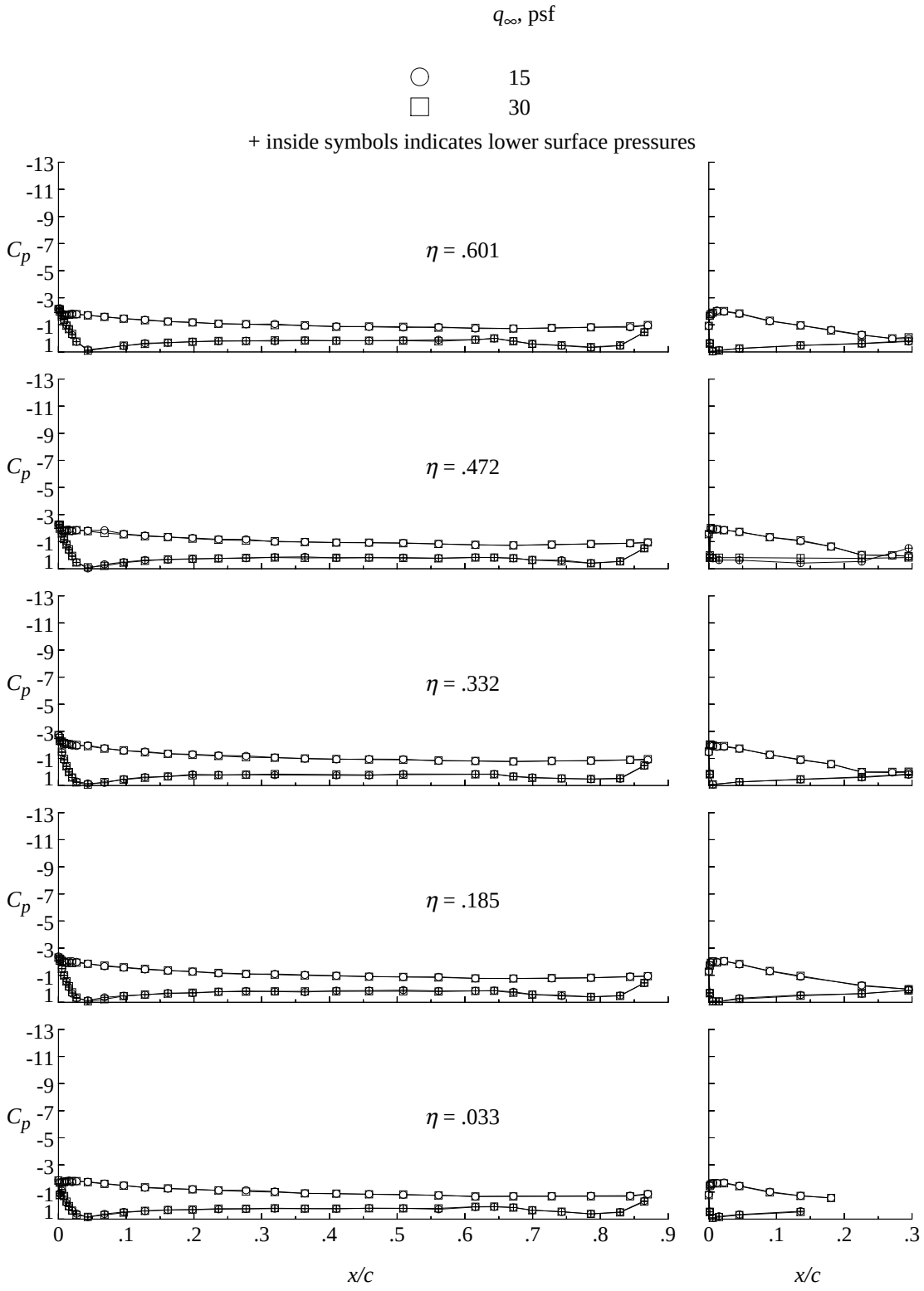


(e) $\alpha = 4°$.

Figure 12. Continued.

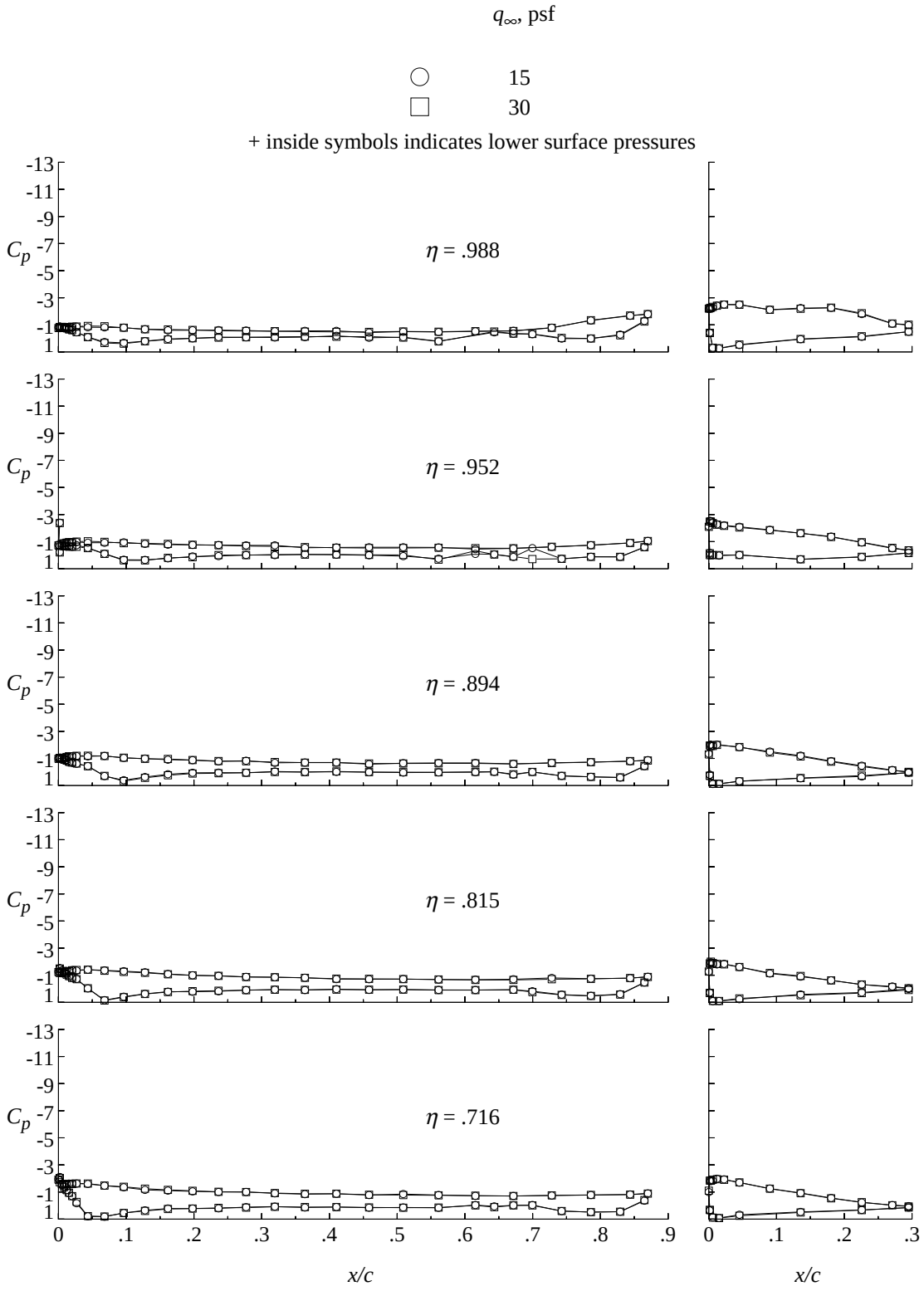


(e) Concluded.

Figure 12. Continued.

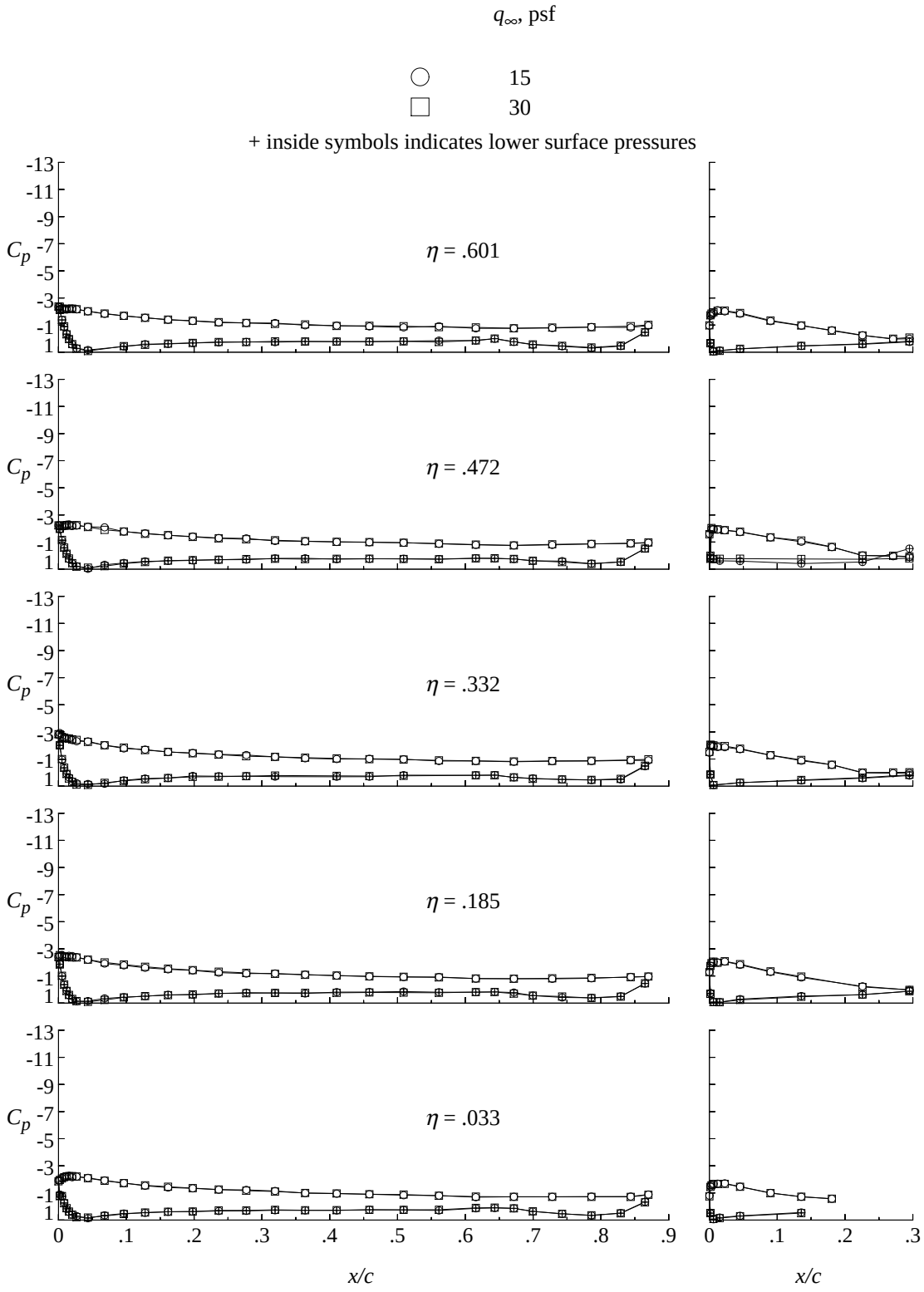


(f) $\alpha = 6°$.

Figure 12. Continued.

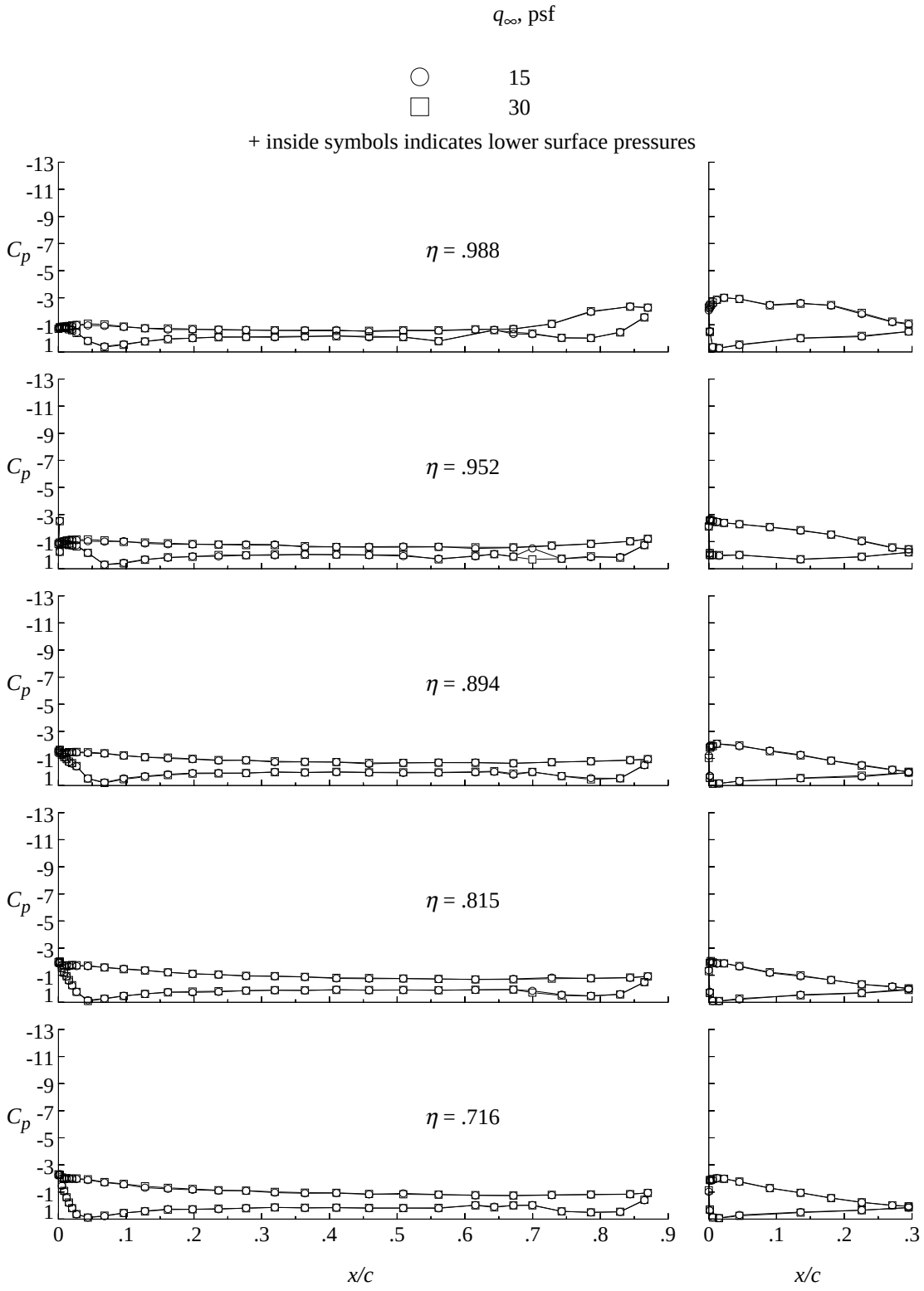


(f) Concluded.

Figure 12. Continued.

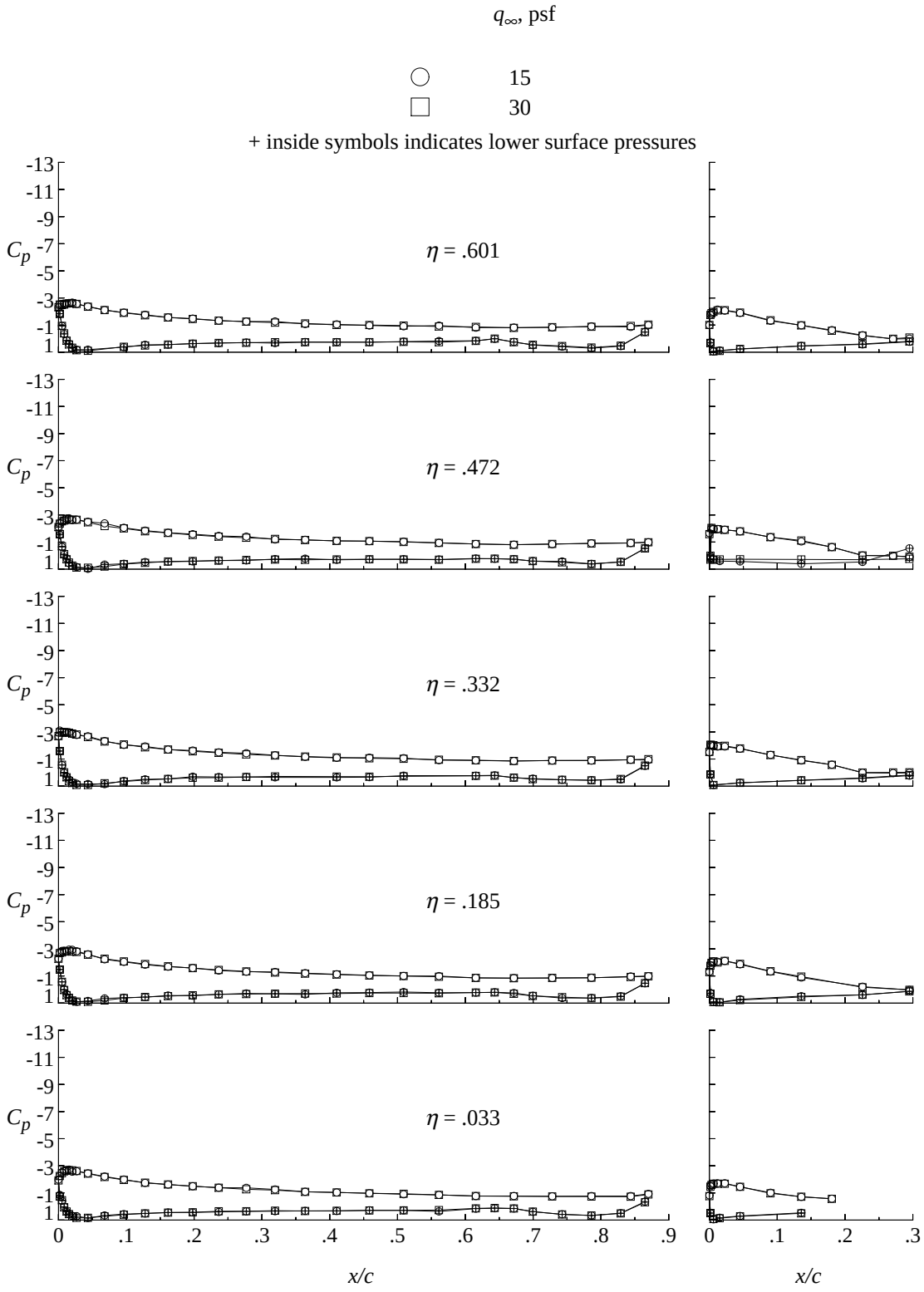


(g) $\alpha = 8°$.

Figure 12. Continued.

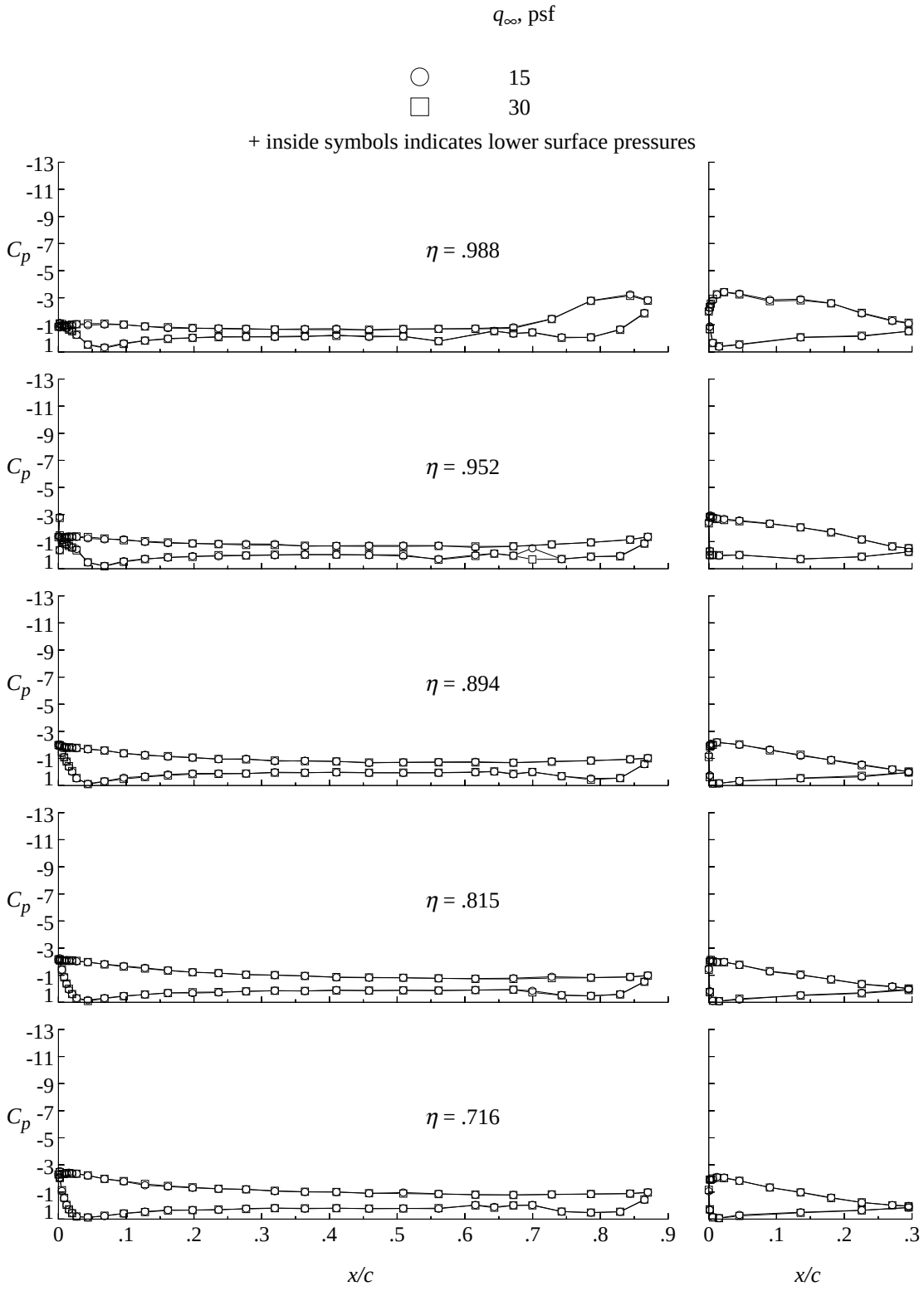


(g) Concluded.

Figure 12. Concluded.